

NONLINEAR DYNAMICS OF A DUAL-BACKPLATE CAPACITIVE MEMS
MICROPHONE

By

JIAN LIU

A DISSERTATION PRESENTED TO THE GRADUATE SCHOOL
OF THE UNIVERSITY OF FLORIDA IN PARTIAL FULFILLMENT
OF THE REQUIREMENTS FOR THE DEGREE OF
DOCTOR OF PHILOSOPHY

UNIVERSITY OF FLORIDA

2007

Copyright 2007

by

Jian Liu

To my parents and my beloved wife, Zhen

ACKNOWLEDGMENTS

Financial support for this research was provided in part by a National Science Foundation grant (ECS-0097636), and financial support from a NSF CAREER award (CMS-0348288) is also gratefully acknowledged.

First, I would like to express my sincere gratitude to my advisor, Professor Mark Sheplak, for giving me the opportunity to work at the Interdisciplinary Microsystems Group. His guidance over the years has been invaluable and his desire for excellence has had a very positive influence on me. I would like to thank my chair, Professor Brian P. Mann, for many valuable insightful talks and encouragement during this research. His guidance and help will always be cherished. I would also like to thank Professors Toshikazu Nishida, Louis N. Cattafesta, and Bhavani V. Sankar for their help and discussions on different aspects of this multidisciplinary research and for serving on my committee.

My acknowledgements go to all my colleagues at the Interdisciplinary Microsystems Group. Special thanks go to David Martin and Karthik Kadirvel for working together over the past five years and many valuable discussions on this research. In particular, I want to thank David Martin for helping me improve my English over the years.

I would like to express my deep appreciation to my parents for their endless support, understanding and guidance throughout my life. Finally, I would like to thank

my beloved wife, Zhen, for her love, patience and sacrifice, without which this dissertation would not have been done. I am forever grateful for her love.

TABLE OF CONTENTS

	<u>page</u>
ACKNOWLEDGMENTS	iv
LIST OF TABLES	x
LIST OF FIGURES	xii
ABSTRACT	xvii
CHAPTER	
1 INTRODUCTION	1
Nonlinear Dynamics Issues	2
Objective and Approach	5
Research Contributions.....	5
Dissertation Organization	6
2 BACKGROUND	7
Microphone Basics	7
Conventional versus Silicon Microphones	7
Metrics of Performance	8
Transduction Mechanisms	11
Introduction to Electromechanical Transducers	11
Piezoelectric Microphones	12
Piezoresistive Microphones.....	13
Optical Microphones	13
Electrostatic Microphones	14
Electrostatic Microphones	15
Electret Microphones.....	19
Condenser Microphones	22
Single-backplate condenser microphones	22
Dual-backplate condenser microphones.....	29
Major Previous Work on Capacitive Silicon Microphones	30
Basics of Nonlinear Dynamics	37
Nonlinearities	37
Steady State, Autonomous System and Fixed Point	37
Stability, Basin of Attraction and Phase Portrait.....	39

	Bifurcation	41
	Previous Work on Nonlinear Dynamics of Electrostatic MEMS Devices	42
3	NONLINEAR DYNAMIC MODEL.....	51
	Microphone Structure	51
	Displacement Solutions of the Diaphragm	52
	Small Displacement Solution	53
	Energy Method and Large Displacement Solution	54
	Procedure of energy method	55
	Large displacement solution.....	55
	Lumped Element Modeling of the Microphone	58
	Lumped Parameters of Diaphragm.....	59
	Lumped mass.....	60
	Lumped linear stiffness and compliance	61
	Lumped area	62
	Lumped cubic stiffness.....	63
	Lumped Damping Coefficient.....	63
	Lumped Stiffness of the Cavity	66
	Nonlinear Dynamic Model	70
	Discussion of Nonlinearities.....	72
	Nonlinear Finite Element Analyses.....	76
	Stiffnesses of the Diaphragm.....	77
	Electrostatic Forces by CoSolveEM Simulations.....	80
	Summary	83
4	APPROXIMATE SOLUTIONS OF NONLINEAR GOVERNING EQUATIONS..	84
	Introduction.....	84
	Governing Equation for the Electrical Square Wave Excitation	86
	Approximate MTS Solution for the Electrical Square Wave Excitation.....	89
	Approximate Solution by the MTS Method.....	90
	Discussion of the MTS Approximate Solution.....	92
	Approximate solution with zero initial conditions	93
	Approximate solutions in other applications.....	94
	Validity Region of the Approximate MTS Solution	94
	Results of linear case.....	95
	Results of weakly nonlinear case	96
	Results of highly nonlinear case.....	98
	Governing Equation for the Electrical Sinusoidal Excitation.....	100
	Approximate HB Solution for the Electrical Sinusoidal Excitation.....	103
	Approximate Solution by a HB Method.....	103
	Validity Region of the Approximate HB Solution.....	106
	Results of small THD case	106
	Results of transition THD case.....	108
	Results of large THD case.....	110
	Governing Equation for the Sinusoidal Acoustical Pressure Excitation	113

Approximate Solutions for the Sinusoidal Acoustical Pressure Excitation.....	116
HB Approximate Solution.....	117
MTS Approximate Solution.....	118
Validity Region of Approximate Solutions.....	120
Results of linear case.....	121
Results of weakly nonlinear case.....	122
Results of highly nonlinear case.....	123
Summary.....	125
5 PULL-IN INSTABILITIES.....	126
Quasi-Static Pull-in due to an Applied DC Voltage.....	126
Equilibrium Points and Local Stabilities.....	128
Graphical Analysis.....	131
Critical Quasi-Static Pull-in Voltage.....	132
Quasi-Static Pull-in by a Subcritical Pitchfork Bifurcation.....	134
Potential Advantage of Geometric Nonlinearity.....	136
Compact Quasi-Static Stable Operation Range.....	138
Quasi-Static Pull-in due to an Applied Acoustical Pressure.....	140
Equilibrium Points and Local Stabilities.....	141
Critical Quasi-Static Pull-in Pressure.....	144
Dynamic Pull-in due to a Mechanical Shock Load.....	148
Problem Formulation.....	149
Equilibrium Points and Local Stabilities.....	153
Phase Portrait and Basins of Attraction.....	155
Dynamic Pull-in due to a Mechanical Shock Load.....	158
Potential Advantage of Geometric Nonlinearity.....	162
Dynamic Pull-in due to an Acoustic Shock Load.....	164
Problem Formulation.....	164
Numerical Simulation Results.....	167
Simulated Dynamic Pull-in Results.....	169
Effect of Damping on Dynamic Pull-in.....	172
Effect of Geometric Nonlinearity on Dynamic Pull-in.....	173
Summary.....	175
6 SYSTEM IDENTIFICATION BY PRELIMINARY EXPERIMENTS.....	177
Experiment Setup and Procedures.....	177
Experiment Setup.....	177
Experiment Procedures.....	179
Procedures for the electrical square wave excitation.....	179
Procedures for the electrical sinusoidal excitation.....	180
Results of Electrical Square Wave Excitation.....	181
Results of Bottom Backplate Excitation.....	182
Results of Top Backplate Excitation.....	185
Results of Electrical Sinusoidal Excitation.....	187
Results of Bottom Backplate Excitation.....	188

Results of Top Backplate Excitation	190
Discussion of Analysis Results.....	191
Summary	193
7 CONCLUSIONS AND FUTURE WORK.....	194
Conclusions.....	194
Recommendations for Future Work.....	196
APPENDIX	
A LARGE DISPLACEMENT ENERGY SOLUTION OF A CIRCULAR DIAPHRAGM.....	199
B APPROXIMATE SOLUTION FOR A GENERAL NONLINEAR SECOND ORDER SYSTEM.....	204
Introduction.....	204
Approximate Solution by the Multiple Time Scales Method.....	205
C COEFFICIENTS OF THE APPROXIMATE HARMONIC BALANCE SOLUTION	213
D APPROXIMATE SOLUTIONS FOR A SINUSOIDAL ACOUSTICAL PRESSURE EXCITATION	215
HB Approximate Solution	217
MTS Approximate Solution	220
E UNCERTAINTY ANALYSIS	227
Uncertainty Analysis Methods	227
Uncertainty Sources.....	229
Uncertainty in the Experimental Data	229
Errors of Approximate Solutions and Nonlinear Least-Squares Algorithms....	230
Uncertainties Caused by the Fabrication Process.....	231
Preliminary Uncertainty Analysis Results.....	231
LIST OF REFERENCES.....	237
BIOGRAPHICAL SKETCH	248

LIST OF TABLES

<u>Table</u>	<u>page</u>
2-1 Major previous work in capacitive silicon microphones.	31
3-1 Material properties and physical parameters of the 2000Pa microphone in metric units (material: polysilicon).	67
3-2 Major specifications of the diaphragm mesh with converged displacement results.	78
3-3 Comparison of nonlinear FEA and LEM results.....	80
4-1 Given and extracted (via MTS solution) parameters for a linear case.....	96
4-2 Given and extracted parameters (via MTS solution) for a weakly nonlinear case...97	
4-3 Given and extracted (via MTS solution) parameters for a highly nonlinear case...98	
4-4 Results of the maximum error and sum of residual squares for each test case.	100
4-5 Given and extracted (via HB solution) parameters for the small THD case.....	108
4-6 Given and extracted (via HB solution) parameters for the transition THD case. ...	110
4-7 Given and extracted (via HB solution) parameters for the large THD case.....	112
4-8 Results of the maximum error and sum of residual squares for each test case.	112
4-9 Parameters used for the comparison of approximate and numerical solutions.	121
5-1 Force parameters for a designed 2000Pa capacitive MEMS microphone.....	128
5-2 Parameters for the numerical study of an N-wave excitation.	168
6-1 Results of system parameters of the bottom backplate excitation.....	184
6-2 Results of system parameters of the top backplate excitation.....	187
6-3 Amplitudes and phase of the integrated averaged steady-state center displacement of the bottom backplate excitation.	189

6-4	Results of system parameters of the bottom backplate excitation.....	190
6-5	Amplitudes and phase of the integrated averaged steady-state center displacement of the top backplate excitation.	190
6-6	Results of system parameters of the top backplate excitation.....	191
6-7	Theoretical mean values and uncertainties of system parameters for a given 95% confidence level.....	191
6-8	Nominal values of system parameters of the microphone.	192
E-1	Uncertainties caused by the fabrication process for a 95% confidence level.	231
E-2	Sensitivity coefficients used in the uncertainty analysis.	235
E-3	Theoretical mean values and uncertainties of system parameters caused by fabrication for a given 95% confidence level.....	236

LIST OF FIGURES

<u>Figure</u>	<u>page</u>
1-1 Schematic of a dual-backplate capacitive MEMS microphone.....	3
1-2 Schematic of an electrical model of the microphone.	3
2-1 A typical frequency response plot with a defined sensitivity and bandwidth.	8
2-2 Typical noise power spectral density plot for a microphone.	9
2-3 Time histories and power spectra of a pure and two distorted sinusoidal waves.....	10
2-4 A simplified model of an electrostatic microphone.	15
2-5 Schematic of a capacitive microphone with an electret diaphragm.	19
2-6 A simplified quasi-static model of an electret microphone.....	20
2-7 Illustration of the critical bias charge of an electret microphone.	21
2-8 Schematic of a single-backplate condenser microphone.....	22
2-9 Illustration of mechanical and electrostatic forces for a single-backplate condenser microphone.....	24
2-10 Illustration of quasi-static pull-in of a single-backplate condenser microphone.	25
2-11 Simplified circuit of a single-backplate condenser microphone with a preamplifier.	26
2-12 Effect of cubic nonlinearity on the system frequency response.....	38
2-13 Phase plane trajectories around fixed points of a dual-backplate capacitive MEMS microphone (sink points are indicated by blue crosses, and saddle points are indicated by blue circles).....	40
2-14 Typical bifurcation diagrams for one-dimensional autonomous systems: (a) Saddle-node bifurcation; (b) Pitchfork bifurcation; (c) Transcritical bifurcation.	41
3-1 3D cross-section view of the microphone structure (not to scale).	52

3-2	Top-view photograph of the microphone.....	52
3-3	Schematic of a clamped circular diaphragm under a transverse uniform pressure loading.....	53
3-4	Displacement components in the neutral plane of a circular diaphragm.	56
3-5	Normalized mode shape for several pressure values (2000, 10000 and 100000 Pascals).....	58
3-6	Repetitive pattern of holes in the top backplate.	64
3-7	Simplified lumped element model of a dual-backplate capacitive microphone.	68
3-8	A nonlinear dynamic model of a dual-backplate capacitive microphone.	70
3-9	Free body diagram of the nonlinear dynamic model.....	71
3-10	Nonlinear vs. linearized mechanical and electrical forces of a single-backplate capacitive microphone.....	74
3-11	Nonlinear vs. linearized mechanical and electrical forces of a dual-backplate capacitive microphone.....	76
3-12	3D mesh of the diaphragm in CoventorWare 2003.....	77
3-13	Transverse center deflections of the diaphragm under the uniform pressure.....	78
3-14	Displacement contour of the diaphragm under the 2000Pa uniform pressure (not to scale in the thickness direction).	79
3-15	Plot of simulated and modeled electrostatic forces for the top capacitor.....	81
3-16	Plot of simulated and modeled electrostatic forces for the bottom capacitor.	82
4-1	Dynamic model for an electrical square wave excitation on the top backplate.	86
4-2	Plot of electrostatic and approximate electrostatic forces.	87
4-3	Comparison of simulated and MTS-based curve fitting center displacement results.	96
4-4	Comparison of simulated and MTS-based curve fitting center displacement results.	97
4-5	Comparison of simulated and MTS-based curve fitting center displacement results.	99
4-6	Dynamic model for an electrical sinusoidal excitation on the bottom backplate...101	

4-7	Simulated sinusoidal response of the diaphragm.	107
4-8	Simulated power spectrum of the steady state displacement.	108
4-9	Simulated sinusoidal response of the diaphragm.	109
4-10	Simulated power spectrum of the steady state displacement.	109
4-11	Simulated sinusoidal response of the diaphragm.	111
4-12	Simulated power spectrum of the steady state displacement.	111
4-13	Dynamic model for the sinusoidal acoustical pressure excitation.	113
4-14	Plot of net electrostatic and approximate net electrostatic forces.	114
4-15	Comparison of the steady-state non-dimensional amplitudes of the approximate and numerical solutions for a linear case.	122
4-16	Comparison of the steady-state non-dimensional amplitudes of the approximate and numerical solutions for a weakly nonlinear case.	123
4-17	Comparison of the steady-state non-dimensional amplitudes of the approximate and numerical solutions for a highly nonlinear case.	124
5-1	Plot of the ND mechanical and net electrostatic forces.	131
5-2	Plot of the ND mechanical and net electrostatic forces.	133
5-3	A subcritical pitchfork bifurcation illustrating quasi-static pull-in due to an applied DC voltage.	135
5-4	A subcritical pitchfork bifurcation illustrating quasi-static pull-in due to an applied DC voltage (versus bias voltages).	136
5-5	Plot of a non-dimensional net electrostatic force and different non-dimensional mechanical forces.	137
5-6	Quasi-static stable operation range of the microphone in a 3D space.	138
5-7	Quasi-static stable operation range of the microphone in a 3D space (versus DC voltages).	139
5-8	Plot of the ND net restoring and electrostatic forces.	143
5-9	Plot of the ND net restoring and electrostatic forces.	145
5-10	Quasi-static pull-in due to varying ND parameters.	146

5-11	Quasi-static pull-in due to varying acoustic pressure and DC bias voltage.	147
5-12	Three commonly used nonlinear mechanical shock load models (impulse, half sine and triangle).	152
5-13	Phase plane trajectories around the equilibrium points.	155
5-14	Three basins of attraction for a DC bias of 25 V.	156
5-15	Basins of attraction within the physical backplates for a DC bias of 25 V.	157
5-16	Stable and unstable non-dimensional center displacement responses with two initial non-dimensional velocities.	159
5-17	Phase plots of a stable response and a dynamic pull-in due to a large initial velocity imposed by a mechanical shock load.	159
5-18	Dynamic pull-in due to a combination of DC bias voltage and a mechanical shock load.	161
5-19	Phase plane trajectories for an added geometric nonlinearity case. Sink points are indicated by blue crosses, and saddle points are indicated by blue circles.	162
5-20	Expanded stable operation region of the microphone due to the added geometric nonlinearity.	163
5-21	A typical N-wave with an amplitude and a duration time.	165
5-22	The Fourier transform of a typical N-wave.	166
5-23	Transient non-dimensional center displacement response of diaphragm due to an N-wave with an amplitude of 125 dB SPL and a duration time of 2 ms.	168
5-24	Transient non-dimensional center velocity response of diaphragm due to an N-wave with an amplitude of 125 dB SPL and a duration time of 2 ms.	169
5-25	Dynamic pull-in due to an N-wave with a ND amplitude of 1.29 and a ND duration time of 2.3.	170
5-26	Threshold of dynamic pull-in due to an N-wave.	170
5-27	Threshold of dynamic pull-in due to an N-wave with a normalized pressure parameter.	172
5-28	Effect of damping on dynamic pull-in threshold.	173
5-29	Effect of geometric nonlinearity on dynamic pull-in threshold.	174
6-1	Block diagram of the experiment setup.	178

6-2	Laser beam spot (red dot) impinges the diaphragm through the center hole of the top backplate.	179
6-3	Simplified circuit to generate the high voltage signal.	181
6-4	Measured averaged center velocity response for an applied square wave with an amplitude of 5V.	182
6-5	Integrated center displacement response for an applied square wave with an amplitude of 5V.	183
6-6	Constructed phase plot for an applied square wave with an amplitude of 5V.	183
6-7	Comparison of integrated and curve-fit center displacements for an applied square wave with an amplitude of 5V.	184
6-8	Measured averaged center velocity response for an applied square wave with an amplitude of 18V.	185
6-9	Integrated center displacement response for an applied square wave with an amplitude of 18V.	186
6-10	Constructed phase plot after 12 μ s for an applied square wave with an amplitude of 18V.	186
6-11	Comparison of integrated and curve-fit center displacements for an applied square wave with an amplitude of 18V.	187
6-12	Measured averaged steady-state center velocity response (asterisk) for a sinusoidal excitation with an amplitude of 9V and a frequency of 114.4 kHz.	188
6-13	Comparison of the integrated (red asterisk) and curve-fitting (blue solid line) steady-state center displacement results for a sinusoidal excitation with an amplitude of 9V and a frequency of 114.4 kHz.	189

Abstract of Dissertation Presented to the Graduate School
of the University of Florida in Partial Fulfillment of the
Requirements for the Degree of Doctor of Philosophy

NONLINEAR DYNAMICS OF A DUAL-BACKPLATE CAPACITIVE MEMS
MICROPHONE

By

Jian Liu

May 2007

Chair: Brian P. Mann

Cochair: Mark Sheplak

Major Department: Mechanical and Aerospace Engineering

This work presents an investigation of the electromechanical nonlinear dynamics of a dual-backplate capacitive MEMS (microelectromechanical systems) microphone. A large displacement solution via an energy method has been utilized to provide linear and cubic lumped stiffnesses of the circular diaphragm of the microphone. A nonlinear dynamic model of the microphone is developed using lumped element modeling. Theoretical lumped stiffnesses of the diaphragm are verified by nonlinear finite element analyses and the errors for the linear and cubic stiffnesses are approximately 1.3% and 5.0% respectively.

The critical quasi-static pull-in voltage of the microphone is found to be approximately 41V both analytically and numerically. The phenomenon of quasi-static pull-in due to an applied DC voltage is illustrated by a subcritical pitchfork bifurcation. By using a phase portrait and basin of attraction, a mechanical shock load is related to

dynamic pull-in. Further study shows that dynamic pull-in could potentially take place below the critical quasi-static pull-in voltage when the microphone is subject to a large mechanical shock load. The dynamic pull-in due to an acoustical pulse, in the form of an N-wave, has been investigated by using numerical simulation. A dynamic pull-in threshold curve has been obtained in terms of the duration time and amplitude of the N-wave for a given DC bias voltage.

Studies of dynamic pull-in also show that several nonlinearities (geometric, electrostatic and mechanical/acoustical shock) compete with each other. An increased electrostatic nonlinearity and/or an increased mechanical/acoustical shock load destabilize the system while an increased geometric nonlinearity helps to stabilize the microphone and expands the stable operational range.

The multiple time scales and harmonic balance methods are applied to obtain approximate solutions of the nonlinear governing equations under the electrical square, electrical sinusoidal and sinusoidal acoustical excitations. Based on the two approximate solutions for the electrical excitations and a nonlinear least-squares curve-fitting technique, system parameters are extracted from two types of experimental data. The preliminary uncertainty analysis, which includes only the uncertainties caused by fabrication, shows that the experimentally extracted linear natural frequency, damping ratio and nonlinear stiffness parameter fall within their conservative theoretical ranges for a 95% confidence level.

CHAPTER 1 INTRODUCTION

During the past three decades, the demand for reducing noise pollution, especially in communities surrounding airports, has increased. To abate the aircraft noise, the generation and propagation of noise sources must be characterized. Aeroacoustic measurement tools are required to both investigate mechanisms of noise generation and validate methods of noise reduction [1]. To enable aeroacoustic measurements, measurement microphones with the instrumentation grade, cost efficiency, and small size must be developed. Currently, commercial traditional microphones such as B&K condenser microphones are widely used in the field of aeroacoustic measurements; however, those microphones are costly and not suitable for miniaturization. With the recent advancements in microelectromechanical systems (MEMS) technology, batch fabrication of microphones with smaller sizes and lower prices is now possible. A variety of transduction schemes, such as piezoelectric, piezoresistive, capacitive and optical, have been used in MEMS microphones [2]. Capacitive MEMS microphones have shown the potential to provide a dynamic range of 160 dB and a bandwidth of 90 kHz, which are the key requirements to accommodate $1/8^{\text{th}}$ -scale aeroacoustic testing [1].

However, the development of capacitive MEMS microphones comes with several issues. The electrostatic force between the diaphragm and backplate of the microphone is inherently nonlinear. Pull-in instability [3, 4], a phenomenon in which the diaphragm collapses to the backplate or vice versa, occurs due to a large applied voltage and/or a large displacement. Since pull-in results in structural failure of the device when the

process is not reversible, the microphone needs to be carefully designed to operate in a stable domain. In addition, the mechanical restoring force of the diaphragm becomes nonlinear for large displacements. Both mechanical and electrostatic nonlinearities interact with each other, which adds more nonlinear distortion and lowers the fidelity of the microphone. Moreover, an increased electrostatic nonlinearity could potentially destabilize the microphone system while a larger mechanical geometric nonlinearity could help to stabilize the microphone and expands the stable operation range. Therefore, a thorough understanding of aforementioned nonlinear issues becomes vital for the success of the capacitive MEMS microphone.

This dissertation is part of a larger effort to develop a dual-backplate capacitive MEMS microphone for aeroacoustic applications. The focus of this dissertation is to investigate the electromechanical nonlinear dynamics of the microphone through theoretical analysis, numerical simulation and preliminary experimental characterization. In summary, the study of this dissertation will help improve the overall performances of the microphone through a better understanding of the nonlinear dynamics issues.

Nonlinear Dynamics Issues

This section presents an overview of the nonlinear dynamics of a dual-backplate capacitive MEMS microphone. Different types of nonlinearities are discussed and some physical mechanisms are provided. Further details concerning the nonlinear model will be discussed in Chapter 3.

A simplified schematic of a typical dual-backplate capacitive MEMS microphone is shown in Figure 1-1. The backplates of the microphone are perforated to let the air pass through them and hence reduce the air-streaming resistance. Two gaps are formed

between the diaphragm and each backplate respectively. A cavity under the bottom backplate is vented to the ambient pressure resulting in an AC measurement device.

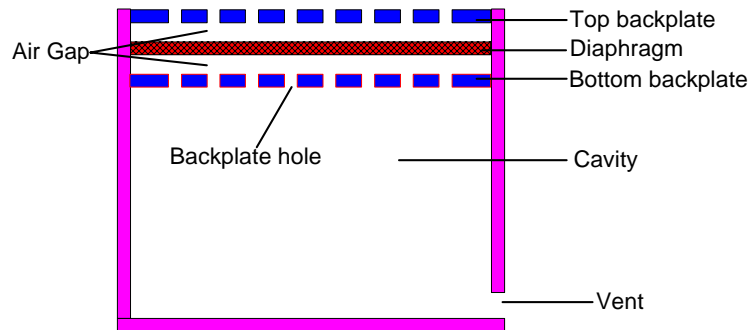


Figure 1-1. Schematic of a dual-backplate capacitive MEMS microphone.

The three plates of the microphone are made conductive; therefore, two capacitors are formed between the diaphragm and each backplate. When an acoustic wave impinges on the microphone, the incident pressure deflects the middle diaphragm and thereby alters the capacitance of the two capacitors as shown in Figure 1-2. The differential capacitance change is detected through various types of interface circuitry [5] to determine the input sound pressure level.

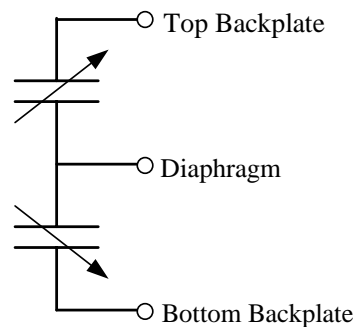


Figure 1-2. Schematic of an electrical model of the microphone.

When the diaphragm with a fixed boundary undergoes a large deflection with respect to its thickness, geometric nonlinearity [6] occurs and the restoring spring force becomes nonlinear. Under large deflections, the diaphragm behaves like a mechanical Duffing's spring, in which a hardening nonlinearity is caused by the mid-plane stretching.

This mechanical nonlinearity directly affects the upper limits of the linearity and dynamic range of the microphone. The details of geometric nonlinearity will be discussed in Chapter 3.

The net electrostatic force on the diaphragm is a nonlinear function of the mechanical displacement of the diaphragm, the gaps and the applied voltages between the backplates and diaphragm respectively. The net electrostatic force has singularities at the backplates, which will affect the upper dynamic range of the microphone. Although larger applied voltages and smaller gaps are desirable, because they increase the sensitivity of the microphone, the nonlinear net electrostatic force increases dramatically with larger applied voltages and smaller gaps. When the increasing net electrostatic force overcomes the nonlinear mechanical force, pull-in occurs. In a phase portrait, the pull-in point is an unstable fixed point for the microphone, which means that the displacement of the diaphragm continuously increases until the diaphragm crashes into one of the backplates.

Damping plays a very important role in determining the bandwidth and the dynamic response of the microphone. Damping in a dual-backplate capacitive MEMS microphone is dominated by viscous damping and a linearized version is usually used to approximate the actual damping. When the diaphragm vibrates, the gas flow between the diaphragm and backplates can be divided into the horizontal flow between the plates and the vertical flow through the backplate holes. Viscous damping caused by the horizontal gas flow is often called squeeze-film damping, and the viscous damping caused by the vertical gas flow is called holes resistance [7, 8]. The structural damping of the

diaphragm mainly consists of the thermoelastic energy dissipation inside the diaphragm and the vibration energy dissipation in the compliant boundary of the diaphragm [9, 10].

Objective and Approach

The objective of this research is to study the electromechanical nonlinear dynamics of a dual-backplate capacitive MEMS microphone. An investigation of the existing nonlinear dynamics issues is targeted to help improve the overall performance of the microphone. In addition, the knowledge gained from this study can be applied to other electrostatic devices, such as dynamic nano-indenters [11, 12] and MEMS mass sensors [13, 14]. To achieve the above research goal, several approaches are employed in this dissertation. Specifically, the nonlinear dynamical system is modeled via lumped element modeling and a general form of the nonlinear governing equation is obtained. Approximate analytical solutions to the nonlinear governing equations are obtained with multiple scales and harmonic balance analyses. Pull-in instabilities are explored by both analytical and numerical approaches. Finally, the microphone is experimentally characterized and system parameters of the nonlinear dynamic model are identified from the measured data.

Research Contributions

The contributions of this dissertation are summarized as follows.

- Development of a nonlinear dynamic model for a dual-backplate capacitive MEMS microphone and numerical solutions of the nonlinear governing equation.
- Development of approximate analytical solutions of the nonlinear governing equations via multiple time scales (MTS) and harmonic balance (HB) methods.
- Preliminary experimental characterization and application of the uncertainty analysis to the experimentally identified system parameters.

Dissertation Organization

The dissertation is organized into seven chapters. Chapter 1 introduces and describes the research work in this dissertation. The next chapter provides a background of the microphone, basics of nonlinear dynamics and a review of previous work done on both capacitive microphones and nonlinear dynamics of electrostatic MEMS devices. A nonlinear dynamical model for a dual-backplate capacitive MEMS microphone is developed in Chapter 3. Nonlinear finite element analyses are performed to verify some theoretical results. In Chapter 4, the multiple time scales and harmonic balance methods are applied to obtain approximate solutions of the nonlinear governing equations under the electrical square, electrical sinusoidal and sinusoidal acoustical excitations. Numerical tests are conducted to provide the validity ranges of approximate solutions. Chapter 5 focuses on the theoretical studies of pull-in instabilities, including both quasi-static and dynamic pull-ins. In Chapter 6, the approximate solutions obtained in Chapter 4 are applied to identify system parameters through a series of preliminary experiments. Preliminary uncertainty analysis is also conducted for the experimentally identified system parameters. Finally, conclusions and future work are provided in Chapter 7.

CHAPTER 2 BACKGROUND

This chapter provides background information about microphone basics and some introductory information about nonlinear dynamics. A review of the published work on both capacitive silicon microphones and nonlinear dynamics of electrostatic MEMS devices is also presented in this chapter.

Microphone Basics

A microphone is a transducer that converts unsteady pressure inputs into an electrical signal. So far, many transduction mechanisms have been developed for microphones; these include electrodynamic, piezoelectric, piezoresistive, capacitive, optical and contact (carbon) transduction mechanisms [2, 15]. Microphones are widely employed in a variety of applications such as sound field measurements [16, 17], hearing aids [18-20], telecommunications [16] and noise localization using acoustic arrays [21, 22]. Also, the use of microphones in ultrasonic and underwater applications have also been reported [23, 24].

Conventional versus Silicon Microphones

Based on the manufacturing technique, microphones can be categorized into two major types: conventional and silicon micromachined microphones. Conventional microphones are usually fabricated from separate metal parts and polymer foils with most of the assembly process done by hand [16]. On the other hand, silicon microphones are fabricated from modern silicon micromachining technology. In comparison with conventional microphones, silicon microphones are easier to integrate with the sensing

and supporting electronics, which offers the potential for higher performance by reducing parasitic elements in the sensing subsystem. Moreover, the batch fabrication of silicon microphones leads to lower costs since hundreds or thousands of devices are fabricated together on a single silicon wafer simultaneously [25].

Metrics of Performance

The major performance metrics for a microphone are the sensitivity, bandwidth, dynamic range, and noise floor. The open-circuit sensitivity of a microphone is typically defined at some reference frequency (for example, 1 kHz as shown in Figure 2-1). It is defined as the ratio of the output voltage change (before the preamplifier) to the amplitude change of the sound pressure incident on the diaphragm [16].

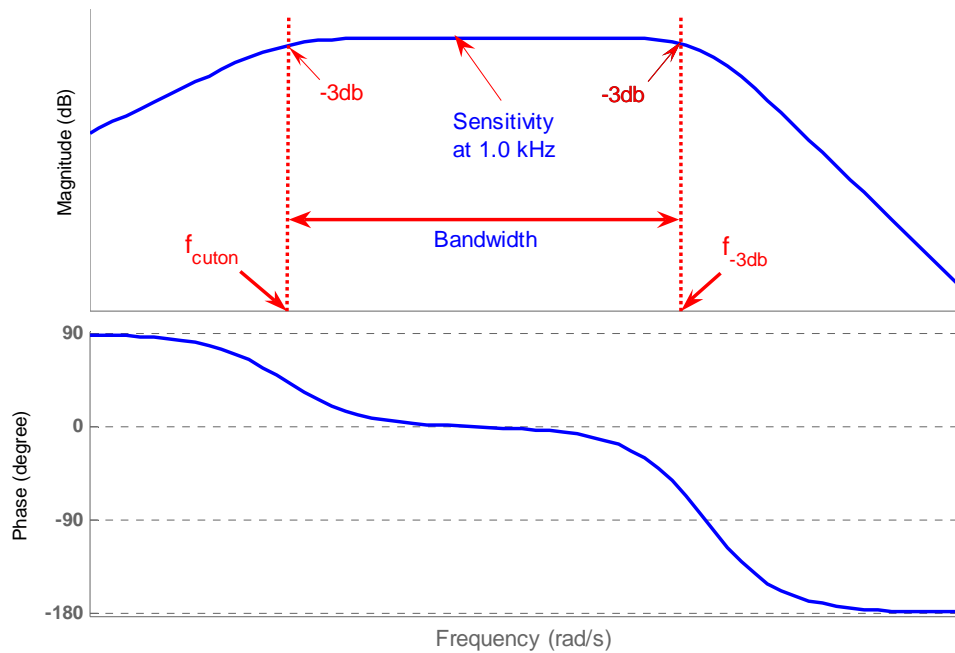


Figure 2-1. A typical frequency response plot with a defined sensitivity and bandwidth.

The bandwidth of a microphone is defined as the frequency range where a microphone ideally maintains a constant sensitivity [16]. In practice, as shown in Figure

2-1, the bandwidth is usually the frequency range from a -3dB low cut-on point to a high -3dB frequency point.

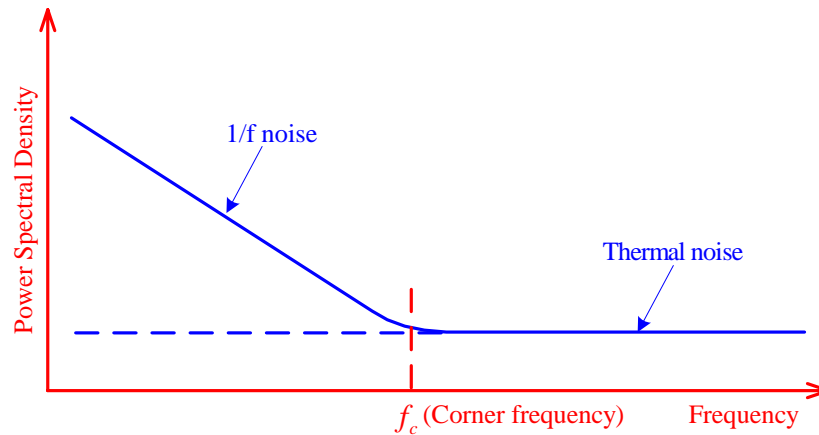


Figure 2-2. Typical noise power spectral density plot for a microphone.

Noise floor level is one of most important specifications of a microphone, since it determines the lowest measurable sound pressure level and affects the signal to noise ratio (SNR) of a microphone. For microphones, common noise sources could be environmental noise (such as power line, radio frequency interference, and environment vibration), noise in a microphone (such as thermomechanical noise, Johnson noise, shot noise and 1/f noise [26]) and noise in the interface electronics. Shown in Figure 2-2 is a typical noise power spectral density plot for a microphone. The corner frequency is where the power from 1/f noise equals the power from thermal noise. As seen from the plot, 1/f noise is dominant at low frequencies, while thermal and/or shot noise becomes important at high frequencies. In practice, a noise floor is typically specified by a linear method, an A-weighted approach, or a narrow-band method [27]. In a linear method, the noise is integrated over a specified frequency range (for example, 20 Hz to 20 kHz for audio microphones) without any weighting. An A-weighted noise floor is obtained by integrating noise spectrum after amplitude-weighting, which simulates the perceived

noise by the human ear [27]. A narrow-band noise floor is obtained by calculating the total noise within a very narrow frequency band, for example, a 1 Hz bin centered at 1 kHz. For measurement microphones, a narrow-band method is usually adapted since the microphone signals are often sampled and analyzed in the frequency domain.

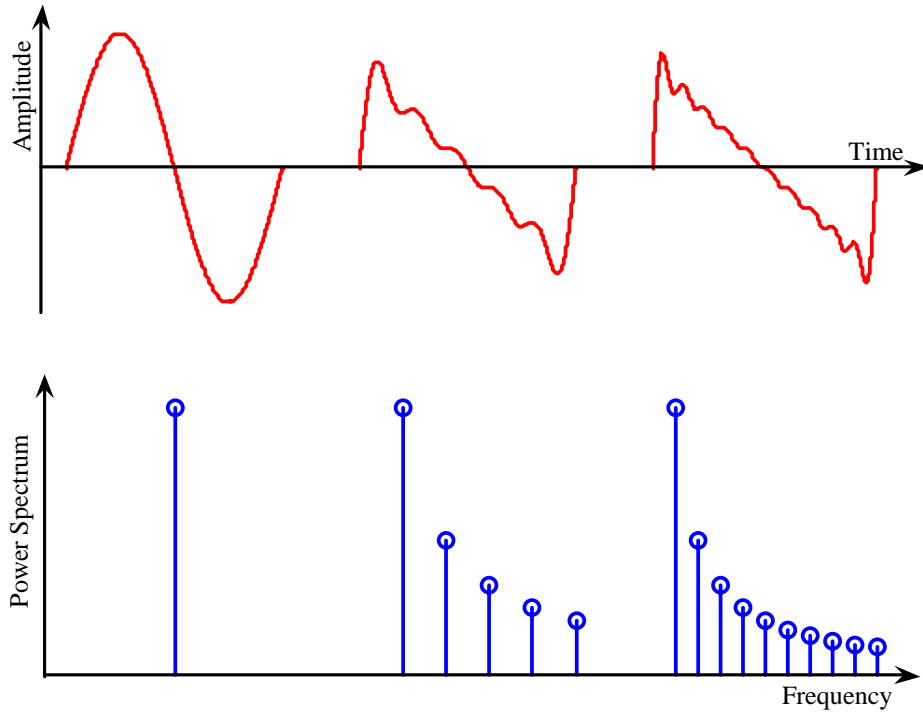


Figure 2-3. Time histories and power spectra of a pure and two distorted sinusoidal waves.

The range between the upper and lower measurable sound pressure levels of a microphone is defined as the dynamic range [16]. The lower measurable pressure level is typically determined by its noise floor. The upper limit of the dynamic range is usually set by a specific sound pressure level, which results in 3% total harmonic distortion (THD) within the frequency range from 160 Hz to 1000 Hz for measurement microphones [28]. The THD is defined as follows

$$THD = \sqrt{\frac{P_H}{P_{Total}}} \times 100\%, \quad (2.1)$$

where P_H is the sum of power within all harmonics, and P_{total} is the sum of power within the fundamental and all harmonics [28-31].

Figure 2-3 provides an illustration of harmonic distortion for a sinusoidal wave in both time and frequency domains. As more harmonics are added to the original single-tone sinusoidal signal in the frequency domain, more distortion is observed in the time history plot. For capacitive microphones, the possible sources of harmonic distortion are the nonlinear elastic behavior of the diaphragm, the electrostatic nonlinearity and the preamplifier “clipping” [16, 27].

Transduction Mechanisms

In this section, the basics of electromechanical transducers are introduced. This section also briefly reviews some major types of transduction mechanisms, including piezoelectric, piezoresistive, electrostatic and optical. A detailed discussion of capacitive microphones is provided in the next section.

Introduction to Electromechanical Transducers

An electromechanical transducer is a device that converts a mechanical input into an electrical output or vice versa [3]. Properties of electromechanical transducers include linear vs. nonlinear, reciprocal vs. non-reciprocal, conservative vs. non-conservative, and direct vs. indirect [3, 29]. An electromechanical transducer is linear if its output quantities are linear functions of the input quantities. Minor nonlinear harmonic distortion is generally allowed in linear electromechanical transducers [3]. The reciprocal property is used to describe the ability of an electromechanical transducer to convert signals in either direction between two different energy domains. The transduction coefficients are all reversible in reciprocal electromechanical transducers [3]. An

electromechanical transducer is conservative if there is no energy dissipation during the transduction, otherwise it is non-conservative. An electromechanical transducer is indirect if there exists a transition energy domain between its input and output quantities, otherwise it is a direct transducer.

Typically, transducers can be classified into two major categories: sensors and actuators. By definition, microphones fall into the category of a sensor. A wide range of transduction schemes are employed in electromechanical microphones, including piezoelectric, piezoresistive, optical and electrostatic. These types of microphones and their properties are briefly discussed in the following sections.

Piezoelectric Microphones

Some materials (for example, quartz) develop electric surface charges when compressed by a mechanical force, and this effect is referred to as the direct piezoelectric effect [32]. In addition, a mechanical strain is generated when an electric field is applied to these same materials, and this effect is referred to as the converse piezoelectric effect [32]. Those materials are often called piezoelectric materials. The relations between the electric quantities (electric displacement and field) and mechanical quantities (stress and strain) are generally described linearly by a set of piezoelectric coefficients [33].

A piezoelectric microphone typically consists of a thin diaphragm (cantilever, rectangular or circular plates) and a multilayer piezoelectric material [2]. When an incident sound wave impinges and deflects the diaphragm, the induced mechanical stress in the piezoelectric material results in an output voltage due to the piezoelectric effect. Piezoelectric microphones possess many advantages including inherently low power consumption [34]. Disadvantages of piezoelectric microphones include the relatively low

sensitivity [35] and high noise level [34, 36]. For the electromechanical property, piezoelectric microphones are reciprocal, linear, conservative and direct transducers.

Piezoresistive Microphones

The piezoresistive property of a material is defined as the change in its resistivity due to a mechanical strain or stress. For silicon, the resistivity change is due to a change in the mobility (or number of charge carriers) [37]. The piezoresistive transduction scheme can be used to design silicon microphones. A piezoresistive microphone is constructed mainly by a diaphragm with two pairs of piezoresistors. When a sound wave impinges and deflects the diaphragm, the induced mechanical stresses in the two pairs of piezoresistors results in opposite strain changes, which leads to the opposite resistance changes. By implementing a fully active Wheatstone bridge, the resistance modulation in the two pairs of piezoresistors is further expressed by the output voltage change; therefore, the incoming sound pressure can be determined [2, 38]. Piezoresistive microphones have many advantages, such as the scaling, robustness, micromachining convenience, and the absence of a need for on-chip circuitry due to its low output impedance [38, 39]. However, piezoresistive microphones have some drawbacks, such as a high noise floor [21], high power consumption, temperature drift and thermal degradation of the piezoresistors due to Joule heating [38]. For the electromechanical property, piezoresistive microphones are linear, direct, non-reciprocal and non-conservative transducers.

Optical Microphones

The classification of optical transduction is generally based on the property of modulated light. Three common transduction schemes are: 1) intensity modulation, 2) phase modulation and 3) polarization modulation [40, 41]. An optical microphone

transforms an acoustic signal into an electrical signal by modulating a reference light signal [40]. Unlike other types of microphones, an acoustic signal is first converted into an optical signal before it is converted to an electrical signal for optical microphones. The detection electronics can be remotely located away from the acoustic field, which makes optical microphones immune to harsh environments [42, 43], and less vulnerable to electromagnetic and radio frequency interference [36]. Disadvantages of optical microphones include the requirement of a stable reference optical source in a physical environment and the packaging since all the system components, such as light sources, optical sensor, and photo detectors, must be well aligned and positioned [42, 44]. Optical microphones are linear, non-reciprocal, non-conservative and indirect transducers.

Electrostatic Microphones

The electrostatic transduction mechanism has established more than two centuries for actuator applications [3]. To realize an electrostatic conversion between electrical and mechanical quantities, a capacitor with a deformable electrode is generally needed [29]. Since the electrostatic force in a capacitor is nonlinear by nature, it needs to be linearized to be suitable for the electrostatic conversion. The linearization process is typically enabled by one of two polarization schemes: a charge polarization or a voltage polarization [29].

The electrostatic transduction can be utilized to create microphones. There are two general types of electrostatic or capacitive microphones – a condenser and an electret microphone. Condenser microphones are polarized with a constant voltage, while electret microphones are polarized with a constant permanent charge. Electrostatic microphones are linear, reciprocal, conservative and direct transducers.

A capacitive microphone mainly consists of a diaphragm and a backplate, which are separated by a dielectric, which is usually an air gap. The diaphragm and backplate are made either of conducting materials or connected with electrodes to realize the capacitive detection mechanism [29, 45]. When the sound pressure deflects the diaphragm, the induced capacitance change between the diaphragm and backplate is detected via various types of interface circuitry [5]. Capacitive microphones have many advantages such as a relatively high sensitivity, a large bandwidth, an inherently low power consumption and a low noise floor [18, 46]. However, capacitive microphones have some potential issues such as electrostatic pull-in instability, output signal attenuation due to the parasitic capacitance, and decreased sensitivity at high frequencies due to the viscous damping of the perforated backplate [2].

Electrostatic Microphones

This section provides details of electret microphones and two major types of condenser microphones. A summary of previous work on capacitive microphones is provided in the next section.

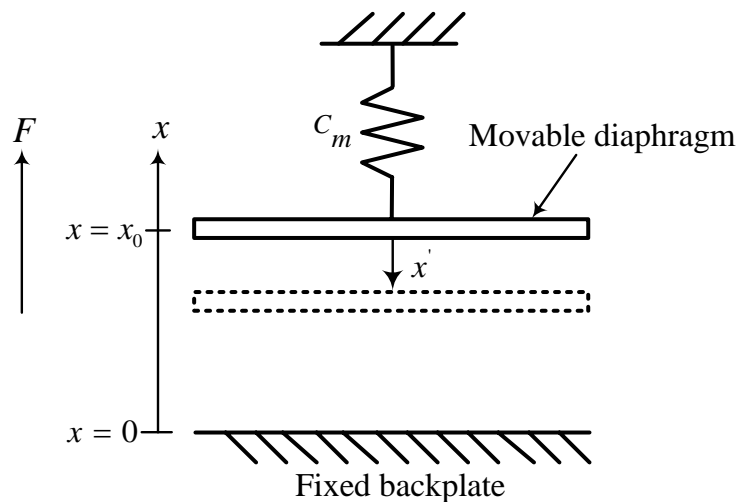


Figure 2-4. A simplified model of an electrostatic microphone (adapted from Rossi [29]).

First, we need to see how the electrostatic transduction is realized by the linearization process. Shown in Figure 2-4 is a simplified model of an electrostatic microphone in air. The backplate is assumed to be fixed and the diaphragm is movable and located at $x = x_0$ due to some loading (for example, acoustic pressure). The mechanical restoring force for the diaphragm is modeled by a spring.

If a small displacement fluctuation x' is assumed, the position of the diaphragm is given by

$$x = x_0 - x'. \quad (2.2)$$

By using a parallel-plate assumption, the capacitance C is given by

$$C = \frac{\epsilon_0 A}{x_0 - x'} = \frac{\epsilon_0 A}{x_0} \left(1 - \frac{x'}{x_0}\right)^{-1} = C_0 \left(1 - \frac{x'}{x_0}\right)^{-1}, \quad (2.3)$$

where ϵ_0 is the dielectric constant of the air, A is the area of the diaphragm and $C_0 = (\epsilon_0 A)/x_0$ is the mean capacitance.

If a charge, Q , is applied to the movable diaphragm, and we assume

$$Q = Q_0 + Q', \quad (2.4)$$

where Q_0 is the mean charge and Q' is the small charge fluctuation.

Therefore, the voltage, V , across the diaphragm and backplate is

$$V = \frac{Q}{C} = \frac{Q}{C_0} \left(1 - \frac{x'}{x_0}\right) = \left(V_0 + \frac{Q'}{C_0}\right) \left(1 - \frac{x'}{x_0}\right), \quad (2.5)$$

where $V_0 = Q_0/C_0$ is the mean voltage.

The stored electrical potential energy in the capacitor, U_e , is given by [5]

$$U_e = \frac{Q^2}{2C} = \frac{Q^2}{2C_0} \left(1 - \frac{x'}{x_0}\right). \quad (2.6)$$

Therefore, the electrostatic force acting on the diaphragm is

$$F_e = \frac{dU_e}{dx'} = -\frac{Q^2}{2x_0 C_0}. \quad (2.7)$$

The mechanical restoring force is given by

$$F_m = \frac{x}{C_m}, \quad (2.8)$$

where C_m is the mechanical compliance of the spring.

Therefore, the net force acting on the diaphragm is

$$F = \frac{x}{C_m} - \frac{Q^2}{2x_0 C_0}. \quad (2.9)$$

Eqs. (2.3), (2.5) and (2.9) are three nonlinear coupled equations. In order to linearize these equations to realize the electrostatic transduction, we must assume

$$\frac{x}{x_0} \approx 1, \quad (2.10)$$

$$\frac{Q}{Q_0} \approx 1 \quad (2.11)$$

and

$$\frac{V}{V_0} \approx 1 \quad (2.12)$$

Physically, this linearization process can be done by one of two polarization schemes: a charge polarization or a voltage polarization [29]. If a constant voltage V_0 is applied across the diaphragm and backplate, a condenser microphone is created. An

electret microphone is created if a constant charge Q_0 is stored permanently on the diaphragm or backplate.

Once the polarization is applied, Eqs. (2.3), (2.5) and (2.9) can be linearized as

$$C = \frac{\varepsilon_0 A}{x_0 - x'} = \frac{\varepsilon_0 A}{x_0} \left(1 - \frac{x'}{x_0}\right)^{-1} = C_0 \left(1 - \frac{x'}{x_0}\right), \quad (2.13)$$

$$V' = \frac{Q'}{C_0} - \frac{V_0}{x_0} x', \quad (2.14)$$

and

$$F' = \frac{x'}{C_m} - \frac{V_0}{x_0} Q', \quad (2.15)$$

where V' and F' are the fluctuating components of the voltage and force applied on the diaphragm, respectively.

Eqs. (2.14) and (2.15) represent the linearized electrostatic coupling equations in the displacement and charge form. These two equations can be further rewritten in power variables [29] as follows

$$V' = \frac{1}{j\omega C_0} I' - \frac{V_0}{j\omega x_0} v', \quad (2.16)$$

and

$$F' = \frac{1}{j\omega C_m} v' - \frac{V_0}{j\omega x_0} I', \quad (2.17)$$

where I' is the fluctuating component of the current passing through the diaphragm and v' is the fluctuating component of the velocity of the diaphragm. In matrix form, the coupling equations are written as

$$\begin{Bmatrix} V' \\ F' \end{Bmatrix} = \begin{bmatrix} \frac{1}{j\omega C_0} & -\frac{V_0}{j\omega x_0} \\ -\frac{V_0}{j\omega x_0} & \frac{1}{j\omega C_m} \end{bmatrix} \begin{Bmatrix} I' \\ v' \end{Bmatrix}. \quad (2.18)$$

Electret Microphones

For an electret microphone, the permanent charge is usually fixed by a thin layer of charge-holding electret material on the backplate or diaphragm [47, 48]. The electret material is dominated by Teflon for conventional electret microphones and silicon dioxide/nitride for silicon electret microphones [47]. In electret microphones, integration of the electret layer on the diaphragm is a common choice since the backplate is usually perforated [48-50].

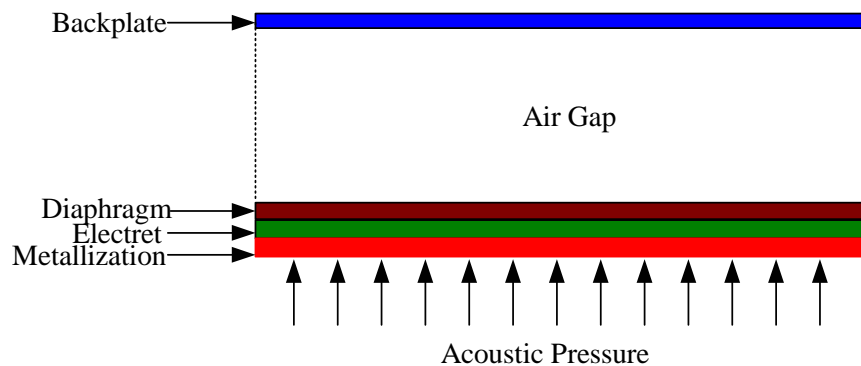


Figure 2-5. Schematic of a capacitive microphone with an electret diaphragm.

A schematic of a capacitive microphone with an electret diaphragm is shown in Figure 2-5. An air gap separates a metallized electret diaphragm from a backplate. A metallization layer is used to charge the electret layer prior to the operation. At the interface between the diaphragm and electret, a charge layer with certain charge density (total charge divided by the cross section area) is formed to generate the electrical field inside the gap. One advantage of electret microphones is the absence of an external power supply and the potential for portable applications [46, 50]. However, integration

of electret microphones with MEMS suffers from the poor quality of thin film electrets and charge loss due to humidity [46].

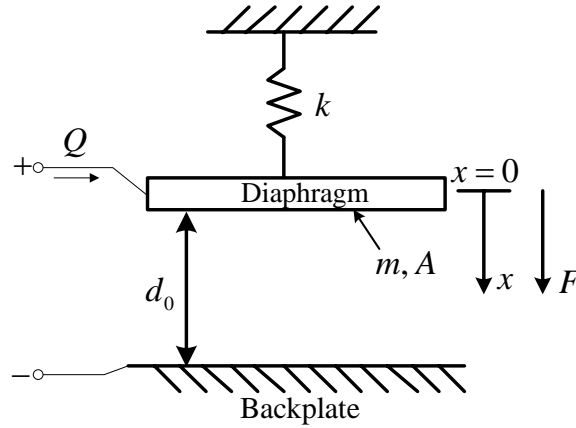


Figure 2-6. A simplified quasi-static model of an electret microphone.

Critical bias charge. To illustrate the idea of the critical bias charge for electret microphones, shown in Figure 2-6 is a simplified quasi-static model of an electret microphone. The mass and mechanical stiffness of the movable diaphragm are modeled by a point mass (m) and a spring (k) respectively. The nominal gap between the diaphragm and backplate is d_0 and x is a vertical displacement of the diaphragm.

Since only the quasi-static process is considered here, the inertial force and damping force are neglected since they are time-dependent. In the following analysis, only the mechanical restoring and electrostatic forces are considered. The diaphragm and backplate are conductive, thus one capacitor is formed. For electret microphones, the electrostatic force, F_e , is given as [5]

$$F_e = \frac{Q^2}{2\epsilon_0 A}. \quad (2.19)$$

As seen from Eq. (2.19), the electrostatic force is a quadratic function of the bias charge and independent of the vertical displacement x of the diaphragm. For a given

constant bias charge, the electrostatic force remains as a constant force. By using a linear spring model, the mechanical restoring force, F_m , is given as

$$F_m = kx, \quad 0 \leq x \leq d_0. \quad (2.20)$$

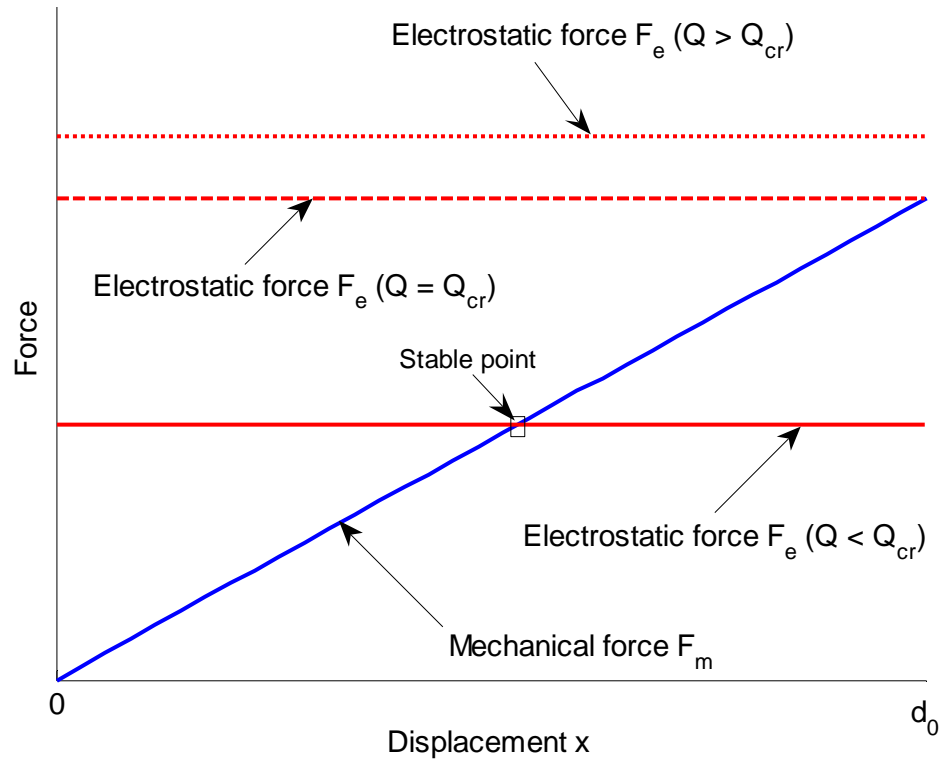


Figure 2-7. Illustration of the critical bias charge of an electret microphone.

Shown in Figure 2-7 is a plot with both electrostatic and mechanical forces for different bias charge cases. When the bias constant charge Q is smaller than a critical value Q_{cr} , the electrostatic force can be always balanced by the mechanical force and the diaphragm moves to a stable position as shown in the plot. When the constant bias charge Q reaches Q_{cr} , the electrostatic force is greater than the mechanical force when $x < d_0$ and the diaphragm is forced to move to the rigid backplate position $x = d_0$, which represents a non-functioning microphone. When the constant bias charge Q is greater than Q_{cr} , the electrostatic force is always greater than the mechanical force and the

diaphragm always moves to the rigid backplate. Therefore, electret microphones must operate with a bias charge less than its critical value.

To find the quasi-static critical bias charge, the electrostatic attraction force is set to be equal to the mechanical restoring force at $x = d_0$, which results in

$$\frac{Q_{cr}^2}{2\epsilon_0 A} = kd_0. \quad (2.21)$$

Namely, the critical charge Q_{cr} is [51]

$$Q_{cr} = \sqrt{2\epsilon_0 A k d_0}. \quad (2.22)$$

Condenser Microphones

The majority of condenser microphones can be categorized into single-backplate condenser microphones and dual-backplate condenser microphones based on the backplate configuration. In 1996, Bay *et al.* proposed a dual-diaphragm condenser microphone [19]; however, it was not fabricated. In 2002, Rombach *et al.* fabricated the first dual-backplate condenser microphone [52]. The details of two major types of condenser microphones are provided in the following.

Single-backplate condenser microphones

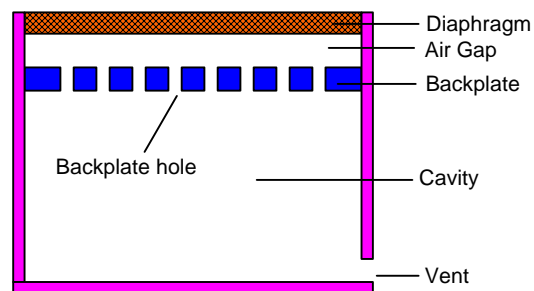


Figure 2-8. Schematic of a single-backplate condenser microphone.

A typical single-backplate condenser microphone with a diaphragm and a backplate is shown in Figure 2-8. A backplate is perforated to reduce the air-streaming resistance, a

vent is provided to equilibrate the pressure inside the cavity to the ambient atmospheric pressure. A capacitor is formed between the conductive backplate and diaphragm.

Quasi-static pull-in. Based on a similar dynamic model as shown in Figure 2-6, for single-backplate condenser microphones, the electrostatic force F_e is given as [5]

$$F_e = \frac{\epsilon_0 A V^2}{2d^2}, \quad (2.23)$$

where $d = d_0 - x$ is the distance between the diaphragm and backplate. By using a linear spring model, the mechanical restoring force, F_m , is given by

$$F_m = k(d_0 - d). \quad (2.24)$$

To find the quasi-static pull-in voltage, the electrostatic attraction force is set to be equal to the mechanical restoring force at $d_{PI} = 2d_0/3$ or $x_{PI} = d_0/3$, which results in

$$\frac{\epsilon_0 A V_{PI}^2}{2\left(\frac{2d_0}{3}\right)^2} = k\left(d_0 - \frac{2d_0}{3}\right). \quad (2.25)$$

Namely, the critical pull-in voltage V_{PI} in the constant bias voltage case is [5]

$$V_{PI} = \sqrt{\frac{8kd_0^3}{27\epsilon_0 A}}. \quad (2.26)$$

It should be pointed out that the above analysis results are valid based on a simple parallel-plate assumption and a linear spring model. When the displacement of the diaphragm becomes nonlinear, geometric nonlinearity of the diaphragm needs to be considered to obtain more accurate results.

As seen from Eq. (2.23), the electrostatic force is a nonlinear function of the applied voltage and the displacement of the diaphragm. Shown in Figure 2-9 is the plot

with both electrostatic and mechanical forces when the constant bias voltage V is less than the critical pull-in voltage V_{PI} .

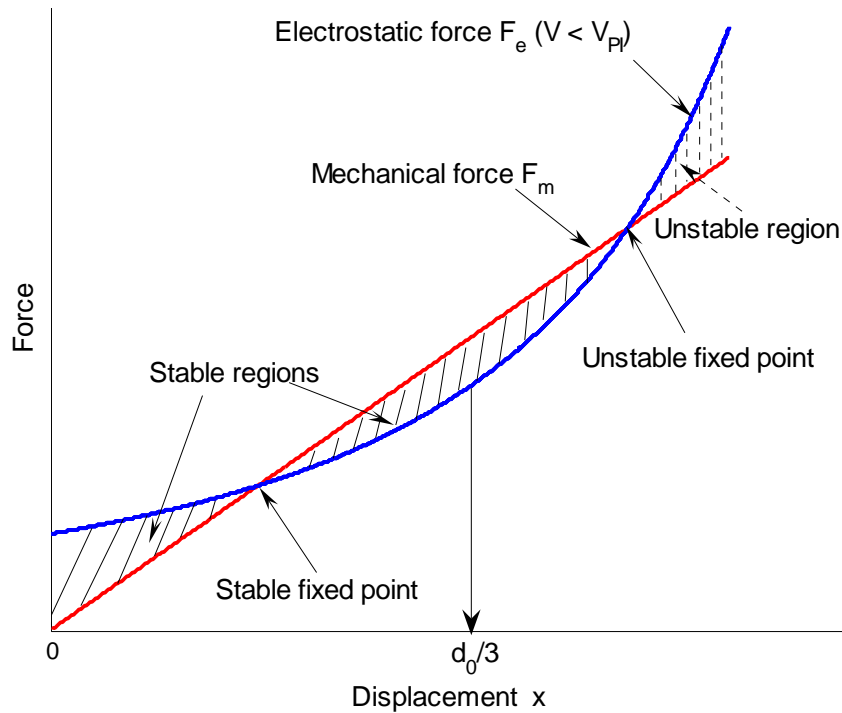


Figure 2-9. Illustration of mechanical and electrostatic forces for a single-backplate condenser microphone ($V < V_{PI}$).

As seen from Figure 2-9, there are three regions and two equilibrium points. Below the stable fixed point, the electrostatic force is always greater than the mechanical force and attracts the diaphragm to the stable fixed point. Between stable and unstable fixed points, the mechanical force is always greater than the electrostatic force and pulls the diaphragm back to the stable fixed point. Above the unstable fixed point, the electrostatic force is always greater than the mechanical restoring force and the displacement of the diaphragm keeps increasing until the diaphragm crashes into the backplate. Therefore, the stable operation range of the microphone is from the rest position to the unstable fixed point when $V < V_{PI}$.

As the applied bias voltage becomes larger and reaches its critical pull-in value, the electrostatic force is larger than the mechanical restoring force except for one critical point ($d_{PI} = 2d_0/3$ or $x_{PI} = d_0/3$) as shown in Figure 2-10. When pull-in occurs, the two fixed points shown in Figure 2-9 move towards each other and coalesce at the pull-in position as shown in Figure 2-10. When the applied bias voltage is over its critical pull-in value, the electrostatic force is always larger than the mechanical restoring force and all regions in Figure 2-9 become unstable.

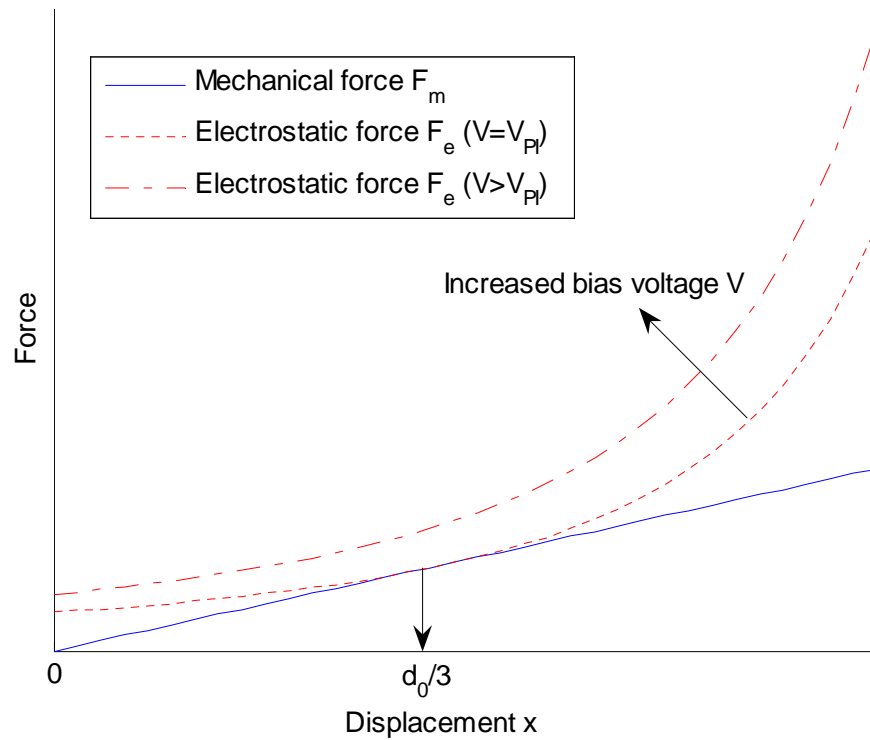


Figure 2-10. Illustration of quasi-static pull-in of a single-backplate condenser microphone ($V \geq V_{PI}$).

Scaling. In practice, a condenser microphone needs to be connected to a preamplifier to make a measurement to avoid a signal attenuation or loss. The preamplifier serves as an impedance converter and it is commonly modeled as a source follower with an input capacitance C_i and a gain H_a . The overall sensitivity far below

resonance [2] of a single-backplate condenser microphone is compliance dominated and can be expressed as follows

$$S_{overall} = S_m S_e H_c H_a, \quad (2.27)$$

where S_m is the mechanical sensitivity, S_e is the electrical sensitivity, H_c is the capacitance signal attenuation due to the input capacitance of the preamplifier C_i , the parasitic capacitance C_p , and the gain of the preamplifier H_a as shown in Figure 2-11.

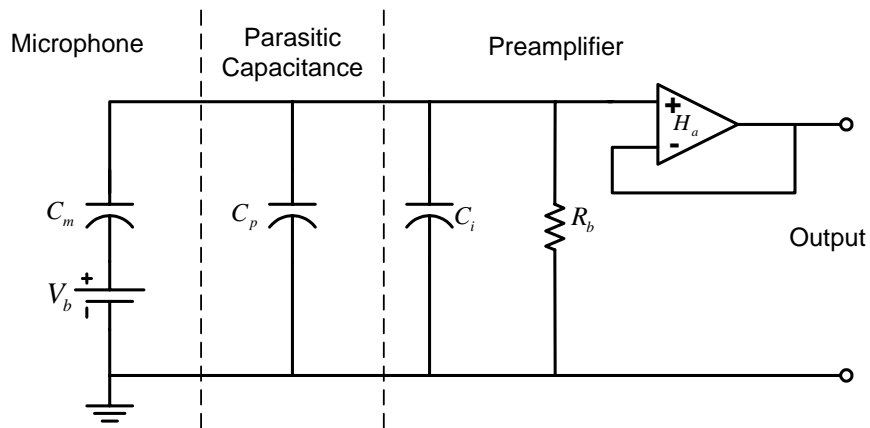


Figure 2-11. Simplified circuit of a single-backplate condenser microphone with a preamplifier (adapted from Scheeper et al. [2]).

The mechanical sensitivity S_m of the microphone is defined as the change of the diaphragm center deflection resulting from a unit change in the applied sound pressure level. For a circular diaphragm with a residual tensile stress σ_0 , the mechanical sensitivity, S_m , is given by [2]

$$S_m = \frac{a^2}{8\sigma_0 h}, \quad (2.28)$$

where a and h are the radius and the thickness of the diaphragm respectively. It should be pointed out that Eq. (2.28) is obtained based on a pure linear mechanical membrane model, which does not account for the bending forces and moments.

The electrical sensitivity S_e is defined as the change in the voltage across the air gap resulting from a unit change of the air gap. If the electric field strength E in the air gap is assumed homogeneous, and the electrical sensitivity, S_e , is given by

$$S_e = E = \frac{V_b}{d_0}, \quad (2.29)$$

where V_b is the DC bias voltage.

From the simplified circuit, as shown in Figure 2-11, the capacitive signal attenuation H_c is

$$H_c = \frac{C_m}{C_m + C_i + C_p}, \quad (2.30)$$

where

$$C_m = \frac{\epsilon_0 A}{d_0}, \quad (2.31)$$

and

$$A = \pi a^2. \quad (2.32)$$

The microphone capacitance is represented by C_m , and A is the area of the diaphragm.

For the designer, the gain of the preamplifier H_a is close to unity and signal attenuation is not desired. Ideally, the following can be obtained

$$H_c \approx 1, \quad (2.33)$$

if

$$C_m \gg C_i + C_p. \quad (2.34)$$

Ideally, the overall sensitivity is then changed into

$$S_{overall} \approx S_m S_e = S_{open}, \quad (2.35)$$

where S_{open} is the open-circuit sensitivity.

In practice, as the radius of the diaphragm decreases, the capacitance of the microphone C_m also decreases. Therefore, Eq. (2.34) does not hold and the microphone will suffer from the output signal attenuation due to the parasitic capacitance.

By using Eqs. (2.26) and (2.28), the critical pull-in voltage for a single-backplate condenser microphone can be rewritten as

$$V_{PI} = \sqrt{\frac{1}{S_m} \frac{8d_0^3}{27\epsilon_0}}. \quad (2.36)$$

If the applied bias voltage is always kept at a fixed fraction of the critical pull-in voltage, from Eqs.(2.28), (2.29), (2.31), (2.35) and (2.36), the following relations can be obtained

$$C_m \sim \frac{A}{d_0}, \quad (2.37)$$

$$V_{PI} \sim d_0^{\frac{3}{2}}, \quad (2.38)$$

and

$$S_{open} \sim \sqrt{\frac{S_m V_b}{d_0}} \sim \sqrt{\frac{A V_b}{\sigma_0 h d_0}} \sim \sqrt{\frac{A V_b}{d_0}}. \quad (2.39)$$

From Eq. (2.39), as the area of diaphragm becomes smaller, the open-circuit sensitivity decreases. Also to maintain Eq. (2.34) for the overall sensitivity, the gap needs to become smaller. As the gap becomes smaller, the critical pull-in voltage becomes smaller too; therefore, the open-circuit sensitivity eventually becomes smaller. Hence, from the sensitivity point of view, the gap and area of the diaphragm could be the inherent limitations with the miniaturization of single-backplate condenser microphones.

The air-streaming resistance due to the holes of the backplate plays an important role in determining the frequency response or the bandwidth of condenser microphones.

For a rigid circular backplate, the mechanical air-streaming resistance R_m is obtained as follows [53]

$$R_m = \frac{4\mu\pi a^4}{3nd_0^3} \left[\frac{1}{4} \ln \left(\frac{1}{A_p} \right) - \frac{3}{8} + \frac{1}{2} A_p - \frac{1}{8} A_p^2 \right], \quad (0.40)$$

where μ is dynamic viscosity of the air, n is the total number of holes and A_p is the ratio of the total area of holes to the backplate area. Therefore the following scaling relation is obtained

$$R_m \sim \frac{1}{nd_0^3}, \quad (2.41)$$

As the gap becomes smaller, the air-streaming resistance increases quickly and decreases the bandwidth of the microphone. Therefore, from the bandwidth point of view, the gap could be one of inherent limitations with miniaturization of single-backplate condenser microphones. However, a very high number of holes (for example, hundreds or thousands) can be used to maintain a small air-streaming resistance for micromachined condenser microphones with narrow air gaps [20]. On the other hand, as the number of holes in the backplate increases, the backplate becomes more compliant and electrostatic pull-in will occur with a lower voltage.

Dual-backplate condenser microphones

A schematic of a typical dual-backplate condenser microphone is shown in Figure 1-1. It consists of two perforated backplates with a diaphragm in between, a cavity and a vent. Two capacitors are formed by the conductive backplates and diaphragm respectively. Due to the existence of symmetric backplates, a dual-backplate condenser microphone ideally can generate twice the signal of a single-backplate condenser

microphone [17]. The configuration of symmetric backplates could lead to a higher sensitivity, a higher capacitance, a wider linear dynamic range [18] and a broader bandwidth. In addition, the applied bias voltage can be higher for a double backplate condenser microphone, since the electrostatic forces acting on both sides of the diaphragm can balance with each other. Furthermore, the dual-backplate condenser microphone has the potential to operate in a closed loop [54].

Details of a dynamic model for a dual-backplate condenser microphone are provided in Chapter 3. Pull-in issues associated with dual-backplate condenser microphone are studied in Chapter 5.

Major Previous Work on Capacitive Silicon Microphones

Major previous work and recent developments of capacitive silicon microphones [17, 49, 50, 52, 55-67] are listed in Table 2-1. It can be seen that there is a significant trend towards developing instrumentation grade silicon condenser microphones in terms of smaller size, larger sensitivity and signal-to-noise ratio, and broader bandwidth.

Hohm and Gerhard-Multhaupt (1984) developed the first electret silicon microphone. Its backplate consisted of a $1\text{ cm} \times 1\text{ cm}$ p-type silicon layer, a $2\ \mu\text{m}$ SiO_2 top electret layer and a $0.1\ \mu\text{m}$ bottom aluminum electrode layer. A circular hole with a diameter of 1 mm was perforated in the center of the backplate. The diaphragm was an aluminum-coated Mylar foil with a thickness of $13\ \mu\text{m}$ and a diameter of 8 mm. A Mylar foil was used as a spacer to form an air gap of $30\ \mu\text{m}$. The reported open-circuit sensitivity was approximately $8.8\text{ mV} / \text{Pa}$, but the measured sensitivity at the frequency of 1 kHz was approximately $3\text{ mV} / \text{Pa}$ due to the parasitic capacitance.

Table 2-1. Major previous work in capacitive silicon microphones.

Authors	Diaphragm Area (mm^2)	Air Gap (μm)	Upper Frequency (kHz)	Sensitivity (mV/Pa)	Noise Level ($dB A$)
^a Hohm and Gerhard-Multhaupt [49]	≈ 50.3	30	8.5	3.0	--
^a Sprenkels <i>et al.</i> [50]	6.0	20	>15	25 ^a	--
^b Bergqvist and Rudolf [55]	4.0	4.0	16	13 ^a	--
^b Bergqvist <i>et al.</i> [56]	4.0	2.0	20	1.6	40
^b Kuhnel and Hess [57]	0.64	2	20	1.8	43
^b Bourouina <i>et al.</i> [58]	1.0	7.5	10	2.4	38
^b Scheeper [59]	4.0	3.0	>14	7.8 ^c	30.
^b Zou <i>et al.</i> [60]	1.0	2.6	9.0	14.2	--
^b Schafer <i>et al.</i> [61]	0.5	4.0	17	14	28
^b Torkkeli <i>et al.</i> [62]	1.0	1.3	12	4.0	33.5
^b Rombach <i>et al.</i> [52, 63]	4.0	0.9	>20	13 ^c	22.5
^b Scheeper <i>et al.</i> [17]	≈ 12	20	20	22 ^c	23
^b Hansen <i>et al.</i> [64]	≈ 0.01	1	100	7.3	63.6
^b Martin <i>et al.</i> [65, 66]	≈ 0.17	2	230	0.28 ^{c, d}	42 ^e
^b Pedersen [67]	≈ 0.1	1.24	100	0.5	22 ^e
^b Loeppert and Lee [68]	≈ 0.25	4	20	--	--

^aElectret microphone

^bCondenser microphone

^cOpen-circuit sensitivity

^dCharge amplifier

^e1 Hz bin

Sprenkels et al. (1989) reported an electret silicon microphone. It had a metallized

Mylar foil diaphragm with a thickness of $2.5 \mu m$ and a $20 \mu m$ air gap. A SiO_2 layer with a thickness of $1.1 \mu m$ was used as electret material and was biased by a permanent charge with an effective voltage of approximately -300 V . The open-circuit sensitivity was approximately $25 \text{ mV} / \text{Pa}$ at the frequency of 1 kHz .

Bergqvist and Rudolf (1990) published the first silicon condenser microphones. A microphone with a $5 \mu m$ thick p-type silicon diaphragm and a $4 \mu m$ air gap demonstrated an open-circuit sensitivity of $13 \text{ mV} / \text{Pa}$ at the frequency of 1 kHz . Microphones with a $8 \mu m$ thick p-type silicon diaphragm showed a bandwidth ($\pm 1 \text{ dB}$) of 16 kHz . Low parasitic capacitances ($< 0.5 \text{ pF}$) and a large number of holes in the backplate were reported on those microphones.

Bergqvist *et al.* (1991) presented a condenser microphone with a $2 \text{ mm} \times 2 \text{ mm}$ stress-free p-type silicon diaphragm and a $2 \mu m$ air gap. The backplate was perforated with 640 acoustic holes per mm^2 to reduce the air-streaming resistance; however, the backplate size was not reported. The microphone operated with a 5 V bias voltage. Its frequency response was flat within $\pm 3 \text{ dB}$ from 2 to 20 kHz . The measured microphone noise was dominated by the preamplifier noise and the equivalent noise level was 40 dBA . The measured sensitivity was $1.6 \text{ mV} / \text{Pa}$ at the frequency of 1 kHz . The total harmonic distortion was less than 0.08% at a sound pressure level of 120 dB .

Kuhnel and Hess (1992) developed a condenser microphone with a specially designed backplate to reduce the air-streaming resistance. The microphone consisted of a $0.8 \text{ mm} \times 0.8 \text{ mm}$ silicon nitride diaphragm with a thickness of 150 nm . The backplate was structured with either anisotropically etched holes or plasma-etched grooves. Microphones with grooves in backplates and stress-free diaphragms demonstrated an

open-circuit sensitivity of $10\text{ mV} / \text{Pa}$ ($1.8\text{ mV} / \text{Pa}$ measured sensitivity due to the signal attenuation caused by the parasite capacitance) and the measured bandwidth was up to 20 kHz .

Bourouina *et al.* (1992) developed a condenser microphone design without acoustic holes in the backplate. In order to lower the air-streaming resistance, a relatively thick air gap was used (5 or $7.5\ \mu\text{m}$). The diaphragm was made with heavily boron-doped silicon and had a residual tension stress of 70 MPa . A Pyrex wafer was bonded to the diaphragm wafer by anodic bonding. A microphone with an air gap of $7.5\ \mu\text{m}$ and a bias voltage of 20 V showed a flat frequency response up to 10 kHz and a sensitivity of $2.4\text{ mV} / \text{Pa}$. The noise of the microphone mainly came from the preamplifier, and was measured to be 38 dBA .

Scheeper (1993) presented a condenser microphone with a high density of acoustic holes in the backplate. The microphone possessed an open-circuit sensitivity of $7.8\text{ mV} / \text{Pa}$, a capacitance of 8.6 pF and a flat frequency response from 0.1 kHz to 14 kHz ($\pm 2\text{ dB}$). Due to the existence of a narrow air gap, the microphone operated at a relatively low bias voltage to avoid pull-in. The pull-in voltage was not reported in the paper.

Zou *et al.* (1997) developed a silicon condenser microphone with a corrugated diaphragm. The microphone had an air gap of $2.6\ \mu\text{m}$ and a $1\text{ mm} \times 1\text{ mm}$ diaphragm with a residual tension stress of 70 MPa and a thickness of $1.2\ \mu\text{m}$. A corrugated diaphragm was fabricated by an anisotropic etching to improve the sensitivity by reducing the effect of high tension stress. A microphone with a corrugation depth of $8\ \mu\text{m}$ and a 10 V bias voltage showed a measured sensitivity of $14.2\text{ mV} / \text{Pa}$. The

simulated bandwidth was reported to be 9 kHz . The finite element method (FEM) and equivalent circuit method were used to predict the microphone performance.

Schafer *et al.* (1998) from Knowles Acoustics, reported a silicon micromachined condenser microphone for the hearing aid application. The microphone had an air gap of $4\ \mu\text{m}$ and a circular silicon nitride diaphragm with a radius of $0.4\ \text{mm}$ and a thickness of $0.75\ \mu\text{m}$. A highly compliant diaphragm was achieved by the support in the middle rather than the clamped support at the perimeter. A lumped element model was built to predict the sensitivity, bandwidth and noise floor of the microphone. The measured sensitivity of the microphone with a bias voltage of $12\ \text{V}$ was $14\ \text{mV}/\text{Pa}$ at the frequency of $1\ \text{kHz}$. The measured A-weighted noise level was as low as $28\ \text{dBA}$ and the measured resonant frequency was up to $17\ \text{kHz}$.

Torkkeli *et al.* (2000) fabricated a capacitive microphone with a low-stress ($2\ \text{MPa}$) polysilicon diaphragm. The microphone had an air gap of $1.3\ \mu\text{m}$ and a $1\ \text{mm} \times 1\ \text{mm}$ diaphragm with a thickness of $0.8\ \mu\text{m}$. The measured sensitivity of the microphone with a $2\ \text{V}$ bias voltage was $4\ \text{mV}/\text{Pa}$ at the frequency of $1\ \text{kHz}$. The measured A-weighted noise level was $33.5\ \text{dBA}$. The measured capacitance was $11\ \text{pF}$ and the bandwidth was $12\ \text{kHz}$.

Rombach *et al.* (2002) fabricated the first dual-backplate silicon condenser microphone. Due to the symmetric arrangement of backplates, a thin air gap of $0.9\ \mu\text{m}$ was fabricated to generate a high electrical field and a high sensitivity with a low bias voltage. The microphone consisted of a $2\ \text{mm} \times 2\ \text{mm}$ multilayer diaphragm with a thickness of only $0.5\ \mu\text{m}$ and an overall residual tensile stress of $45\ \text{MPa}$. The total sensitivity with a bias voltage of $1.5\ \text{V}$ was measured to be $13\ \text{mV}/\text{Pa}$ and the A-

weighted equivalent noise level was measured to be 22.5 *dB*A . The upper limit of its dynamic range was determined to be 118 *dB* and the total harmonic distortion at 80 *dB*A *SPL* was less than 0.26% .

Scheeper *et al.* (2003) fabricated a condenser MEMS measurement microphone. The microphone had an air gap of 20 μm and an octagonal silicon nitride diaphragm with a tensile stress of 340 *MPa* and a thickness of 0.5 μm . The area of a circular diaphragm was approximately 11.95 mm^2 , while the area of a square backplate was approximately 8 mm^2 . The measured average open-circuit sensitivity was 22 *mV* / *Pa* with a 200*V* bias voltage and the measured noise level (including the preamplifier) was 23 *dB*A . The measured frequency response was flat up to 20 *kHz* , and the resonance frequency was reported between 47 and 51 *kHz* . Other important specifications of this microphone such as the measured temperature coefficient, humidity coefficient for the sensitivity and 3% distortion limit were also reported.

Hansen *et al.* (2004) reported a wide-bandwidth micromachined capacitive microphone based on radio frequency detection. The microphone consisted of a metallized rectangular silicon nitride membrane, which was suspended over a silicon substrate to form a small sealed volume. A sensitivity of 7.3 *mV* / *Pa* was measured with a gap of 1 μm and a 70 μm \times 190 μm membrane with a thickness of 0.4 μm . The measured bandwidth was flat within 0.5 *dB* over the range from 0.1 *Hz* to 100 *kHz* . However, the microphone suffered from its relatively high noise floor, which was measured to be 63.6 *dB*A .

Martin *et al.* (2005) fabricated a dual-backplate capacitive MEMS microphone by using SUMMiT V process at Sandia National Laboratories. Due to the symmetric

arrangement of backplates, a thin air gap of $2 \mu m$ was fabricated. The microphone consisted of a circular polysilicon diaphragm with a $230 \mu m$ radius and a thickness of $2.25 \mu m$. The measured sensitivity with a charge amplifier and a bias voltage of $9 V$ was $0.28 mV/Pa$ and the measured noise level was $42 dB/\sqrt{Hz}$ at $1 kHz$. The measured dynamic range was over $118 dB$ and a linear response up to $160 dB$ was observed. The predicted resonance frequency was approximately $185.5 kHz$ and the measured resonance frequency was approximately $230 kHz$ [66].

Pedersen (2006) presented an aero-acoustic capacitive MEMS microphone. By utilizing the Knowles SiSonic MEMS microphone technology, the microphone consisted of a circular diaphragm with a $180 \mu m$ radius and a thickness of $2 \mu m$. An air gap of $1.24 \mu m$ was fabricated between the diaphragm and backplate. The measured sensitivity at $1 kHz$ was approximately $0.5 mV/Pa$. The measured total harmonic distortion at $130 dB SPL$ was 1.5% . The predicted bandwidth was approximately $100 kHz$ and the measured noise level was $22 dB/\sqrt{Hz}$ at $1 kHz$.

Loeppert and Lee in Knowles Electronics, LLC (2006) presented the first commercialized condenser MEMS microphone. Fabricated by Knowles's 10-mask, dual-poly process, the microphone consisted of a silicon nitride backplate with a thickness of $1.5 \mu m$ and a polysilicon circular diaphragm with an effective $280 \mu m$ radius and a thickness of $1 \mu m$. An air gap of $4 \mu m$ was fabricated between the diaphragm and backplate. The circular backplate of the microphone was perforated with circular holes with a radius of $4 \mu m$ and the porosity of the backplate was 22.8% . The measured capacitance of the microphone was $0.5 pF$. The measured frequency response was flat

from 100 Hz to approximate 20 kHz . However, the measured sensitivity and noise floor were not reported in the paper.

Basics of Nonlinear Dynamics

Nonlinear dynamics is the study of the time evolving behavior of a nonlinear system. These systems are often governed by nonlinear partial/ordinary differential and/or algebraic equations [69]. To date, nonlinear dynamics has been applied to many fields of engineering and science [69-77]. To help provide the reader with some familiarity to the field of nonlinear dynamics, some general terminologies and theories are introduced. In the sections that follow, several key concepts, such as nonlinearities, autonomy, fixed points, stability and bifurcation, are discussed.

Nonlinearities

Although there are many types of nonlinearities, the major nonlinearities in the field of engineering can be categorized into the following four types [6, 73]:

- Material or constitutive nonlinearity, examples include the inelastic phenomena (plasticity, creep, hysteresis, etc.) in solid mechanics, and nonlinear resistor (for example, thermal effect on resistance) in electrical engineering.
- Kinematic nonlinearity, examples include Coriolis acceleration and the convective acceleration term in the Navier-Stokes equations in fluid mechanics.
- Nonlinear force or boundary, examples include the nonlinear electrostatic force, magnetic force and a beam attached to a nonlinear torsional spring at one of its pinned end.
- Geometric nonlinearity, examples include a Hertzian contact model for two elastic bodies and a Duffing's spring.

Steady State, Autonomous System and Fixed Point

The steady state refers to the asymptotic behavior of the dynamical system as time goes to infinity [69]. The behavior prior to the steady state is often called transient [69].

An autonomous dynamical system is a system that does not contain time as an explicit

independent variable [69]. Otherwise, a dynamical system is defined as a non-autonomous dynamical system if it explicitly depends on time [69].

An example of an autonomous dynamical system is the unforced Duffing's equation,

$$m\ddot{x} + b\dot{x} + k_1x + k_3x^3 = 0, \quad (2.42)$$

where x is the displacement, m is the mass, b is the damping coefficient, and k_1 and k_3 are the linear and nonlinear spring stiffnesses, respectively.

An example of a non-autonomous dynamical system is the damped Duffing's equation with an external harmonic excitation,

$$m\ddot{x} + b\dot{x} + k_1x + k_3x^3 = A\cos(\Omega t), \quad (2.43)$$

where A and Ω are the forcing amplitude and frequency, respectively.

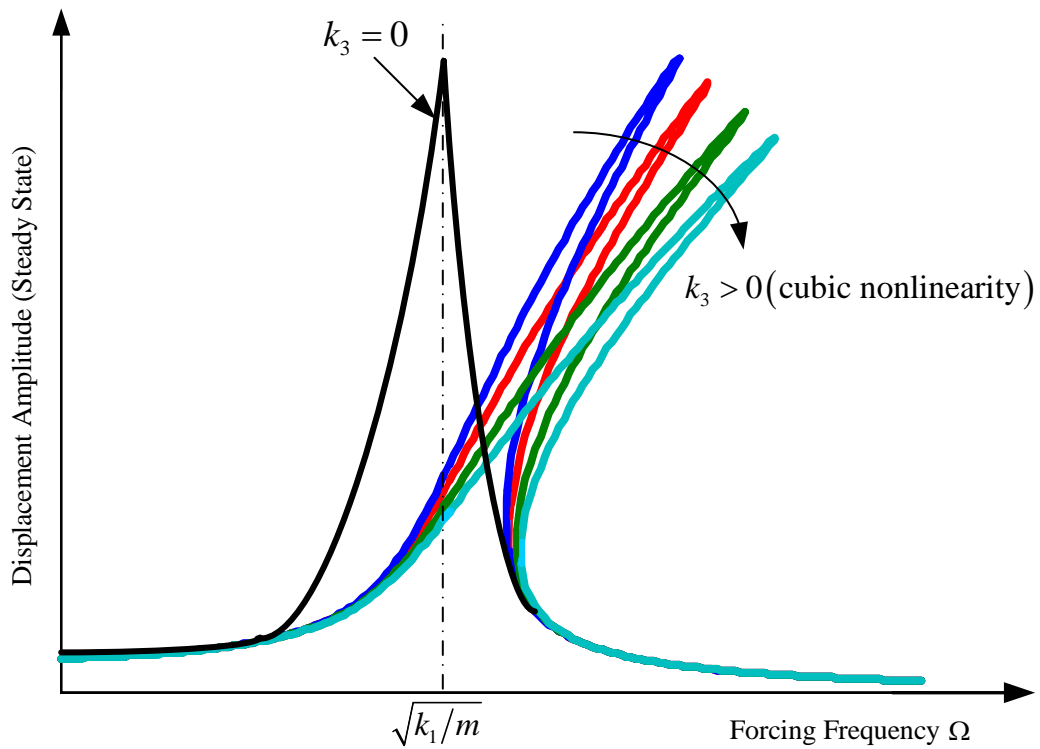


Figure 2-12. Effect of cubic nonlinearity on the system frequency response.

Shown in Figure 2-12 is the effect of cubic nonlinearity on the frequency response of the system defined in Eq. (2.43). As the cubic nonlinearity increases, more bending is observed in the response curve. Also, multiple steady-state solutions could be obtained in some frequency range, which indicates the system is nonlinear.

To define the term fixed point, consider the following general autonomous dynamical system as follows

$$\dot{\vec{x}} = \vec{f}(\vec{x}), \quad (2.44)$$

where \vec{x} represents a column vector of all state variables, and \vec{f} is a column vector of all corresponding general functions. Physically, a fixed point \vec{x}_e (also known as steady state solution) corresponds to an equilibrium position of a system. Mathematically, it is the solution to the following equation

$$\vec{f}(\vec{x}_e) = \vec{0}. \quad (2.45)$$

Stability, Basin of Attraction and Phase Portrait

For stability, a fixed point is locally stable if, given an initial condition sufficiently close to the fixed point, the system eventually approaches this fixed point. A fixed point is globally stable if it is approached for all initial conditions [69, 75]. For a linear system, a locally stable fixed point is always globally stable. However, for a nonlinear system, starting from different initial conditions could result in different steady-state solutions. Local stability does not guarantee global stability, which leads to the concept of a basin of attraction. The domain of all initial conditions that eventually converges to a fixed point is called the basin of attraction (stability region) of the fixed point. More details about basins of attraction will be provided in Chapter 5.

A phase portrait is a collection of all trajectories that represent the solutions (both transient and steady state solutions) of the governing equation in the state space [69, 77]. Phase portrait is one of most important tools in studying the behavior of nonlinear systems since usually there is no closed-form solution for most nonlinear systems.

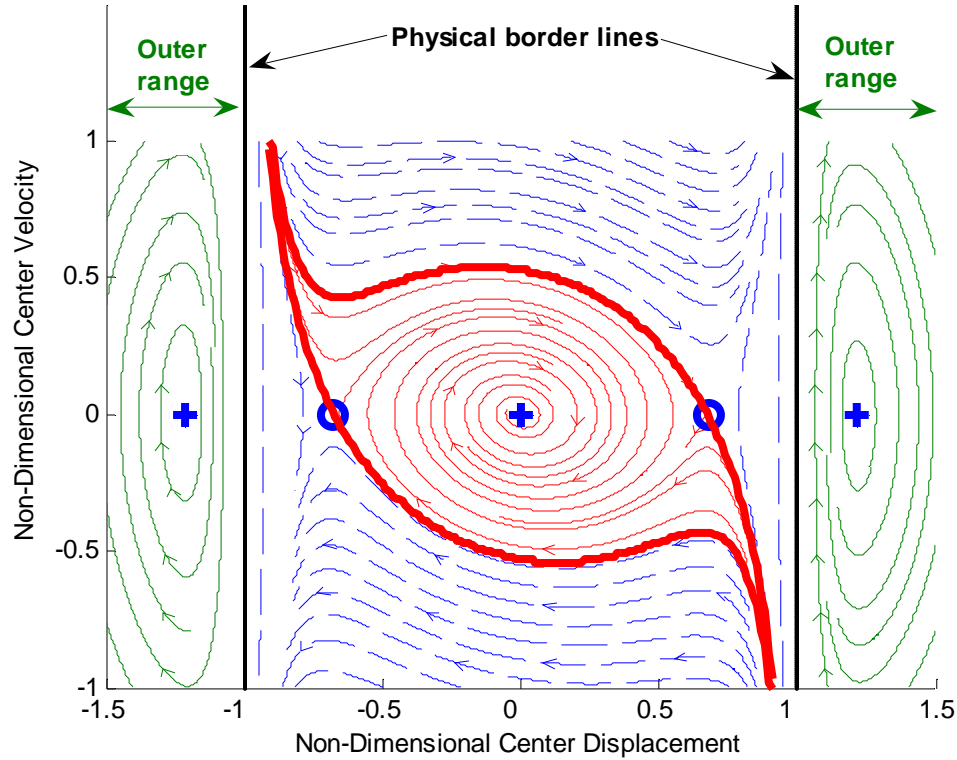


Figure 2-13. Phase plane trajectories around fixed points of a dual-backplate capacitive MEMS microphone (sink points are indicated by blue crosses, and saddle points are indicated by blue circles).

For the illustration purpose, shown in Figure 2-13 is an example phase portrait of a dual-backplate capacitive MEMS microphone under the electrostatic DC excitation only.

The non-dimensional nonlinear governing equation in state-space form is

$$\begin{cases} \dot{x}_1 \\ \dot{x}_2 \end{cases} = \begin{cases} x_2 \\ -2\zeta x_2 - x_1 - \theta x_1^3 + \kappa \frac{x_1}{(1-x_1^2)^2} \end{cases}, \quad (2.46)$$

where the two states x_1 and x_2 are the non-dimensional center displacement and velocity of the diaphragm respectively, and other non-dimensional parameters are assumed to be fixed in the phase portrait. From the plot, we can see the coexistence of multiple fixed points: two locally stable sink points (attractors) outside the physical border lines, one locally stable sink point in the center and two unstable saddle nodes (repellers) between the center point and physical border lines respectively.

Bifurcation

When one or more parameters of the dynamical system are varied, the qualitative change of response behavior, such as a change in the number of stable solutions, is called a bifurcation [69]. The varying parameter is often called the bifurcation parameter. Diagrams, in which the variation of fixed point solutions and their stability are displayed in the space of state variables and bifurcation parameters, are often called bifurcation diagrams [69]. The critical location, at which a bifurcation occurs in the bifurcation diagrams, is called a bifurcation point [69].

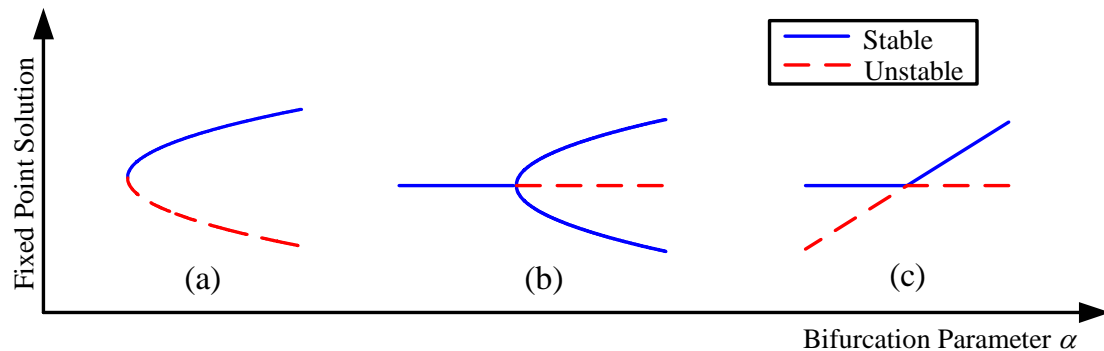


Figure 2-14. Typical bifurcation diagrams for one-dimensional autonomous systems: (a) Saddle-node bifurcation; (b) Pitchfork bifurcation; (c) Transcritical bifurcation (adapted from Nayfeh and Balachandran [69]).

For simplicity, one-dimensional autonomous systems are used here to illustrate the basic idea of a bifurcation. Shown in Figure 2-14 are three typical static bifurcation

diagrams. The saddle-node bifurcation diagram is generated by considering the following dynamical system

$$\dot{x} = \alpha - x^2, \quad (2.47)$$

where α is the bifurcation parameter. In the saddle-node bifurcation, two solution branches start growing from the bifurcation point at $\alpha = 0$, one is stable and another is unstable.

The pitchfork bifurcation diagram is generated by considering the following dynamical system

$$\dot{x} = \alpha x - x^3. \quad (2.48)$$

In the pitchfork bifurcation, initially, there is only one stable solution branch. As the bifurcation parameter increases, the stable solution branch evolves into three different solution branches: two stable solution branches outside and one unstable solution branch between them. The bifurcation point is located at $\alpha = 0$.

Finally, the following dynamical system is considered to generate the transcritical bifurcation

$$\dot{x} = \alpha x - x^2. \quad (2.49)$$

In the transcritical bifurcation, stabilities of the original solution branches change into their counterparts when the bifurcation parameter is sweeping over its bifurcation point (in this example, it is located at $\alpha = 0$).

Previous Work on Nonlinear Dynamics of Electrostatic MEMS Devices

Recently, many electrostatic MEMS devices, such as microphones [65], micropumps [78], microswitches [79], pressure sensors [80] and mass sensors [14], have been fabricated due to the advances of modern silicon micromachining technology.

Many types of nonlinear forces and geometrical nonlinearities were encountered in those MEMS devices. To adequately study these nonlinear behaviors, one analysis approach is to assume a linear relationship between the physical quantities and neglect or linearize those nonlinearities. It turns out that the linear method produces erroneous results, for example, when the device is under the large deflection or large excitation. Therefore, one has to resort to a nonlinear analysis. In this section, previous work on nonlinear dynamics of electrostatic MEMS devices is summarized.

In 1954, F. V. Hunt [3] studied pull-in instability for a single-sided electrostatic loudspeaker. By equating a linear mechanical restoring force to a nonlinear electrostatic force, he found that quasi-static pull-in (referred to it as “fall in” in his book) occurs at two thirds of the gap between the diaphragm and bottom electrode of the loudspeaker. Pull-in experiments were carried for the loudspeaker by monitoring the displacement of the diaphragm; pull-in occurred at a value of 78% of the gap. To explain the difference between the theoretical and measured critical pull-in locations, he suggested that the most likely reason was the exclusion of the curvature of diaphragm in the model.

H. C. Nathanson and his coworkers [4] in 1967 studied pull-in of an electrostatic resonant gate transistor. To understand the electrostatic actuation in their device, a simplified mass-spring model based on the parallel-plate assumption was constructed and analyzed, and pull-in instability was predicted and explained by using the 1-D model.

In 1968, Taylor [81] observed pull-in phenomenon when he increased the voltage between the two closed-spaced liquid drops. The two drops remained apart when the applied voltage was small, and coalesced when the voltage was beyond a threshold voltage. The threshold voltage is referred to as pull-in voltage.

Puers and Lapadatu [51] studied electrostatic forces and their effects on capacitive mechanical MEMS sensors (accelerometer and pressure sensor). In a constant bias charge mode, the critical pull-in charge and mechanical force were obtained analytically based on a simple parallel-plate assumption and a linear spring model. The influence of damping on the critical pull-in charge was also discussed. In a constant bias voltage mode, the critical pull-in voltage and mechanical force were also obtained analytically. Moreover, possible solutions, such as the use of symmetrical structures, were suggested to avoid pull-in in a constant bias charge mode.

Pedersen et al. [82] investigated the harmonic distortion in micromachined silicon condenser microphones. A quasi-static model, which includes a more realistic shape of the diaphragm deflection, was applied to study the harmonic distortion for frequencies far below the resonance of the diaphragm. Instead of an analytical series solution, an iterative numerical approach based on finite differences was implemented to find the quasi-static diaphragm deflection and open-circuit sensitivity of the microphone. The harmonic distortion generated by the sound pressure and nonlinear electrostatic force due to a bias DC voltage was studied numerically and experimentally for a silicon condenser microphone. Both numerical and experimental results showed that the total harmonic distortion of the microphone was linearly dependent on the applied sound pressure level and was a nonlinear function of the applied DC bias voltage.

On the other hand, some researchers are looking for ways to take advantage of pull-in in their MEMS devices. Gupta and Senturia [80] presented a MEMS absolute pressure sensor utilizing pull-in. The device operated with two modes: non-contact and contact modes. During the contact mode, the device was dynamically actuated by an applied step

voltage higher than the pull-in voltage, pull-in time from rest to contact was measured and found to be a nearly linear function of the absolute pressure inside the sensor. A simple 1-D lumped mass-spring-damper model was constructed to theoretically calculate the pull-in time for an electrostatically actuated fixed-fixed microbeam. The electrostatic force was modeled based on the parallel-plate assumption and the fringing field effect [83] was neglected. Also, simulated pull-in times were found to be in good agreement with the measured values.

Zavracky et al. [79] reported a micromechanical switch with three electrodes: a source, a gate and a drain. When the applied voltage between the gate electrode and a microbeam, which connects to the source electrode and hangs over the gate and drain electrodes, was over the pull-in voltage, contact was made between the source and drain electrodes. Both numerical and analytical methods were used to investigate the pull-in of the microbeam; however, the analytical model based on the parallel plate assumption yielded poor results. A nonlinear spring constant of the microbeam was extracted from the numerical simulation results and applied back to the analytical model to obtain good results.

Nemirovsky and Bochobza-Degani [84] presented a generalized model for the quasi-static pull-in parameters of electrostatic actuators with a single charge or voltage input. By setting the first and second derivatives of the total energy (the summation of mechanical and electrical energy) with respect to the displacement of the moving electrode plate to zero, two general algebraic equations were obtained to solve for the pull-in parameters for each type of input respectively. The obtained equations were applied to a wide range of case studies, including parallel-plate and tilted-plate

electrostatic actuators with the fringing field capacitance, the parasitic capacitance, residual charges, constant external forces and nonlinear mechanical forces. Specifically, the analyses results showed that the addition of cubic mechanical nonlinearity in the form of a Duffing's hardening spring extends the stable range of electrostatic actuators quasi-statically. In addition, it was showed that the quasi-static pull-in parameters (such as voltage and displacement) can be affected by the constant external force or pressure. For example, the quasi-static pull-in voltage was reduced when the external force or pressure was in the same direction with the electrostatic force and vice versa.

Zhang et. al. [13, 14, 85] investigated the nonlinear behavior of a parametric resonance-based MEMS mass sensor. Cubic nonlinearities were modeled for the mechanical restoring force of a fixed-fixed beam and the electrostatic force of a comb finger. The sensor was modeled by a lumped mass-spring-damper system with an external electrostatic force. A Duffing equation and a nonlinear Mathieu equation [69] were derived to model the behaviors of nonlinear harmonic and parametric resonances. A perturbation method (multiple scales method) [72] was used to explore the effect of damping and cubic nonlinearity on the parametric resonance. Two pitch-fork bifurcations and three different stability regions were finally obtained for the dynamic characteristics of the nonlinear Mathieu equation. Experimental frequency responses showed that the system is linear with a small AC excitation and nonlinear with a large AC excitation. Also some model parameters, such as the Q factor, cubic mechanical stiffness and linear electrostatic stiffness, were extracted from the experimental data.

Nayfeh and his co-workers presented a series of nonlinear models for the electrically actuated annular plates [78], fixed-fixed rectangular beams [86, 87], simply

supported rectangular plates [88], and clamped circular plates [89, 90]. The static deflections of those microstructures are determined by either an analytical reduced-order model (macromodel) or a numerical shooting method, which is widely used to determine the periodic solutions of autonomous and non-autonomous systems [69]. The shooting method is an iterative procedure and computationally costly, and becomes numerically unstable when pull-in is approached; therefore, it is not suitable for the prediction of pull-in. On the other hand, the reduced-order model [86-90] usually approximates the system dynamics with N coupled nonlinear ordinary-differential equations, which are obtained by the spatial discretization of the distributed-parameter governing equation and associated boundary conditions via a Galerkin approach or finite-element method. The reduced-order model is robust up to the pull-in point, and it also has the capability to account for the in-plane residual stress, general material and geometric nonlinearities.

Younis et al. [86] and Abdel-Rahman et. al. [91] applied the reduced-order model to simulate the dynamical behavior of a MEMS switch and predict its pull-in time. A saddle-node bifurcation of a microbeam was found due to the pull-in. Two deflection solution branches of the microbeam moved closer to each other as the DC voltage increased, and finally coalesced when pull-in voltage was reached. Based on the reduced-order model, they also calculated that the deflection at the pull-in is approximately 57% of the gap.

Younis and Nayfeh [92] studied the nonlinear response of a resonant microbeam under an electrostatic actuation. A nonlinear model was first built to account for the mid-plane stretching and an electrostatic load with both DC and AC components. A perturbation method was applied directly to analyze the nonlinear forced response to a

primary-resonance excitation of its first mode. The analysis results showed that the resonance frequency can be affected by the damping, mid-plane stretching, and electrostatic nonlinearity. This paper showed that the DC electrostatic load could result in both softening and hardening spring behaviors. In addition, the method of multiple scales was applied to investigate a three-to-one internal resonance between the first and second modes of the clamped-clamped beam. The analysis result showed that those two modes are nonlinearly uncoupled and therefore the internal resonance cannot be activated.

Chowdhury et. al. [93] studied the nonlinear effects in a MEMS capacitive microphone. The microphone was modeled as a second-order single-degree-of-freedom system. The spring hardening effect due to the mid-plane stretching and the spring softening effect due to the nonlinear electrostatic force were presented. By using Taylor series expansion, the nonlinear electrostatic force was linearized and pull-in voltage was derived for a fully clamped square diaphragm with a built-in tension stress. Finally, nonlinear finite element analyses were carried out to verify the analytical results.

Nadal-Guardia et al. [94] presented a compact 1-D lumped model of capacitive silicon sensors. By applying a perturbation method to the dynamic governing equations, transfer functions of the system were developed analytically. When comparing to the traditional equivalent analog circuit model, the obtained transfer functions can account for the effect of pull-in instability. Numerical simulations with the transfer functions were conducted, and the results were compared with the experimental data for a capacitive MEMS microphone. Both simulation and experimental results showed that pull-in instability improved the low-frequency response of the microphone for DC bias

voltages close to its critical pull-in value. However, the developed transfer function could not predict the sensitivity change of the microphone as a function of the bias voltage. This limitation is mainly due to the application of constant model parameters, which was obtained for a certain DC voltage value, for a whole range of the bias voltage.

Fargas-Marques and Shkel [95] studied both static and dynamic pull-in conditions for an electrostatic MEMS resonator based on the parallel-plate actuation. They used a 1-D lumped mass-spring-damper model and derived the condition for AC dynamic pull-in based on the kinetic and potential energy of the system. The experimental results for the pull-in voltages agreed well with their analytical results. The dynamic pull-in voltage was reported to be approximately 8% lower than the static pull-in voltage. Their energy analysis results also showed that the quality factor or damping of the system had an impact on the dynamic pull-in voltage.

Elata and Bamberger [96] presented a purely theoretical study on the dynamic pull-in of electrostatic actuators when subjected to instantaneous application of DC voltages. Based on Hamilton's principle [97] and quasi-static equilibrium equations, dynamic pull-in for general undamped electrostatic actuators with multiple degrees of freedom and voltage sources was formulated. Specifically, the critical dynamic pull-in voltages were found approximately 8% lower than the corresponding quasi-static pull-in voltages for electrostatic actuators with parallel-plates, double parallel-plates, and clamped-clamped beams. For the electrostatic actuator with a block of comb drives with no initial overlap, the critical dynamic pull-in voltage was found approximately 16% lower than its quasi-static pull-in voltage. If damping exists in electrostatic actuators (which is always the

case in practice), they concluded that the actual dynamic pull-in voltage was bounded between the quasi-static pull-in voltage and the dynamic pull-in voltage without damping.

Although previous research work provided a good understanding of various aspects of nonlinear dynamics of electrostatic MEMS devices, none of these studies is helpful for a dual-backplate capacitive MEMS microphone. The rest of this dissertation is devoted to investigating the nonlinear dynamics issues associated with a dual-backplate capacitive MEMS microphone.

CHAPTER 3 NONLINEAR DYNAMIC MODEL

This chapter derives a nonlinear model for the dynamics of a dual-backplate MEMS microphone. First, general displacement solutions (small displacement by an analytical method and large displacement by an energy approach) of the middle diaphragm are provided based on the plate theory. Based on the general displacement solutions, lumped element modeling is used to extract the parameters of the diaphragm. Other lumped parameters of the microphone, including the damping coefficient and stiffness of the cavity, are also presented. After all the lumped parameters of the microphone are obtained, the general nonlinear governing equation is derived and the model nonlinearities are discussed. Finally, nonlinear finite element analyses (FEA) are carried out to verify the theoretical lumped stiffnesses of the diaphragm.

Microphone Structure

The dual-backplate capacitive MEMS microphone studied here has been fabricated using the SUMMiT V process at Sandia National Laboratories as well as facilities at the University of Florida for post-processing [65, 66]. A 3D cross-section view of the microphone is shown in Figure 3-1. It has a 2.25 μm thick circular solid diaphragm with a 230 μm radius and a 2 μm gap between each circular perforated backplate. The 5 μm radius holes in the backplates allow the incident acoustic pressure to act on the diaphragm. A cavity under the bottom backplate is formed via a deep reactive ion etch, and vented to the ambient pressure resulting in an AC measurement device.

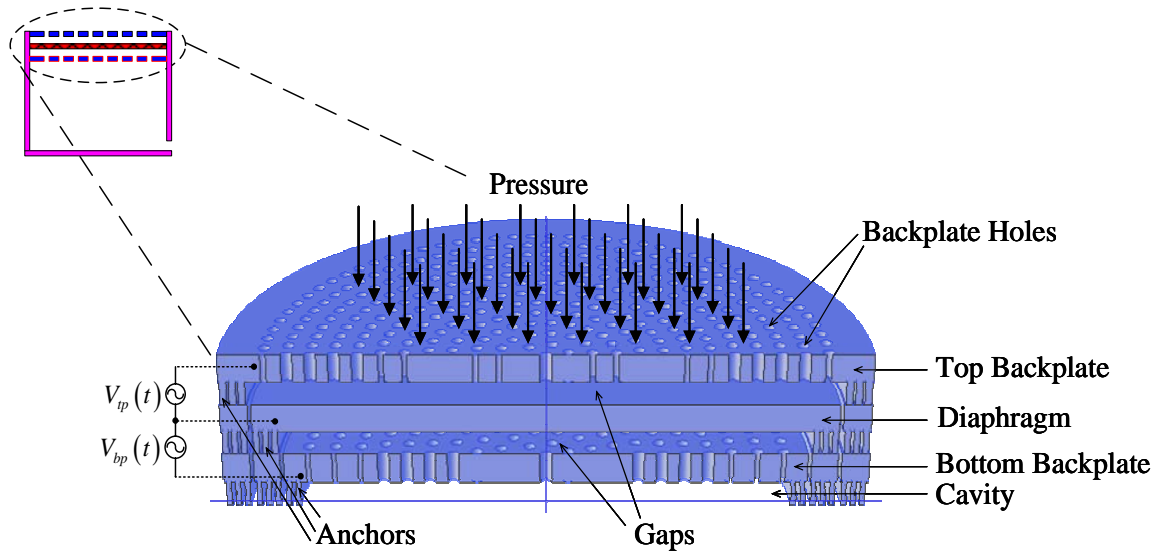


Figure 3-1. 3D cross-section view of the microphone structure (not to scale).

Figure 3-2 shows a microscope photograph of the microphone top with a field of view of approximately $1\text{ mm} \times 1\text{ mm}$. The bond pads shown in the photograph enable electrical connections between the backplates and diaphragm.

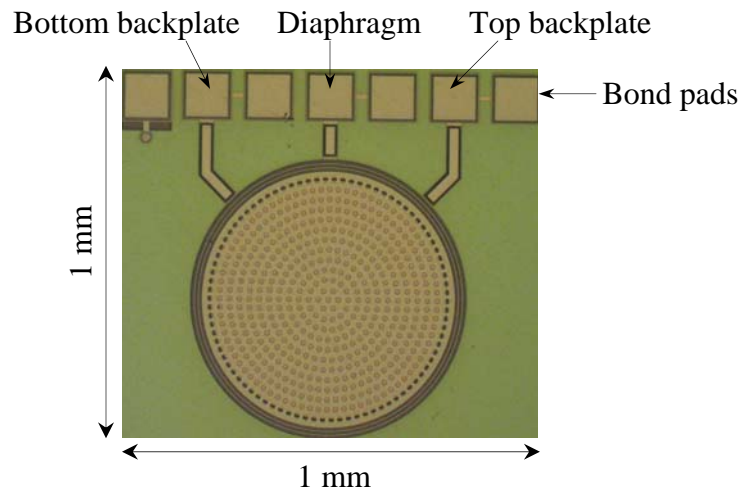


Figure 3-2. Top-view photograph of the microphone.

Displacement Solutions of the Diaphragm

The diaphragm is a key energy transduction component and plays a significant role in determining the performance of the microphone. Therefore, its mechanical behavior

under the uniform transverse pressure loading is studied first. It is assumed that the circular polysilicon diaphragm is linearly elastic, isotropic and axisymmetric. Also, zero in-plane residual stress [98] and a clamped boundary condition are assumed in the analysis.

Small Displacement Solution

Shown in Figure 3-3, a clamped circular diaphragm is subject to a transverse uniform pressure loading p . The radius and thickness of the diaphragm are denoted by a and h respectively. From the plate theory, if the transverse deflection of the diaphragm is much smaller than its thickness, the strain in the neutral plane of the diaphragm can be neglected and the solution in this case is called the small displacement solution [99].

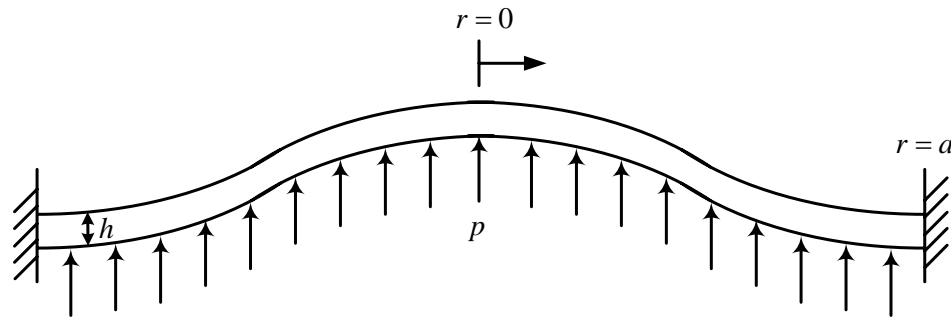


Figure 3-3. Schematic of a clamped circular diaphragm under a transverse uniform pressure loading.

For the static small displacement solution, the governing differential equation for the transverse deflection $w(r)$ in a polar coordinate system is given as follows [99]

$$\frac{d}{dr} \left\{ \frac{1}{r} \frac{d}{dr} \left(r \frac{dw}{dr} \right) \right\} = \frac{pr}{2D}, \quad (3.1)$$

where r is the distance of any radial point along the radius and D is the flexural rigidity of the diaphragm defined as

$$D = \frac{Eh^3}{12(1-\nu^2)}. \quad (3.2)$$

The parameters E and ν are the Young's modulus and Poisson's ratio of polysilicon respectively. The boundary conditions are

$$w(a) = \left. \frac{dw}{dr} \right|_{r=a} = 0, \quad (3.3)$$

and

$$w(0) < \infty. \quad (3.4)$$

Solving Eq. (3.1) with Eqs. (3.3) and (3.4), the small displacement solution becomes

$$w(r) = \frac{pa^4}{64D} \left[1 - \left(\frac{r}{a} \right)^2 \right]^2. \quad (3.5)$$

The center displacement of the diaphragm is then

$$w_0 = w(0) = \frac{pa^4}{64D}. \quad (3.6)$$

Energy Method and Large Displacement Solution

From the plate theory, if the transverse deflection of the diaphragm is comparable to its thickness, the strain in the neutral plane of the diaphragm cannot be neglected and the solution in this case is called the large displacement solution. For the large displacement solution, it can be assumed from the plate theory that the deflected surface in such a case is still symmetrical with respect to the origin of the circular diaphragm. In this section, an energy approach is used to obtain an approximate large displacement solution. A more rigorous theory of the nonlinear mechanics of transducer diaphragms including the effects of in-plane stress is given in the reference [100].

Procedure of energy method

By applying an energy method [97, 99], trial functions with unknown coefficients for the transverse displacement and in-plane displacement need to be chosen first. Typical choices for the trial functions are polynomials and orthogonal functions such as sinusoidal or cosine functions. However, trial functions must satisfy the boundary condition, which limits the choices of trial functions.

Once the trial displacement functions are assumed, the strain energy can be then calculated by using the strain-displacement relation (linear and nonlinear) and constitutive equation. Also, the work done by the external load can be calculated. The potential energy of the system is the summation of strain energy and work done by the external load.

Finally, by applying the principle of minimum potential energy for the equilibrium condition, a set of linear algebraic equations is obtained and further solved to yield the unknown coefficients in the trial functions. Thereafter, the approximate solutions for the transverse displacement and in-plane displacement are determined. The next section presents the application of an energy method to solving the large displacement solution for a clamped circular diaphragm, and the detailed steps are provided in Appendix A.

Large displacement solution

The polar coordinate frame is introduced here to facilitate the analysis for a circular diaphragm. As mentioned previously, the radial displacement in the neutral plane of a diaphragm cannot be neglected when large transverse deflections occur. The displacement of a point in the neutral plane of a circular diaphragm is decomposed into two components: $u(r)$ in the radial direction and $w(r)$ perpendicular to the neutral

plane as shown in Figure 3-4. The shape of the transverse deflection surface of a circular diaphragm is assumed to be similar with the one in a small displacement case, which is defined in Eq. (3.5) as follows

$$w(r) = w_0 \left(1 - \frac{r^2}{a^2} \right)^2, \quad (3.7)$$

where w_0 is the unknown center displacement that needs to be determined. The assumed transverse deflection satisfies the clamped boundary conditions defined in Eqs. (3.3) and (3.4).

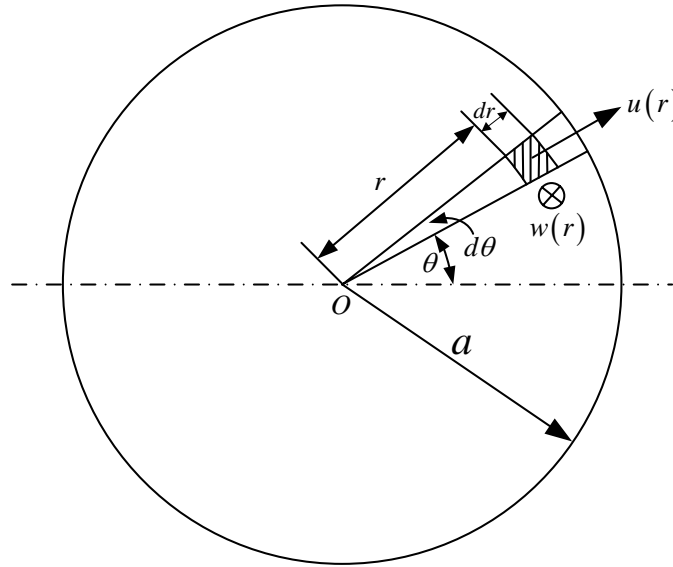


Figure 3-4. Displacement components in the neutral plane of a circular diaphragm.

To satisfy the clamped boundary conditions, the radial displacement $u(r)$ must vanish at the edge and the origin of the circular diaphragm; therefore, the following polynomial is used to approximate the complex expression of the radial displacement [99]

$$u(r) = r(a - r)(C_1 + C_2 r), \quad (3.8)$$

where C_1 and C_2 are the two unknown constants.

Based on the von Kármán plate theory [99, 101] and energy method (detailed derivation steps are provided in Appendix A), finally we can determine the three unknown coefficients for a polysilicon diaphragm (Poisson's ratio $\nu = 0.22$ is used in the derivation, note that the following results are only valid for this specific Poisson's ratio) as follows

$$C_1 = 1.2652 \frac{w_0^2}{a^3}, \quad (3.9)$$

$$C_2 = -1.8129 \frac{w_0^2}{a^3}, \quad (3.10)$$

and

$$w_0 = \frac{pa^4}{64D} \frac{1}{1 + 0.4708 \frac{w_0^2}{h^2}}. \quad (3.11)$$

Eq. (3.11) can be rewritten as

$$w_0 \left(1 + 0.4708 \frac{w_0^2}{h^2} \right) = \frac{pa^4}{64D}. \quad (3.12)$$

The final approximate expression for the large displacement solution can be determined by substituting the solution of w_0 from Eq. (3.12) into Eq. (3.7). As we can see from Eq. (3.11), the small factor $0.4708 w_0^2/h^2$ represents a geometric nonlinearity (nonlinear spring hardening effect) due to the in-plane stretching when large displacements occur. The diaphragm can now be modeled as a nonlinear Duffing spring, where the two spring constants can be obtained via further lumped element modeling in the following section.

As seen from Eq. (3.7), the assumed mode shape based on this energy approach is not affected by the applied pressure. Shown in Figure 3-5 is a plot of different normalized mode shapes for several pressure values. In the plot, three normalized mode

shapes are generated based on the exact solution given in the reference [100]. As we can see from the plot, for larger pressure values (for example, 100000 Pa), the assumed mode shape used in the energy approach is not accurate. However, for our 2000Pa microphone design, the assumed mode shape used in the energy approach is in good agreement with the exact mode shape as shown in the above plot.

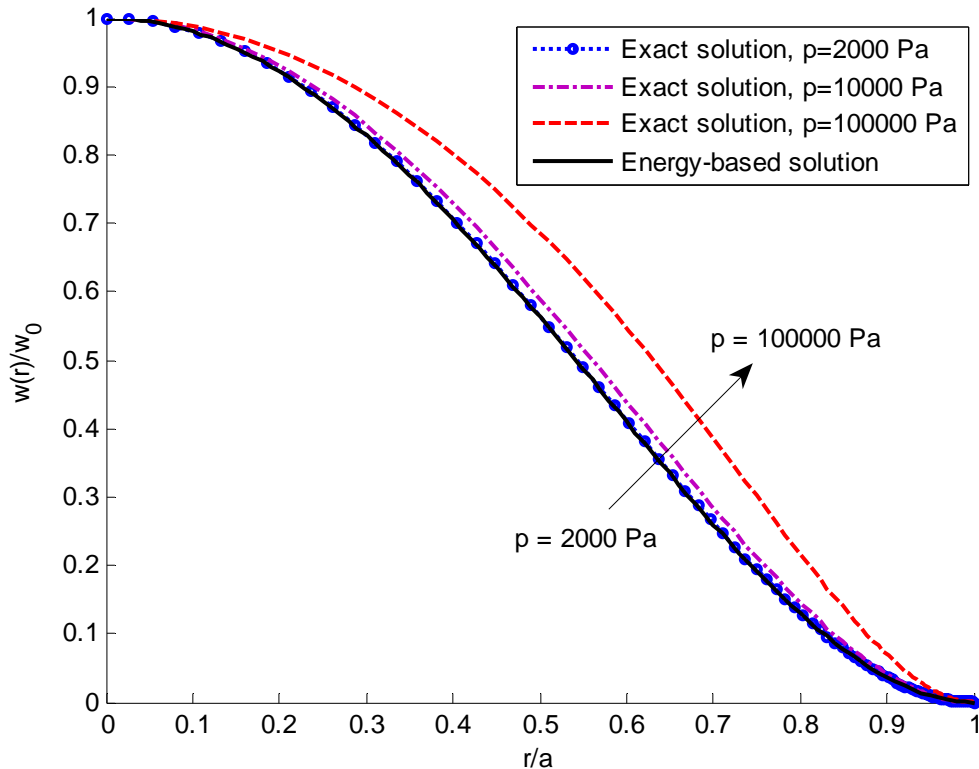


Figure 3-5. Normalized mode shape for several pressure values (2000, 10000 and 100000 Pascals).

Lumped Element Modeling of the Microphone

The microphone is a typical multi-domain (acoustical, mechanical and electrical) system and its dynamics are usually governed by a set of coupled nonlinear partial differential equations, which are difficult and complex to study. As we can see from Eq. (3.7), the displacement of the diaphragm is not uniform but distributed along the radial direction. The associated potential and kinetic energy are also distributed along the radial

direction of the diaphragm, which indicates that the microphone is a distributed-parameter system.

One alternative for approximating the coupled distributed-parameter system dynamics is through the construction of a lumped-element model. In general, lumped element modeling is based on the assumption that the device length scale of interest is much smaller than the characteristic length scale (for example, wavelength) of the physical phenomena [29, 102, 103]. By using lumped element modeling, the spatial variations of the quantities of interest can be decoupled from the temporal variations. The coupled distributed-parameter system can be then divided into many idealized lumped impedances (mass, stiffness and dissipation) [29]. The dynamic behavior of the system can be described only by ordinary differential equations with time being the only independent variable, which is comparatively easier (than coupled nonlinear partial differential equations) to analyze in practice.

To carry out lumped element modeling, usually a lumped reference point needs to be defined first to lump a distributed-parameter system into a single/multiple degree of freedom system. In the case of a circular diaphragm, the center point is chosen. In this section, the lumped parameters for the microphone are discussed. Since the diaphragm is a key part of the microphone and plays a crucial role in determining the overall performances of the microphone, the diaphragm is studied first by the lumped element modeling.

Lumped Parameters of Diaphragm

Before proceeding to extract lumped parameters, the reference point for the circular diaphragm is chosen to be at its center position $r = 0$. The general applied transverse pressure is assumed for simplicity to be a harmonic oscillation

$$p(t) = p_0 e^{j\omega t}, \quad (3.13)$$

where ω is the angular frequency of the pressure oscillation.

The dynamic small displacement solution is obtained by modifying Eq. (3.5)

$$w(r, t) = \frac{p(t) a^4}{64D} \left[1 - \left(\frac{r}{a} \right)^2 \right]^2 = \frac{p_0 a^4}{64D} \left[1 - \left(\frac{r}{a} \right)^2 \right]^2 e^{j\omega t}. \quad (3.14)$$

The velocity is

$$v(r, t) = \frac{\partial}{\partial t} w(r, t) = j\omega w(r, t). \quad (3.15)$$

Therefore the displacement and velocity at the reference point are

$$w_0(t) = w(0, t) = \frac{p_0 a^4}{64D} e^{j\omega t}, \quad (3.16)$$

and

$$v_0(t) = j\omega w_0(t). \quad (3.17)$$

Lumped mass

The total kinetic energy of the diaphragm is given by

$$W_{KE} = \frac{1}{2} \int v^2(r, t) \rho' dA = \frac{1}{2} \int_0^a v^2(r, t) \rho' 2\pi r dr, \quad (3.18)$$

where ρ' is the mass per unit area. Substituting Eqs. (3.15), (3.16) and (3.17) into Eq.

(3.18) yields

$$W_{KE} = \frac{\pi a^2 \rho'}{5} \frac{v_0^2(t)}{2} \triangleq M_{me} \frac{v_0^2(t)}{2}. \quad (3.19)$$

Therefore, the work-equivalent lumped mass is calculated as

$$M_{me} = W_{KE} / \left[\frac{v_0^2(t)}{2} \right] = \frac{\pi a^2 \rho'}{5} = \frac{\pi a^2 h \rho}{5}, \quad (3.20)$$

where ρ is the mass per unit volume and M_{me} is 1/5 of the mass of the actual diaphragm. Physically, the diaphragm with distributed deflections has been replaced by a rigid disk (piston) and a linear spring. In order to conserve the kinetic energy, a rigid disk with 1/5 of the mass of the actual diaphragm is used.

Lumped linear stiffness and compliance

The total potential energy of the diaphragm can be expressed as

$$W_{PE} = \int F dx = \iint p(t) 2\pi r dr dw(r, t). \quad (3.21)$$

From Eqs. (3.13), (3.14) and (3.16), we know

$$p(t) = \frac{64D}{a^4} w_0(t), \quad (3.22)$$

and

$$dw(r, t) = \left[1 - \left(\frac{r}{a} \right)^2 \right]^2 dw_0(t). \quad (3.23)$$

Substituting Eqs. (3.22) and (3.23) into Eq. (3.21) yields

$$W_{PE} = \frac{64D}{a^4} \int_0^{w_0(t)} \left\{ \int_0^a 2\pi r \left[1 - \left(\frac{r}{a} \right)^2 \right]^2 dr \right\} w_0(t) dw_0(t) = \frac{64\pi D}{3a^2} \frac{w_0^2(t)}{2}. \quad (3.24)$$

Therefore, the work-equivalent mechanical stiffness is calculated as

$$k_1 = W_{PE} / \left[\frac{w_0^2(t)}{2} \right] = \frac{64D\pi}{3a^2}. \quad (3.25)$$

The mechanical compliance is

$$C_{me} = \frac{1}{k_1} = \frac{3a^2}{64\pi D}. \quad (3.26)$$

Physically, the diaphragm with distributed deflections has been replaced by a rigid disk (piston) and a linear spring. By using the lumped stiffness or compliance, the conservation of potential energy in the physical diaphragm and an idealized linear spring is ensured.

Lumped area

To ensure the continuity of volumetric velocity in physical and lumped domains, the lumped area of the diaphragm needs to be found. The volumetric velocity through the diaphragm is given by

$$Q = \iint_A v(r, t) dA = \int_0^a v(r, t) 2\pi r dr. \quad (3.27)$$

From Eqs. (3.15) and (3.17), we have

$$v(r, t) = \left[1 - \left(\frac{r}{a} \right)^2 \right]^2 v_0(t). \quad (3.28)$$

Substituting Eq. (3.28) into (3.27), we can get

$$Q = \frac{\pi a^2}{3} v_0(t) \triangleq A_{me} v_0(t). \quad (3.29)$$

Therefore the equivalent lumped area is calculated as

$$A_{me} = Q / v_0(t) = \frac{\pi a^2}{3} = \frac{A}{3}, \quad (3.30)$$

where A_{me} is 1/3 of the area A of the actual diaphragm. The distributed deflection of the diaphragm has been replaced by the translation of a rigid disk (piston) with an area that is 1/3 that of the actual diaphragm.

Lumped cubic stiffness

The lumped cubic stiffness of the diaphragm is developed in this section. Eq. (3.25) only shows the linear spring constant of the diaphragm for a small displacement case. For a large displacement case, a nonlinear Duffing spring model is considered for the diaphragm, which is

$$F \triangleq pA_{me} = k_1 w_0 + k_3 w_0^3. \quad (3.31)$$

Comparing Eqs. (3.12) and (3.30), we have

$$k_1 = \frac{64D\pi}{3a^2}, \quad (3.32)$$

and

$$k_3 = \frac{10.044D\pi}{a^2 h^2}. \quad (3.33)$$

Eq. (3.32) is same with Eq. (3.25) because both energy-based large displacement and small displacement solutions used a same deflection shape defined in Eq. (3.7). When the diaphragm vibrates, the equivalent structural damping of the diaphragm mainly consists of two parts: the thermoelastic energy dissipation in the diaphragm and the vibration energy dissipation in the compliant boundary of the diaphragm [9, 10]. Usually the equivalent structural damping is determined experimentally, it is neglected in the current model since it is small comparing with the dominant viscous damping. The experimental result for the dominant viscous damping will be discussed in Chapter 6.

Lumped Damping Coefficient

The two backplates of the microphone are designed to be perforated with a large number of holes. One purpose of these holes is to let the air pass through without deflecting the backplates and make them acoustically transparent. A repetitive pattern of

holes in the top backplate is shown in Figure 3-6. The top backplate has a radius of 256 μm and 557 holes with a radius of 5 μm . A similar hole pattern exists for the bottom backplate, which has a radius of 213 μm and 367 holes with a radius of 5 μm .

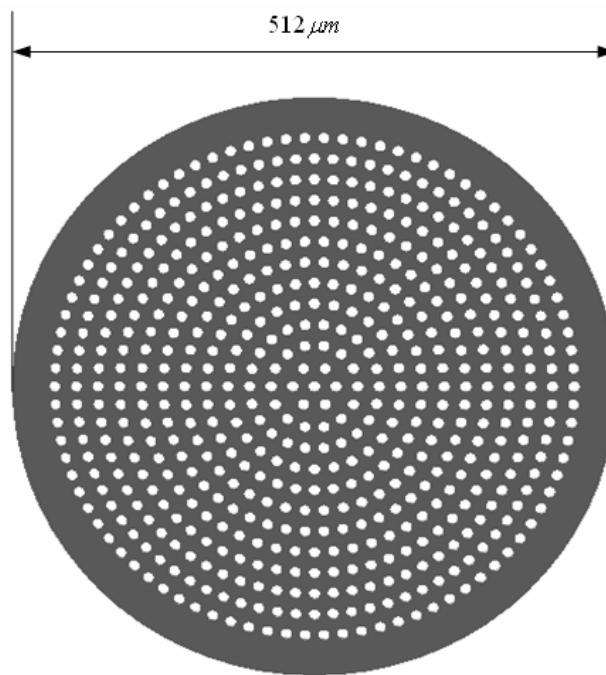


Figure 3-6. Repetitive pattern of holes in the top backplate.

When the diaphragm vibrates, the gas flow between the diaphragm and backplate can be divided into two parts, the horizontal gas flow between the parallel plates and the vertical gas flow through the backplate holes. Viscous damping caused by the horizontal gas flow is often called squeeze-film damping, and the viscous damping caused by the vertical gas flow is called holes resistance. The latter becomes important and cannot be neglected especially when the thickness of backplate is comparable to the gap thickness [7, 8].

Since the viscous damping plays a very important role in determining the bandwidth and noise floor of the microphone, its modeling becomes important for this

research. For the squeeze-film damping in the gap, the mechanical lumped damping coefficients are given as follows [8, 53]

$$b_{tp}^s = \frac{4\mu\pi a^4}{3n_{tp}d_0^3} B(A_{tp}) \quad (3.34)$$

and

$$b_{bp}^s = \frac{4\mu\pi a^4}{3n_{bp}d_0^3} B(A_{bp}), \quad (3.35)$$

where μ is the dynamic viscosity of air, d_0 is the nominal gap between backplates and diaphragm, n_{tp} and n_{bp} are the numbers of holes in the top and bottom backplates respectively. The porosity of the top and bottom backplates is given by A_{tp} and A_{bp} respectively, and $B(\lambda)$ is a function defined as

$$B(\lambda) = \frac{1}{4} \ln\left(\frac{1}{\lambda}\right) - \frac{3}{8} + \frac{1}{2}\lambda - \frac{1}{8}\lambda^2. \quad (3.36)$$

When the thickness of the backplate is comparable to the gap, the viscous damping due to the vertical gas flow through the backplate holes becomes important. By modeling the motion in the holes as a pressure-driven Poiseuille flow in a pipe, the mechanical lumped damping coefficients are given as follows [7, 8]

$$b_{tp}^h = \frac{8\mu\pi h_{tp} n_{tp}}{A_{tp}^2}, \quad (3.37)$$

and

$$b_{bp}^h = \frac{8\mu\pi h_{bp} n_{bp}}{A_{bp}^2}, \quad (3.38)$$

where h_p and h_{bp} are the thicknesses of the top backplate and bottom backplate respectively. Therefore, the total viscous damping of the microphone is,

$$b = b_p^s + b_{bp}^s + b_p^h + b_{bp}^h. \quad (3.39)$$

Lumped Stiffness of the Cavity

The cavity of the microphone impedes the movement of diaphragm by storing potential energy and acts as a spring. Based on the lumped element assumption, the work-equivalent lumped acoustic compliance of the cavity is given as follows [104]

$$C_c^a = \frac{V_c}{\rho c_0^2}, \quad (3.40)$$

where V_c is the volume of the cavity, ρ is the density of air, and c_0 is the isentropic speed of sound in air. It should be pointed out that Eq. (3.40) is valid for $kd_c < 0.3$, where k is the wave number [104] and d_c is the depth of the cavity.

For the cylindrical cavity with a circular cross section, the volume is

$$V_c = \pi a_c^2 d_c, \quad (3.41)$$

where a_c is the radius of the cavity. Therefore the mechanical lumped stiffness of the cavity is

$$k_c = \frac{(\pi a_c^2)^2}{C_c^a}, \quad (3.42)$$

where $(\pi a_c^2)^2$ is used to convert the acoustic stiffness into the mechanical stiffness.

Since the lumped stiffness of the cavity is in parallel with the linear stiffness of the diaphragm, the first resonant frequency of the system is approximated by

$$f_{nature} = \frac{1}{2\pi} \sqrt{\frac{k_1 + k_c}{M_{me}}} \quad (3.43)$$

As seen from the Eq.(3.43), the existence of the cavity increases the bandwidth of the capacitive microphone. Based on the results of the lumped element modeling, the calculated nominal values of lumped parameters as well as the material properties and physical dimensions of the designed 2000Pa dual-backplate condenser microphone are summarized in Table 3-1 [65, 66].

Table 3-1. Material properties and physical parameters of the 2000Pa microphone in metric units (material: polysilicon).

Parameter	Nominal value
Young's modulus (E)	1.60e11 (Pa)
Poisson's ratio (ν)	0.22
Density (ρ)	2.23e3 (kg/m ³)
Thickness of the diaphragm (h)	2.25e-6 (m)
Radius of the diaphragm (a)	230e-6 (m)
Linear spring constant of the diaphragm (k_1)	202 (N/m)
Cubic spring constant of the diaphragm (k_3)	1.88e13 (N/m ³)
Lumped mass of the diaphragm (M_{me})	16.7e-11 (kg)
Lumped area of the diaphragm (A_{me})	5.54e-8 (m ²)
Gap (d_0)	2.00e-6 (m)
Depth of the cavity (d_c)	650e-6 (m)
Radius of the cavity (a_c)	187e-6 (m)
Linear spring constant of the cavity (k_c)	24.3 (N/m)
Thickness of the top backplate (h_{tp})	2.25e-6 (m)
Thickness of the bottom backplate (h_{bp})	2.50e-6 (m)
Number of holes for top backplate (n_{tp})	557
Number of holes for bottom backplate (n_{bp})	367
Ratio of the total holes area to the backplate area ($A_{tp} = A_{bp}$)	0.22
First resonant frequency of the microphone system (f_{nature})	185 (kHz)
Total lumped damping coefficient (b)	3.15e-5 (N·s/m)
Total damping ratio	8.09e-2
*First resonant frequency of diaphragm	175 (kHz)
*First resonant frequency of bottom backplate	203 (kHz)
*First resonant frequency of top backplate	130 (kHz)

*FEA results with fixed boundaries

Further calculations show that the first natural frequency of the system is increased by approximately 5.9% due to the existence of cavity. If the cavity stiffness is neglected in Eq. (3.43), the first natural frequency of the diaphragm via LEM is approximately 175.3 kHz. One way to check the accuracy of the modeled first natural frequency of the diaphragm is to solve the transverse bending wave equation for the circular diaphragm with a fixed boundary [105]. Further studies show that the theoretical first natural frequency of the diaphragm is approximately 173.3 kHz. The error due to the lumped element assumption is approximately 1.1%.

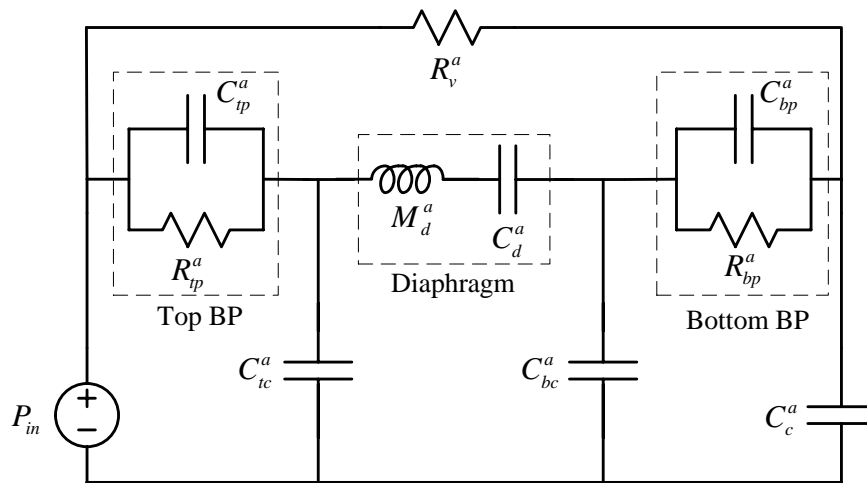


Figure 3-7. Simplified lumped element model of a dual-backplate capacitive microphone (adapted from Martin et al. [66]).

In the current lumped element model, the backplates are assumed to be acoustically transparent and the compliance of the cavities between the diaphragm and top/bottom backplates are neglected. A simplified lumped element model of the microphone shown in Figure 3-7 is used to verify these assumptions. This model describes the microphone in the acoustic domain, where the mechanical lumped parameters derived in the above section are converted to their analogous acoustic parameters. Additionally, other features of the microphone, such as the vent resistance and the compliance of each backplate, are

also included in this model [66]. Readers are referred to [66] for more details of constructing this lumped model.

In the model, P_{in} represents the incident acoustic pressure. C_{tp}^a , C_d^a , C_{bp}^a and C_c^a are the acoustic compliances of the top backplate, diaphragm, bottom backplate and bottom cavity, respectively. C_{tc}^a and C_{bc}^a are the acoustic compliance of the cavities between the diaphragm and top/bottom backplates, respectively. R_{tp}^a and R_{bp}^a are the acoustic resistance of the top backplate and bottom backplate, respectively. M_d^a is the acoustic mass of the diaphragm and R_v^a is the acoustic vent resistance from the cavity to the incident acoustic pressure.

For the cavities between the diaphragm and top/bottom backplates, each cavity volume is less than 0.5% of that of the bottom cavity. Therefore, the acoustic compliance of each small cavity (C_{tc}^a and C_{bc}^a) is less than 0.5% of the compliance (C_c^a) of the bottom cavity (the acoustic compliance of the cavity is proportional to its volume). The impedance of the cavities ($1/(j\omega C_{tc}^a)$ and $1/(j\omega C_{bc}^a)$) between the diaphragm and top/bottom backplates are much larger than the impedance of the bottom cavity and the diaphragm. Therefore, in the equivalent circuit, C_{tc}^a and C_{bc}^a can be treated as open circuit and are neglected in the lumped element model.

As seen from Figure 3-7, for each backplate, its acoustic compliance is in parallel with its resistance (a RC loop is formed). Therefore, the impedance of each backplate will be approximately equal to its resistance [66] when

$$f \ll \frac{1}{2\pi R_{tp}^a C_{tp}^a} = 1.3\text{MHz}, \quad (3.44)$$

and

$$f \ll \frac{1}{2\pi R_{bp}^a C_{bp}^a} = 3.3\text{MHz}, \quad (3.45)$$

where f is the frequency of the incident acoustic pressure.

As seen from Figure 3-7, the pressure drop across each plate is proportional to the impedance of each plate (note that C_{tc}^a and C_{bc}^a are neglected). Based on the microphone design, the impedance of each backplate is much less than the impedance of the diaphragm [66] when Eqs. (3.44) and (3.45) are satisfied; therefore, the pressure drop across each backplate is negligible. Since the small backplate deflection is proportional to the pressure drop across it; therefore, the backplate deflection is negligible and the backplate can be treated as being acoustically transparent.

Nonlinear Dynamic Model

A general nonlinear dynamic model for the microphone is shown schematically in Figure 3-8. The top and bottom backplates are assumed to be rigid and have equal areas with the diaphragm. The diaphragm is modeled by a Duffing spring with two spring constants k_1 and k_3 and a lumped mass M_{me} with a lumped area A_{me} .

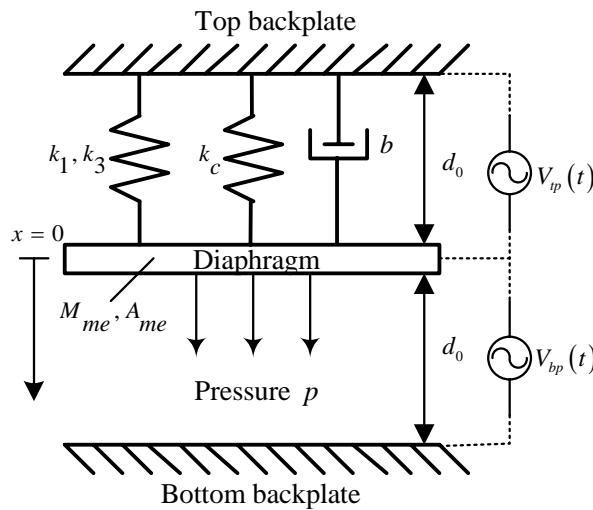


Figure 3-8. A nonlinear dynamic model of a dual-backplate capacitive microphone.

Shown in Figure 3-9 is the free body diagram of the dynamic model, pA_{me} is the lumped mechanical force caused by the incoming acoustic pressure, and $M_{me}\ddot{x}$ is the lumped inertia force due to the acceleration. For simplicity, during the derivation of the dynamic governing equation, the diaphragm is assumed to move downwards with a certain displacement x .

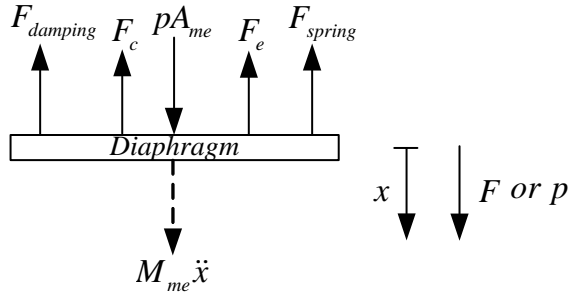


Figure 3-9. Free body diagram of the nonlinear dynamic model.

The nonlinear lumped spring force is given by

$$F_{spring} = -k_1x - k_3x^3. \quad (3.46)$$

The lumped damping force is

$$F_{damping} = -b\dot{x} \quad (3.47)$$

where \dot{x} is the center velocity of the diaphragm.

By using the equal-area parallel-plate assumption and neglecting the fringing field effect of the holes in the backplates, the total electrostatic co-energy, U , stored in the system is calculated as follows

$$U = \sum_i \left(\frac{1}{2} C_i V_i^2 \right) = \frac{1}{2} \frac{\epsilon A_{me}}{d_0 + x} V_p^2(t) + \frac{1}{2} \frac{\epsilon A_{me}}{d_0 - x} V_{bp}^2(t), \quad (3.48)$$

where ε is the dielectric constant of the air, and $V_{tp}(t)$ and $V_{bp}(t)$ are the instantaneous voltages applied to the top backplate and bottom backplate respectively. It follows that the net lumped electrostatic force is

$$F_e = \frac{dU}{dx} = -\frac{\varepsilon A_{me}}{2} \left[\frac{V_{tp}^2(t)}{(d_0 + x)^2} - \frac{V_{bp}^2(t)}{(d_0 - x)^2} \right]. \quad (3.49)$$

The lumped mechanical reaction force from the cavity is

$$F_c = -k_c x. \quad (3.50)$$

After obtaining all the lumped forces acting on the diaphragm, by applying Newton's second law, the general dynamic governing equation is

$$M_{me} \ddot{x} = \sum F_i = F_{spring} + F_{damping} + F_e + F_c + pA_{me}. \quad (3.51)$$

By substituting Eqs. (3.46), (3.47), (3.49) and (3.50) into Eq. (3.51), the governing equation is

$$M_{me} \ddot{x} = -(k_1 + k_c)x - k_3 x^3 - b\dot{x} - \frac{\varepsilon A_{me}}{2} \left[\frac{V_{tp}^2(t)}{(d_0 + x)^2} - \frac{V_{bp}^2(t)}{(d_0 - x)^2} \right] + pA_{me}. \quad (3.52)$$

Rewriting Eq. (3.52) becomes

$$M_{me} \ddot{x} + b\dot{x} + (k_1 + k_c)x + k_3 x^3 = -\frac{\varepsilon A_{me}}{2} \left[\frac{V_{tp}^2(t)}{(d_0 + x)^2} - \frac{V_{bp}^2(t)}{(d_0 - x)^2} \right] + pA_{me}. \quad (3.53)$$

Discussion of Nonlinearities

The above governing equation physically represents a general damped second-order system with a cubic mechanical nonlinearity and under both nonlinear electrostatic loading and uniform pressure loading. Since the cubic stiffness parameter k_3 is positive, it physically represents a spring hardening effect. The electrostatic forces between backplates and diaphragm in nature are nonlinear, even when the displacement of the

diaphragm is not large. From the expressions of nonlinear lumped electrical forces shown in Eq. (3.53), the electrical nonlinearity is coupled with the mechanical nonlinearity, which indicates that the microphone system is an electromechanically coupled system.

To facilitate the nonlinear analyses throughout this dissertation, it is necessary to quantify the mechanical and electrical nonlinearities in this section. The definitions are given by the following equations. For the mechanical nonlinearity, NL_m , we have

$$\begin{aligned}
 NL_m &= \left| \frac{\text{nonlinear mechanical force} - \text{linearized mechanical force}}{\text{linearized mechanical force}} \right| \times 100\% \\
 &= \left| \frac{k_1 x + k_3 x^3 - k_1 x}{k_1 x} \right| \times 100\% = \frac{k_3}{k_1} x^2, \tag{3.54}
 \end{aligned}$$

where x is the center displacement under the interested pressure or electrical loading.

Based on the above equation, we need to know the linear stiffness, cubic stiffness, and center displacement of the diaphragm to be able to calculate the mechanical nonlinearity.

The expression for electrical nonlinearity, NL_e , is

$$NL_e = \left| \frac{\text{nonlinear electrical force} - \text{linearized electrical force}}{\text{linearized electrical force}} \right| \times 100\%. \tag{3.55}$$

To further quantify and gain physical insight into the definition of electrical nonlinearity, we consider a single-backplate capacitive microphone with an applied DC bias V_0 only. Following the definition in Eq. (3.49), the nonlinear electrostatic force is

$$F_e = \frac{\varepsilon A_{me}}{2} \frac{V_0^2}{(d_0 - x)^2}. \tag{3.56}$$

By using a Taylor's series expansion about $x = 0$, we can linearize the above nonlinear force as follows

$$F_{eL} = \frac{\varepsilon A_{me} V_0^2}{2d_0^2} \left(1 + 2 \frac{x}{d_0} \right). \quad (3.57)$$

Therefore, the electrical nonlinearity in this case is

$$NL_e = \left| \frac{\frac{\varepsilon A_{me} V_0^2}{2} \frac{V_0^2}{(d_0 - x)^2} - \frac{\varepsilon A_{me} V_0^2}{2d_0^2} \left(1 + 2 \frac{x}{d_0} \right)}{\frac{\varepsilon A_{me} V_0^2}{2d_0^2} \left(1 + 2 \frac{x}{d_0} \right)} \right| = \frac{d_0^3}{(d_0 - x)^2 (d_0 + 2x)} - 1. \quad (3.58)$$

As we can see from the above equation, the electrical nonlinearity can be calculated based on the gap and center displacement of the diaphragm. The gap is an independent parameter; however, the center displacement of the diaphragm is dependent on the electrostatic loading (DC bias voltage in this case) and pressure loading. From Eqs. (3.54) and (3.58), clearly the electrical nonlinearity is coupled with the mechanical nonlinearity through the center displacement of the diaphragm.

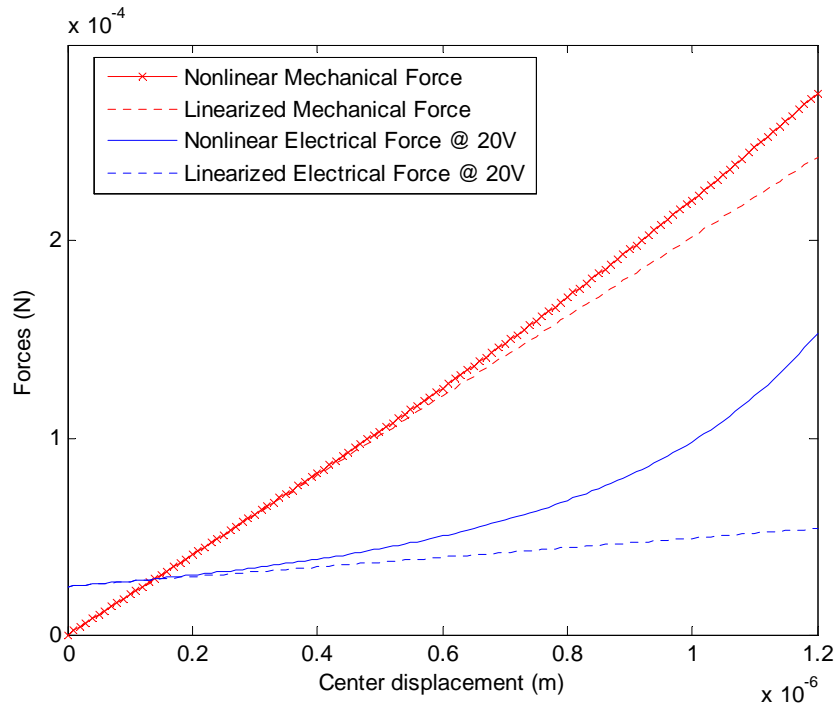


Figure 3-10. Nonlinear vs. linearized mechanical and electrical forces of a single-backplate capacitive microphone.

An example is given here to help understand the above defined nonlinearities. Shown in Figure 3-10 is a plot of calculated nonlinear versus linearized mechanical and electrical forces by using the parameters in Table 3-1 for a given 20V DC voltage. As we can see from the plot, the electrical nonlinearity is dominant for the large center displacement of the diaphragm. For example, if the center displacement is $0.6 \mu m$, the electrical nonlinearity at 20V is $NL_e \approx 27.6\%$ and the mechanical nonlinearity is $NL_m \approx 3.4\%$.

Similarly, if a dual-backplate capacitive microphone with an applied DC bias V_0 is considered, the electrical nonlinearity, followed by the definition in Eq. (3.55), is given as

$$NL_e = \frac{d_0^6}{(d_0^2 - x^2)^2 (d_0^2 + 2x^2)} - 1. \quad (3.59)$$

From Eqs. (3.54) and (3.59), again the electrical nonlinearity is coupled with the mechanical nonlinearity through the center displacement of the diaphragm.

An example is given here to help understand the electrostatic nonlinearity of a dual-backplate capacitive microphone. Shown in Figure 3-11 is a plot of calculated nonlinear versus linearized mechanical and electrical forces by using the parameters in Table 3-1 for a given 20V DC voltage. As we can see from the plot, the electrical nonlinearity becomes smaller and is on the same level with the mechanical nonlinearity, even when the center displacement of the diaphragm is large. For example, if the center displacement is $0.6 \mu m$, the electrical nonlinearity at 20V is $NL_e \approx 2.3\%$ and the mechanical nonlinearity is $NL_m \approx 3.4\%$. Physically, the two opposite electrostatic forces in a dual-backplate capacitive microphone help to reduce the electric nonlinearity.

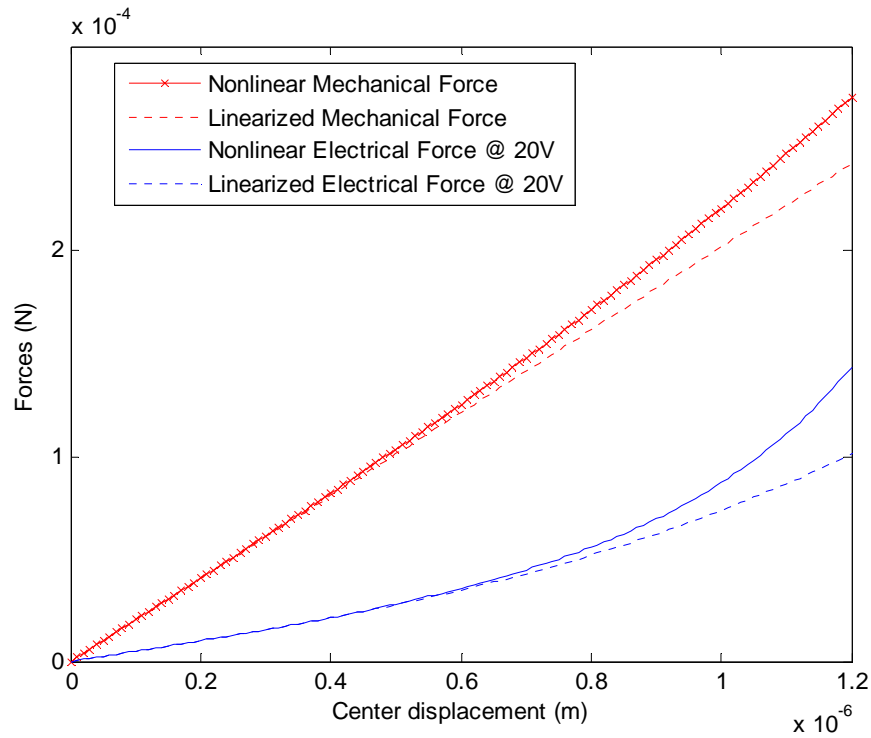


Figure 3-11. Nonlinear vs. linearized mechanical and electrical forces of a dual-backplate capacitive microphone.

Since it is impossible to solve the governing nonlinear equation Eq. (3.53) in closed form, alternative approaches are used in this dissertation to study the nonlinear dynamic system. Nonlinear finite element analyses (FEA) are carried out in the next section to verify the theoretical lumped stiffnesses of the diaphragm. The approximate analytical solutions (specifically via multiple time scales and harmonic balance methods) and numerical simulations through the direct integration of nonlinear governing equation are provided in the next chapter. The instability analyses for pull-ins are carried out in Chapter 5.

Nonlinear Finite Element Analyses

In this section, nonlinear mechanical finite element analyses are carried out in CoventorWare 2003 [106] to extract the equivalent lumped stiffnesses (k_1, k_3) of the

diaphragm and the accuracy of theoretical lumped stiffnesses is verified. This section also provides discussions of the modeling error for the electrostatic force through the coupled electromechanical simulation.

Stiffnesses of the Diaphragm

Based on the solid model shown in Figure 3-1, a 3D mesh of the diaphragm is generated and shown in Figure 3-12. Based on this mesh, converged displacement results are achieved with the diaphragm under the applied uniform pressure. Some major specifications of the mesh are listed in Table 3-2.

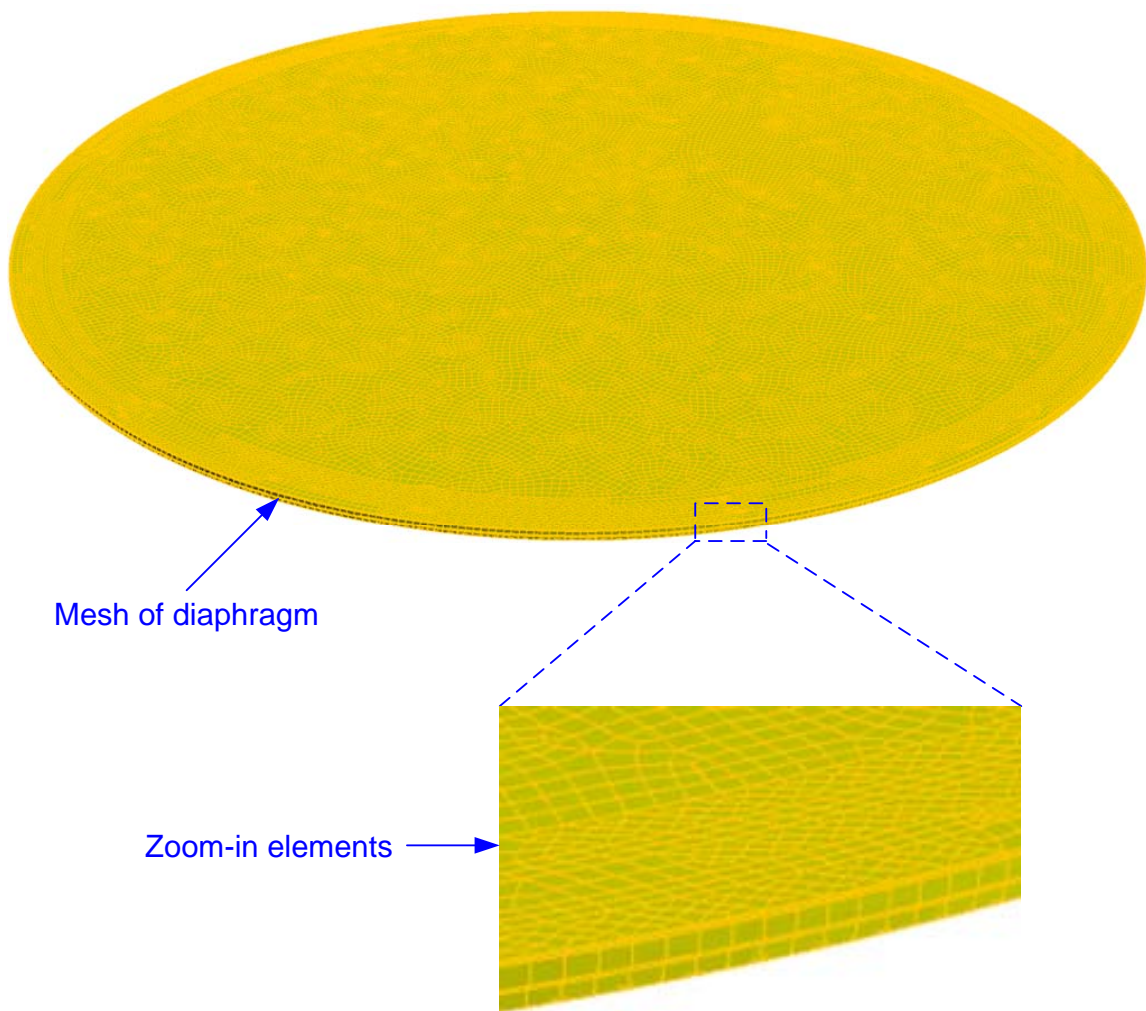


Figure 3-12. 3D mesh of the diaphragm in CoventorWare 2003.

Table 3-2. Major specifications of the diaphragm mesh with converged displacement results.

Parameter	Value
Volume element type	Solid hexahedron
Number of volume elements	82452
Number of nodes	43671
Average aspect ratio	1.6223

The material properties and physical dimensions of the diaphragm used in nonlinear FEA are taken partially from Table 3-1. The side surface of the diaphragm is fixed to be the boundary condition. To obtain the lumped stiffnesses of the diaphragm, different pressure loads with amplitudes varying from 10 to 4000 Pa are applied to the top surface of the diaphragm, and the nonlinear FEA are carried out to yield the center displacement of the diaphragm for each applied pressure respectively.

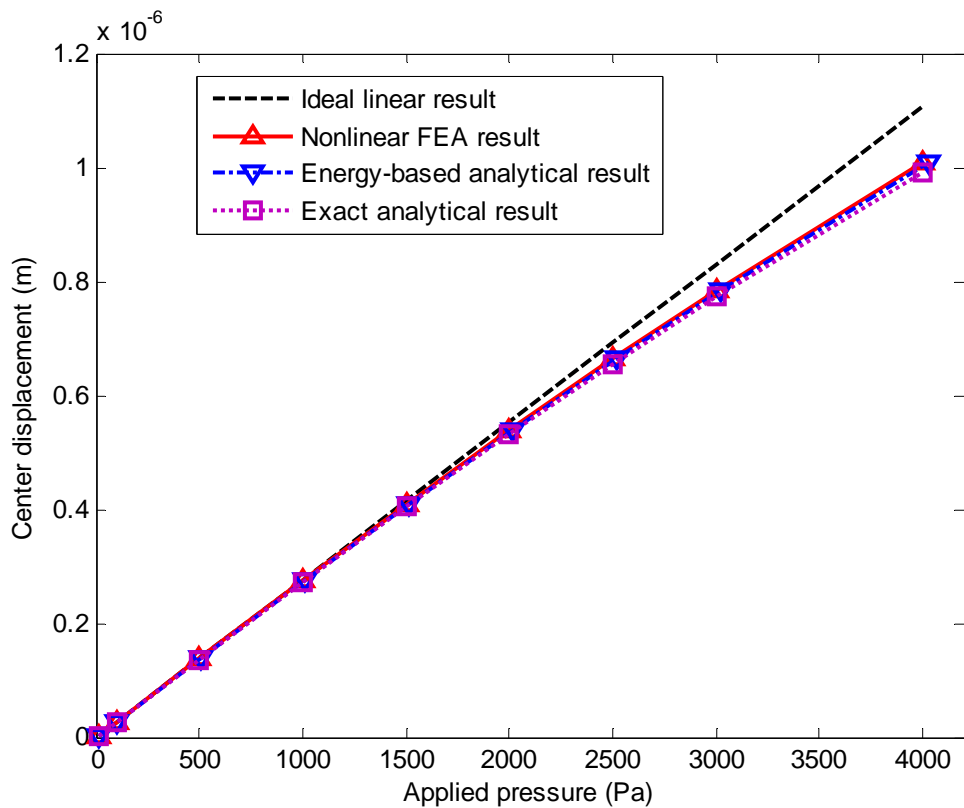


Figure 3-13. Transverse center deflections of the diaphragm under the uniform pressure.

Shown in Figure 3-13 is the plot of transverse center deflections of the diaphragm. The ideal linear, energy-based analytical as well as exact analytical deflection results (obtained from the reference [100]) are also plotted in Figure 3-13. As we can see from the plot, three sets of nonlinear deflection results agree very well with each other. The mechanical nonlinearity becomes important for the large applied pressure, for example, when the pressure value is above 2000Pa.

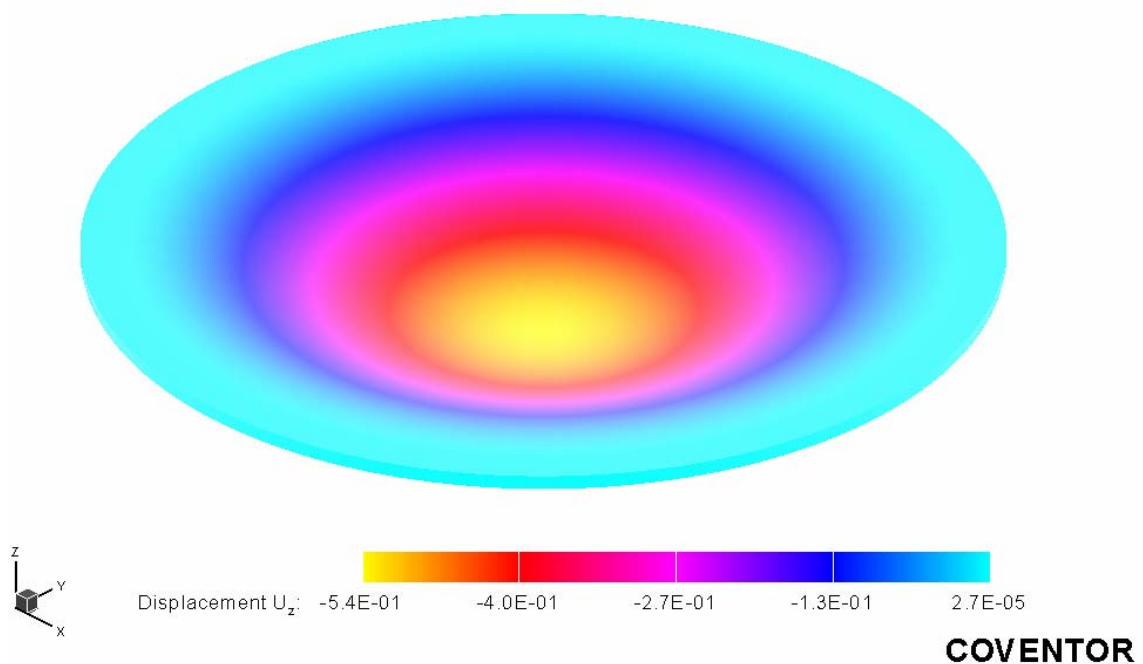


Figure 3-14. Displacement contour of the diaphragm under the 2000Pa uniform pressure (not to scale in the thickness direction, unit: μm).

Shown in Figure 3-14 is a displacement contour plot of the diaphragm under a 2000Pa uniform pressure. As seen from the plot, the center deflection of the diaphragm is approximately $5.4\text{e-}7$ m. Further calculation indicates that the mechanical nonlinearity (NL_m) at 2000Pa is approximately 2.7% based on the definition in Eq. (3.54).

The lumped linear and cubic stiffnesses can be extracted by curve-fitting the simulated nonlinear center displacements of the diaphragm with the formula in Eq. (3.31)

and the final results are listed in Table 3-3. From Table 3-3, the differences for the linear stiffness k_1 and cubic stiffness k_3 are approximately 1.3% and 5.0% respectively. Since the differences are small, the accuracy of the theoretical lumped stiffnesses of the diaphragm is verified by the nonlinear FEA results. In the following chapters, the theoretical lumped stiffnesses of the diaphragm will be used.

Table 3-3. Comparison of nonlinear FEA and LEM results.

Parameter	Nonlinear FEA result	LEM result	Difference
Linear stiffness k_1 (N/m)	199.7	202.2	1.3%
Cubic stiffness k_3 (N/m ³)	1.979e13	1.880e13	5.0%

Electrostatic Forces by CoSolveEM Simulations

In the real microphone device, the area of three plates is not same. As shown in Figure 3-1, the top backplate has the largest area while the bottom backplate has the smallest area. In addition, the backplates are perforated with hundreds of holes. The capacitance between the backplate and diaphragm is reduced due to the backplate area loss; however, extra fringing fields generated by the holes could compensate the loss. The electrostatic forces in the previous sections are modeled based on the equal-area parallel-plate assumption; therefore, some errors exist between the modeled and real electrostatic forces. One possible way to examine the difference between the real and modeled electrostatic forces is through nonlinear finite element analyses, for example, the CoSolveEM (coupled electromechanical analysis) simulation in CoventorWare 2003. The simulation runs between the mechanical and electrostatic domains until a converged equilibrium point is found. By using the solid model shown in Figure 3-1, the CoSolveEM simulation takes into account the effects of unequal area, perforated holes, and the fringing field on the electrostatic force; therefore, the simulated electrostatic force can be treated as an accurate measure of the real electrostatic force. In the following, the

CoSolveEM simulations are conducted for top and bottom capacitors of the microphone respectively, and the simulation results are compared with the results based on lumped element modeling.

During the simulations for the top capacitor, the side surfaces of the diaphragm and top backplate are assumed to be fixed and the applied DC voltage varies from 10 to 25V. When the applied DC voltage is greater than 25V, the simulation becomes diverged and quasi-static pull-in occurs. Similarly, for the bottom capacitor, the side surfaces of the diaphragm and bottom backplate are assumed to be fixed, and the simulated quasi-static pull-in voltage is approximately 33.5V.

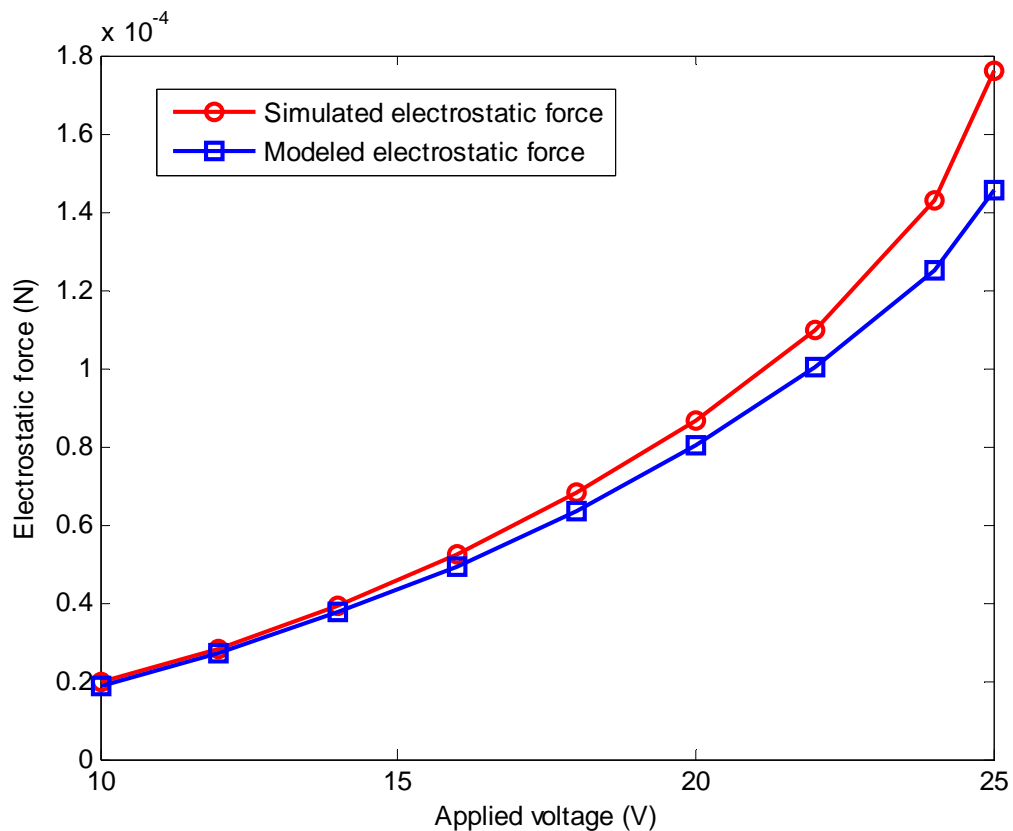


Figure 3-15. Plot of simulated and modeled electrostatic forces for the top capacitor.

Shown in Figure 3-15 is a plot of simulated electrostatic forces for the top capacitor when the applied DC voltage varies. The corresponding modeled electrostatic forces are

also plotted in Figure 3-15 by using the parameters in Table 3-1. As seen from Figure 3-15, the difference between the simulated and model electrostatic forces becomes larger when the applied voltage increases. Further calculations show that the difference at 10V is approximately 4% and 17% at 25V.

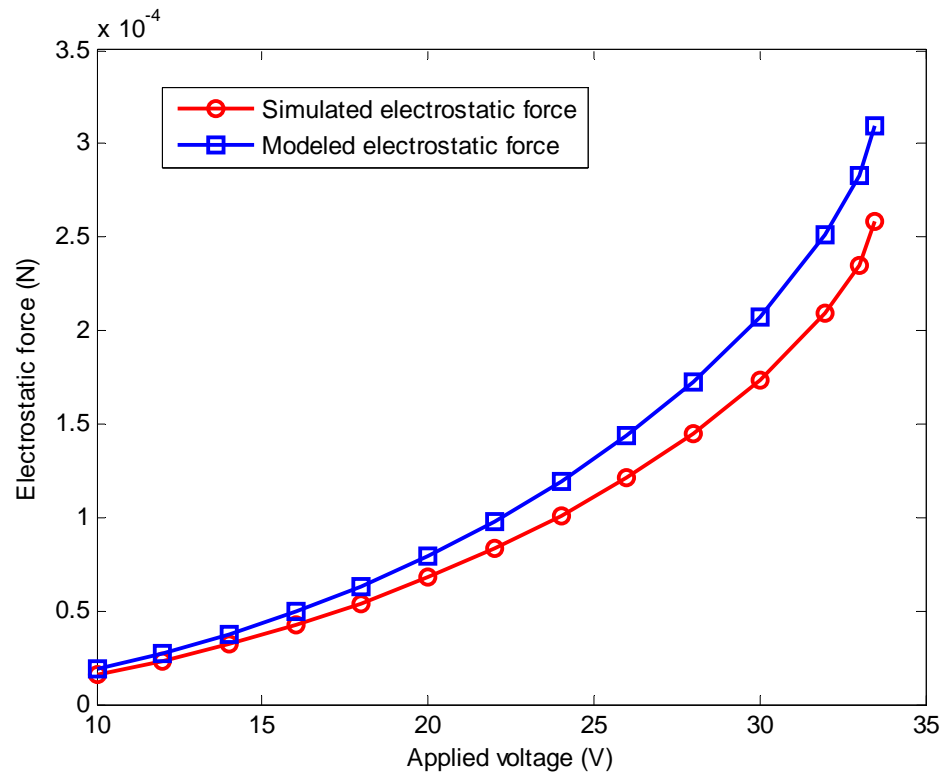


Figure 3-16. Plot of simulated and modeled electrostatic forces for the bottom capacitor.

For the bottom capacitor, similarly, shown in Figure 3-16 is the comparison plot of the simulated and modeled electrostatic forces. A similar trend of the difference between the simulated and model electrostatic forces is observed. And further calculations show that the difference at 10V is approximately 13% and 17% at 33.5V.

Based on the results shown in Figure 3-15 and Figure 3-16, when the applied DC voltage increases, the error generated by the model with an equal-area parallel-plate assumption increases. Specifically, the error is up to 17% when the applied voltage is up

to 25V for the top capacitor, and the error is up to 17% when the applied voltage is up to 33.5V for the bottom capacitor.

Summary

In this chapter, a nonlinear model for a dual-backplate MEMS microphone is developed. Specifically, lumped element modeling is applied to the microphone and lumped parameters of the microphone are extracted including the cubic mechanical stiffness of the diaphragm. Based on the lumped parameters, the nonlinear governing equation is obtained and nonlinearities in the governing equation are discussed. Theoretical lumped stiffnesses of the diaphragm are verified by nonlinear finite element analyses and the differences for the linear stiffness k_1 and cubic stiffness k_3 of the diaphragm are approximately 1.3% and 5.0% respectively.

CHAPTER 4
APPROXIMATE SOLUTIONS OF NONLINEAR GOVERNING EQUATIONS

A primary goal for this research is the development of a system characterization approach for the microphone with electrical excitation. This chapter provides the mathematical background and derivation of the formulae used in the characterization experiments to extract real system parameters. Specifically, the multiple time scales (MTS) and harmonic balance (HB) methods are applied to two nonlinear governing equations to obtain their approximate solutions. Further discussion and validity check for each approximate solution are also provided. In addition, this chapter presents approximate analytical solutions for the microphone under the sinusoidal acoustical pressure excitation. Major findings and contributions are summarized at the end of this chapter.

Introduction

To facilitate the analysis in this chapter, the general nonlinear governing equation Eq. (3.53) in Chapter 3 is further rewritten by using the system parameters (combination of lumped parameters) as follows

$$\ddot{x} + 2\zeta\omega_0\dot{x} + \omega_0^2x + \beta x^3 = -\frac{\varepsilon\Gamma}{2} \left[\frac{V_{ip}^2(t)}{(d_0 + x)^2} - \frac{V_{bp}^2(t)}{(d_0 - x)^2} \right] + p(t)\Gamma, \quad (4.1)$$

where system parameters are defined as

$$\omega_0 = \sqrt{(k_1 + k_c)/M_{me}}, \quad (4.2)$$

$$\zeta = \frac{b}{2M_{me}\omega_0}, \quad (4.3)$$

$$\beta = \frac{k_3}{M_{me}}, \quad (4.4)$$

and

$$\Gamma = \frac{A_{me}}{M_{me}}, \quad (4.5)$$

where ω_0 is the first system resonant frequency, ζ is the damping ratio, β is the nonlinear stiffness parameter and Γ is the ratio of the lumped area over lumped mass. Also the gap, d_0 , is treated here as a system parameter although it is a structural dimension of the microphone.

As we can see from Eq. (4.1), along with the defined system parameters, the dynamic system response can be determined for given electrical and pressure inputs. Although system parameters can be calculated theoretically from LEM, it is well-known that some of the modeling assumptions are idealizations. For example, the actual device possesses a finite amount of compliance in the diaphragm boundary conditions, and variations in physical dimensions and material properties, which are usually caused by the fabrication process, can often substantially alter the model parameters of the device. Therefore, some modeling errors exist between the theoretical and actual system parameters, and characterization experiments are required to determine the actual system parameters to evaluate the accuracy of the theoretical model. In the following sections, the mathematical background and derivation of the formulae used in the characterization experiments are presented. Details of the experiments as well as the analysis results are discussed in Chapter 6.

Governing Equation for the Electrical Square Wave Excitation

During the characterization tests for the electrical square wave excitation, no acoustical pressure exists on the diaphragm and only a uni-polar square wave $V(t)$ is applied directly to bottom (or top) backplate with diaphragm and the other backplate electrically grounded. The expression for the applied uni-polar square wave is given by

$$V(t) = \begin{cases} V_0 & nT_0 \leq t < nT_0 + \frac{T_0}{2} \\ 0 & nT_0 + \frac{T_0}{2} \leq t < (n+1)T_0 \end{cases}, \quad (4.6)$$

where V_0 and T_0 are the voltage amplitude and period of the square wave respectively, and $n=0, 1, 2, \dots$

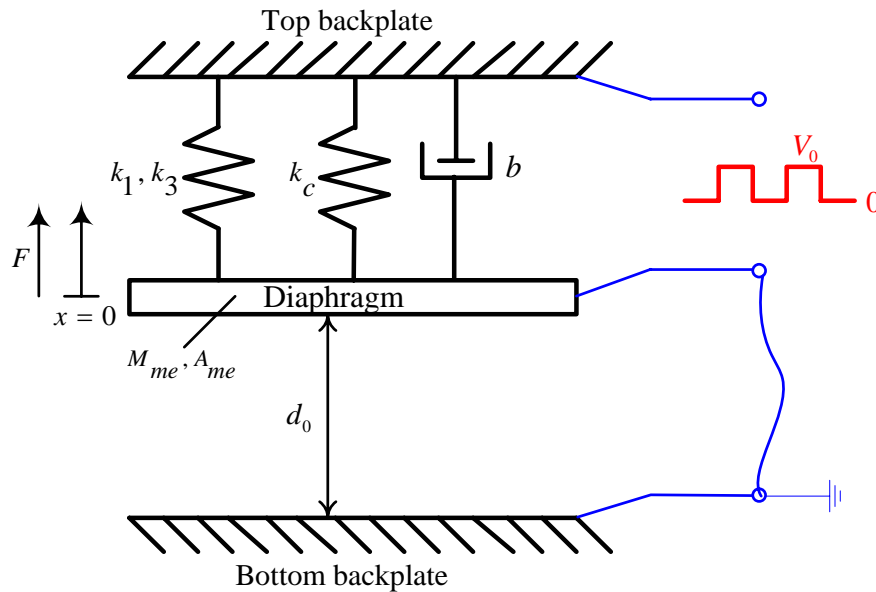


Figure 4-1. Dynamic model for an electrical square wave excitation on the top backplate.

Since the backplates are assumed to be symmetric around the center diaphragm, it turns out that the two governing equations are similar when either of backplates is under the electrical square wave excitation. For simplicity, the following analysis only studies

the case of an excitation voltage being applied to the top backplate. The dynamic model for this study is shown in Figure 4-1.

During the time $nT_0 \leq t < nT_0 + \frac{T_0}{2}$, an electrostatic force acts on the diaphragm to

force it to vibrate, and the corresponding governing equation can be reduced to

$$\ddot{x} + 2\zeta\omega_0\dot{x} + \omega_0^2x + \beta x^3 = \frac{\varepsilon_0\Gamma}{2} \frac{V_0^2}{(d_0 - x)^2}. \quad (4.7)$$

A Taylor's series expansion for the above nonlinear electrostatic force up to 3rd order results in

$$\frac{\varepsilon_0\Gamma}{2} \frac{V_0^2}{(d_0 - x)^2} \approx \frac{\varepsilon_0\Gamma V_0^2}{2d_0^2} \left[1 + 2\frac{x}{d_0} + 3\left(\frac{x}{d_0}\right)^2 + 4\left(\frac{x}{d_0}\right)^3 \right]. \quad (4.8)$$

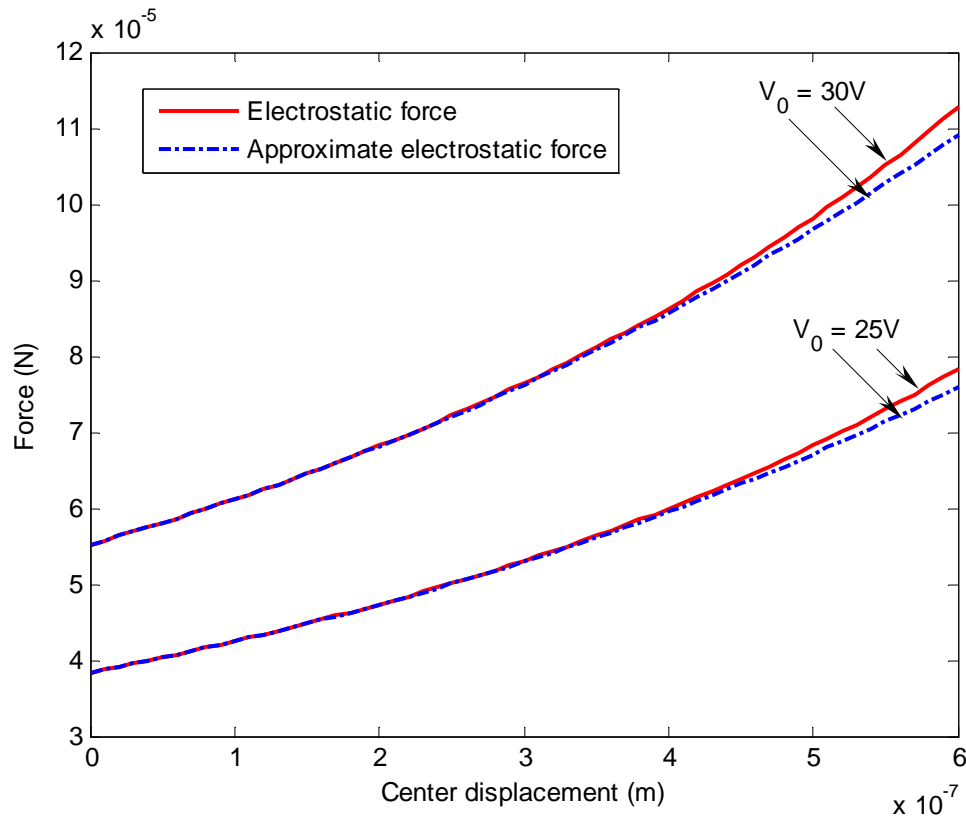


Figure 4-2. Plot of electrostatic and approximate electrostatic forces for $V_0 = 25V$ and $V_0 = 30V$ respectively.

In order to verify the accuracy of the 3rd order Taylor's series expansion in Eq. (4.8), by using the parameters in Table 3-1, the electrostatic and approximate electrostatic forces based on the 3rd order Taylor's series expansion are plotted in Figure 4-2 for two different voltages $V_0 = 25\text{V}$ and $V_0 = 30\text{V}$ respectively. Those two voltages are chosen since they are used in the numerical validity tests in the next section. As we can see from the plot, the two electrostatic forces are similar for each voltage case. Further calculations show that the approximation error caused by the 3rd order Taylor's series expansion is up to 3.0% for $V_0 = 25\text{V}$ and 3.1% for $V_0 = 30\text{V}$ when the center displacement is up to $0.6\mu\text{m}$. Mathematically, the approximation error becomes larger if the center displacement is over $0.6\mu\text{m}$. Physically, the curvature of the diaphragm needs to be considered if the center displacement becomes large (for example, $x > 0.6\mu\text{m}$). The parallel plate assumption used to model the electrostatic force (left hand side of Eq. (4.8)) might not be able to hold for the large displacement case. Therefore, the 3rd order Taylor's series approximation in Eq. (4.8) carries a maximum error of approximately 3.1% when the center displacement is $0 \leq x \leq 0.6\mu\text{m}$ and the applied voltage is $V_0 = 30\text{V}$.

To proceed, substitution of Eq. (4.8) into (4.7) yields

$$\ddot{x} + 2\zeta\omega_0\dot{x} + \left[\omega_0^2 - \frac{\varepsilon_0\Gamma V_0^2}{d_0^3} \right] x - \frac{3\varepsilon_0\Gamma V_0^2}{2d_0^4} x^2 + \left[\beta - \frac{2\varepsilon_0\Gamma V_0^2}{d_0^5} \right] x^3 = \frac{\varepsilon_0\Gamma V_0^2}{2d_0^2}. \quad (4.9)$$

Physically, Eq. (4.9) represents a damped second order system with both quadratic and cubic nonlinearities and a non-zero external step loading. During the time

$nT_0 + \frac{T_0}{2} \leq t < (n+1)T_0$, no electrostatic force acts on the diaphragm, the diaphragm is under the free vibration and the corresponding governing equation is

$$\ddot{x} + 2\zeta\omega_0\dot{x} + \omega_0^2x + \beta x^3 = 0. \quad (4.10)$$

The above equation is the so-called damped Duffing's equation, in which only the cubic mechanical nonlinearity exists. Eq. (4.10) is a special case of Eq. (4.9) when the applied voltage V_0 is zero. The solution of Eq. (4.9) is important since it can be easily tailored and applied to other applications. In the following section, the MTS method is utilized to find its approximate analytical solution.

Approximate MTS Solution for the Electrical Square Wave Excitation

From Chapter 3, we know that the nonlinearities in the designed microphone are small. In the field of nonlinear dynamics, the commonly used methods to find the approximate solution of a weakly nonlinear system are the method of harmonic balance, the method of averaging and perturbation methods. The method of multiple time scales is one of widely used perturbation methods with high accuracy and efficiency.

The basic idea of the MTS method is to consider the expansion of the time response to be a function of multiple independent time variables, or scales, instead of a single time variable [72]. The different scales will allow us to "observe" the system behavior on the different scales and also capture the characteristics of different dynamics (such as the fast dynamics of the linear response and slow dynamics of the nonlinear response). Typically, the approximate solution is assumed as some integer order expansion of a small positive dimensionless parameter, which is artificially introduced to order terms in the governing equation. This parameter eventually is substituted back into the solution, and the final results are often obtained independent of this book-keeping parameter [69]. In this

section, the MTS approach is adopted to find the approximate analytical solution to Eq. (4.9). Some discussions of the approximate solution are also presented.

Approximate Solution by the MTS Method

To proceed with the approximate solution, we need to non-dimensionalize the governing equation in Eq. (4.9), which finally leads to

$$y'' + \alpha_1 y' + \alpha_2 y + \alpha_3 y^2 + \alpha_4 y^3 = \alpha_5, \quad (4.11)$$

where

$$y = \frac{x}{d_0}, \quad (4.12)$$

$$y' = \frac{dy}{d\tau}, \quad (4.13)$$

$$y'' = \frac{d^2 y}{d\tau^2}, \quad (4.14)$$

$$\tau = \omega_0 t, \quad (4.15)$$

$$\omega_0 = \sqrt{(k_1 + k_c)/M_{me}}, \quad (4.16)$$

$$\alpha_1 = \frac{b}{M_{me} \omega_0}, \quad (4.17)$$

$$\alpha_2 = 1 - \frac{\varepsilon_0 A_{me} V_0^2}{M_{me} \omega_0^2 d_0^3}, \quad (4.18)$$

$$\alpha_3 = -\frac{3\varepsilon_0 A_{me} V_0^2}{2M_{me} d_0^3 \omega_0^2}, \quad (4.19)$$

$$\alpha_4 = \frac{k_3 d_0^2}{M_{me} \omega_0^2} - \frac{2\varepsilon_0 A_{me} V_0^2}{M_{me} d_0^3 \omega_0^2}, \quad (4.20)$$

and

$$\alpha_5 = \frac{\varepsilon_0 A_{me} V_0^2}{2M_{me} d_0^3 \omega_0^2}. \quad (4.21)$$

In Eq. (4.11), y and y' are the non-dimensional center displacement and velocity of the diaphragm respectively, ω_0 is the linear natural frequency of the system, τ is the dimensionless time, and α_1 through α_5 are non-dimensional coefficients. By using the MTS method, the approximate solution of Eq. (4.11) is assumed as a second order expansion in terms of a small positive parameter ε ,

$$y(\tau) = y_0(\tau_0, \tau_1, \tau_2) + \varepsilon y_1(\tau_0, \tau_1, \tau_2) + \varepsilon^2 y_2(\tau_0, \tau_1, \tau_2), \quad (4.22)$$

where the multiple independent time scales are defined as

$$\tau_0 = \tau, \tau_1 = \varepsilon\tau, \text{ and } \tau_2 = \varepsilon^2\tau. \quad (4.23)$$

The coefficients in Eq. (4.11) are further ordered to show up in the $O(\varepsilon^2)$ by doing the following substitution

$$\alpha_1 = \varepsilon^2 \mu_1, \alpha_2 = \Omega^2, \alpha_3 = \varepsilon^2 \mu_3 \text{ and } \alpha_4 = \varepsilon^2 \mu_4. \quad (4.24)$$

Eqs. (4.22), (4.23) and (4.24) are then substituted into Eq. (4.11), by collecting and equating the coefficients (detailed derivation steps are provided in Appendix B), finally the approximate solution for $y(\tau)$ is obtained as follows

$$y(\tau) \approx \frac{\alpha_5}{\alpha_2} + R_0 e^{-\frac{1}{2}\mu_4\tau_2} \cos\left(\Omega\tau_0 + \frac{2\mu_3\alpha_5\alpha_2 + 3\mu_4\alpha_5^2}{2\Omega\alpha_2^2}\tau_2 - \frac{3\mu_4R_0^2}{8\Omega\mu_1}e^{-\mu_4\tau_2} + \phi_0\right), \quad (4.25)$$

where R_0 and ϕ_0 are constants determined by the initial conditions.

From Eqs. (4.15), (4.23) and (4.24), we have the following expressions

$$\tau_0 = \omega_0 t, \quad (4.26)$$

$$\mu_1 \tau_2 = \alpha_1 \omega_0 t, \quad (4.27)$$

$$\frac{2\mu_3\alpha_5\alpha_2 + 3\mu_4\alpha_5^2}{2\Omega\alpha_2^2}\tau_2 = \frac{2\alpha_2\alpha_3\alpha_5 + 3\alpha_4\alpha_5^2}{2\Omega\alpha_2^2}\omega_0 t, \quad (4.28)$$

and

$$\frac{\mu_4}{\mu_1} = \frac{\alpha_4}{\alpha_1}. \quad (4.29)$$

Combining Eqs. (4.12), (4.24), (4.25), (4.26), (4.27), (4.28) and (4.29), finally the MTS solution for $x(t)$ is given by

$$x(t) = \frac{\alpha_5}{\alpha_2} d_0 + R_0 d_0 e^{-\frac{1}{2}\alpha_1 \omega_0 t} \cos \left[\left(\sqrt{\alpha_2} + \frac{2\alpha_2\alpha_3\alpha_5 + 3\alpha_4\alpha_5^2}{2\alpha_2^{\frac{5}{2}}} \right) \omega_0 t - \frac{3\alpha_4 R_0^2}{8\alpha_1 \sqrt{\alpha_2}} e^{-\alpha_1 \omega_0 t} + \phi_0 \right]. \quad (4.30)$$

Discussion of the MTS Approximate Solution

From Eq. (4.30), during the up-stroke of the square wave, the transient center displacement response is an exponentially decaying cosine function oscillating around some DC offset. The decaying speed is uniquely determined by the quotient of system damping coefficient over lumped mass $\left(\alpha_1 \omega_0 = \frac{b}{M_{me}} \right)$. The oscillation frequency is affected by all nonlinearities (α_3 and α_4) and external step loading (α_5). Also further analysis shows that the phase angle is affected by all nonlinearities and external loading. If an initial displacement χ_0 is imposed and the diaphragm starts from rest, the resulting transient displacement $x(t)$ becomes

$$x(t) = \frac{\alpha_5}{\alpha_2} d_0 + \widehat{\chi}_0 e^{-\frac{1}{2}\alpha_1 \omega_0 t} \cos \left[\left(\sqrt{\alpha_2} + \frac{2\alpha_2\alpha_3\alpha_5 + 3\alpha_4\alpha_5^2}{2\alpha_2^{\frac{5}{2}}} \right) \omega_0 t - \frac{3\alpha_4 \widehat{\chi}_0^2}{8\alpha_1 \sqrt{\alpha_2} d_0^2} (e^{-\alpha_1 \omega_0 t} - 1) \right], \quad (4.31)$$

where

$$\widehat{\chi}_0 = \chi_0 - \frac{\alpha_5}{\alpha_2} d_0. \quad (4.32)$$

Approximate solution with zero initial conditions

If the initial displacement is zero ($\chi_0 = 0$), the resulting transient displacement becomes

$$x(t) = x_{ss} - x_{ss} e^{-\frac{1}{2}\alpha_1\omega_0 t} \cos \left[\left(\sqrt{\alpha_2} + \frac{2\alpha_2\alpha_3\alpha_5 + 3\alpha_4\alpha_5^2}{2\alpha_2^{\frac{5}{2}}} \right) \omega_0 t - \frac{3\alpha_4 x_{ss}^2}{8\alpha_1 \sqrt{\alpha_2} d_0^2} (e^{-\alpha_1\omega_0 t} - 1) \right], \quad (4.33)$$

where x_{ss} represents the steady state displacement and is defined as follows

$$x_{ss} = \frac{\alpha_5}{\alpha_2} d_0. \quad (4.34)$$

Eq. (4.33) will be used in Chapter 6 for the system parameter extraction from the experimental data. The identification process is outlined as follows. For a square wave excitation with a given amplitude of V_0 , a nonlinear least-squares curve-fitting technique is applied and the real values of ω_0 , d_0 , α_1 , α_2 , α_3 , α_4 and α_5 are obtained by curve-fitting Eq. (4.33) with the experimental up-stroke center displacement response of the diaphragm. After obtaining the values of ω_0 and d_0 from the experimental data, other system parameters ζ , β and Γ are extracted as follows

$$\zeta = \frac{\alpha_1}{2}, \quad (4.35)$$

$$\beta = \frac{(\alpha_4 + 4\alpha_5)\omega_0^2}{d_0^2}, \quad (4.36)$$

and

$$\Gamma = \frac{2\alpha_5\omega_0^2 d_0^3}{\varepsilon_0 V_0^2}. \quad (4.37)$$

Approximate solutions in other applications

If there are no external step loading and quadratic nonlinearity in the system, which means

$$\alpha_3 = 0, \quad (4.38)$$

and

$$\alpha_5 = 0. \quad (4.39)$$

Then Eq. (4.31) is reduced into

$$x(t) = \chi_0 e^{-\frac{1}{2}\alpha_1 \omega_0 t} \cos \left[\sqrt{\alpha_2} \omega_0 t - \frac{3\alpha_4 \chi_0^2}{8\alpha_1 \sqrt{\alpha_2} d_0^2} (e^{-\alpha_1 \omega_0 t} - 1) \right], \quad (4.40)$$

which is the general expression derived in the reference [107]. The oscillation frequency in this case is given by $\sqrt{\alpha_2} \omega_0$. As we can see from Eq. (4.18), as the square wave voltage amplitude V_0 increases, the oscillation frequency decreases due to the electrostatic spring-softening effect.

In terms of applications, Eq. (4.31) can be applied to study the large-angle free-fall response of a parametrically excited pendulum [107]. Also Eq. (4.31) can be altered and applied to find the approximate solution to Eq. (4.10) for the free vibration of the diaphragm during the down-stroke of the applied square wave. The resulting transient displacement response becomes

$$x(t) = \chi_0 e^{-\zeta \omega_0 t} \cos \left[\omega_0 t - \frac{3\beta \chi_0^2}{16\zeta \omega_0^2} (e^{-2\zeta \omega_0 t} - 1) \right]. \quad (4.41)$$

Validity Region of the Approximate MTS Solution

Since Eq. (4.33) basically represents an approximate solution to Eq. (4.7) via the MTS method, it is important to find out where the solution fails, in other words, its

validity region. In this section, numerical simulations via the ODE45 command in MATLAB are used to determine the validity region of Eq. (4.33). The ODE45 command is based on an explicit, variable-step, Runge-Kutta (4,5) integration formula, which utilizes a 4th order predictor and a 5th order corrector [108, 109]. First, we conduct three test simulations with three different applied voltages (V_0) and given theoretical system parameters (ω_0 , ζ , β , Γ and d_0). The three different voltages are chosen such that the system responses fall into the linear, weakly nonlinear and highly nonlinear regions respectively. Then, based on the simulated system responses, the approximate MTS solution is applied to extract system parameters for each test case. Finally, extracted system parameters are compared with their given values and errors are calculated for each test case respectively. From the errors obtained, we can obtain the validity region for the approximate MTS solution.

Results of linear case

For the linear test case, the applied voltage is chosen to be $V_0 = 5V$. Shown in Figure 4-3 is the comparison of simulated and MTS-based nonlinear least squares curve fitting center displacement results. As seen from the plot, the simulated and MTS solution results agree very well and the maximum mechanical and electrical nonlinearities (see Eqs. (3.54) and (3.58) for their definitions) are calculated to be $NL_m \approx 0\%$ and $NL_e \approx 0\%$. Table 4-1 summarizes the results for the linear test case and the given input system parameters are generated based on the theoretical LEM (also see Table 3-1). From the table, the maximum error of 0.89% occurs for the nonlinear stiffness parameter, and other errors are smaller.

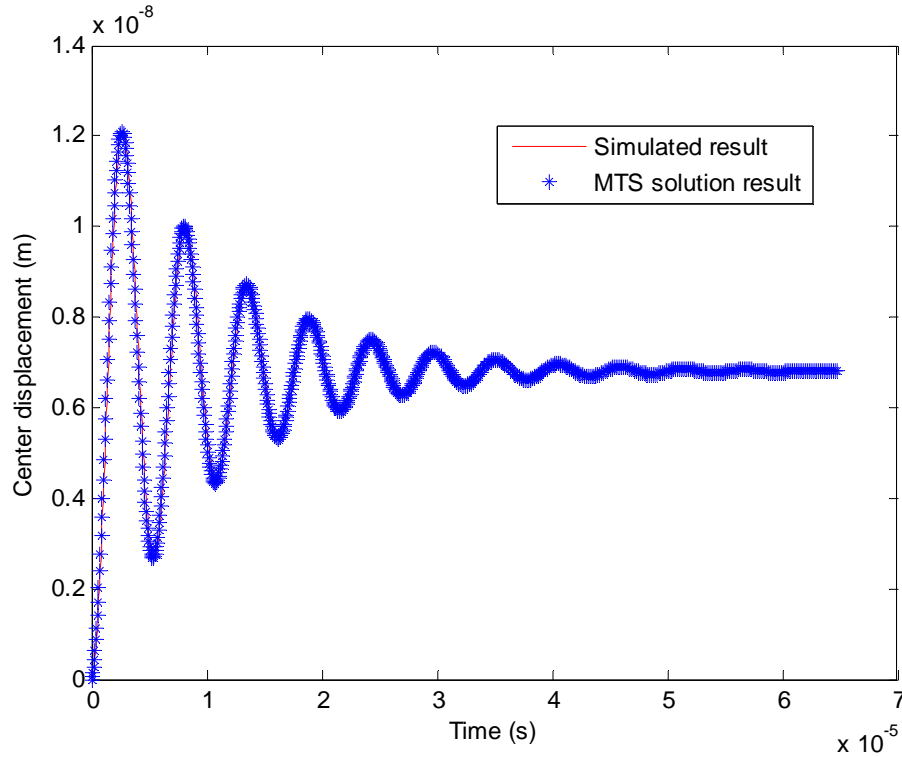


Figure 4-3. Comparison of simulated and MTS-based curve fitting center displacement results ($V_0 = 5V$).

Table 4-1. Given and extracted (via MTS solution) parameters for a linear case.

Parameter	Given	Extracted	Error
Damping ratio ζ	8.091e-2	8.050e-2	0.51%
Natural frequency $f_0 = \omega_0/2\pi$ (kHz)	185.5	185.4	0.054%
Nonlinear parameter β ($N/m^3/kg$)	1.128e23	1.138e23	0.89%
Ratio Γ (m^2/kg)	332.2	332.0	0.060%
Gap d_0 (m)	2.000e-6	1.990e-6	0.50%

Results of weakly nonlinear case

For the weakly nonlinear test case, the applied voltage is chosen to be $V_0 = 25V$. Shown in Figure 4-4 is the comparison of simulated and MTS-based nonlinear least squares curve fitting center displacement results. As we can see from the plot, the simulated and MTS solution results still agree very well. Part of transient center

displacement response is within the nonlinear range (for example, the maximum transient displacement is larger than $0.3 \mu\text{m}$).

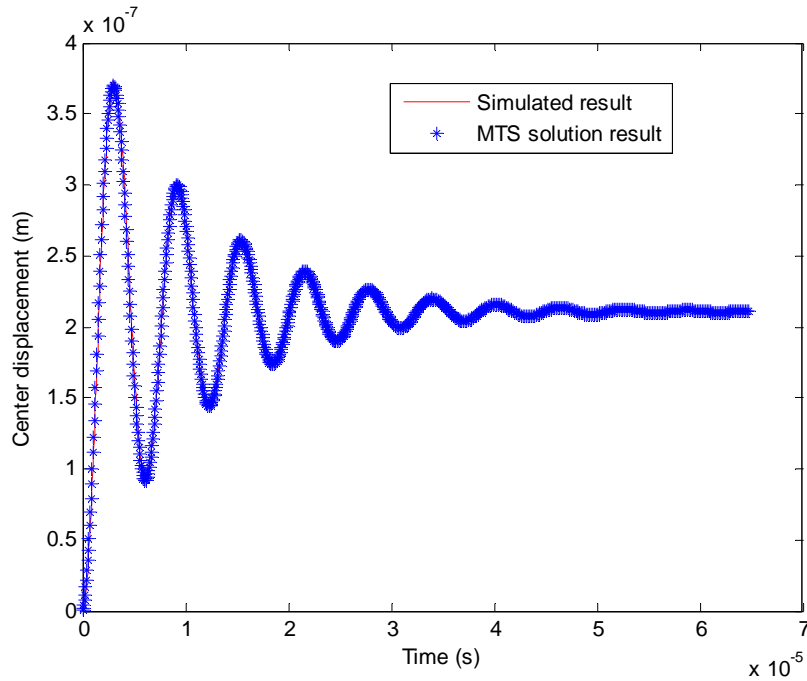


Figure 4-4. Comparison of simulated and MTS-based curve fitting center displacement results ($V_0 = 25V$).

Table 4-2. Given and extracted parameters (via MTS solution) for a weakly nonlinear case.

Parameter	Given	Extracted	Error
Damping ratio ζ	$8.091\text{e-}2$	$8.030\text{e-}2$	0.75%
Natural frequency $f_0 = \omega_0/2\pi$ (kHz)	185.5	184.1	0.22%
Nonlinear parameter β ($N/m^3/kg$)	$1.128\text{e}23$	$1.139\text{e}23$	0.98%
Ratio Γ (m^2/kg)	332.2	329.9	0.69%
Gap d_0 (m)	$2.000\text{e-}6$	$1.980\text{e-}6$	1.0%

In this case, the maximum mechanical and electrical nonlinearities are calculated to be $NL_m \approx 1.3\%$ and $NL_e \approx 9.9\%$. Table 4-2 summarizes the results for the weakly nonlinear test case and the maximum error of 1.0% occurs for the gap, and other errors are smaller.

Results of highly nonlinear case

It turns out from the simulation that we cannot achieve higher mechanical nonlinearities ($\geq 10\%$) from our physical microphone system (2000Pa design) due to the electrostatic pull-in. To be able to generate higher mechanical nonlinearities and further test the validity of the MTS solution in a highly nonlinear region, we numerically increase the nonlinear stiffness parameter, for example, $k_3^* = 3k_3$ or $\beta^* = 3\beta$ (where the asterisk sign represents new parameters). With an applied voltage $V_0 = 30V$ and the new nonlinear stiffness parameter β^* , the plot of simulated and MTS-based nonlinear least squares curve fitting center displacements is shown in Figure 4-5. Also part of transient center displacement response is within the nonlinear range (for example, the maximum transient displacement is larger than $0.5\mu m$). The maximum mechanical and electrical nonlinearities are calculated to be $NL_m \approx 10\%$ and $NL_e \approx 28.6\%$.

Table 4-3. Given and extracted (via MTS solution) parameters for a highly nonlinear case.

Parameter	Given	Extracted	Error
Damping ratio ζ	8.091e-2	7.700e-2	4.8%
Natural frequency $f_0 = \omega_0/2\pi$ (kHz)	185.5	182.7	1.5%
Nonlinear parameter β^* ($N/m^3/kg$)	3.384e23	3.690e23	9.0%
Ratio Γ (m^2/kg)	332.2	338.9	2.0%
Gap d_0 (m)	2.000e-6	1.970e-6	1.5%

Table 4-3 summarizes the results for this case and the maximum error of 9.0% occurs for the nonlinear stiffness parameter. It should be pointed out that in this case the 3rd Taylor's series approximation for the electrostatic force is accurate with an error of approximately 3.1% (Figure 4-2).

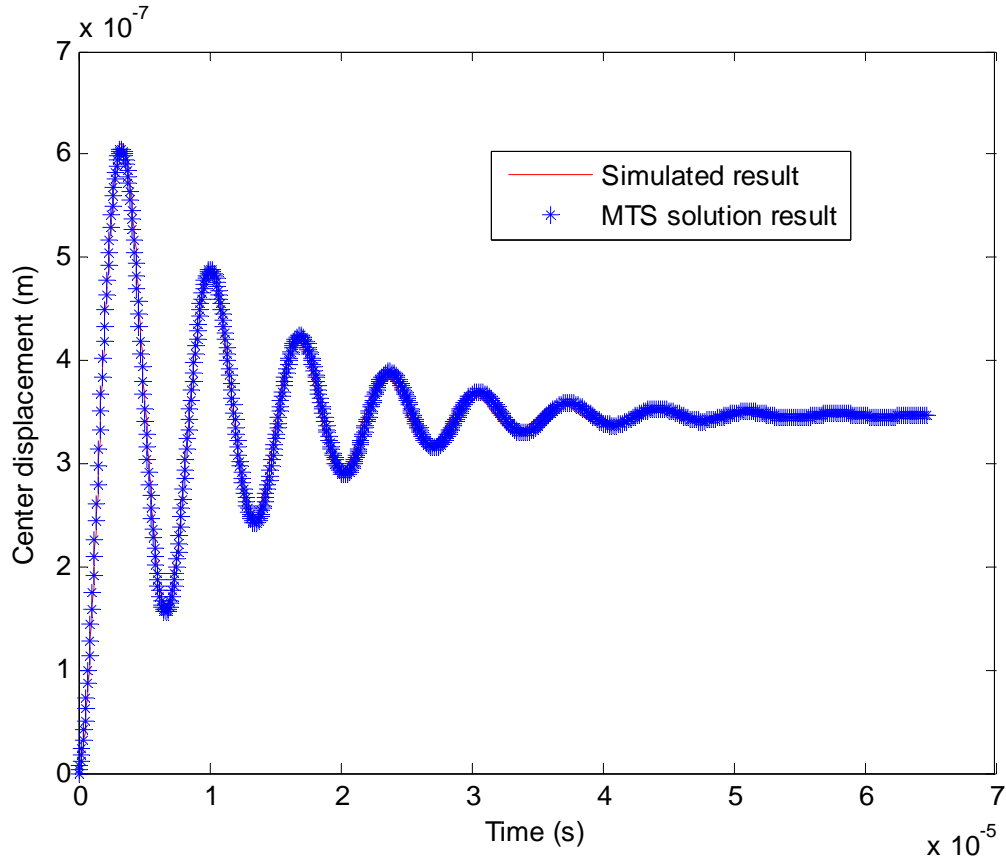


Figure 4-5. Comparison of simulated and MTS-based curve fitting center displacement results ($V_0 = 30V$, $k_3^* = 3k_3$).

Table 4-4 summarizes the nonlinear curve-fitting results of the maximum error and sum of residual squares (an indicator of the accuracy of the curve-fitting), which is defined as follows [108]

$$S_r = \sum_{i=1}^{npts} [x_{i,simulated}(t) - x_{i,MTS}(t)]^2, \quad (4.42)$$

where S_r is the sum of residual squares, $npts$ is the total number of simulated (MTS-based) points, $x_{i,simulated}(t)$ is the simulated displacement value for i^{th} point, and $x_{i,MTS}(t)$ is the MTS-based displacement value for i^{th} point.

As we can see from Table 4-4, the maximum error and S_r increases as the nonlinearity (mechanical or electrical) becomes larger, which means the MTS

approximate solution is getting less accurate. The maximum error for the weakly nonlinear case is 1.0% and will be increasing as the nonlinearity (mechanical or electrical) exceeds 10%. Therefore, we can conclude the MTS approximate solution holds with an error of less than 1.0% for a weakly nonlinear system with the electrostatic nonlinearity up to 10%.

Table 4-4. Results of the maximum error and sum of residual squares for each test case.

Test case	Maximum error	Sum of residual squares (S_r)
Linear case	0.89%	2.0e-17
Weakly nonlinear case	1.0%	6.5e-15
Highly nonlinear case	9.0%	8.0e-14

Governing Equation for the Electrical Sinusoidal Excitation

During the characterization tests for the electrical sinusoidal excitation, no acoustic pressure is incident on the diaphragm and a designed electrical signal $V(t)$ is applied directly to either top or bottom backplate with diaphragm and the other backplate electrically grounded.

Physically, the designed signal has 60 sinusoidal cycles in three quarters of its period and is equal to zero for the remainder of the period. During the sinusoidal excitation in each period, the system goes to the steady state. The transient response dies out completely when no voltage is applied during the last portion of each period. The mathematical expression for the designed excitation signal is

$$V(t) = \begin{cases} V_0 \cos[\Omega(t - nT_0)], & nT_0 \leq t < nT_0 + \frac{3T_0}{4}, n = 0, 1, 2, \dots \\ 0, & nT_0 + \frac{3T_0}{4} \leq t < (n+1)T_0 \end{cases} \quad (4.43)$$

where V_0 is the voltage amplitude and T_0 is the period of the designed signal. Since there are 60 sinusoidal cycles in three quarters of T_0 , the angular sinusoidal excitation frequency Ω is given by

$$\Omega = 2\pi \frac{1}{\frac{3T_0}{4 \times 60}} = 2\pi \frac{80}{T_0}. \quad (4.44)$$

Since the backplates are assumed to be symmetric around the center diaphragm, it turns out that the two governing equations are similar when either of backplates is under the electrical sinusoidal excitation. For simplicity, the following analysis only studies the case of an excitation voltage being applied to the bottom backplate. The dynamic model for an electrical sinusoidal excitation on the bottom backplate is shown in Figure 4-6.

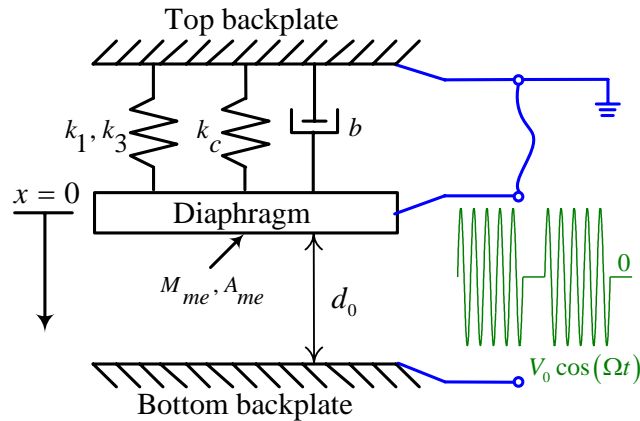


Figure 4-6. Dynamic model for an electrical sinusoidal excitation on the bottom backplate.

During the time $nT_0 + \frac{3T_0}{4} \leq t < (n+1)T_0$, no electrostatic force acts on the

diaphragm, the governing equation for the free vibration of diaphragm is

$$\ddot{x} + 2\zeta\omega_0\dot{x} + \omega_0^2x + \beta x^3 = 0. \quad (4.45)$$

If the diaphragm starts from rest and an initial displacement, x_0 , is imposed, the resulting transient displacement response is given by Eq. (4.41).

During the time $nT_0 \leq t < nT_0 + \frac{3T_0}{4}$, an electrostatic force acts on the diaphragm and forces it to vibrate. Based on the dynamic model in Figure 4-6, the governing equation is derived as

$$\ddot{x} + 2\zeta\omega_0\dot{x} + \omega_0^2x + \beta x^3 = \frac{\varepsilon_0\Gamma V_0^2 \cos^2(\Omega t)}{2(d_0 - x)^2}. \quad (4.46)$$

The square of the sinusoidal input contains both constant and harmonic terms as follows

$$V_0^2 \cos^2(\Omega t) = \frac{V_0^2}{2} + \frac{V_0^2}{2} \cos(2\Omega t). \quad (4.47)$$

By introducing the non-dimensional center displacement, Eq. (4.46) can be further rewritten as

$$\ddot{y} + \gamma_1\dot{y} + \gamma_2y + \gamma_3y^3 = \frac{F_0 + F_2 \cos(2\Omega t)}{(1 - y)^2}, \quad (4.48)$$

where

$$y = \frac{x}{d_0}, \quad (4.49)$$

$$\gamma_1 = 2\zeta\omega_0, \quad (4.50)$$

$$\gamma_2 = \omega_0^2, \quad (4.51)$$

$$\gamma_3 = \beta d_0^2, \quad (4.52)$$

$$F_0 = \frac{\varepsilon_0\Gamma V_0^2}{4d_0^3}, \quad (4.53)$$

and

$$F_2 = \frac{\varepsilon_0\Gamma V_0^2}{4d_0^3}. \quad (4.54)$$

Further rearrangement of Eq. (4.48) results in

$$\left(\ddot{y} + \gamma_1 \dot{y} + \gamma_2 y + \gamma_3 y^3\right)(1-y)^2 = F_0 + F_2 \cos(2\Omega t). \quad (4.55)$$

Eq. (4.55) represents a general damped second order nonlinear system under harmonic excitation. It should be pointed out that no approximation (for example, the 3rd order Taylor's series) is made for the electrostatic force in Eq. (4.46) or (4.48). Therefore, the Taylor's series approximation error for the electrostatic force is not applicable in the validity tests for the following harmonic balance solution.

Approximate HB Solution for the Electrical Sinusoidal Excitation

In this section, an approximate analytical solution to Eq. (4.55) has been investigated by the harmonic balance method. The basic idea of the harmonic balance method is to consider a periodic solution of the time response in a form of a truncated Fourier series, after substituting the periodic solution into the governing ODE and equating the coefficient of each of the lowest N+1 harmonics to zero, a system of N+1 algebraic equations will be obtained and solved to finally yield the approximate solution [72]. In agreement with the input excitations of Eq. (4.55), the approximate steady-state solution of Eq. (4.55) is assumed to be a truncated Fourier series of the following form

$$y = A_0 + A_2 \cos(2\Omega t + \varphi), \quad (4.56)$$

where A_0 and A_2 are the amplitudes of the constant and second harmonic terms respectively, and φ is the phase of the second harmonic term.

Approximate Solution by a HB Method

To facilitate the analysis, it is convenient to introduce a complex form for the harmonic terms in Eq. (4.55)

$$\left(\ddot{y} + \gamma_1 \dot{y} + \gamma_2 y + \gamma_3 y^3\right)(1-y)^2 = F_0 + \frac{F_2}{2} \left(e^{i2\Omega t} + e^{-i2\Omega t}\right). \quad (4.57)$$

Eq. (4.56) is then substituted into Eq. (4.57), from which the constant term and the real and imaginary parts of the second harmonic term are finally found to be

$$\text{Const: } B_{11}\gamma_1 + B_{12}\gamma_2 + B_{13}\gamma_3 - C_1 = F_0, \quad (4.58)$$

$$\text{Real: } B_{21}\gamma_1 + B_{22}\gamma_2 + B_{23}\gamma_3 - C_2 = \frac{1}{2} F_2, \quad (4.59)$$

and

$$\text{Imag: } B_{31}\gamma_1 + B_{32}\gamma_2 + B_{33}\gamma_3 - C_3 = 0, \quad (4.60)$$

the expressions of coefficients B_{ij} and C_i ($i=1,2,3$ and $j=1,2,3$) are summarized in Appendix C.

It follows that $F_0 = F_2$ from Eqs. (4.53) and (4.54); therefore, Eqs. (4.58), (4.59) and (4.60) can be further condensed into the following matrix form

$$[B]\{U\} = \{C\}, \quad (4.61)$$

where

$$[B] \triangleq \begin{bmatrix} B_{11} & B_{12} & B_{13} & B_{14} \\ B_{21} & B_{22} & B_{23} & B_{24} \\ B_{31} & B_{32} & B_{33} & B_{34} \end{bmatrix}, \quad (4.62)$$

$$\{U\} \triangleq \begin{Bmatrix} \gamma_1 \\ \gamma_2 \\ \gamma_3 \\ F_0 \end{Bmatrix}, \quad (4.63)$$

$$\{C\} \triangleq \begin{Bmatrix} C_1 \\ C_2 \\ C_3 \end{Bmatrix}, \quad (4.64)$$

and the expressions for the coefficients B_{i4} ($i=1,2,3$) are provided in Appendix C. Since both matrix $[B]$ and vector $\{C\}$ only contain the spectrum properties (A_0 , A_2 and φ) of the steady-state response of the diaphragm, and vector $\{U\}$ only contains all the unknown system parameters, Eq. (4.61) can be used to identify system parameters from the characterization experiments.

The identification process is outlined as follows. For a given sinusoidal excitation frequency Ω , a nonlinear least-squares curve-fitting technique is applied to extract A_0 , A_2 and φ from the time history of the steady-state displacement response. Matrix $[B]$ and vector $\{C\}$ are then calculated respectively from the equations in the Appendix C. Since there are four unknowns (γ_1 , γ_2 , γ_3 and F_0) in vector $\{U\}$ and the rank of matrix $[B]$ is three, Eq. (4.61) is underdetermined. Therefore, a second test is performed at a different excitation frequency to provide more equations to make the system overdetermined (two redundant equations) and the four unknowns are solved via the linear least-squares method. Once γ_1 , γ_2 , γ_3 and F_0 (or F_2) are estimated, system parameters ζ , ω_0 , β and Γ are extracted by solving Eqs. (4.50), (4.51), (4.52), and (4.53) simultaneously as follows,

$$\omega_0 = \sqrt{\gamma_2}, \quad (4.65)$$

$$\zeta = \frac{\gamma_1}{2\sqrt{\gamma_2}}, \quad (4.66)$$

$$\beta = \frac{\gamma_3}{d_0^2}, \quad (4.67)$$

and

$$\Gamma = \frac{4d_0^3 F_0}{\varepsilon_0 V_0^2}. \quad (4.68)$$

Validity Region of the Approximate HB Solution

Eq. (4.56) basically represents an approximate solution to Eq. (4.55) via the HB method, it has two terms: a constant and a second harmonic. It is important to find out if Eq. (4.56) is still a good approximation when other harmonics exist, in other words, its validity region needs to be determined in terms of the total harmonic distortion (THD). The THD is defined in Eq. (2.1) in Chapter 2. As seen from Eqs. (4.46) and (4.47), a frequency doubling is obtained due to the electrostatic nonlinearity. It should be pointed out that the THD in the approximate harmonic balance solution (Eq. (4.56)) is 0% since only one harmonic, due to the frequency doubling caused by the electrostatic nonlinearity, is considered.

In this section, numerical simulation is used to determine the validity region of the HB approximate solution. First, three test simulations are conducted for three different applied voltages (V_0) and given input system parameters (ω_0 , ζ , β , Γ and d_0), the three different voltages are chosen such that the system responses have different THD levels (<0.1%, 1.0% and 10.6%) respectively. Then, based on the simulated system responses, the HB approximate solution is applied to extract system parameters for each test case. Finally, extracted system parameters are compared with their given values and errors are calculated for each test case respectively. From the errors obtained, we can conclude the validity region for the HB approximate solution.

Results of small THD case

For the small THD case, the applied voltage is chosen to be $V_0 = 5V$. The simulated sinusoidal displacement response of the diaphragm for the excitation with a

frequency of 92.7kHz (half of the system's natural frequency) is shown in Figure 4-7. From the plot, we can see that the steady state displacement amplitude is small and within the linear range.

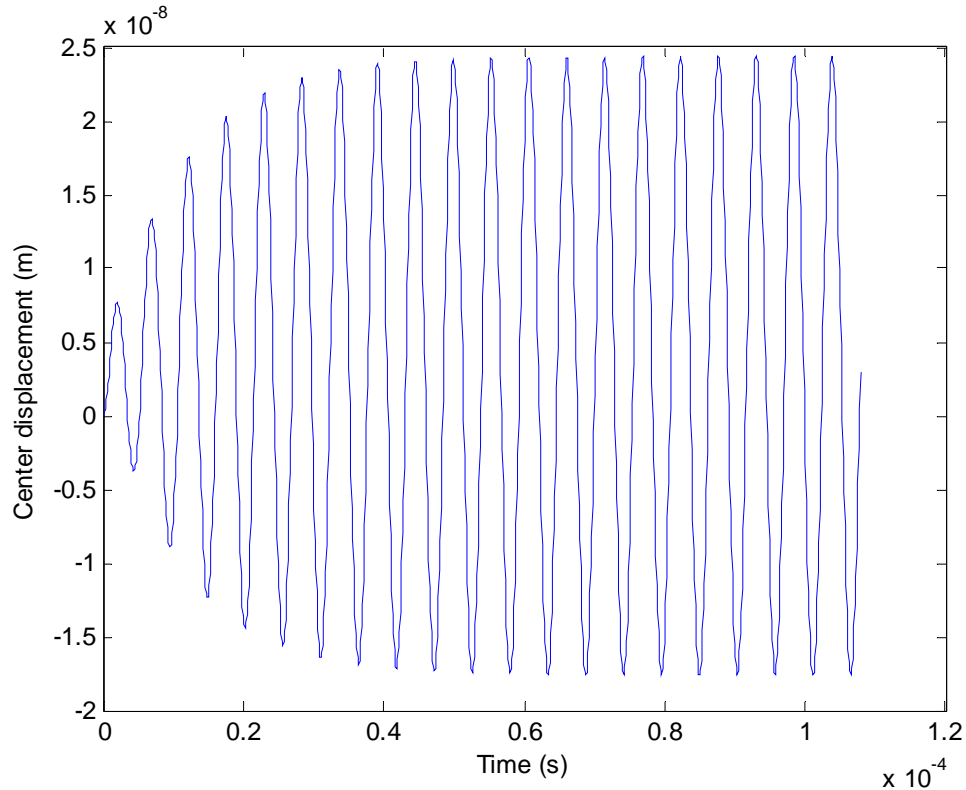


Figure 4-7. Simulated sinusoidal response of the diaphragm ($V_0 = 5\text{V}$, $\Omega/2\pi = 92.7\text{kHz}$).

Shown in Figure 4-8 is the power spectrum of the steady state displacement of the diaphragm, it has a DC component and the calculated THD is approximately less than 0.1%. Finally, the extracted system parameters via the approximate HB solution are listed in Table 4-5. Note that the second frequency test has been conducted to be able to extract system parameters but the results are neglected for the conciseness of this section. As we can see from Table 4-5, the maximum error of 1.5% occurs for the damping ratio, and other errors are smaller.

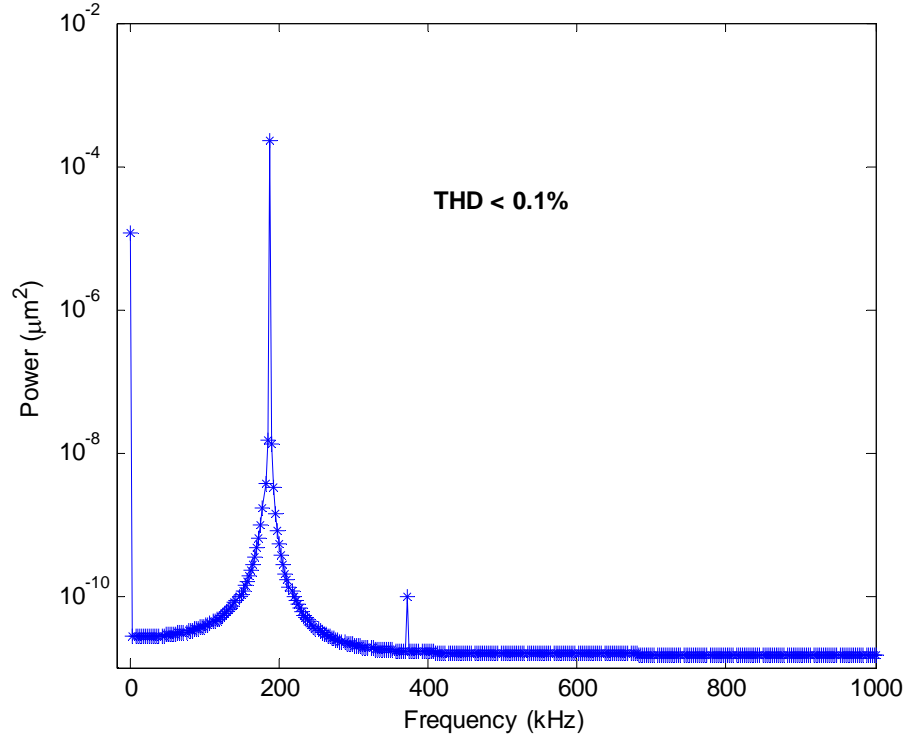


Figure 4-8. Simulated power spectrum of the steady state displacement ($V_0 = 5V$, $\Omega/2\pi = 92.7kHz$).

Table 4-5. Given and extracted (via HB solution) parameters for the small THD case.

Parameter	Given	Extracted	Error
Damping ratio ζ	8.091e-2	8.212e-2	1.5%
Natural frequency $f_0 = \omega_0/2\pi$ (kHz)	185.5	186.4	0.49%
Nonlinear parameter β ($N/m^3/kg$)	1.128e23	1.133e23	0.44%
Ratio Γ (m^2/kg)	332.2	328.9	0.99%

Results of transition THD case

For the transition THD case, the applied voltage is chosen to be $V_0 = 20V$. The simulated sinusoidal displacement response of the diaphragm for the excitation with a frequency of $92.7kHz$ is shown in Figure 4-9. From the plot, we can see that the steady state displacement amplitude is within the quasi-linear range and the maximum mechanical nonlinearity is approximately 1.5%.

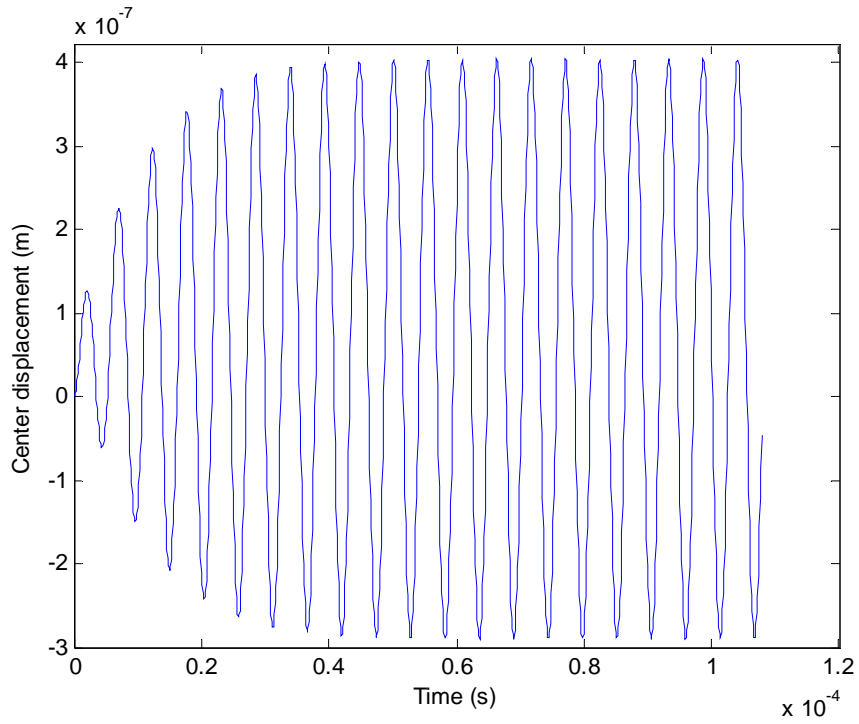


Figure 4-9. Simulated sinusoidal response of the diaphragm
 ($V_0 = 20V$, $\Omega/2\pi = 92.7kHz$).

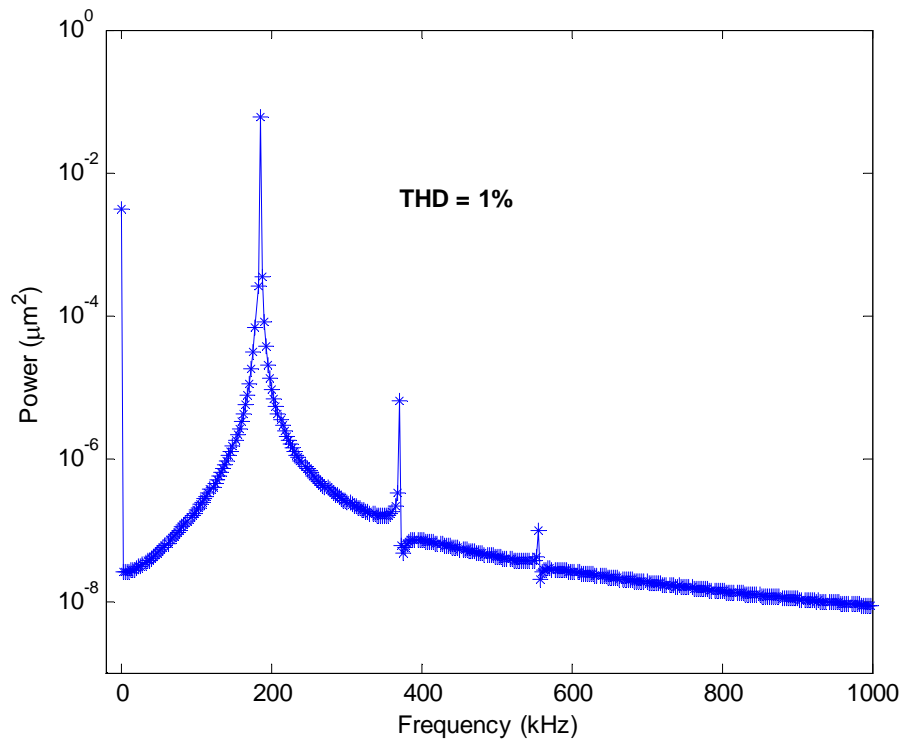


Figure 4-10. Simulated power spectrum of the steady state displacement
 ($V_0 = 20V$, $\Omega/2\pi = 92.7kHz$).

Shown in Figure 4-10 is the power spectrum of the steady state displacement of the diaphragm, it has a DC component and the calculated THD is approximately 1.0%. Finally, the extracted system parameters via the approximate HB solution are listed in Table 4-6. As we can see from Table 4-6, the maximum error of 4.8% occurs for the damping ratio, and other errors are smaller.

Table 4-6. Given and extracted (via HB solution) parameters for the transition THD case.

Parameter	Given	Extracted	Error
Damping ratio ζ	8.091e-2	7.701e-2	4.8%
Natural frequency $f_0 = \omega_0/2\pi$ (kHz)	185.5	190.1	2.5%
Nonlinear parameter β (N/m ³ /kg)	1.128e23	1.116e23	1.1%
Ratio Γ (m ² /kg)	332.2	345.5	4.0%

Results of large THD case

For the large THD case, it turns out from the simulation that we cannot achieve higher harmonic distortions ($THD \geq 10\%$) from our physical microphone system (2000Pa design) due to the electrostatic pull-in. To be able to generate higher harmonic distortions and further test the validity of the HB solution, we numerically increase the nonlinear stiffness parameter, for example, $k_3^{**} = 40k_3$ or $\beta^{**} = 40\beta$ (where the double asterisk sign represents new parameters).

With the new nonlinear stiffness parameter β^{**} , the plot of the simulated sinusoidal displacement response of the diaphragm is shown in Figure 4-11 for the excitation with a frequency of 92.7kHz and a voltage of 45V. As seen from Figure 4-11, the steady state displacement amplitude is within the nonlinear range (for example, the steady state displacement amplitude is larger than 0.5 μm).

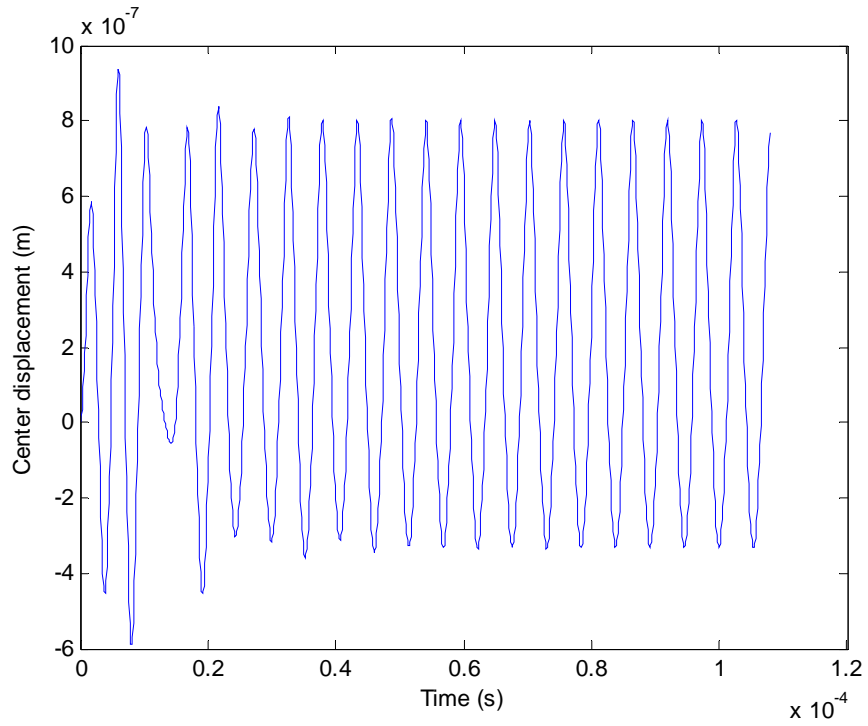


Figure 4-11. Simulated sinusoidal response of the diaphragm ($V_0 = 45V$, $k_3^{**} = 40k_3$, $\Omega/2\pi = 92.7kHz$).

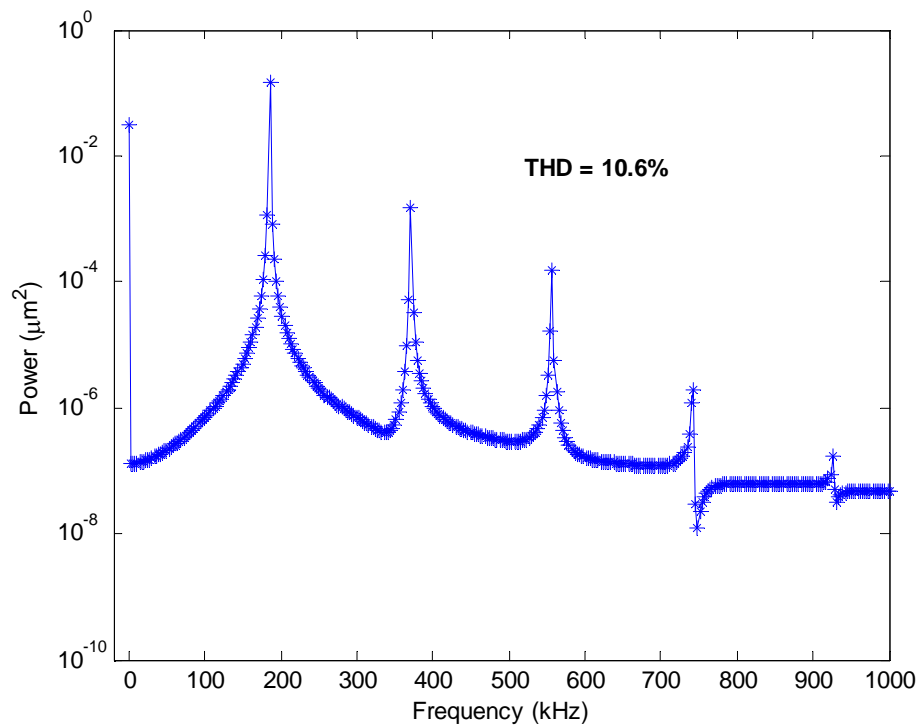


Figure 4-12. Simulated power spectrum of the steady state displacement ($V_0 = 45V$, $k_3^{**} = 40k_3$, $\Omega/2\pi = 92.7kHz$).

Shown in Figure 4-12 is the power spectrum of the steady state displacement of the diaphragm, it has a DC component and the calculated THD is approximately 10.6%. Finally, the extracted system parameters via the approximate HB solution are listed in Table 4-7.

Table 4-7. Given and extracted (via HB solution) parameters for the large THD case.

Parameter	Given	Extracted	Error
Damping ratio ζ	8.091e-2	7.603e-2	6.0%
Natural frequency $f_0 = \omega_0/2\pi$ (kHz)	185.5	203.2	9.5%
Nonlinear parameter β^{**} (N/m ³ /kg)	4.512e24	4.285e23	5.0%
Ratio Γ (m ² /kg)	332.2	355.4	7.0%

As we can see from Table 4-7, the maximum error of 9.5% occurs for the natural frequency. Table 4-8 summarizes the maximum error and sum of residual squares for each test case, the sum of residual squares S_r for Eq. (4.61) is defined as follows [108]

$$S_r = \text{sum}([B]\{U\} - \{C\})^2 = \sum_{i=1}^6 \left(\left(\sum_{j=1}^4 B_{ij} U_j \right) - C_i \right)^2. \quad (4.69)$$

Table 4-8. Results of the maximum error and sum of residual squares for each test case.

Test case	Maximum error	Sum of residual squares (S_r)
Small THD case	1.5%	4.9e18
Transition THD case	4.8%	2.9e21
Large THD case	9.5%	4.2e22

As we can see from the table, the maximum error and S_r increase as the THD becomes large, which means the HB approximate solution is getting less accurate. The maximum error for the $THD = 10.6\%$ case is 9.5% and will be increasing as the THD becomes larger. Therefore, we can conclude the HB approximate solution holds with an error of less than 9.6% for a nonlinear system with a THD up to 10.6%.

Governing Equation for the Sinusoidal Acoustical Pressure Excitation

Previous studies focus on the responses of the microphone under electrical excitations. Since microphones serve as pressure sensors and sense acoustical signals, it is necessary to investigate the microphone response to acoustic excitation. This section presents the study of the steady state response of the microphone when excited by a typical sinusoidal acoustical pressure signal. The study of the transient response of the microphone when subject to shock (mechanical or acoustical) loads, in the form of dynamic pull-in, is presented in Chapter 5.

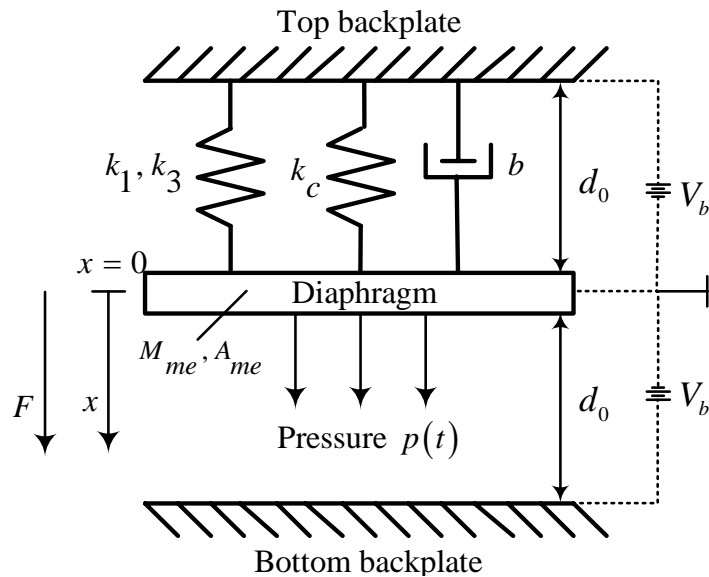


Figure 4-13. Dynamic model for the sinusoidal acoustical pressure excitation.

Figure 4-13 shows the dynamic model for the sinusoidal acoustical pressure excitation. In the model, $p(t)$ represents a sinusoidal acoustical pressure signal. The expression for the applied sinusoidal pressure wave is given by

$$p(t) = p_0 \cos(\omega_p t), \quad (4.70)$$

where p_0 and ω_p are the amplitude and driving frequency of the sinusoidal

acoustical wave, respectively. In this case, the general governing equation in Eq. (3.53) of Chapter 3 can be reduced to

$$M_{me}\ddot{x} + b\dot{x} + (k_1 + k_c)x + k_3x^3 = -\frac{\varepsilon A_{me}}{2} \left[\frac{V_b^2}{(d_0 + x)^2} - \frac{V_b^2}{(d_0 - x)^2} \right] + A_{me} p_0 \cos(\omega_p t), \quad (4.71)$$

where V_b is the applied DC bias voltage.

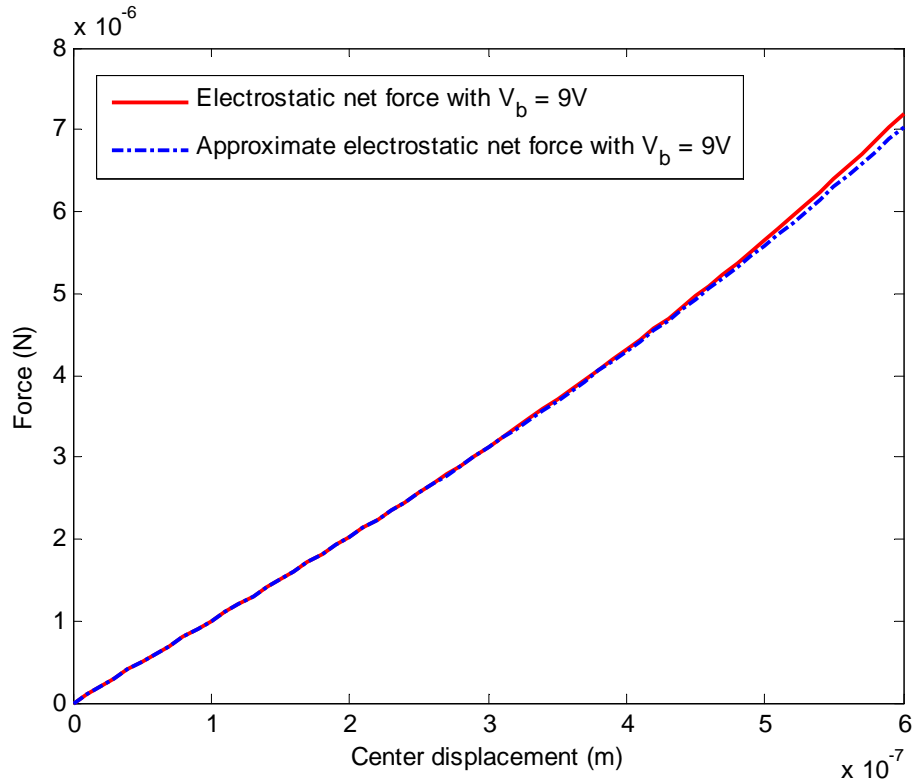


Figure 4-14. Plot of net electrostatic and approximate net electrostatic forces for $V_b = 9\text{V}$.

Unfortunately, due to the complexity of Eq. (4.71), no closed-form solution exists. To find an approximate solution to Eq. (4.71), first we need to approximate the nonlinear net electrostatic force. Further Taylor's series expansion for the nonlinear net electrostatic force up to the 3rd order results in

$$-\frac{\varepsilon_0 A_{me}}{2} \left[\frac{V_b^2}{(d_0 + x)^2} - \frac{V_b^2}{(d_0 - x)^2} \right] \approx \frac{2\varepsilon_0 A_{me} V_b^2}{d_0^3} x + \frac{4\varepsilon_0 A_{me} V_b^2}{d_0^5} x^3. \quad (4.72)$$

In order to verify the accuracy of the 3rd order Taylor's series expansion used in the above equation, by using the parameters in Table 3-1, the net electrostatic and approximate net electrostatic forces are plotted in Figure 4-14 for an applied voltage $V_0 = 9\text{V}$. This voltage is chosen since it is used in the numerical validity test in the next section.

As we can see from the plot, the two net electrostatic forces are close to each other when the center displacement is up to $0.6\mu\text{m}$. Further calculations show that the maximum approximation error caused by the 3rd order Taylor's series expansion is 2.3%. The approximation error becomes larger if the center displacement is over $0.6\mu\text{m}$. Physically, the curvature of the diaphragm needs to be considered if the center displacement becomes large.

The parallel plate assumption used to model the net electrostatic force (left hand side of Eq. (4.72)) might not be able to hold for the large displacement case. Therefore, the 3rd order Taylor's series approximation in Eq. (4.72) carries a maximum error of approximately 2.3% when the center displacement is $0 \leq x \leq 0.6\mu\text{m}$ and the applied voltage is $V_0 = 9\text{V}$.

To proceed, substitution of Eq. (4.72) into Eq. (4.71) yields

$$M_{me}\ddot{x} + b\dot{x} + \left[k_1 + k_c - \frac{2\epsilon_0 A_{me} V_b^2}{d_0^3} \right] x + \left[k_3 - \frac{2\epsilon_0 A_{me} V_b^2}{d_0^5} \right] x^3 = A_{me} p_0 \cos(\omega_p t). \quad (4.73)$$

Physically, the above equation represents a damped second order system with only cubic mechanical and electrical nonlinearities and an external excitation. Mathematically, Eq. (4.73) represents a forced damped Duffing's equation [72].

Approximate Solutions for the Sinusoidal Acoustical Pressure Excitation

In this section, the steady-state approximate solutions to Eq. (4.73) are obtained by both harmonic balance and multiple time scales methods. First, let's define two equivalent spring constants as follows,

$$k_{1E} \triangleq \frac{2\varepsilon_0 A_{me} V_b^2}{d_0^3} \quad (4.74)$$

and

$$k_{3E} \triangleq \frac{2\varepsilon_0 A_{me} V_b^2}{d_0^5}, \quad (4.75)$$

where k_{1E} is a linear electrical spring constant and k_{3E} is a cubic electrical spring constant.

Prior to finding the approximate solutions, we need to non-dimensionalize the governing equation in Eq. (4.73), which finally leads to

$$y'' + 2\bar{\zeta} y' + y + \bar{\theta} y^3 = \bar{P} \cos(\Omega\tau), \quad (4.76)$$

where

$$y = \frac{x}{d_0}, \quad (4.77)$$

$$y' = \frac{dy}{d\tau}, \quad (4.78)$$

$$y'' = \frac{d^2 y}{d\tau^2}, \quad (4.79)$$

$$\tau = \bar{\omega}_0 t, \quad (4.80)$$

$$\bar{\omega}_0 = \sqrt{(k_1 + k_c - k_{1E})/M_{me}}, \quad (4.81)$$

$$\bar{\zeta} = \frac{b}{2M_{me}\bar{\omega}_0}, \quad (4.82)$$

$$\bar{\theta} = \frac{k_3 - k_{3E}}{M_{me} \bar{\omega}_0^2} d_0^2, \quad (4.83)$$

$$\bar{P} = \frac{p_0 A_{me}}{M_{me} \bar{\omega}_0^2 d_0}, \quad (4.84)$$

and

$$\Omega = \frac{\omega_p}{\bar{\omega}_0}, \quad (4.85)$$

where y and y' are the non-dimensional center displacement and velocity of the diaphragm respectively, $\bar{\omega}_0$ is the modified natural frequency of the system, τ is the dimensionless time, $\bar{\zeta}$ is the modified damping ratio, $\bar{\theta}$ is the modified nonlinear stiffness parameter, \bar{P} is the external forcing parameter and Ω is the ratio of the pressure driving frequency over the system's natural frequency. As seen from Eqs. (4.81) and (4.83), physically the linear and cubic stiffnesses of the diaphragm are reduced by the applied DC voltage or the electrostatic softening nonlinearity.

HB Approximate Solution

The harmonic balance approximate solution to Eq. (4.76) in the steady state is expressed in a Fourier series as follows [72]

$$y(\tau) = \sum_{n=0}^{\infty} a_n \cos[n(\Omega\tau + \phi)], \quad (4.86)$$

where a_n is the amplitude of the n^{th} harmonic and ϕ is the phase angle.

After substituting Eq. (4.86) into Eq. (4.76), by collecting and equating the coefficients of the harmonics, the approximate solution for $y(\tau)$ can be obtained (detailed derivations are provided in Appendix D). In agreement with the input excitation

of Eq. (4.76), for a first-order approximation, the harmonic balance solution for $y(\tau)$ in the steady state is given by

$$y(\tau) \approx a_1 \cos(\Omega\tau + \phi), \quad (4.87)$$

where a_1 and ϕ are determined from the following equations respectively,

$$\frac{9}{16}\bar{\theta}^2 a_1^6 + \frac{3}{2}\bar{\theta}(1-\Omega^2)a_1^4 + \left[(1-\Omega^2)^2 + (2\bar{\zeta}\bar{\Omega})^2 \right] a_1^2 - \bar{P}^2 = 0, \quad (4.88)$$

and

$$\phi = \tan^{-1} \frac{2\bar{\zeta}\bar{\Omega}}{(1-\Omega^2) + 0.75\bar{\theta}a_1^2}. \quad (4.89)$$

From Eqs. (4.77), (4.80), (4.85), (4.87) and (4.89), finally we can obtain the following approximate harmonic balance solution for Eq. (4.73) in the steady state as follows

$$x(t) = yd_0 \approx a_1 d_0 \cos \left[\omega_p t + \tan^{-1} \frac{2\bar{\zeta}\bar{\Omega}}{(1-\Omega^2) + 0.75\bar{\theta}a_1^2} \right], \quad (4.90)$$

where a_1 can be determined by solving Eq. (4.88) for given parameters.

MTS Approximate Solution

For the multiple time scales solution, it is convenient to introduce the following transformations to rewrite the governing equation in Eq. (4.76)

$$\varepsilon = \bar{\theta}, \quad (4.91)$$

$$\bar{\zeta} = \varepsilon\mu, \quad (4.92)$$

and

$$\bar{P} = 2\varepsilon f, \quad (4.93)$$

where ε is a small perturbation parameter, μ and f are new introduced variables.

Substituting Eqs. (4.92), and (4.93) into Eq. (4.76) yields

$$y'' + y + \varepsilon(2\mu y' + y^3) = 2\varepsilon f \cos(\Omega\tau). \quad (4.94)$$

If we are seeking a first order approximation to the above equation, which takes the form

$$y(\tau) \approx y_0(\tau_0, \tau_1) + \varepsilon y_1(\tau_0, \tau_1), \quad (4.95)$$

where y_0 and y_1 are unknown functions that need to be determined, τ_0 and τ_1 are the fast time scale (representing the fast dynamics) and slow time scale (representing the slow dynamics) respectively,

$$\tau_0 = \tau \quad (4.96)$$

and

$$\tau_1 = \varepsilon\tau. \quad (4.97)$$

After substituting Eq. (4.95) into Eq. (4.94), by collecting and equating the coefficients (detailed derivations are provided in Appendix D), the first-order approximate solution for $y(\tau)$ in the steady state is obtained as follows

$$y(\tau) \approx a_1 \cos \left[\Omega\tau - \sin^{-1} \left(\frac{2\bar{\zeta} a_1}{P} \right) \right], \quad (4.98)$$

where a_1 is the root of the following equation,

$$\frac{9}{64} a_1^6 + \frac{3}{4} \sigma a_1^4 + (\sigma^2 + \mu^2) a_1^2 - f^2 = 0. \quad (4.99)$$

The non-dimensional parameters in Eq. (4.99) are defined as

$$\sigma = \frac{\Omega - 1}{\varepsilon}, \quad (4.100)$$

$$\mu = \frac{\bar{\zeta}}{\varepsilon}, \quad (4.101)$$

and

$$f = \frac{\bar{P}}{2\varepsilon}. \quad (4.102)$$

From Eqs. (4.77), (4.80), (4.85) and (4.98), finally the multiple time scales solution for $x(t)$ in the steady state is

$$x(t) = yd_0 \approx a_1 d_0 \cos \left[\omega_p t - \sin^{-1} \left(\frac{2\bar{\zeta} a_1}{\bar{P}} \right) \right], \quad (4.103)$$

where a_1 can be determined by solving Eq. (4.99) for given parameters.

Validity Region of Approximate Solutions

In this section, the steady-state approximate solutions obtained in Eqs. (4.90) and (4.103) are compared to the steady-state numerical solution to the full-blown nonlinear equation in Eq. (4.71). The numerical solution to the full-blown nonlinear equation in Eq. (4.71) is obtained by doing the direct integration via the ODE45 command in MATLAB. To check the validity of the approximate solutions, three different pressure amplitudes are chosen such that the steady-state system responses fall into the linear, weakly nonlinear and highly nonlinear regions, respectively. For each case, three different solutions (HB, MTS and numerical) are compared to obtain the errors of the approximate solutions.

For this study, a bias DC voltage of 9V is chosen since it will be used for the future experiments and the parameters from Table 3-1 are used to calculate non-dimensional parameters as shown in Table 4-9. Three different pressure amplitudes are chosen to be 100Pa, 350Pa and 700Pa, respectively. The corresponding non-dimensional forcing parameters are also listed in Table 4-9.

Table 4-9. Parameters used for the comparison of approximate and numerical solutions.

Parameter	Value
Acoustical pressure amplitudes p_0	100.0, 350.0 and 700.0 (Pa)
Bias DC voltage (V_b)	9.000 (V)
Modified natural frequency ($\bar{\omega}_0/2\pi$)	181.4 (kHz)
Modified damping ratio ($\bar{\zeta}$)	8.270e-2
Modified nonlinear parameter ($\bar{\theta}, \varepsilon$)	2.556e-1
External forcing parameters (\bar{P})	1.279e-2, 4.477e-2 and 8.954e-2

As seen from Eqs. (4.71), (4.88) and (4.99), the non-dimensional amplitude a_1 represents the most difference between the approximate (HB and MTS) and numerical solutions. Therefore, only the non-dimensional displacement amplitudes of the approximate and numerical solutions are studied in the following when the frequency of the incident acoustical pressure is swept.

Results of linear case

For the linear test case, the pressure amplitude is chosen to be $p_0 = 100Pa$. Shown in Figure 4-15 is the comparison of the non-dimensional amplitudes of the approximate and numerical solutions for the frequency sweep of the incident acoustical pressure. From the plot, the maximum non-dimensional amplitude is approximately 0.08, where the corresponding mechanical and electrical nonlinearities (see Eqs. (3.54) and (3.59) for their definitions) are calculated to be $NL_m \approx 0\%$ and $NL_e \approx 0\%$. As seen from Figure 4-15, the difference between the non-dimensional amplitudes of the approximate and numerical solutions in the steady state is small around $\Omega = 1$. Further studies show that the maximum amplitude error between the harmonic balance and numerical solutions is approximately 1.2% when $0.1 \leq \Omega \leq 2$. For the multiple time scales solution, the maximum amplitude error is approximately 2.1% when $0.95 \leq \Omega \leq 1.05$. Away from $\Omega = 1$, the non-dimensional amplitudes of the harmonic balance and numerical solutions

are in good agreement with each other, while the non-dimensional amplitude difference between the multiple time scales and numerical solutions becomes larger.

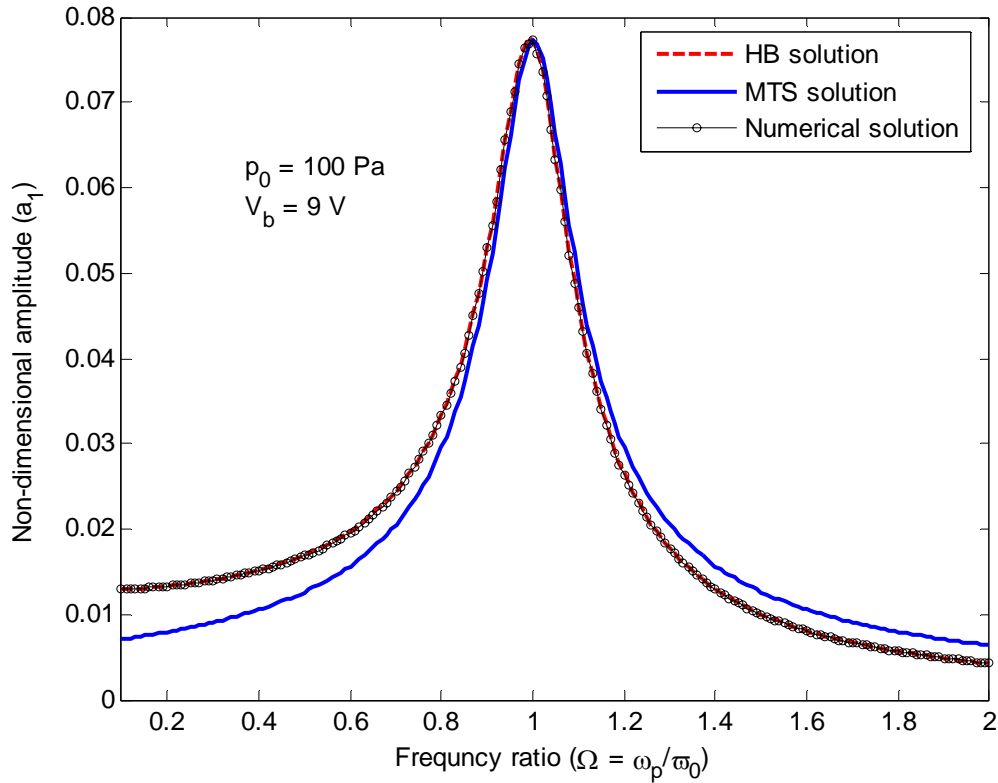


Figure 4-15. Comparison of the steady-state non-dimensional amplitudes of the approximate and numerical solutions for a linear case.

Results of weakly nonlinear case

For the weakly nonlinear test case, the pressure amplitude is chosen to be $p_0 = 350 \text{ Pa}$. Shown in Figure 4-16 is the comparison of the non-dimensional amplitudes of the approximate and numerical solutions in the steady state. From the plot, the maximum non-dimensional amplitude is approximately 0.27, where the corresponding mechanical and electrical nonlinearities are calculated to be $NL_m \approx 2.7\%$ and $NL_e \approx 1.5\%$. As seen from Figure 4-16, the difference between the non-dimensional amplitudes of the approximate and numerical solutions in the steady state is small around $\Omega = 1$. Further studies show that the maximum amplitude error between the harmonic

balance and numerical solutions is approximately 3.0% when $0.1 \leq \Omega \leq 2$. For the multiple time scales solution, the maximum amplitude error is approximately 4.5% when $0.95 \leq \Omega \leq 1.05$. Away from $\Omega = 1$, the non-dimensional amplitudes of the harmonic balance and numerical solutions are still in good agreement with each other, while the non-dimensional amplitude difference between the multiple time scales and numerical solutions becomes larger.

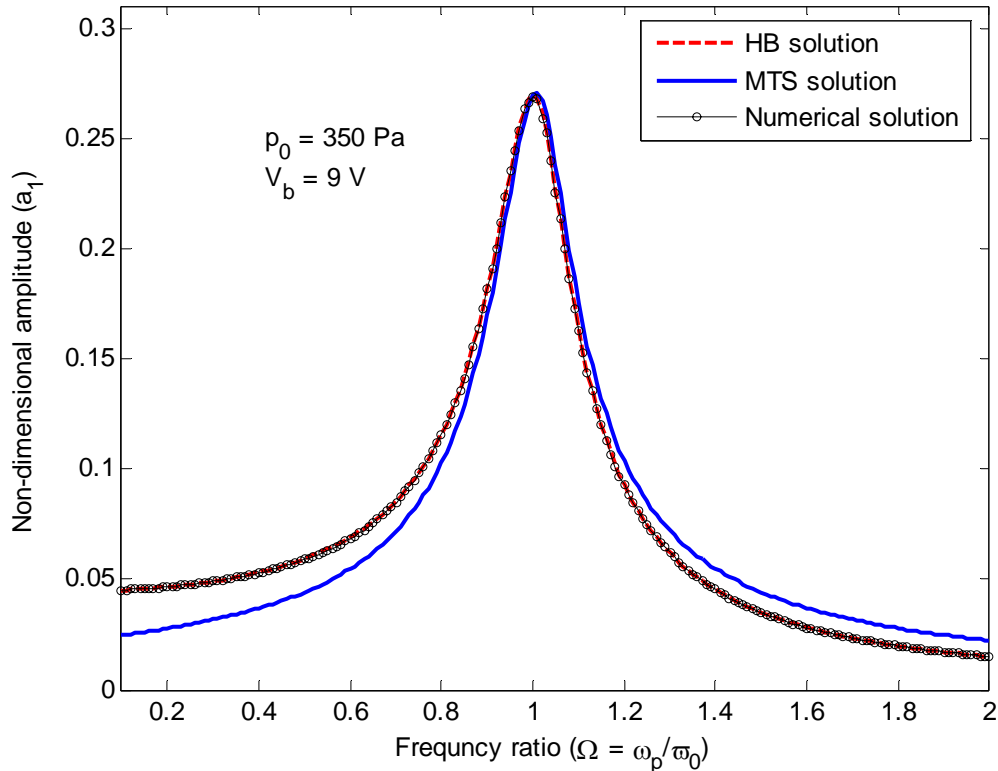


Figure 4-16. Comparison of the steady-state non-dimensional amplitudes of the approximate and numerical solutions for a weakly nonlinear case.

Results of highly nonlinear case

For the highly nonlinear test case, the pressure amplitude is chosen to be $p_0 = 700 \text{ Pa}$. Shown in Figure 4-17 is the comparison of the non-dimensional amplitudes of the approximate and numerical solutions in the steady state. From the plot, the maximum non-dimensional amplitude is approximately 0.55, where the corresponding

mechanical and electrical nonlinearities are calculated to be $NL_m \approx 10.6\%$ and $NL_e \approx 24.8\%$.

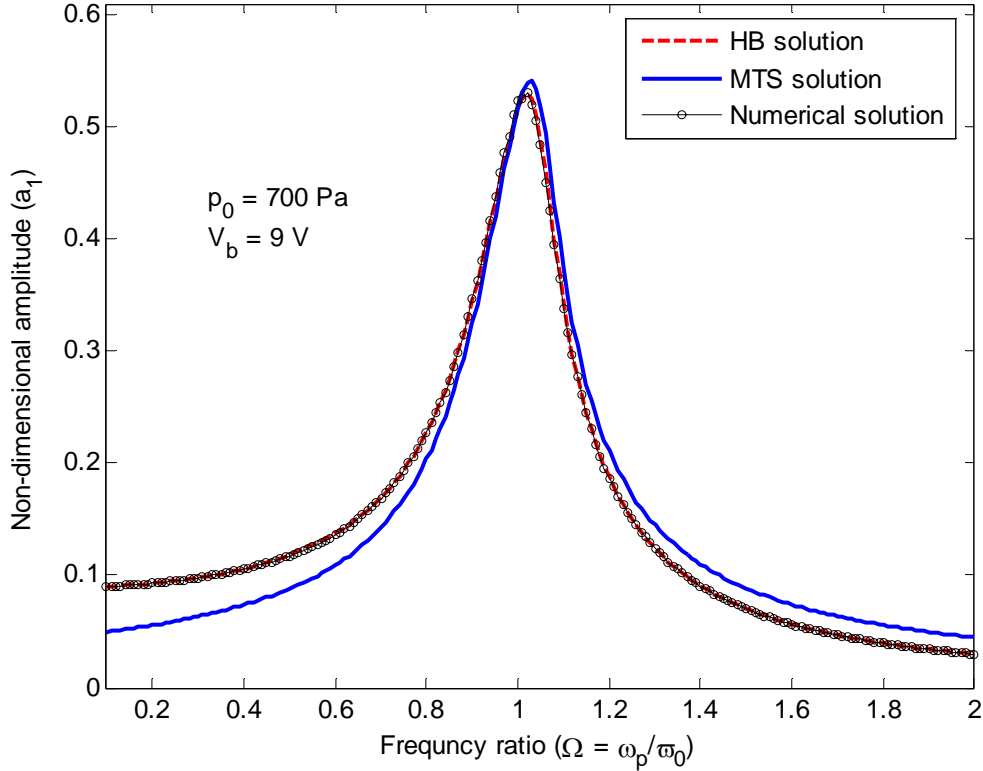


Figure 4-17. Comparison of the steady-state non-dimensional amplitudes of the approximate and numerical solutions for a highly nonlinear case.

As seen from Figure 4-17, the difference between the non-dimensional amplitudes of the approximate and numerical solutions in the steady state becomes larger around $\Omega = 1$. Further studies show that the maximum amplitude error between the harmonic balance and numerical solutions is approximately 4.5% when $0.1 \leq \Omega \leq 2$. For the multiple time scales solution, the maximum amplitude error is approximately 7.5% when $0.95 \leq \Omega \leq 1.05$. Away from $\Omega = 1$, the harmonic balance and numerical solutions are still in good agreement with each other, while the large difference exists between the multiple time scales and numerical solutions. Also it can be observed that the resonance

occurs after $\Omega = 1$ and all three response curves are bending to the right, which indicates the existence of a Duffing's hardening spring in the system.

Based on the results from the above three test cases, among the two obtained approximate solutions, the HB approximate solution is more accurate to predict the microphone response under the sinusoidal acoustical pressure excitation. Away from $\Omega = 1$, the multiple time scales solution will generate large errors and therefore it is not recommended for use. In conclusion, the HB approximate solution holds with an error of less than 4.5% for the microphone under a bias voltage of 9V and a sinusoidal acoustical pressure excitation with an amplitude of up to 750Pa.

Summary

In this chapter, nonlinear analyses are presented for the response behavior due to the electrical square and sinusoidal excitations. The approximate analytical solutions to those two governing equations are obtained via the MTS and HB methods respectively. Discussions and validity regions of the derived MTS and HB approximate solutions are also provided. The obtained approximate solutions will be applied in Chapter 6 to extract system parameters experimentally. This chapter also provides HB and MTS approximate solutions for the microphone under the sinusoidal acoustical pressure excitation. Comparison of the obtained two approximate solutions to the numerical solution in the steady state is presented. The major contributions made in this chapter are 1) a MTS approximate solution to a general damped second-order system with quadratic and cubic nonlinearities and non-zero step loading as defined in Eq. (4.11); and 2) a HB approximate solution to a general inhomogeneous nonlinear damped second order system under the harmonic excitation as defined in Eq. (4.55).

CHAPTER 5 PULL-IN INSTABILITIES

As noted in the previous chapters, the microphone must be carefully designed to avoid unstable parameter domains and possible structural failure. This chapter focuses on the theoretical and numerical analyses of pull-in instabilities of the microphone. The next section examines the microphone quasi-static pull-in instability, due to an applied DC voltage, through a standard nonlinear analysis process. Then, quasi-static pull-in due to a combination of an applied DC voltage and static pressure is provided. In addition, the effect of a mechanical shock load on dynamic pull-in instability is also discussed. By using a phase portrait and the basins of attraction, a mechanical shock load is related to dynamic pull-in. Finally, dynamic pull-in due to an acoustical pulse, in the form of an N-wave, is investigated via numerical simulation.

Quasi-Static Pull-in due to an Applied DC Voltage

During the quasi-static pull-in analysis in this section, it is assumed that no acoustical pressure exists on the diaphragm ($p(t) = 0$) and only DC voltages are applied to the top and bottom backplates. Since all the time derivatives go to zero in the quasi-static process, based on the general nonlinear governing equation in Eq. (3.53) of Chapter 3, finally the corresponding governing equation for the static response is given by

$$k_1x + k_3x^3 = -\frac{\varepsilon A_{me}}{2} \left[\frac{V_b^2}{(d_0 + x)^2} - \frac{V_b^2}{(d_0 - x)^2} \right]. \quad (5.1)$$

Notice that the stiffness of the cavity is not included in the mechanical restoring force since the process is quasi-static. With the rearrangement of the net electrostatic

force, Eq. (5.1) can be further changed into

$$k_1x + k_3x^3 = 2\varepsilon A_{me}d_0V_b^2 \frac{x}{(d_0^2 - x^2)^2}. \quad (5.2)$$

It should be pointed out that no approximation (for example, the 3rd order Taylor's series) is made for the net electrostatic force throughout this chapter. To proceed, we need to non-dimensionalize the above static equation to simplify the analysis

$$f(y) = \kappa_s \frac{y}{(1-y^2)^2} - y - \theta_s y^3 = 0, \quad (5.3)$$

where $\kappa_s \frac{y}{(1-y^2)^2}$ is the non-dimensional net electrostatic force, $y + \theta_s y^3$ is the non-dimensional mechanical force, $f(y)$ is a nonlinear function of y and represents a net non-dimensional force applied on the diaphragm. Other non-dimensional parameters in Eq. (5.3) are defined as

$$y = \frac{x}{d_0}, \quad (5.4)$$

$$\theta_s = \frac{k_3 d_0^2}{k_1} \triangleq \frac{k_3 d_0^3}{k_1 d_0}, \quad (5.5)$$

and

$$\kappa_s = \frac{2\varepsilon A_{me} V_b^2}{k_1 d_0^3} \triangleq \frac{2\varepsilon A_{me} V_b^2}{k_1 d_0^2}, \quad (5.6)$$

where y is the ND center displacement of the diaphragm, θ_s is a ND mechanical force parameter, and κ_s is a ND electrostatic force parameter with a square dependence on the DC voltage. Physically, y is a ratio of the center displacement of the diaphragm over the

nominal gap, which serves as a reference displacement. The parameter θ_s represents a ratio of the nonlinear component of the spring force, at the reference displacement, over its linear component. The parameter κ_s represents a ratio of the nonlinear electrostatic force over the linear component of the spring force at the reference displacement. To further investigate the stability of Eq. (5.3), first we need to find equilibrium points of the governing equation and study their local stabilities.

Equilibrium Points and Local Stabilities

The equilibrium points of the system can be obtained by finding the roots of Eq. (5.3). Physically, at equilibrium points, the nonlinear mechanical spring force equals to the nonlinear electrostatic force. Therefore, the equilibrium points satisfy the following nonlinear equation

$$\kappa_s \frac{y_e}{(1 - y_e^2)^2} - y_e - \theta_s y_e^3 = 0. \quad (5.7)$$

The above nonlinear equation is a seventh order nonlinear algebraic equation, which does not have an analytical solution. However, it is possible to obtain an analytical solution for this particular problem. As seen from Eq. (5.7), $y_e = 0$ is always one of seven roots. Therefore, Eq. (5.7) can be changed into a sixth order equation with only even terms, which can be solved analytically.

Table 5-1. Force parameters for a designed 2000Pa capacitive MEMS microphone.

Parameter	Value
DC bias voltage (V_b)	20 (V)
ND mechanical force parameter (θ_s)	0.37
ND electrostatic force parameter (κ_s)	0.24

In order to facilitate the analysis, some values for the non-dimensional parameters are required. By using the physical parameters in Table 3-1 for the designed 2000Pa

MEMS microphone, non-dimensional parameters are calculated and listed in Table 5-1 for a DC voltage of 20V (it should be pointed out that this DC voltage value is chosen just for illustration purposes).

From Table 5-1, we can see that the mechanical and electrostatic nonlinearities of the system are on the same order. As we will discuss later, a larger mechanical geometric nonlinearity k_3 (or θ_s) stabilizes the system while a larger electrostatic nonlinearity V_b (or κ_s) destabilizes the system. Those two types of nonlinearities compete with each other and some interesting phenomena occur when one of them becomes dominant. For example, when the value of V_b (or κ_s) reaches a certain extreme point, quasi-static pull-in occurs since the geometric nonlinearity becomes insignificant comparing with the competing electrostatic nonlinearity.

After substituting the values of θ_s and κ_s into Eq. (5.7), five real solutions are finally obtained. Therefore, the five corresponding equilibrium points are

$$(y_e)_1 = 0, \quad (5.8)$$

$$(y_e)_{2,3} = \pm 0.74, \quad (5.9)$$

and

$$(y_e)_{4,5} = \pm 1.18. \quad (5.10)$$

The negative sign in above equations means the diaphragm moves towards the top backplate while the positive sign means the diaphragm moves towards the bottom backplate. The above equilibrium points are symmetric around the rest position due to the symmetric structure assumption utilized in the modeling.

To study the local stability of each equilibrium point, we need to linearize the net nonlinear force around each equilibrium point. To realize a linearization, mathematically, the Jacobian matrix needs to be introduced. By definition, the Jacobian is a matrix containing all of the first partial derivatives with respect to each state variable. For this study, the calculated Jacobian matrix only has one element as follows

$$J = \frac{\partial f}{\partial y} = \frac{3\theta_s y^8 + (1 - 9\theta_s) y^6 + (9\theta_s - 3) y^4 + (3 + 3\kappa_s - 3\theta_s) y^2 + (\kappa_s - 1)}{(1 - y^2)^3}. \quad (5.11)$$

The local stability is determined from the eigenvalues of the Jacobian matrix evaluated at each equilibrium point. For example, if all the eigenvalues of an equilibrium point have negative real parts, the equilibrium point is a locally stable sink point. If some, but not all, of the eigenvalues of an equilibrium point have positive real parts, while other eigenvalues have negative real parts, the equilibrium point is a locally unstable saddle point [69].

Evaluating the Jacobian matrix in Eq. (5.11) at each equilibrium point yields

$$J_1 = -0.757, \quad (5.12)$$

$$J_{2,3} = 6.86, \quad (5.13)$$

and

$$J_{4,5} = -24.4. \quad (5.14)$$

The eigenvalues of the above Jacobian matrices can be easily calculated since each matrix has only one element. Therefore, based on the criteria of local stability, the first equilibrium point is a locally stable sink point. The second and third equilibrium points are locally unstable saddle points, the fourth and fifth equilibrium points are locally stable sink points.

Graphical Analysis

One alternative to analyze the local stabilities of equilibrium points is by examining the two ND nonlinear forces graphically. Figure 5-1 shows a plot of the ND mechanical and net electrostatic forces for an applied DC voltage of 20V. The border lines are located at $y = \pm 1$, which correspond to two physical backplates. Mathematically, $y = \pm 1$ are two singular points for Eq. (5.3), where the ND net electrostatic force goes to infinity. The range between two border lines is the physical operation range of the diaphragm.

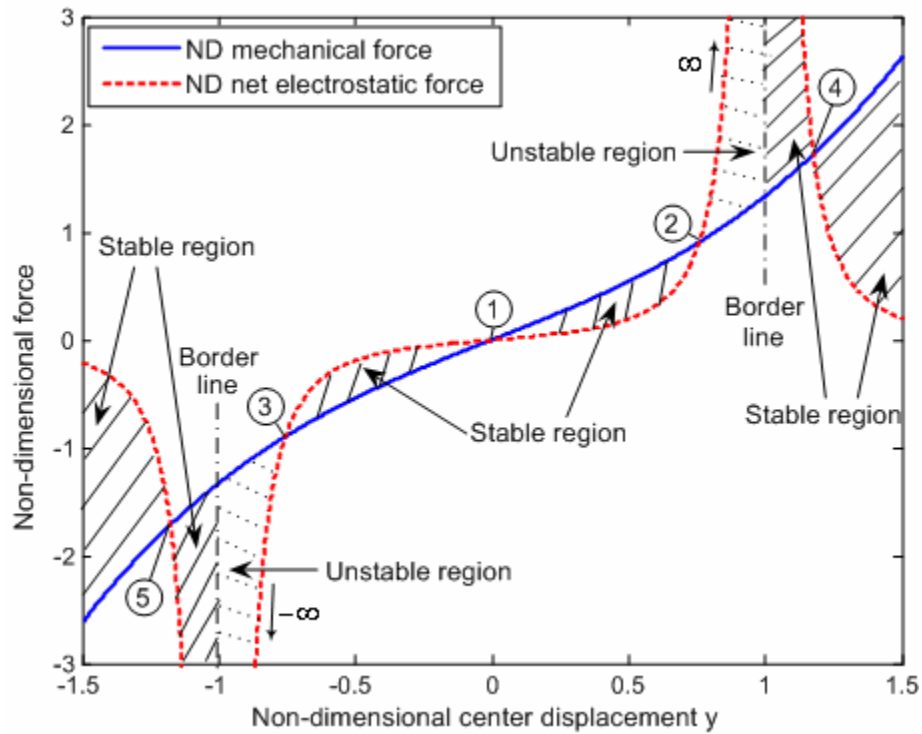


Figure 5-1. Plot of the ND mechanical and net electrostatic forces for $\theta_s = 0.37$ and $\kappa_s = 0.24$.

From Figure 5-1, the five possible equilibrium points are: 1) a locally stable point attractor (node 1) at the rest position of the diaphragm ($y = 0$); 2) two unstable saddle nodes (nodes 2 and 3), situated at $y = \pm 0.74$, which repel motions either toward the desirable stable center position or towards quasi-static pull-in at the border lines; and 3)

two locally stable point attractors (nodes 4 and 5 in the figure), located at $y = \pm 1.18$, which, although physically do not exist, attract relatively larger amplitude displacements.

Further analysis shows that there are several stable and unstable quasi-static regions in Figure 5-1. In the region between the unstable saddle nodes 2 and 3, the ND mechanical force is always greater than the ND net electrostatic force; therefore, the system is always quasi-statically stable. The region between unstable saddle nodes 2 and 3 is called the 1-D basin of attraction of the center equilibrium point, in which all initial displacements quasi-statically converge into the center equilibrium point.

In the regions between the physical border lines and nodes 2 and 3 respectively, the ND mechanical force is always less than the ND net electrostatic force; therefore, the system is unstable and the diaphragm moves quasi-statically to the backplates. In the regions outside the border lines, the system is stable only mathematically. In the following analysis, these non-physical regions will be discarded.

Critical Quasi-Static Pull-in Voltage

From the previous analysis, the quasi-statically stable operation range of the microphone is defined by the 1-D basin of attraction of the center equilibrium point. Further analysis shows that the stable operational range depends on the applied DC voltage. For example, the operation range is $-0.74 < y < 0.74$ or $-1.48\mu\text{m} < x < 1.48\mu\text{m}$ when the microphone is biased by a 20V DC voltage.

The idea of a 1-D basin of attraction can be further applied to find the critical pull-in voltage. Shown in Figure 5-2 is a plot of the ND mechanical force versus ND net electrostatic forces for different DC voltages (20V, 30V and 41V). As the DC voltage increases, the ND net electrostatic force grows, and the 1-D basin of attraction of the

center equilibrium point shrinks quickly. At a critical pull-in voltage, the 1-D basin of attraction of the center equilibrium point is totally lost, which means no stable region exists and the diaphragm is attracted by the ND net electrostatic force to either of backplates.

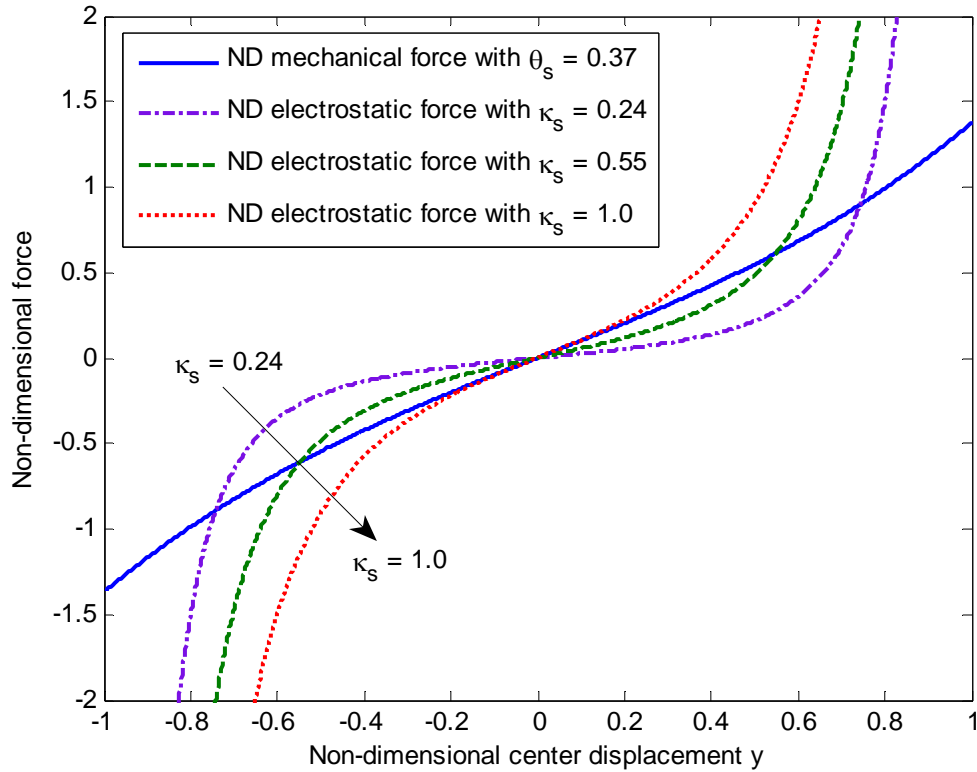


Figure 5-2. Plot of the ND mechanical and net electrostatic forces. For these calculations, $\theta_s = 0.37$ and κ_s has values of 0.24, 0.55 and 1.0.

The largest eigenvalue of the Jacobian matrix in Eq. (5.11) goes to zero at $y = 0$ because the system is neutrally stable when the critical pull-in voltage is reached. From Eq. (5.11), we have

$$J|_{y=0} = \kappa_s - 1 = 0. \quad (5.15)$$

Substituting Eq. (5.6) into Eq. (5.15), finally the critical quasi-static pull-in voltage

$(V_b)_{SPI}$ is

$$(V_b)_{SPI} = \sqrt{\frac{k_1 d_0^3}{2\epsilon A_{me}}} \approx 41 \text{ V}. \quad (5.16)$$

As we can see from Eq. (5.16), the critical quasi-static pull-in voltage is only determined by the air gap, the equivalent linear stiffness and lumped area of the diaphragm respectively. Further calculations show that the critical quasi-static pull-in voltage in Eq. (5.16) is approximately 30% higher than that of a corresponding single-backplate condenser microphone [3]. For the quasi-static pull-in of the single-backplate and dual-backplate condenser microphones, another distinction is that it occurs at 2/3 of the gap for a single-backplate microphone while at the rest position for a dual-backplate microphone [3].

As seen from Figure 2-10, for the quasi-static pull-in of a single-backplate microphone, when the applied DC voltage reaches the critical pull-in voltage, the equilibrium center displacement of the diaphragm is 1/3 of the gap. At this equilibrium point, any small perturbation of the center displacement leads to pull-in since the electrostatic force is larger than the mechanical restoring force and can not be balanced. For a dual-backplate microphone, as shown in Figure 5-2, the equilibrium center displacement of the diaphragm is located at its rest position when a critical pull-in voltage is applied. Similarly, any small displacement perturbation around the equilibrium point leads to pull-in since the electrostatic force is larger than the mechanical restoring force and can not be balanced.

Quasi-Static Pull-in by a Subcritical Pitchfork Bifurcation

Bifurcation diagrams provide a succinct representation of the changes in the equilibrium solutions as a single control parameter is varied in a quasi-static manner. Here, we investigate the quantitative change of equilibrium solutions for Eq. (5.3) as the

applied DC voltage is varied. To this end, we fix the non-dimensional mechanical force parameter θ_s and vary the non-dimensional electrostatic force parameter κ_s by changing the applied DC bias value from 1 to 60V. Shown in Figure 5-3 is the plot of a subcritical pitchfork bifurcation illustrating quasi-static pull-in.

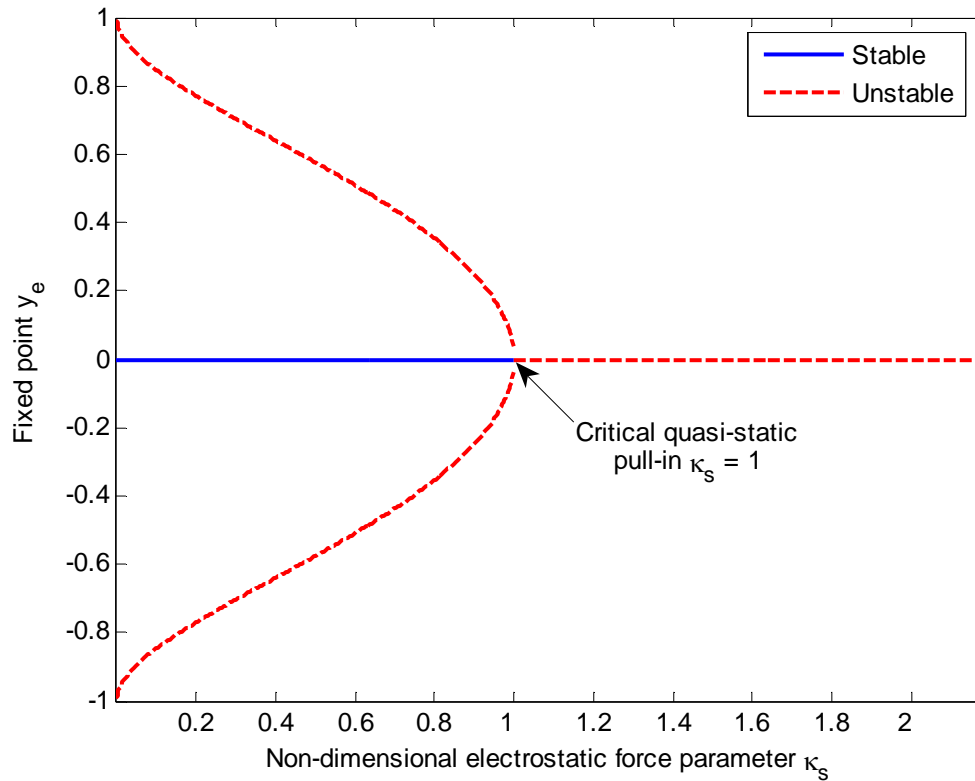


Figure 5-3. A subcritical pitchfork bifurcation illustrating quasi-static pull-in due to an applied DC voltage.

Instead of using the ND electrostatic force parameter κ_s in the bifurcation plot, the DC bias voltage V_b can be used as a bifurcation parameter and the regenerated plot is shown in Figure 5-4. Within the physical border lines ($y = \pm 1$), initially there are three different solution branches: two unstable solution branches (for example, $(y_e)_{2,3} = \pm 0.74$ in Eq. (5.9) when $V_b = 20V$) outside and one stable solution branch between them. As the bifurcation parameter V_b increases, three solution branches converge and finally

evolve into one unstable solution branch. The bifurcation point, at which a bifurcation occurs, is located at $(V_b)_{SPI} = 41V$. Therefore, the critical quasi-static pull-in point is a subcritical pitchfork bifurcation.

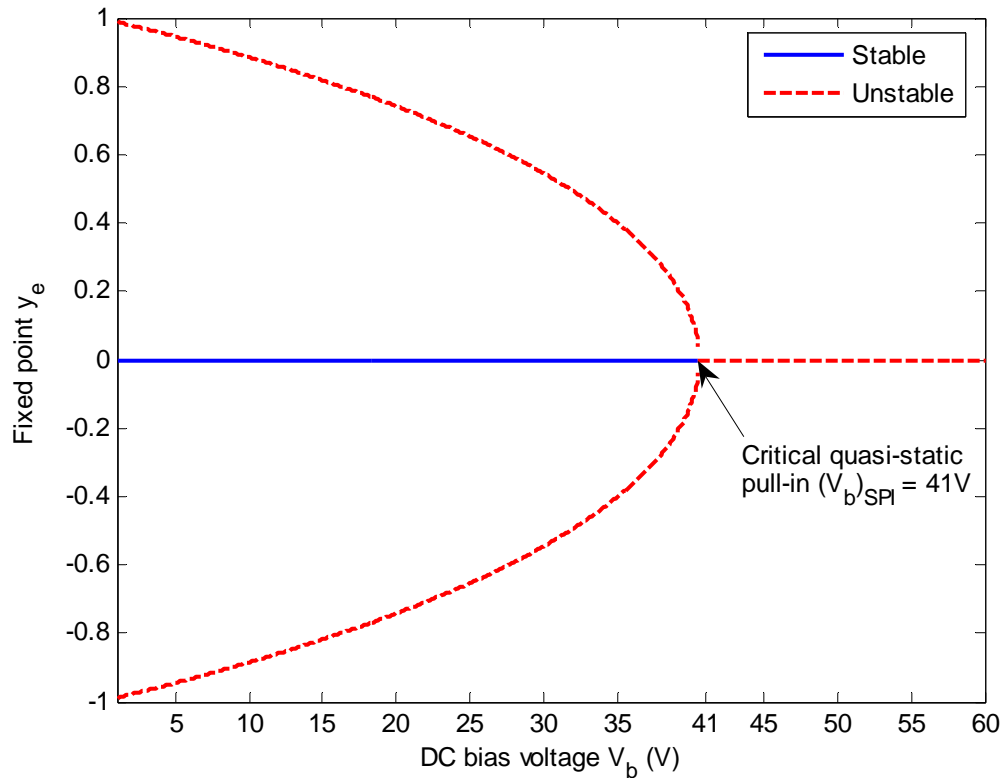


Figure 5-4. A subcritical pitchfork bifurcation illustrating quasi-static pull-in due to an applied DC voltage (versus bias voltages).

Potential Advantage of Geometric Nonlinearity

As shown in Figure 5-5, increasing geometric nonlinearity (k_3 or θ_s) allows designers to relocate saddle nodes at desired positions. This effectively expands the desired 1-D basin of attraction of the stable equilibrium point located at $y = 0$, and hence increases the operational range of the microphone for a given DC voltage below its critical value.

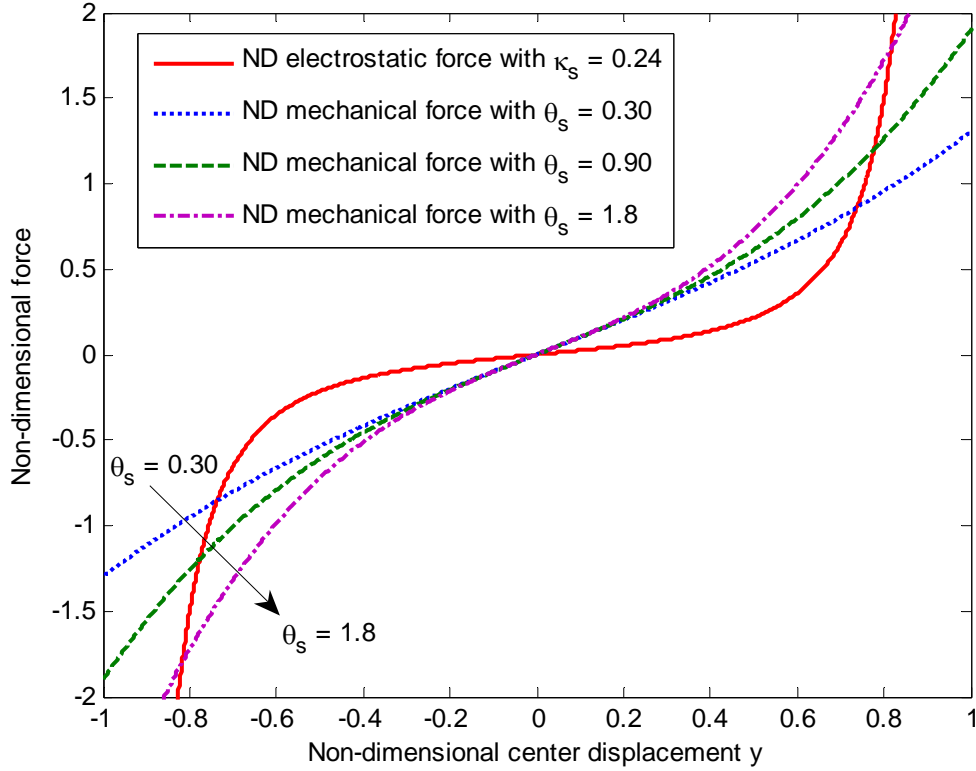


Figure 5-5. Plot of a non-dimensional net electrostatic force and different non-dimensional mechanical forces. For these calculations, $\kappa_s = 0.24$ and θ_s has values of 0.30, 0.90 and 1.8.

To find a scaling relation for the geometric nonlinearity, we need to revisit the expressions of k_1 , k_3 and θ_s . From Eqs. (3.32), (3.33) and Eq. (5.5), we have

$$\theta_s = \frac{k_3 d_0^2}{k_1} \sim \frac{d_0^2}{h^2}, \quad (5.17)$$

where h is the thickness of the diaphragm and d_0 is the gap.

From Eq. (5.17), the quasi-static operational range of the microphone for a given DC voltage below its critical value can be increased by enlarging the gap and/or decreasing the thickness of the diaphragm. Moreover, from Eq. (5.16), the critical quasi-static pull-in voltage increases as the gap becomes larger, which physically makes sense and is desired to further stabilize the microphone.

From the microphone performance perspective, the sensitivity can be increased by decreasing the thickness of the diaphragm while keeping other parameters fixed. However, the dynamic range and linearity of the microphone are affected unfavorably by the addition of geometric nonlinearity as shown in Figure 5-5.

Compact Quasi-Static Stable Operation Range

To better understand the relations between the quasi-static stable operation range and two nonlinearities, a general compact 3D plot is created by using the solutions of Eq. (5.7) for different values of θ_s and κ_s . Shown in Figure 5-6 is a stable range of the diaphragm versus θ_s and κ_s in a 3D space.

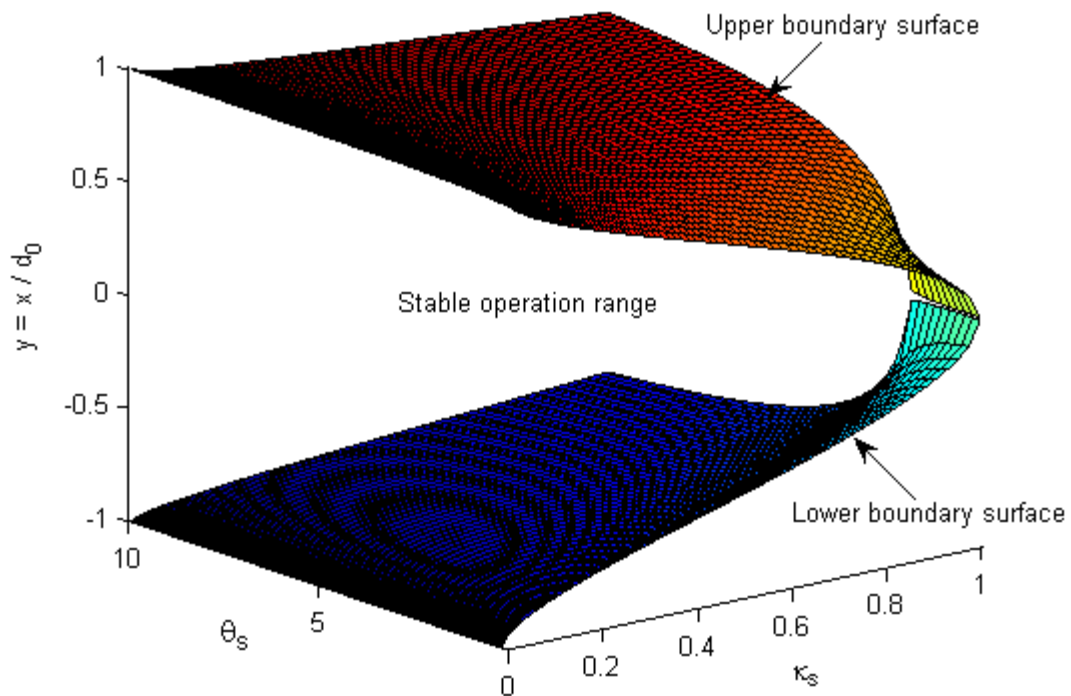


Figure 5-6. Quasi-static stable operation range of the microphone in a 3D space.

In Figure 5-6, the upper boundary surface consists of all positive unstable equilibrium points for given values of θ_s and κ_s (for example, node 2 in Figure 5-1 when $\theta_s = 0.37$ and $\kappa_s = 0.24$), and the lower boundary surface consists of all negative

unstable equilibrium points (for example, node 3 in Figure 5-1 when $\theta_s = 0.37$ and $\kappa_s = 0.24$). Hence, the volume defined by the physical limits of three axes as well as the upper and lower boundary surfaces represents a quasi-static stable operation range of the microphone in a 3D space.

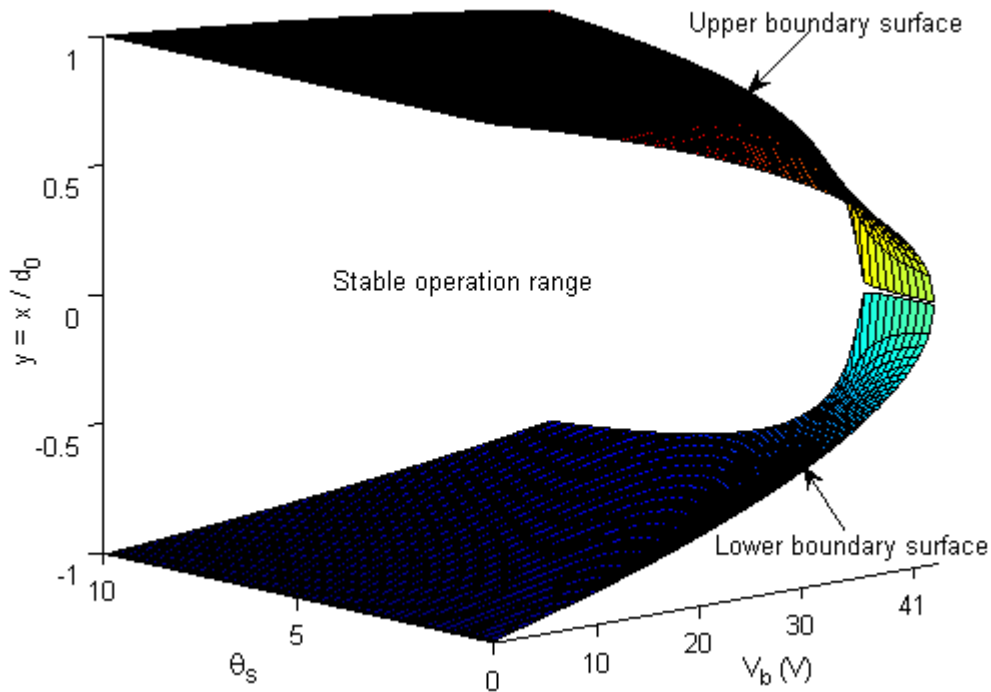


Figure 5-7. Quasi-static stable operation range of the microphone in a 3D space (versus DC voltages).

Instead of using the ND electrostatic force parameter κ_s in the 3D plot, the DC bias voltage V_b can be used and the regenerated plot is shown in Figure 5-7. From the plot, if the value of θ_s is fixed, as the DC bias voltage increases, the corresponding stable operation range becomes smaller. When a critical pull-in voltage is reached, the operation range shrinks to zero. However, for a fixed value of DC bias voltage, as the parameter θ_s increases, the stable operation range becomes larger. Again, the addition of geometric nonlinearity helps stabilize the system while an increased DC bias voltage or

electrostatic nonlinearity destabilizes the system. The stable operation range plots shown in Figure 5-6 and Figure 5-7 also provide a possible tool to choose design parameters, such as the DC bias voltage, physical dimensions of the diaphragm and gap distance, for a desired operation range of the microphone. However, it should be pointed out that the dynamic range and linearity of the microphone are affected unfavorably by the addition of mechanical geometric nonlinearity.

Quasi-Static Pull-in due to an Applied Acoustical Pressure

In this section, quasi-static pull-in due to an applied static acoustic pressure is studied. The model for the analysis is shown in Figure 4-13. To study the quasi-static pull-in due to an applied acoustical pressure, the applied DC voltage is kept lower than the critical quasi-static pull-in voltage derived in the previous section, and the applied pressure difference on the diaphragm is assumed to be time-independent ($p(t) = p_0$).

Since all the time derivatives go to zero in the quasi-static process, based on the general nonlinear governing equation in Eq. (3.53) of Chapter 3, finally the corresponding governing equation for the static response is given by

$$k_1x + k_3x^3 - p_0A_{me} = -\frac{\varepsilon A_{me}}{2} \left[\frac{V_b^2}{(d_0 + x)^2} - \frac{V_b^2}{(d_0 - x)^2} \right]. \quad (5.18)$$

With the rearrangement of the net electrostatic force, the governing equation in Eq. (5.1) can be further changed into

$$k_1x + k_3x^3 - p_0A_{me} = 2\varepsilon A_{me} d_0 V_b^2 \frac{x}{(d_0^2 - x^2)^2}. \quad (5.19)$$

The above static equation is non-dimensionalized by using the non-dimensional displacement y ($y = x/d_0$)

$$f(y) = \kappa_s \frac{y}{(1-y^2)^2} - y - \theta_s y^3 + P_s = 0, \quad (5.20)$$

where $f(y)$ is a nonlinear function of y and represents a net non-dimensional force applied on the diaphragm. The parameter P_s represents the non-dimensional force induced by the acoustical pressure and is defined as

$$P_s = \frac{P_0 A_{me}}{k_1 d_0}. \quad (5.21)$$

The other non-dimensional parameters in Eq. (5.20) are defined in Eqs. (5.5) and (5.6), respectively. To further investigate the stability of Eq. (5.20), similarly we need to find equilibrium points of the governing equation and study their local stabilities.

Equilibrium Points and Local Stabilities

The equilibrium points of the system can be obtained by finding the roots of Eq. (5.20). Physically, at equilibrium points, the net restoring force (the difference between the nonlinear mechanical spring force and the force caused by the pressure) equals the net electrostatic force. Therefore, the equilibrium points y_e satisfy the following nonlinear equation

$$\kappa_s \frac{y_e}{(1-y_e^2)^2} - y_e - \theta_s y_e^3 + P_s = 0. \quad (5.22)$$

The above nonlinear equation can be rewritten as

$$\theta_s y_e^3 (1-y_e^2)^2 + y_e (1-y_e^2)^2 - P_s (1-y_e^2)^2 - \kappa_s y_e = 0 \quad (5.23)$$

or

$$\theta_s y_e^7 + (1-2\theta_s) y_e^5 - P_s y_e^4 + (\theta_s - 2) y_e^3 + 2P_s y_e^2 + (1-\kappa_s) y_e - P_s = 0. \quad (5.24)$$

Eq. (5.24) basically is a general seventh order equation and there is no analytical solution. To proceed with the analysis, a numerical approach is employed to find the roots of the above equation.

In order to carry out the numerical analysis, some values for the non-dimensional parameters are required. To be consistent with we did in the previous section and also for illustration purposes, a DC voltage of 20V is chosen here. Therefore, the corresponding non-dimensional parameters θ_s and κ_s are given in Table 5-1 for the designed 2000Pa MEMS microphone. Also for illustration purposes, a pressure difference of 1000Pa is chosen and the corresponding non-dimensional parameter P_s is calculated to be $P_s = 0.14$.

After substituting the values of θ_s , κ_s and P_s into Eq. (5.24), five real solutions and two complex conjugate roots are finally obtained via the *roots* command (computes the roots of a polynomial) in MATLAB. The two complex conjugate roots are not physical and neglected in the following analysis. The final five corresponding equilibrium points are given as

$$(y_e)_1 = 0.18, \quad (5.25)$$

$$(y_e)_2 = 0.71, \quad (5.26)$$

$$(y_e)_3 = -0.76, \quad (5.27)$$

$$(y_e)_4 = 1.19, \quad (5.28)$$

and

$$(y_e)_5 = -1.18. \quad (5.29)$$

The negative sign in above equations means the diaphragm moves towards the top backplate while the positive sign means the diaphragm moves towards the bottom backplate. The above equilibrium points are non-symmetric around the rest position due to the pressure loading.

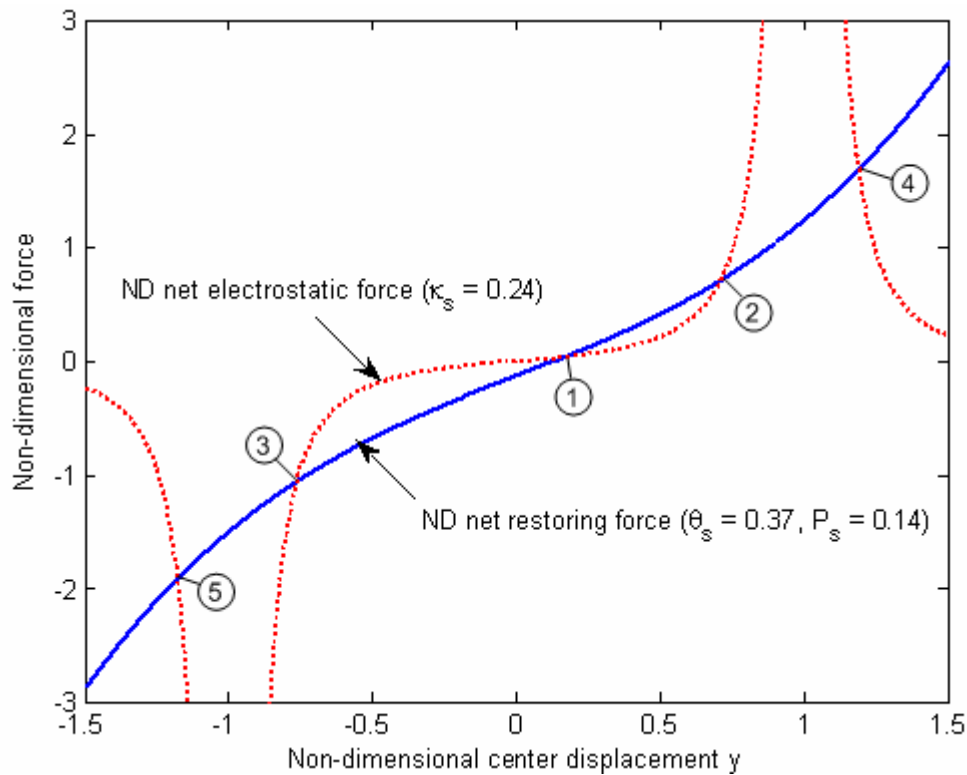


Figure 5-8. Plot of the ND net restoring and electrostatic forces with $\theta_s = 0.37$, $P_s = 0.14$ and $\kappa_s = 0.24$.

The local stabilities of equilibrium points are studied by examining the two non-dimensional (ND) nonlinear forces graphically. Figure 5-8 shows a plot of the ND net restoring and electrostatic forces for an applied pressure difference of 1000Pa and an applied DC voltage of 20V. Again, the border lines are located at $y = \pm 1$, which correspond to two physical backplates.

From Figure 5-8, the five possible equilibrium points are: 1) a locally stable point attractor (node 1) at $y = 0.18$; 2) two unstable saddle nodes (nodes 2 and 3), situated at

$y = 0.71$ and $y = -0.76$; and 3) two locally stable point attractors (nodes 4 and 5), located at $y = 1.19$ and $y = -1.18$. In the region between unstable saddle nodes 2 and 3, the ND net restoring force is always greater than the ND net electrostatic force; therefore, the system is always quasi-statically stable. The region between unstable saddle nodes 2 and 3 is called the 1-D basin of attraction of the equilibrium point located at $y = 0.18$. In the regions outside the border lines, the system is stable only mathematically. In the following analysis, these non-physical regions will be discarded.

Critical Quasi-Static Pull-in Pressure

From the previous analysis, the quasi-statically stable operation range of the microphone is defined by the 1-D basin of attraction between nodes 2 and 3. Further analysis shows that the stable operational range depends on the applied pressure for a given DC voltage. The idea of a 1-D basin of attraction can be further applied to find the critical pull-in pressure when the applied DC voltage is fixed. Shown in Figure 5-9 is a plot of different ND net restoring forces for different pressure values: 1000Pa, 2000Pa and 2464Pa ($P_s = 0.14, 0.27$ and 0.34). The parameter $\theta_s = 0.37$ is used to calculate the ND net restoring forces. Also, a ND net electrostatic force is plotted in Figure 5-9 for an applied DC voltage of 20V ($\kappa_s = 0.24$).

In Figure 5-9, as the value of P_s increases, the ND net restoring force decreases, and the stable region between nodes 1 and 2 shrinks accordingly. At a critical pull-in pressure point, nodes 1 and 2 merge together and the stable region between is totally lost, which means the diaphragm will be attracted by the net electrostatic force to the bottom backplate at $y = 1$. After numerical iterations, for an applied DC voltage of 20V, the

critical value of P_s is found to be $P_s = 0.34$, which corresponds to a critical pull-in pressure of 2464Pa.

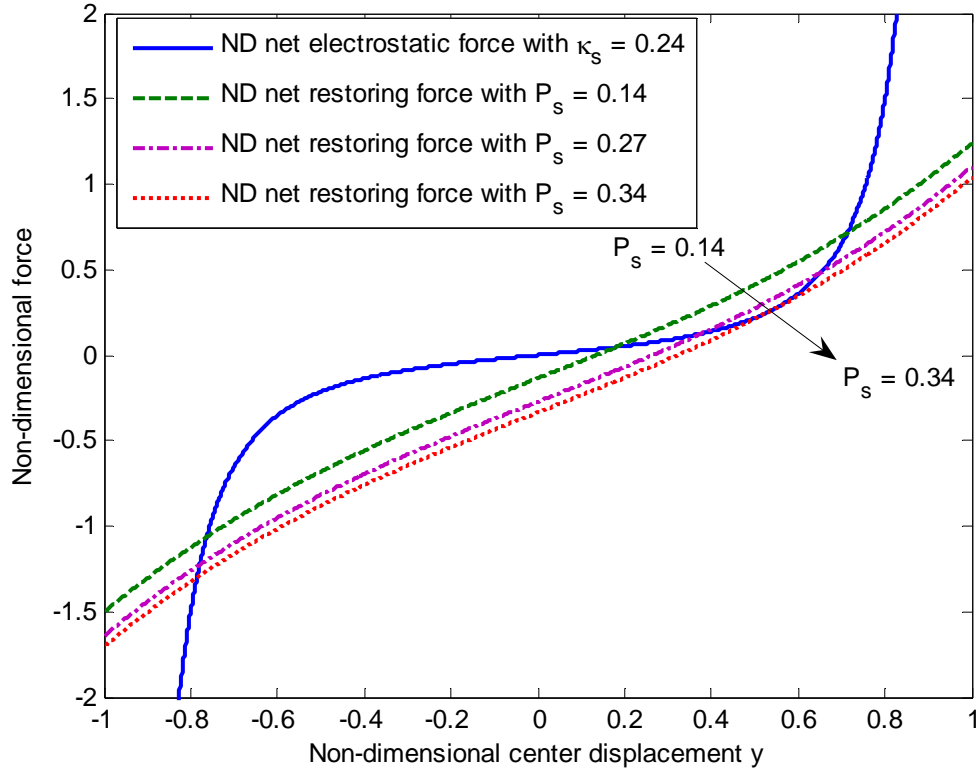


Figure 5-9. Plot of the ND net restoring and electrostatic forces. For these calculations, $\theta_s = 0.37$, $\kappa_s = 0.24$ and P_s has values of 0.14, 0.27 and 0.34.

Since the net electrostatic force is symmetric around the center point at $y=0$, further analysis shows that quasi-static pull-in occurs at the top backplate (at $y=-1$) when a critical negative pressure value of -2464Pa is reached. In summary, with $V_b = 20V$, the microphone system is quasi-statically stable when

$$|P_s| < P_{SPI} = 0.34, \quad (5.30)$$

or

$$|p_0| < (p_0)_{SPI} = 2464Pa, \quad (5.31)$$

where P_{SPI} or $(p_0)_{SPI}$ is the critical quasi-static pull-in parameter at $V_b = 20V$.

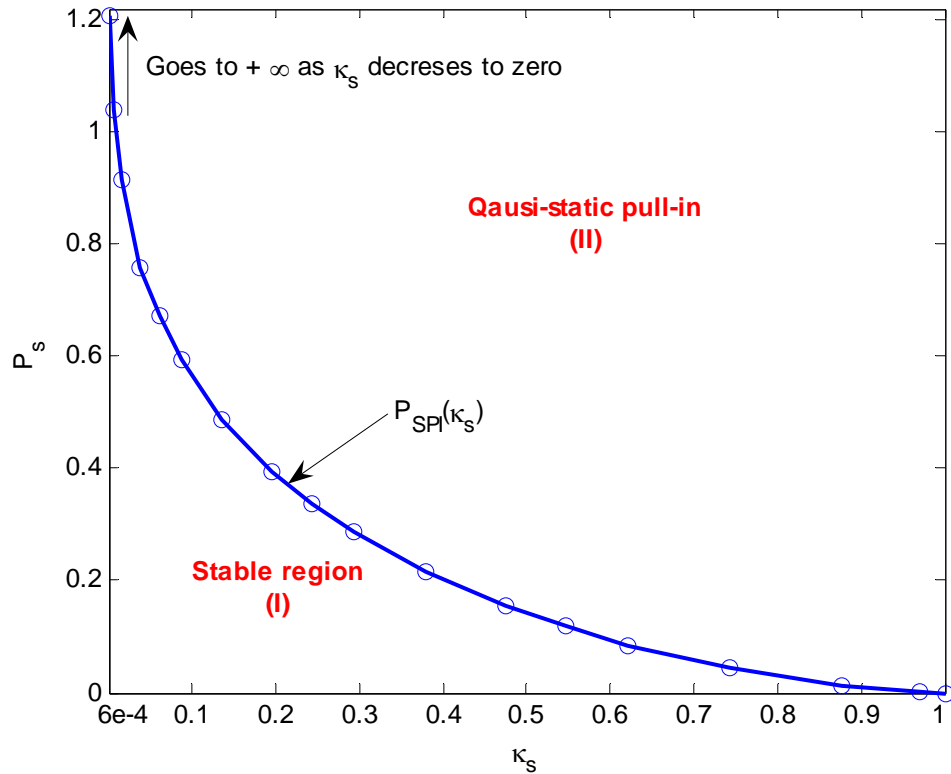


Figure 5-10. Quasi-static pull-in due to varying ND parameters κ_s and P_s .

The above pull-in analysis has been carried out for a single value of the ND electrostatic force parameter κ_s . For other values of κ_s , similar numerical analyses can be carried out. The result for quasi-static pull-in due to varying ND parameters κ_s and P_s is shown in Figure 5-10. As the ND parameter κ_s increases, the critical value of the ND parameter P_s decreases. When the ND parameter κ_s is less than its critical value of $\kappa_s = 1.0$ and the ND parameter P_s is less than its corresponding critical value of P_{SPI} , the system stays stable; otherwise, quasi-static pull-in occurs. Therefore, a stable region (I) and an unstable region (II) are formed in the $P_s - \kappa_s$ plane. Physically, the ND parameters κ_s and P_s both destabilize the system. It should be pointed out that κ_s in the plot of Figure 5-10 only has the value ranging from $6e-4$ ($V_b = 1V$) to 1.0 . As the κ_s

further decreases to zero ($V_b = 0$), the required pressure goes to infinity. Physically, when $V_b = 0$, no pull-in occurs.

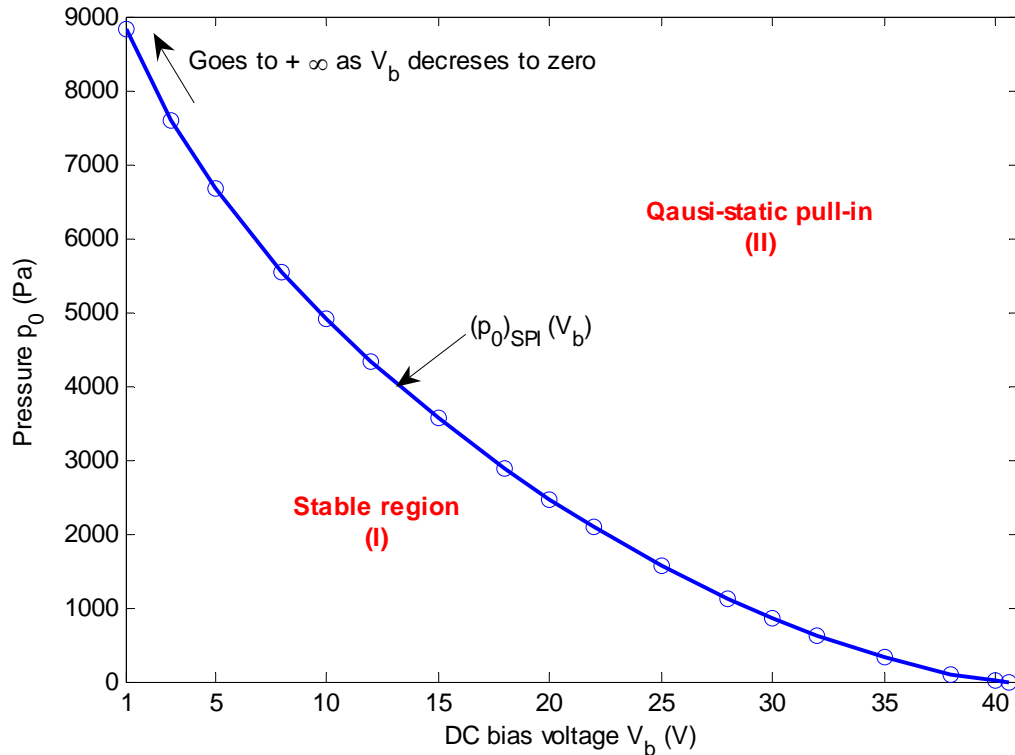


Figure 5-11. Quasi-static pull-in due to varying acoustic pressure and DC bias voltage.

Instead of using the non-dimensional parameters κ_s and P_s in Figure 5-10, the physical DC bias voltage V_b and acoustic pressure p_0 can be used. Based on Table 5-1, the regenerated plot is shown in Figure 5-11. As the DC bias voltage increases, the critical pull-in pressure value decreases, which means less pressure is required to cause quasi-static pull-in. When the DC bias voltage is less than its critical value of $(V_b)_{SPI} = 41V$ and the acoustic pressure amplitude is less than its corresponding critical value of $(p_0)_{SPI}$, the system stays stable; otherwise, quasi-static pull-in occurs. As the DC bias voltage is over $(V_b)_{SPI} = 41V$, no acoustic pressure is required to cause quasi-static pull-in. Figure 5-11 also shows that quasi-static pull-in can potentially take place

below $(V_b)_{SPI} = 41V$ due to the addition of large acoustic pressure. Again, as the applied DC bias voltage further decreases to zero ($V_b = 0$), the required pressure goes to infinity. Physically, when $V_b = 0$, no pull-in occurs.

Dynamic Pull-in due to a Mechanical Shock Load

Although previous quasi-static pull-in analyses provide a good understanding of a stable operation range of a dual-backplate capacitive microphone, it is based on static analysis and does not account for dynamic effects, such as shock (mechanical or acoustical) loads or an AC voltage excitation with a frequency close to the first resonant frequency of the microphone. Since dynamic pull-in can dangerously take place below the quasi-static pull-in voltage due to the complex interaction of nonlinearities, the study of dynamic effects on the pull-in limit is becoming important for many electrostatically actuated MEMS devices. Previous studies [13, 90-92, 95] addressed some aspects of dynamic pull-in instability due to an AC voltage excitation. Mechanical or acoustical shocks could potentially occur during the fabrication, employment and operation of MEMS devices including microphones [110-112]. In addition, for the success of commercialization of MEMS devices, evaluation of reliability needs to be conducted in various test environments (pressure, mechanical shock, temperature, humidity, etc.) [112]. Therefore, it is necessary to investigate the effect of shock loads on the dynamic pull-in instability of the microphone.

Dynamic pull-in due to an acoustical shock load, specifically in the form of an N-wave, is presented in the next section. In this section, dynamic pull-in due to a mechanical shock load is studied for the microphone. First, the dynamic pull-in problem is formulated. The basins of attraction for the microphone are then obtained using

numerical simulation. Finally, the basins of attraction are utilized to map the state of the system immediately after the mechanical shock load to dynamic pull-in.

Problem Formulation

A mechanical shock load, such as shock loads generated by drop tests on a hard surface, is usually specified by the acceleration (for example, 1000g or 10000g) [112]. For modeling and analysis purposes in this section, the acceleration generated by the mechanical shock load is converted into an equivalent pressure $p_m(t)$, which is defined as

$$p_m(t) = \frac{ma_g(t)}{A}, \quad (5.32)$$

where $a_g(t)$ is the acceleration of the mechanical shock load, m is the mass of the diaphragm and A is the area of the diaphragm. In the following analysis, only the equivalent pressure $p_m(t)$ is used. The corresponding acceleration can be obtained by $a_g(t) = [Ap_m(t)]/m$.

During the analysis of dynamic pull-in due to a mechanical shock load, it is assumed that no AC voltage excitations exist between the diaphragm and backplates. Based on the general nonlinear governing equation in Eq. (3.53) of Chapter 3, we can derive the governing equation of dynamic pull-in due to a mechanical shock load as follows

$$M_{me}\ddot{x} + b\dot{x} + (k_1 + k_c)x + k_3x^3 = -\frac{\varepsilon A_{me}}{2} \left[\frac{V_b^2}{(d_0 + x)^2} - \frac{V_b^2}{(d_0 - x)^2} \right] + p_m(t)A_{me}. \quad (5.33)$$

It is convenient to study the non-dimensional form of Eq. (5.33) by introducing the non-dimensional center displacement and time

$$y = \frac{x}{d_0}, \quad (5.34)$$

and

$$\tau = \omega_0 t. \quad (5.35)$$

Eq. (5.33) can be rewritten as

$$y'' + 2\zeta y' + y + \theta_d y^3 - \kappa_d \frac{y}{(1-y^2)^2} = \frac{\Gamma}{\omega_0^2 d_0} p_m(\tau), \quad (5.36)$$

where y' and y'' are the first and second derivatives of the non-dimensional center displacement with respect to the non-dimensional time τ respectively. The non-dimensional force parameters are

$$\theta_d = \frac{k_3 d_0^2}{k_1 + k_c}, \quad (5.37)$$

and

$$\kappa_d = \frac{2\varepsilon A_{me} V_b^2}{(k_1 + k_c) d_0^3}. \quad (5.38)$$

The other parameters in Eq. (5.36) have already been defined in Eqs (4.3)-(4.5). Notice that the stiffness of the cavity k_c is included in the non-dimensional force parameters θ_d and κ_d since the dynamic process is considered in this section.

As seen from Eq. (5.36), the mechanical shock load serves as an external excitation for the nonlinear system. Since there is no closed-form solution to Eq. (5.36), we need to find some assumptions to simplify the study. First, it is assumed that a mechanical shock load has a very short duration time of δt starting at $t=0$. Eq. (5.36) can be then simplified into

$$y'' + 2\zeta y' + y + \theta_d y^3 - \kappa_d \frac{y}{(1-y^2)^2} = \begin{cases} P(\tau), & \text{for } 0 \leq \tau \leq \tau_0, \\ 0, & \text{for } \tau > \tau_0 \end{cases}, \quad (5.39)$$

where the non-dimensional force generated by the pressure is

$$P(\tau) = \frac{\Gamma}{\omega_0^2 d_0} p_m(\tau), \quad (5.40)$$

and the non-dimensional duration time is

$$\tau_0 = \omega_0 \delta t. \quad (5.41)$$

By assuming $\tau_0 = \omega_0 \delta t \ll 1$, based on the concept of convolution integral [113, 114], the original problem in Eq. (5.36) can be further simplified as a following equation subject to an initial non-dimensional velocity v_0 imposed by the mechanical shock load,

$$y'' + 2\zeta y' + y + \theta_d y^3 - \kappa_d \frac{y}{(1-y^2)^2} = 0. \quad (5.42)$$

The total momentum M_0 generated by the mechanical shock load is

$$M_0 = A_{me} \int_0^{\delta t} p_m(t) dt = A_{me} A_p, \quad (5.43)$$

where $A_p \triangleq \int_0^{\delta t} p_m(t) dt$ is defined as a characteristic parameter of the mechanical shock load. Physically it represents the area under any arbitrary mechanical shock signal and its unit is $Pa \cdot s$. From Eq. (5.39), the initial non-dimensional velocity v_0 is obtained as follows

$$v_0 = \frac{M_0}{M_{me} \omega_0 d_0} = \frac{A_{me} \int_0^{\delta t} p_m(t) dt}{M_{me} \omega_0 d_0} \triangleq \frac{A_{me} A_p}{M_{me} \omega_0 d_0}. \quad (5.44)$$

An actual mechanical shock load, such as shock loads generated by drop tests on a hard surface, has an irregular shape [112]. For modeling and analysis purposes, the

actual mechanical shock load is approximated by a simpler shaped signal, characterized by an amplitude of p_0 and a very short duration time of δt .

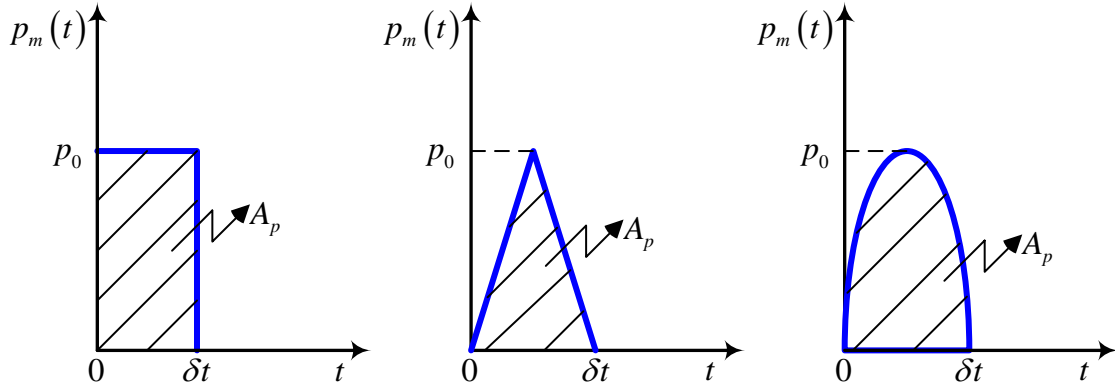


Figure 5-12. Three commonly used nonlinear mechanical shock load models (impulse, half sine and triangle).

Shown in Figure 5-12 are three commonly used nonlinear shock load models (impulse, half sine and triangle signals) [115]. For an impulse shock load with an amplitude of p_0 and a duration time of δt , the characteristic parameter becomes $A_p = p_0 \delta t$. For a half sinusoidal shock load, the characteristic parameter becomes $A_p = \frac{2p_0 \delta t}{\pi}$. Finally the characteristic parameter for a mechanical triangular shock load is $A_p = \frac{p_0 \delta t}{2}$.

After the initial non-dimensional velocity is obtained, we proceed to study Eq. (5.42). Eq. (5.42) can be further rewritten in the state-space form as follows

$$\begin{cases} y_1' = y_2 \\ y_2' = -2\zeta y_2 - y_1 - \theta_d y_1^3 + \kappa_d \frac{y_1}{(1 - y_1^2)^2}, \end{cases} \quad (5.45)$$

where $y_1 = y$ and $y_2 = y'$ are the non-dimensional center displacement and velocity respectively. To investigate the dynamics of the above nonlinear system, we first need to find equilibrium points of the governing equation and study their local stabilities.

Equilibrium Points and Local Stabilities

The equilibrium points of Eq. (5.45) can be obtained by setting $y_1' = 0$ and $y_2' = 0$.

Namely, the equilibrium points $\bar{y}^* = \begin{pmatrix} y_1^* \\ y_2^* \end{pmatrix} = \begin{pmatrix} y_1^* \\ 0 \end{pmatrix}$ satisfy the following nonlinear equation

$$\kappa \frac{y_1^*}{(1 - y_1^{*2})^2} - y_1^* - \theta_d y_1^{*3} = 0. \quad (5.46)$$

Eq. (5.46) has a same function form of Eq. (5.7). Similarly, to solve Eq. (5.46), some values of the non-dimensional parameters are required. By using the physical parameters in Table 3-1 for the designed 2000Pa MEMS microphone and an applied DC voltage of 25V (this DC bias value is chosen here just for the illustration purpose), finally five real solutions to Eq. (5.46) are obtained as follows

$$(y_1^*)_1 = 0, \quad (5.47)$$

$$(y_1^*)_{2,3} = \pm 0.68, \quad (5.48)$$

and

$$(y_1^*)_{4,5} = \pm 1.22. \quad (5.49)$$

To study the local stability of each equilibrium point, we need to find the Jacobian matrix of Eq. (5.45), which is finally calculated to be

$$J = \begin{bmatrix} 0 & 1 \\ \frac{3\theta_d y_1^8 + (1-9\theta_d)y_1^6 + (9\theta_d-3)y_1^4 + (3+3\kappa_d-3\theta_d)y_1^2 + (\kappa_d-1)}{(1-y_1^2)^3} & -2\zeta \end{bmatrix}. \quad (5.50)$$

Evaluating the Jacobian matrix at each equilibrium point defined from Eqs. (5.47) to (5.49) yields

$$J_1 = \begin{bmatrix} 0 & 1 \\ -0.661 & -0.162 \end{bmatrix}, \quad (5.51)$$

$$J_{2,3} = \begin{bmatrix} 0 & 1 \\ 3.59 & -0.162 \end{bmatrix}, \quad (5.52)$$

and

$$J_{4,5} = \begin{bmatrix} 0 & 1 \\ -19.5 & -0.162 \end{bmatrix}. \quad (5.53)$$

The eigenvalues of the above matrices are

$$Eig_{J_1} = \begin{pmatrix} -0.081 + 0.081i \\ -0.081 - 0.081i \end{pmatrix}, \quad (5.54)$$

$$Eig_{J_{2,3}} = \begin{pmatrix} 1.81 \\ -1.98 \end{pmatrix}, \quad (5.55)$$

and

$$Eig_{J_{4,5}} = \begin{pmatrix} -0.081 + 4.41i \\ -0.081 - 4.41i \end{pmatrix}. \quad (5.56)$$

Based on the eigenvalues of each matrix, the first equilibrium point is a locally stable sink point. The second and third equilibrium points are locally unstable saddle points, and the fourth and fifth equilibrium points are locally stable sink points.

Phase Portrait and Basins of Attraction

Based on the local stabilities of all equilibrium points, we can generate a phase plot of Eq. (5.45) for a DC bias voltage of 25V. The phase plane trajectories for different initial conditions are generated by using the *streamslice* command in MATLAB.

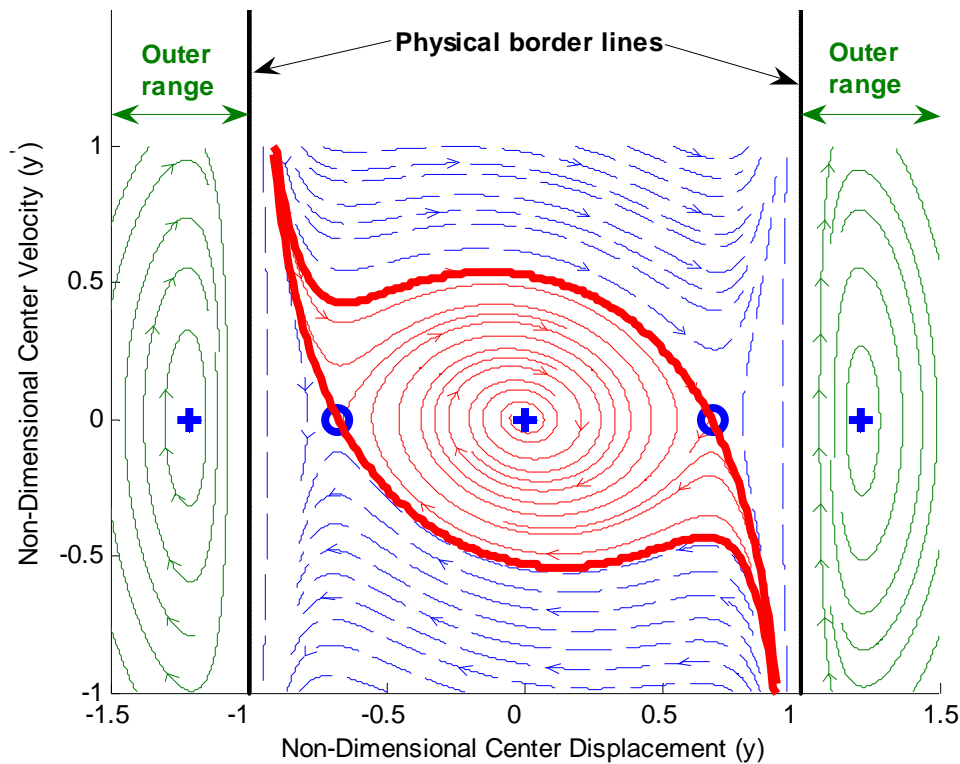


Figure 5-13. Phase plane trajectories around the equilibrium points for a DC bias $V_b = 25V$ (sink points are indicated by blue crosses, and saddle points are indicated by blue circles).

The phase portrait in Figure 5-13 consists of three basins of attraction, illustrating that nonlinearities cause a sensitivity to initial conditions and co-existence of multiple solutions. The five possible equilibrium solutions to Eq. (5.42) or (5.45) are: 1) a stable equilibrium point at the rest position ($y = 0$) of the diaphragm, that attracts the motions starting from the initial conditions within the physical boundaries; 2) two saddle nodes, situated at $y = \pm 0.68$, that limit the amplitude of initial conditions by repelling motions

either toward the desirable rest position or towards pull-in at the physical border lines (top and bottom backplates); and 3) two non-physical stable equilibrium points, located outside the physical border lines ($y = \pm 1.22$), that attract the motions from the relatively larger amplitude initial conditions. The three corresponding basins of attraction are shown in Figure 5-14.

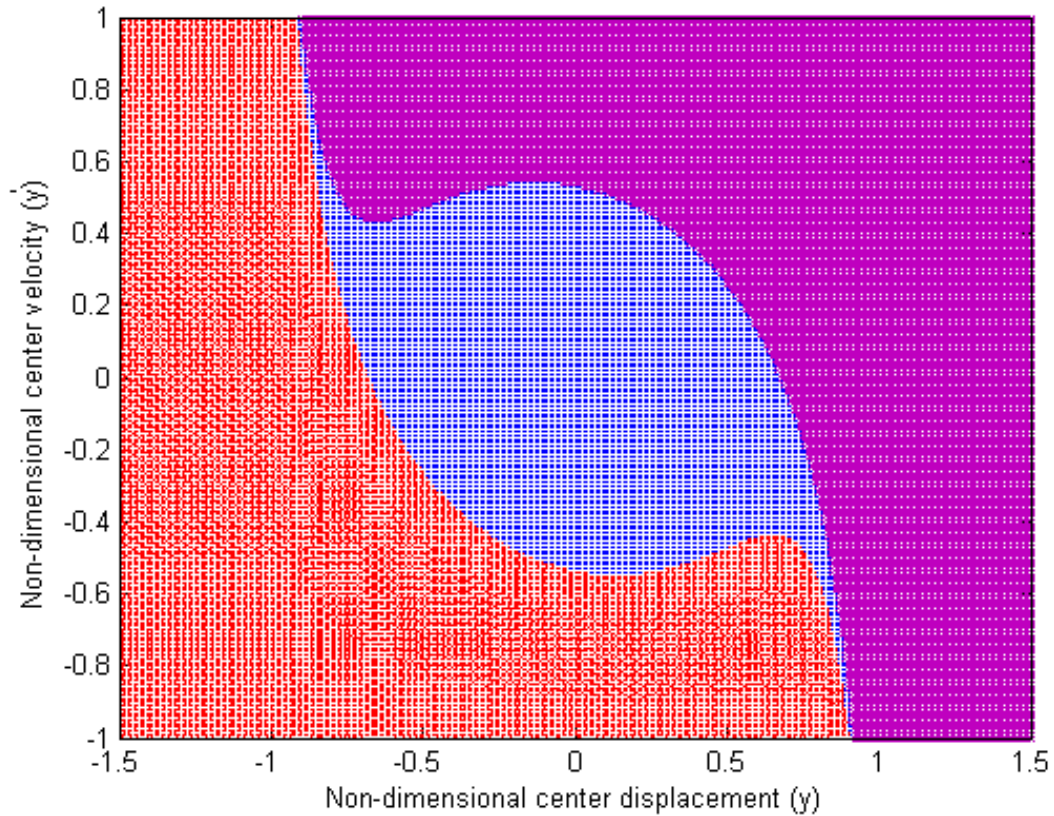


Figure 5-14. Three basins of attraction for a DC bias $V_b = 25V$.

To generate the basins of attraction, numerical simulations are carried out. First, we start by simulating Eq. (5.45) for a grid of initial conditions (non-dimensional velocity and displacement), then we record both the initial condition and the final states. After the overnight simulation is finished, the initial conditions with final states close to the rest position ($y=0$) are plotted together to form a basin of attraction. Those initial conditions with final states close to the other two stable attractors ($y = \pm 1.22$) are plotted

to form other two basins of attraction respectively. Shown in Figure 5-14 is the plot of all three basins of attraction for a DC bias voltage of $25V$. The blue shaded region corresponds to the basin of attraction for the attractor at $y=0$. The red shaded region corresponds to the basin of attraction for the attractor located at $y=-1.22$. Finally, for the attractor located at $y=1.22$, its basin of attraction is shaded by a magenta color.

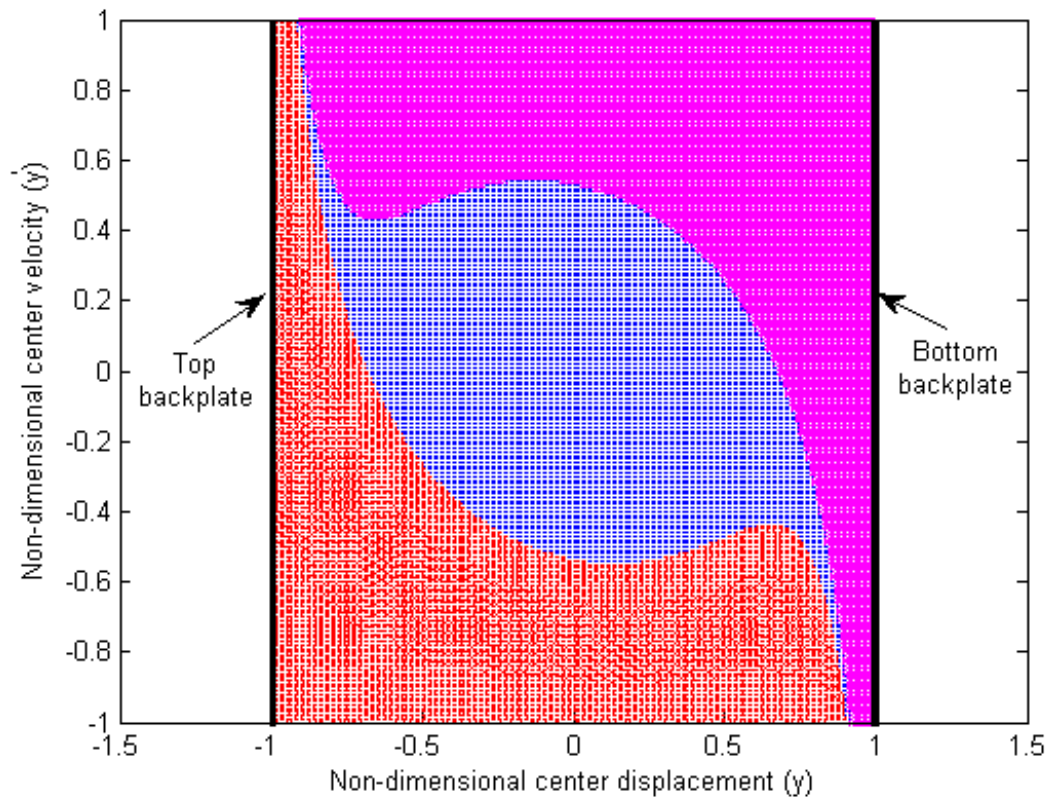


Figure 5-15. Basins of attraction within the physical backplates for a DC bias $V_b = 25V$.

As mentioned earlier, the motion of the diaphragm in a physical microphone device is constrained by backplates. Physically, the two special lines at $y = \pm 1$ in Figure 5-14 represent boundaries imposed by backplates. Mathematically, they cause singularities to the governing equation in Eq. (5.33). As seen from Figure 5-14, mathematically any

initial condition starting outside the basin of attraction of the stable attractor at $y = 0$ will be attracted to either $y = -1.22$ or $y = 1.22$.

Now the physical limits imposed by backplates are considered. Shown in Figure 5-15 is a plot of basins of attraction between physical backplates. Physically, due to the constraints imposed by backplates, any initial condition starting outside the basin of attraction of the stable attractor at $y = 0$ will finally stop at either of backplates and dynamic pull-in occurs. Therefore, the basin of attraction of the rest position represents the physical stable operation domain of the microphone.

Dynamic Pull-in due to a Mechanical Shock Load

With the phase portrait in Figure 5-13, we can relate the initial non-dimensional velocity imposed by a mechanical shock load to dynamic pull-in. If the diaphragm is at rest and the initial non-dimensional velocity imposed by a mechanical shock load is outside the physical stable basin of attraction in Figure 5-15, the diaphragm finally goes to one of backplates and dynamic pull-in occurs. Otherwise, the diaphragm finally goes back to its rest position. For example, when the non-dimensional displacement is zero and the applied DC voltage is 25V, the stable range of the non-dimensional velocity from the phase portrait is

$$-0.53 \leq v_0 \leq 0.53. \quad (5.57)$$

In order to verify the above range of the initial non-dimensional velocity is stable, simulations are carried out in MATLAB. Shown in Figure 5-16 are simulated non-dimensional center displacement responses with two initial non-dimensional velocities $v_0 = 0.53$ and 0.54 . As seen from the plot, the system goes unstable when the initial velocity is 0.54 while the system stays stable when the initial velocity is 0.53 .

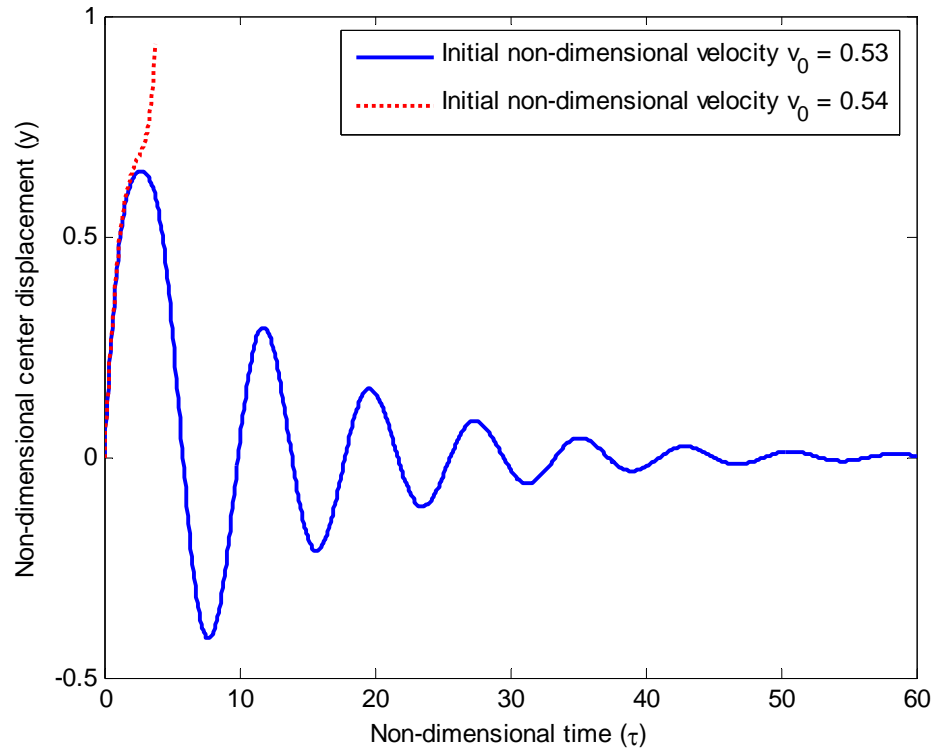


Figure 5-16. Stable and unstable non-dimensional center displacement responses with two initial non-dimensional velocities ($v_0 = 0.53$ and 0.54 , $V_b = 25V$).

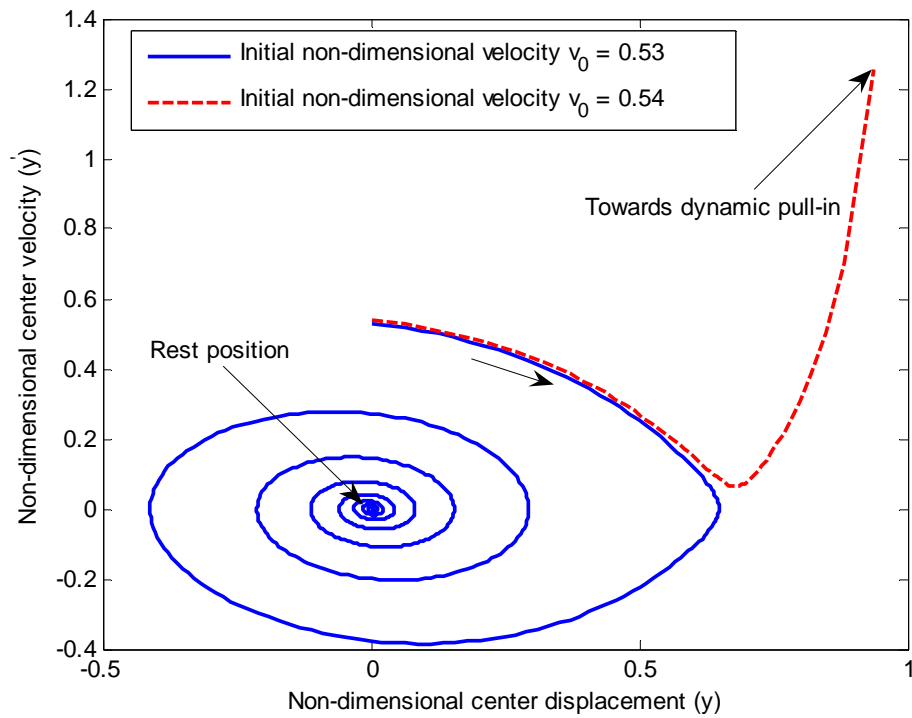


Figure 5-17. Phase plots of a stable response ($v_0 = 0.53$, $V_b = 25V$) and a dynamic pull-in due to a large initial velocity imposed by a mechanical shock load ($v_0 = 0.54$, $V_b = 25V$).

Figure 5-17 shows the corresponding phase plots of simulated stable and unstable responses. As seen from the figure, dynamic pull-in occurs when an initial non-dimensional velocity is $v_0 = 0.54$ and an applied DC voltage is $V_b = 25V$. Please note that due to the singularity at the dynamic pull-in point $y = 1$, the simulation stops a little bit earlier before the dynamic pull-in.

By using the general expression of v_0 in Eq. (5.44), the mechanical shock load can be related to dynamic pull-in as follows

$$-0.53 \leq \frac{A_{me}}{M_{me} \omega_0 d_0} A_p \leq 0.53. \quad (5.58)$$

Substituting the values of the lumped area, lumped mass, and natural frequency of the diaphragm into the above equation, we have

$$-3.72 \times 10^{-3} \leq A_p \leq 3.72 \times 10^{-3} \text{ or } |A_p| \leq A_{pc} = 3.72 \times 10^{-3}, \quad (5.59)$$

where A_{pc} is defined as a critical value of A_p for dynamic pull-in.

Eq. (5.59) shows a relation between dynamic pull-in and a characteristic shock load parameter A_p when an applied DC voltage is 25V. When the absolute value of A_p of a mechanical shock load is greater than its critical value $A_{pc} = 3.72 \times 10^{-3} Pa \cdot s$, dynamic pull-in occurs at 25V; otherwise, the system stays stable and spirals into its rest position. The dynamic pull-in conditions in this case are

$$(V_b)_{DPI} = 25V \text{ if } |A_p| > 3.72 \times 10^{-3}, \quad (5.60)$$

where $(V_b)_{DPI}$ is the critical dynamic pull-in voltage.

Specifically, if the impulse, half sine and triangle signal models are used as mechanical shock loads, the products of the amplitude and duration time of each model are given as follows

$$\text{Impulse signal model: } |p_0\delta t| \leq 3.72 \times 10^{-3}, \quad (5.61)$$

$$\text{Half sine signal model: } |p_0\delta t| \leq 5.84 \times 10^{-3}, \quad (5.62)$$

and

$$\text{Triangle signal model: } |p_0\delta t| \leq 7.43 \times 10^{-3}. \quad (5.63)$$

The above dynamic pull-in analysis has been carried out for a single DC voltage of 25 V. For other applied DC voltages, similar analyses can be carried out. The final results for dynamic pull-in due to a combination of DC bias voltage and mechanical shock load are shown in Figure 5-18.

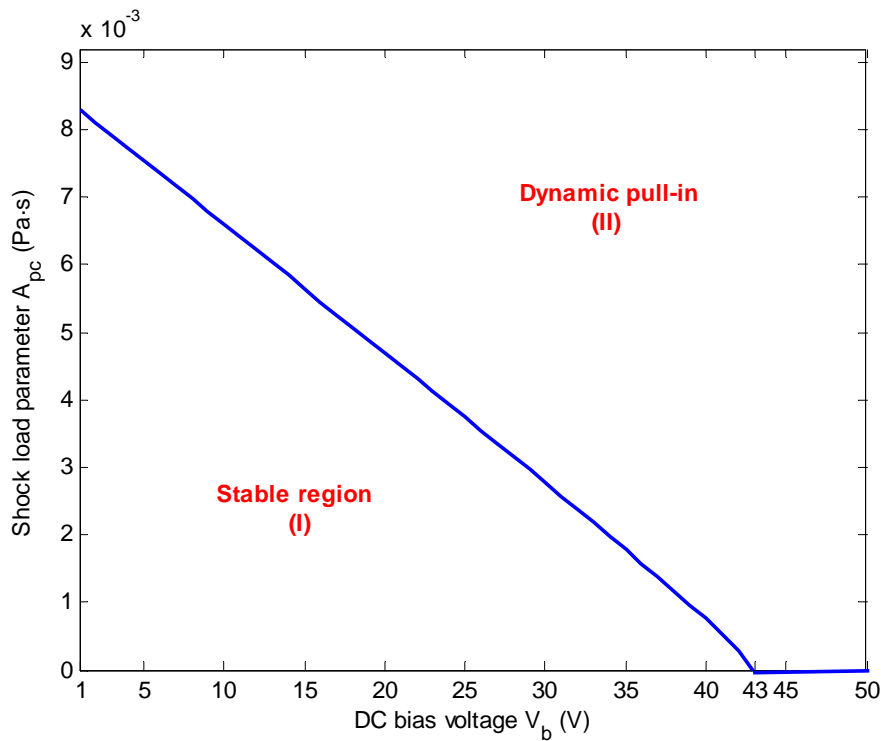


Figure 5-18. Dynamic pull-in due to a combination of DC bias voltage and a mechanical shock load.

As the DC bias voltage increases in Figure 5-18, the critical characteristic shock load parameter decreases, which means less shock loading is required to cause dynamic pull-in. In addition, a stable region (I) and an unstable region (II) are formed in the $A_{pc} - V_b$ plane. When the DC bias voltage is less than a critical value of $V_b = 43V$ (this pull-in voltage value can be theoretically calculated by replacing k_1 in Eq. (5.16) with $k_1 + k_c$) and a characteristic shock load parameter is less than its corresponding critical value, the system stays stable; otherwise, dynamic pull-in occurs. As the DC bias voltage is over $43V$, no shock loading is required to cause dynamic pull-in. Figure 5-18 also verifies that dynamic pull-in can potentially take place below a critical quasi-static pull-in voltage due to a large mechanical shock load.

Potential Advantage of Geometric Nonlinearity

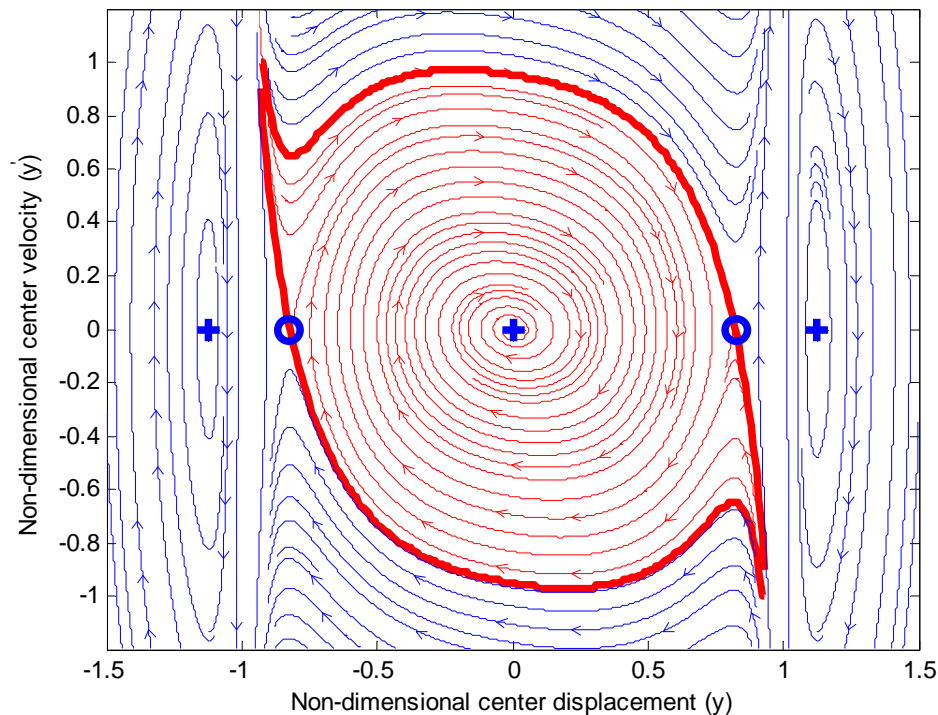


Figure 5-19. Phase plane trajectories for an added geometric nonlinearity case ($k_3^* = 10k_3$, $V_b = 25V$). Sink points are indicated by blue crosses, and saddle points are indicated by blue circles.

As we discussed in the previous section, an increased electrostatic nonlinearity and/or an increased mechanical shock load destabilize the system. As a competing factor, however, a larger geometric nonlinearity helps to stabilize the system. This section focuses on a study of the potential advantage of geometric nonlinearity.

Studies show that increasing the geometric nonlinearity, in the form of a mechanical hardening spring, provides the ability to design the position of saddle points at desired locations. For example, shown in Figure 5-19 is a plot of phase plane trajectories for an added geometric nonlinearity with $k_3^* = 10k_3$ (or $\theta_d^* = 10\theta_d$) and an applied DC voltage of $V_b = 25V$.

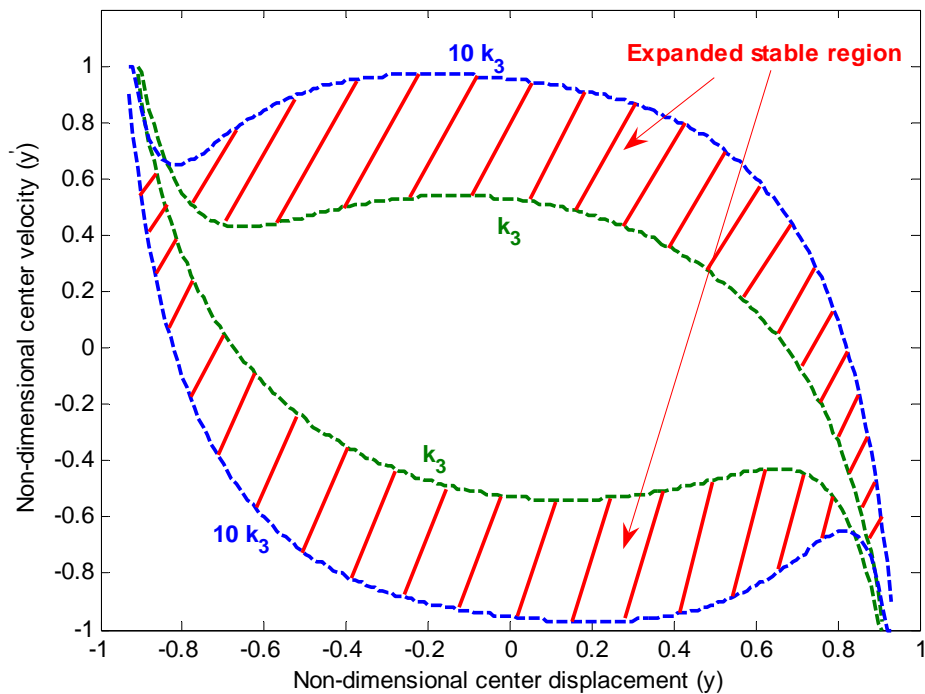


Figure 5-20. Expanded stable operation region of the microphone due to the added geometric nonlinearity ($k_3 \rightarrow 10k_3, V_b = 25V$).

In Figure 5-19, two saddle points are repositioned to $y = \pm 0.82$, which effectively expands the basin of attraction for the stable center equilibrium point ($y = 0$). Hence the dynamic stable operation range of the microphone for a given DC voltage is expanded as

shown in Figure 5-20. Also, an increased geometric nonlinearity enables the microphone to be stabilized for larger amplitude mechanical shock loads and DC bias voltages. However, the dynamic range and linearity of the microphone are affected unfavorably by the addition of geometric nonlinearity as pointed out earlier.

Dynamic Pull-in due to an Acoustic Shock Load

In the previous section, the dynamic pull-in due to a mechanical shock load was studied. In this section, the transient response of the microphone is investigated for a sharp acoustic pulse – such as the acoustic impulse of a car door slam. Dynamic pull-in could occur if the transient displacement of the diaphragm is over certain threshold. In practice, the acoustical signal generated by a real car door slam is complex and strongly depends on the cavity shape (i.e., inside of the car), boundary conditions (i.e., doors, windows, seats), and the excitation (structural characteristics of the door that is slammed) [116, 117]. To simplify and further provide physical insight into the study, an N-wave [118] is used in this section to model the actual acoustic pulse generated by a car door slam. The details of an N-wave will be provided during the analysis. Based on the quasi-static pull-in study in the previous section, the study provided in this section will further differentiate between DC and AC pull-in responses.

Problem Formulation

During the analysis of dynamic pull-in due to an acoustic pulse, it is assumed that no AC voltage excitation exists between the diaphragm and backplates. This assumption is applied to alleviate the complex interaction between the dynamic acoustical and electrical signals. Furthermore, this allows us to focus our efforts on the dynamic effect of an acoustic signal. Based on the general nonlinear governing equation in Eq. (3.53) of

Chapter 3, the governing equation of dynamic pull-in due to an acoustical pulse is as follows

$$M_{me}\ddot{x} + b\dot{x} + (k_1 + k_c)x + k_3x^3 = -\frac{\varepsilon A_{me}}{2} \left[\frac{V_b^2}{(d_0 + x)^2} - \frac{V_b^2}{(d_0 - x)^2} \right] + p_a(t)A_{me}, \quad (5.64)$$

where $p_a(t)$ is the pressure generated by the acoustic pulse.

By using the ND center displacement and time, as defined in Eqs. (5.34) and (5.35), Eq. (5.64) can be rewritten as

$$y'' + 2\zeta y' + y + \theta_d y^3 - \kappa_d \frac{y}{(1-y^2)^2} = \frac{\Gamma}{\omega_0^2 d_0} p_a(\tau), \quad (5.65)$$

where y' and y'' are the first and second derivatives of the ND center displacement with respect to the ND time τ respectively, and the other parameters have already been defined in Eqs (4.3)-(4.5) and Eqs. (5.37)-(5.38).

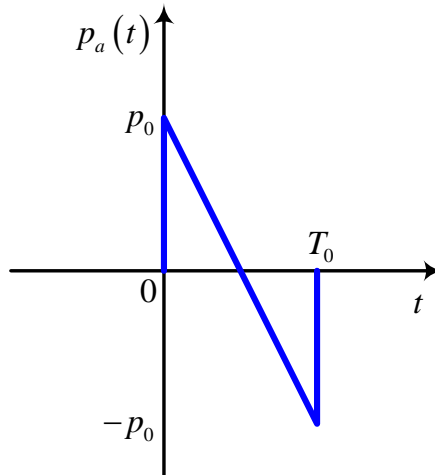


Figure 5-21. A typical N-wave with an amplitude of p_0 and a duration time of T_0 .

For modeling and analysis purposes, the actual acoustic pulse is approximated by a simpler N-wave, characterized by an amplitude of p_0 and a duration time of T_0 as shown

in Figure 5-21 [118]. For a typical N-wave starting at $t = 0$, its mathematical expression is given by [118]

$$p_a(t) = \begin{cases} 0, & \text{for } t \leq 0 \\ p_0 \left(1 - 2\frac{t}{T_0}\right), & \text{for } 0 < t < T_0. \\ 0, & \text{for } t \geq T_0 \end{cases} \quad (5.66)$$

The Fourier transform of Eq. (5.36) by further mathematical manipulation is given by

$$p_a(\omega) = p_0 T_0 \frac{1}{\frac{1}{2}\omega T_0} \left[\frac{\sin\left(\frac{1}{2}\omega T_0\right)}{\frac{1}{2}\omega T_0} - \cos\left(\frac{1}{2}\omega T_0\right) \right]. \quad (5.67)$$

The corresponding Fourier transform defined in Eq. (5.67) is plotted in Figure 5-22.

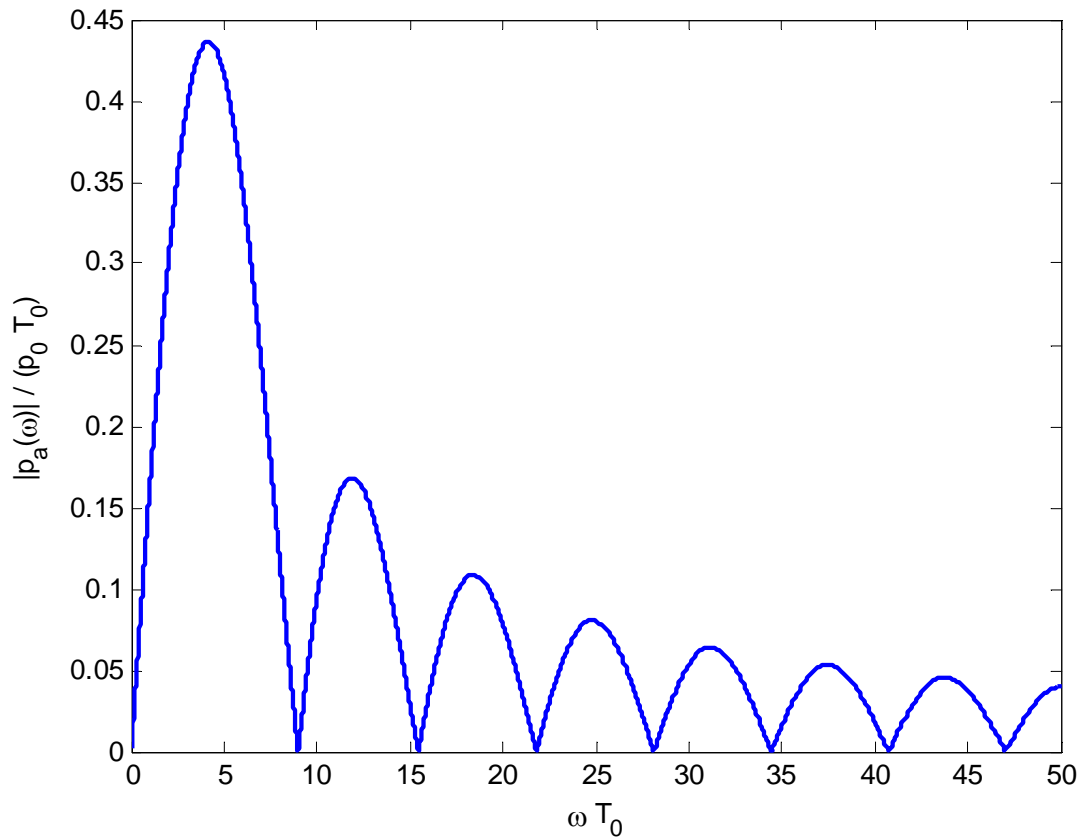


Figure 5-22. The Fourier transform of a typical N-wave.

As we can see from the plot, the magnitude at each frequency is proportional to the product of the amplitude and duration time of the N-wave. For a smaller duration time, a larger pressure amplitude is required to maintain the magnitude at each frequency. Additionally, the magnitude spectrum is continuous and the frequency content is determined by the duration time. Further analysis shows that the maximum magnitude of the Fourier transform occurs at $\omega_{\max} = 4.16/T_0$.

In the time domain, Eq. (5.36) can be further rewritten into

$$y'' + 2\zeta y' + y + \theta_d y^3 - \kappa_d \frac{y}{(1-y^2)^2} = \begin{cases} 0, & \text{for } \tau \leq 0 \\ P_d \left(1 - 2\frac{\tau}{\tau_0}\right), & \text{for } 0 < \tau < \tau_0, \\ 0, & \text{for } \tau \geq \tau_0 \end{cases} \quad (5.68)$$

where the ND pressure amplitude is

$$P_d = \frac{\Gamma p_0}{\omega_0^2 d_0} = \frac{A_{me} p_0}{M_{me} \omega_0^2 d_0} = \frac{p_0 A_{me}}{(k_1 + k_c) d_0} \quad (5.69)$$

and the ND duration time is

$$\tau_0 = T_0 \omega_0. \quad (5.70)$$

As seen in Eq. (5.68), the acoustical excitation term has two discontinuities at $\tau = 0$ and $\tau = \tau_0$. Also, Eq. (5.68) has both mechanical and electrical nonlinearities. Since it is impossible to obtain an analytical solution to Eq. (5.68), numerical simulation is utilized in this section to study the transient response of the microphone due to an N-wave excitation.

Numerical Simulation Results

In order to facilitate the numerical study, some values for the ND parameters in Eq. (5.68) are required. For the purpose of illustration, a DC voltage of 20V is chosen. Also,

an N-wave possessing a 2 ms duration time and a 125 dB SPL ($dB\ SPL = \log(p_0/20e-6)$) amplitude is chosen for this study based on the references [116, 117]. By using the physical parameters in Table 3-1 for the designed 2000Pa MEMS microphone, parameters are calculated and listed in Table 5-2.

Table 5-2. Parameters for the numerical study of an N-wave excitation.

Parameter	Value
DC bias voltage (V_b)	20 (V)
Damping ratio (ζ)	8.1e-2
ND mechanical force parameter (θ_d)	0.33
ND electrostatic force parameter (κ_d)	0.22
ND pressure amplitude (P_d)	4.4e-3
ND duration time (τ_0)	2.3

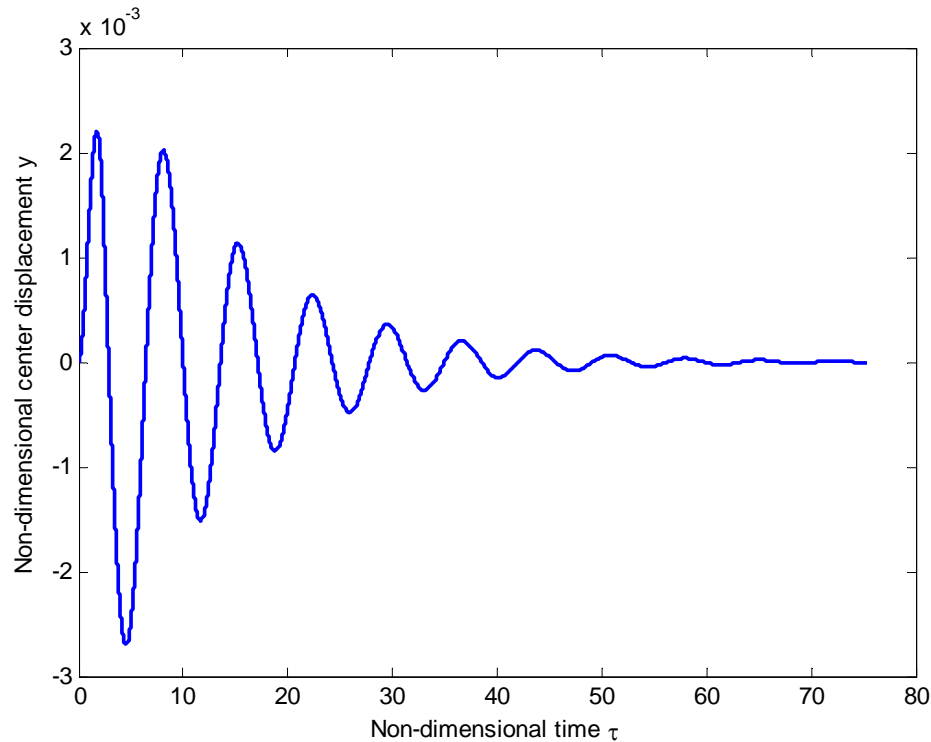


Figure 5-23. Transient non-dimensional center displacement response of diaphragm due to an N-wave with an amplitude of 125 dB SPL and a duration time of 2 ms.

Based on the parameters in Table 5-2, numerical simulations via the *ODE45* command in MATLAB are carried out for Eq. (5.68). Shown in Figure 5-23 is the

transient non-dimensional center displacement response. The corresponding transient non-dimensional center velocity response is shown in Figure 5-24. As seen from both figures, the transient response decays to zero and the microphone system is stable.

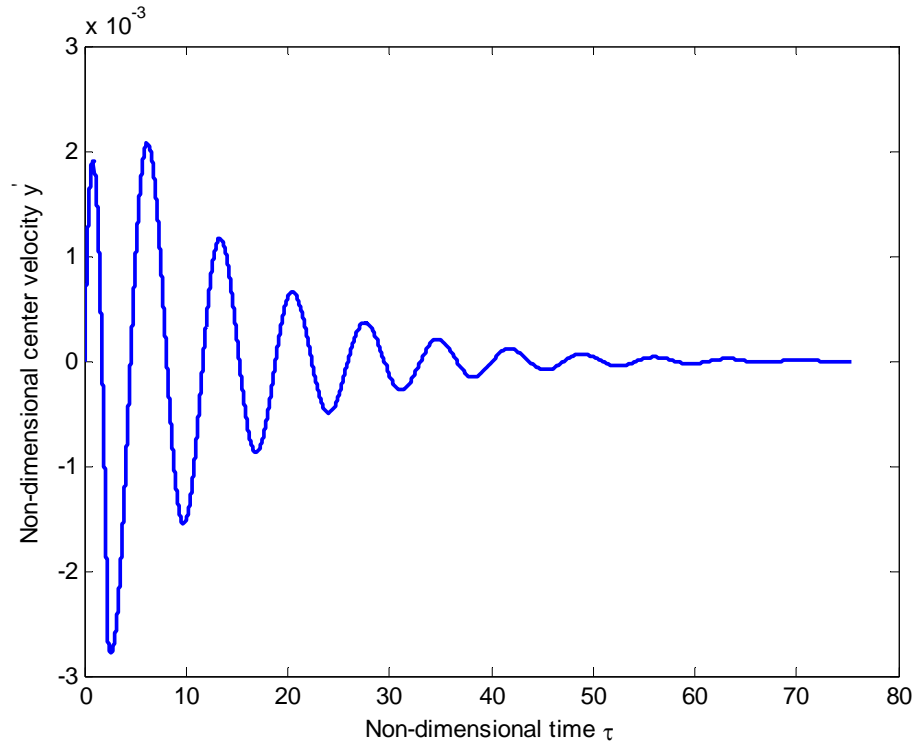


Figure 5-24. Transient non-dimensional center velocity response of diaphragm due to an N-wave with an amplitude of 125 dB SPL and a duration time of 2 ms.

Simulated Dynamic Pull-in Results

From the previous simulation, the microphone system is stable when subject to a DC voltage of 20V and an N-wave possessing a 2 ms duration time and a 125 dB SPL amplitude. In order to simulate the dynamic pull-in, either the amplitude or the duration time of the N-wave needs to be increased in the time domain. If the DC voltage and the duration time of the N-wave are fixed, further simulation shows that the ND amplitude threshold for dynamic pull-in is approximately 1.29, which physically corresponds to approximately 174 dB SPL.

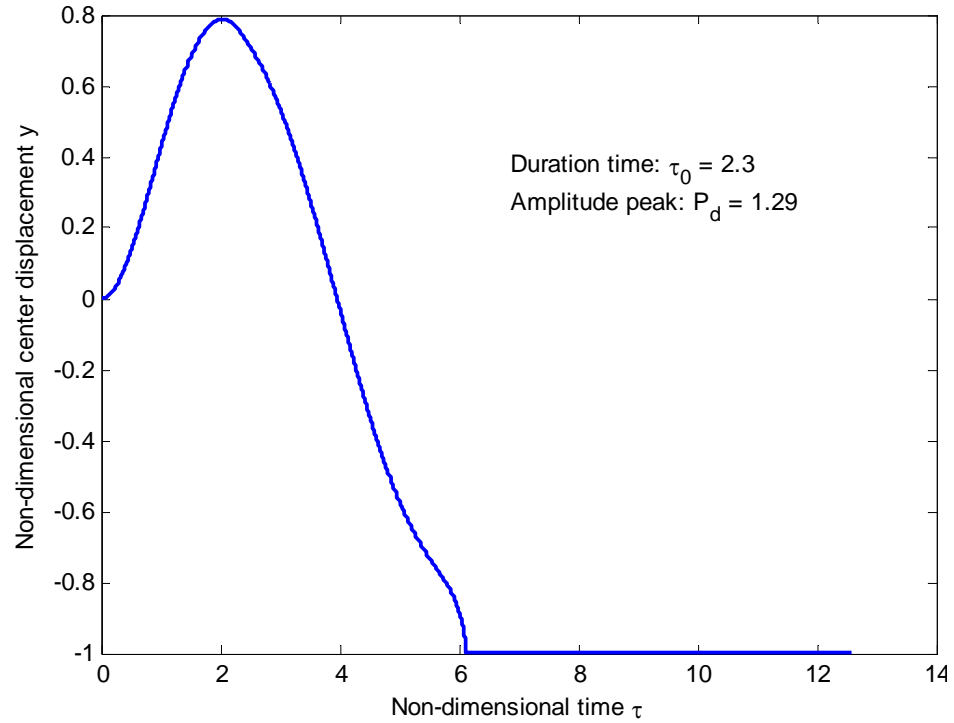


Figure 5-25. Dynamic pull-in due to an N-wave with a ND amplitude of 1.29 and a ND duration time of 2.3.

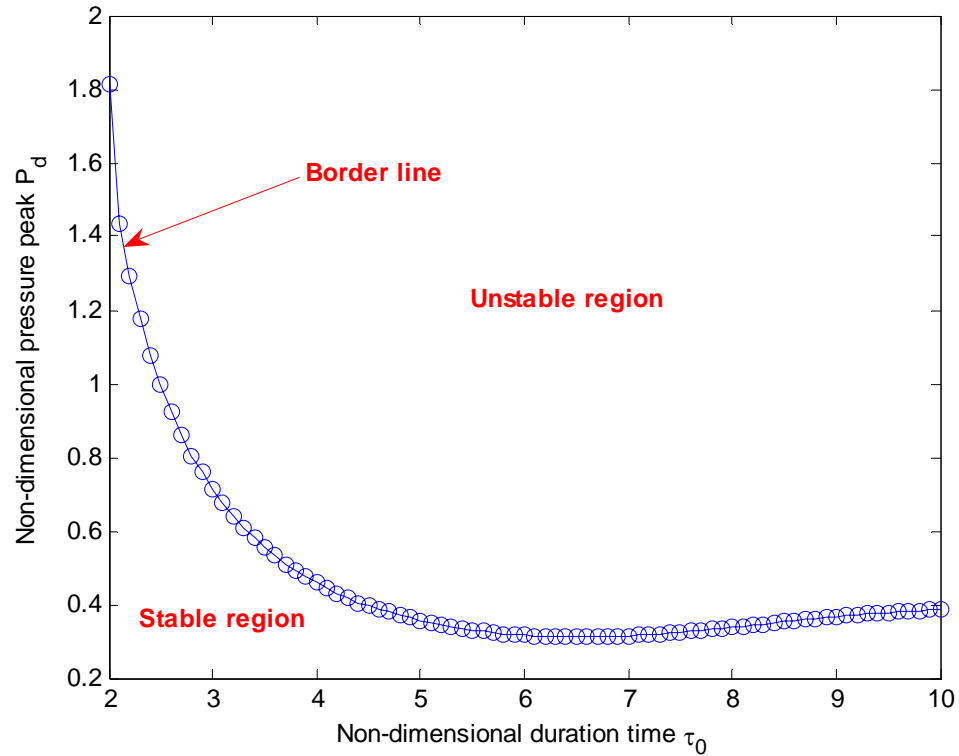


Figure 5-26. Threshold of dynamic pull-in due to an N-wave.

Shown in Figure 5-25 is the simulated transient non-dimensional center displacement response for this dynamic pull-in, which occurs for the top backplate. Since the duration time and amplitude are two characteristics of an N-wave in the time domain, it is important to simulate the dynamic pull-in threshold in terms of these two parameters. By using the damping ratio, the ND electrostatic and mechanical force parameters in Table 5-2, a plot of the dynamic pull-in threshold is shown in Figure 5-26 in terms of the ND duration time and pressure peak. Shown in Figure 5-27 is the regenerated plot of the dynamic pull-in threshold in terms of the normalized dynamic pressure peak (p_0) with respect to the corresponding quasi-static pull-in pressure $((p_0)_{SPI})$. As seen from those two plots, above the threshold curve, dynamic pull-in occurs; otherwise, the microphone system stays stable. Also, when the ND duration time is $2 \leq \tau_0 \leq 7$, a smaller pressure amplitude is required to cause dynamic pull-in as the duration time increases. This means the total input energy (proportional to the square of the magnitude of the Fourier transform function as shown in Eq. (5.67) or Figure 5-22) around the system resonance ω_0 is sufficient to cause dynamic pull-in. However, after $\tau_0 = 7.0$, since there is less energy around the system resonance ω_0 as the duration time keeps increasing, a larger pressure amplitude is required to increase the total amount of input energy to cause dynamic pull-in.

Also, as shown in Figure 5-27, when dynamic pull-in occurs, the critical dynamic pressure peak p_0 is always greater than the corresponding quasi-static pull-in pressure $((p_0)_{SPI})$. The difference between those two pressure values becomes minimal when

$\tau_0 = 7.0$. One of reasons is probably due to the complex interaction of different nonlinearities as shown in Eq. (5.68).

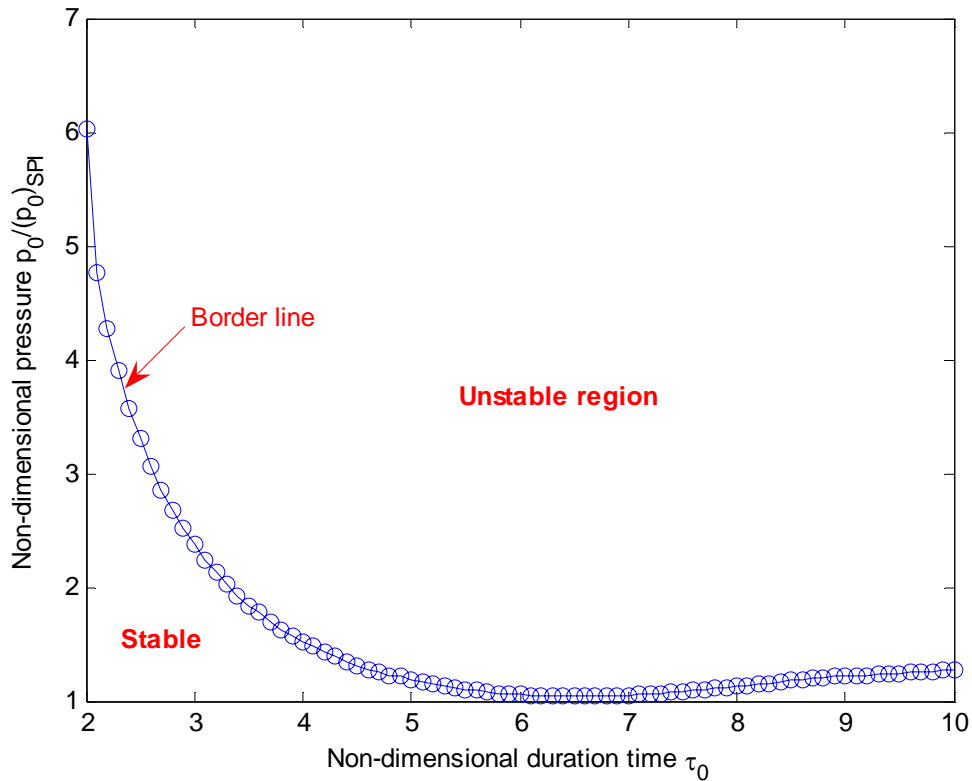


Figure 5-27. Threshold of dynamic pull-in due to an N-wave with a normalized pressure parameter.

Effect of Damping on Dynamic Pull-in

Since damping plays an important role in determining the dynamic response of the system, it is necessary to study the effect of damping on the dynamic pull-in limit. By keeping other parameters in Table 5-2 fixed and simulating Eq. (5.68) with different damping ratios ($\zeta = 0, \zeta = 0.08$ and $\zeta = 0.80$), a plot of different dynamic pull-in threshold curves is shown in Figure 5-28.

As seen from the plot, as the damping ratio increases, a larger pressure amplitude is required to cause dynamic pull-in. As the damping increases, the amplitude of the displacement response becomes smaller under the same N-wave excitation conditions.

Therefore, a larger N-wave excitation amplitude is required to drive the displacement amplitude of the diaphragm over its pull-in threshold. Although larger damping helps stabilize the microphone system from the pull-in point of view, it should be pointed out that the bandwidth of the microphone suffers from larger damping. Therefore, this trade-off needs to be considered when designing a microphone with better performance.

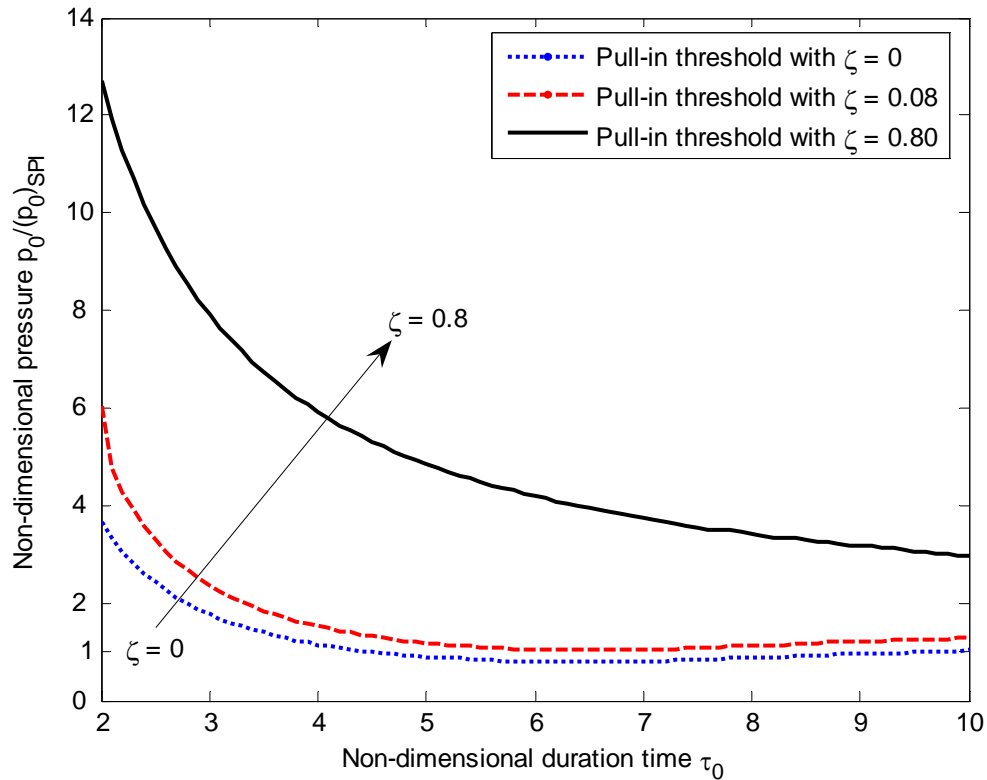


Figure 5-28. Effect of damping on dynamic pull-in threshold.

Effect of Geometric Nonlinearity on Dynamic Pull-in

Previous studies show that geometric nonlinearity helps stabilize the microphone system. In this section, the effect of geometric nonlinearity on the dynamic pull-in limit is investigated to check if it also stabilizes the microphone system due to an N-wave excitation. By keeping other parameters in Table 5-2 fixed and simulating Eq. (5.68)

with different geometric nonlinearities ($\theta_d = 0.33, \theta_d = 1.65$ and $\theta_d = 3.30$), a plot of different dynamic pull-in threshold curves is shown in Figure 5-29.

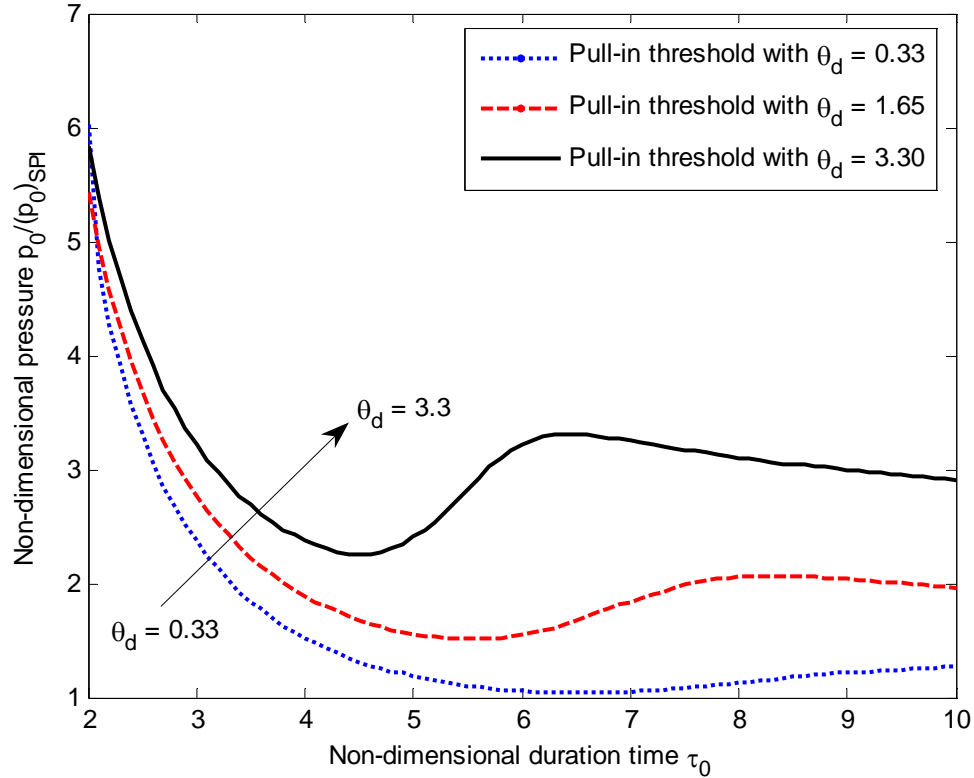


Figure 5-29. Effect of geometric nonlinearity on dynamic pull-in threshold.

As seen from the plot in Figure 5-29, as the geometric nonlinearity increases, a larger pressure amplitude is required to cause dynamic pull-in. As the geometric nonlinearity increases, the large deflection amplitude of the diaphragm becomes smaller under the same N-wave excitation conditions. Therefore, a larger N-wave excitation amplitude is required to drive the displacement amplitude of the diaphragm over its pull-in threshold.

From the above analysis, larger geometric nonlinearity is preferred to stabilize the microphone system. However, as pointed out earlier, the dynamic range and linearity of the microphone are affected unfavorably by the addition of geometric nonlinearity.

Therefore, this trade-off needs to be considered when designing a microphone with better performance.

Summary

In this chapter, pull-in instabilities of a dual-backplate capacitive MEMS microphone have been studied. First, quasi-static pull-in instability due to an applied DC voltage has been studied by both analytical and graphical methods. The quasi-static operation range of the microphone is obtained for a given DC voltage by a 1-D basin of attraction. The critical quasi-static pull-in voltage is found to be 41V analytically and the phenomenon of quasi-static pull-in is illustrated by a subcritical pitchfork bifurcation.

Also, quasi-static pull-in due to a combination of an applied DC voltage and a static pressure has been studied numerically. A quasi-static pull-in threshold curve has been obtained in terms of the applied DC voltage and static pressure amplitude.

In addition, investigation of dynamic pull-in due to a mechanical shock load is presented. By using a phase portrait and the basins of attraction, a mechanical shock load is related to dynamic pull-in. A relation between the critical DC voltage and critical characteristic parameter of a shock load has been established when dynamic pull-in occurs. Further study shows that dynamic pull-in can potentially take place below the critical quasi-static pull-in voltage due to a large mechanical shock load.

The investigation of dynamic pull-in due to an acoustical pulse, in the form of an N-wave, is provided in this chapter. By numerical simulations, a dynamic pull-in threshold curve has been obtained in terms of the duration time and amplitude of the N-wave for a given DC bias voltage. The effects of the damping and geometric nonlinearity on the dynamic pull-in limit are also studied.

Studies in this chapter also show that several nonlinearities (geometric, electrostatic and mechanical/acoustical shock) compete with each other. An increased electrostatic nonlinearity and/or an increased mechanical/acoustical shock load destabilize the system while a larger geometric nonlinearity helps to stabilize the microphone and expands its stable operational range.

CHAPTER 6 SYSTEM IDENTIFICATION BY PRELIMINARY EXPERIMENTS

This chapter focuses on the nonlinear identification of system parameters through a series of preliminary experiments. The work presented in this chapter is organized as follows. First, the experimental setup and procedures are described. Based on two approximate solutions of the electrical excitations discussed previously in Chapter 4, and a nonlinear least-squares curve-fitting technique, system parameters are extracted from the center displacement data. Conservative uncertainty ranges of experimentally extracted system parameters are obtained by the uncertainty analysis. Experimentally extracted system parameters are then compared with their theoretical values and discussions of analysis results are presented.

Experiment Setup and Procedures

The characterization experiment of the dual-backplate capacitive MEMS microphone was conducted using a laser Doppler vibrometer (Polytec MSV 300) in the Interdisciplinary Microsystems Laboratory at the University of Florida. The goal of the experiments is to determine the system parameters of the nonlinear dynamic model for a fabricated device.

Experiment Setup

Generally, a laser Doppler vibrometer operates based on the detection of the Doppler shift of coherent laser light, which is reflected from a small area of the test object. The component of velocity which lies along the axis of the laser beam is determined by the Doppler frequency shift in the reflected laser beam [119]. The block

diagram of the experiment setup is shown in Figure 6-1. The microphone under test is positioned on the stage of the microscope (Olympus BX60), with a 100x objective lens [120]. The output of an external function generator (Agilent 33220A) is used to provide electrical signals to excite the microphone and is also connected to the “Ref” channel of the laser vibrometer. The “Sync” signal coming out of the function generator is connected to the laser vibrometer to trigger the data acquisition process. The laser vibrometer generates the input laser beam and receives the resulting interference optical signal from the microscope. The resulting optical signal is converted into an electrical signal by a photodetector inside the vibrometer and subsequently decoded to generate the velocity output [119]. A data acquisition PC then acquires data from both reference and velocity channels in the laser vibrometer.

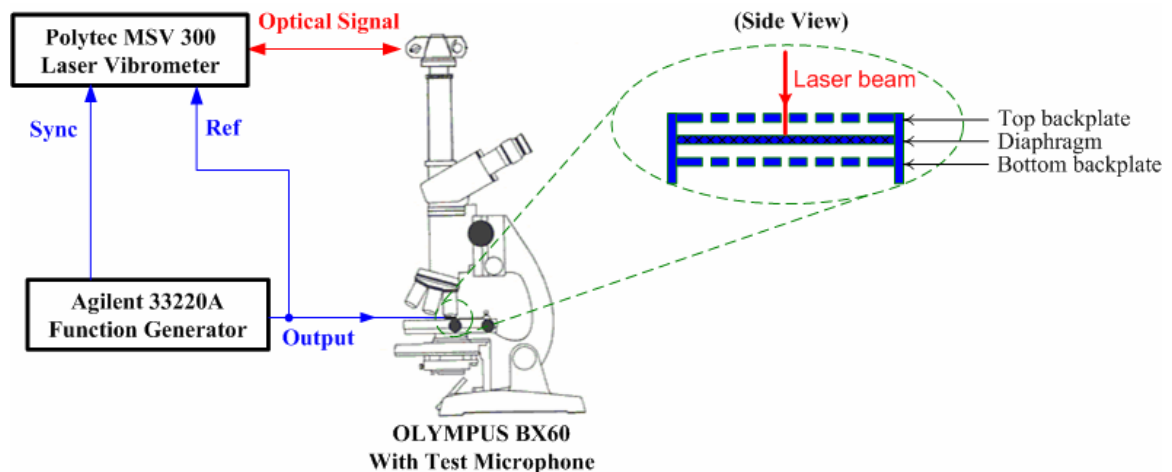


Figure 6-1. Block diagram of the experiment setup.

To be able to measure the center velocity response of the diaphragm during the experiments, a laser beam is adjusted and shone through the center hole of the top backplate as shown in the side view of Figure 6-1. Figure 6-2 shows an optical photograph (zoom-in top view) of a laser beam spot, which was positioned inside the center hole of the top backplate. From the experimental picture, the diameter of the laser

spot is estimated to be approximately $4\ \mu\text{m}$. A sampling rate of 2.56 MHz was used to record the velocity for 3.2 ms; 100 ensemble averages were used to minimize the noise in the measured velocity data.

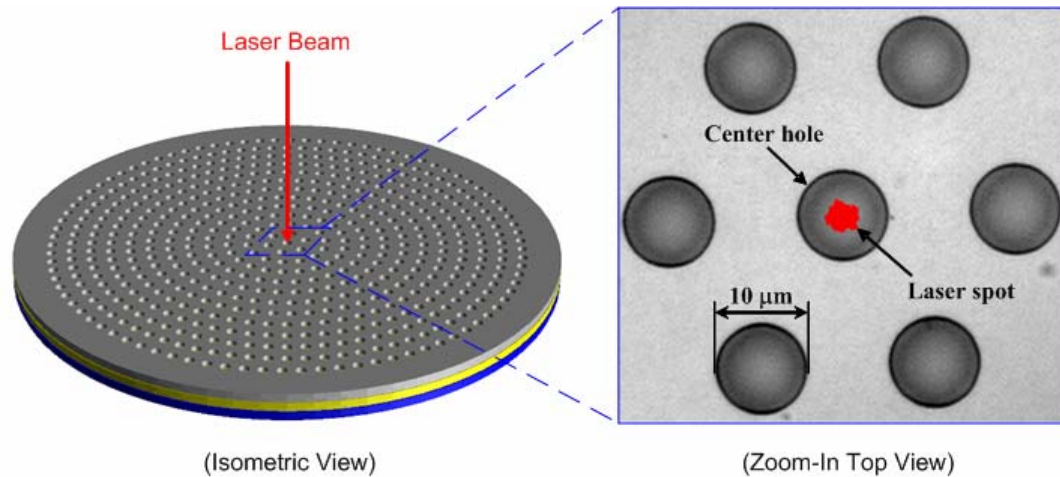


Figure 6-2. Laser beam spot (red dot) impinges the diaphragm through the center hole of the top backplate.

Experiment Procedures

To be able to extract the system parameters from the experimental data, two types of experiments were conducted. In the first set of experiments, the microphone was excited with an electrical square wave to study its transient response using the previously presented MTS approximate solution. For the second series of experiments, the microphone was excited with an electrical sinusoidal wave to study its steady state response using the previously presented HB approximate solution. In the following sections, the general procedures to conduct those two types of experiments are described respectively.

Procedures for the electrical square wave excitation

For the electrical square wave excitation, some major steps to conduct one test using the top backplate for excitation are as follows:

1. Adjust the laser beam from the vibrometer in the focus and position the laser spot inside the center hole of the top backplate so that the center velocity response of the diaphragm can be measured
2. Electrically ground the diaphragm and bottom backplate
3. Initially, apply 1 kHz uni-polar square wave with a voltage amplitude of $V_0 = 5 \text{ V}$ and 50% duty cycle directly to the top backplate of the microphone
4. Measure the dynamic transient response of the center velocity of the diaphragm via the laser vibrometer system shown in Figure 6-1 and save the time-history data for the further analysis
5. Change the applied uni-polar square wave voltage amplitude V_0 to 15 and 30 V and repeat step 4 for the two applied voltages respectively.

Similarly, for the tests using the bottom backplate for excitation, the middle diaphragm and top backplate are electrically grounded. A 1 kHz uni-polar square wave with a voltage amplitude of $V_0 = 5 \text{ V}$ and 50% duty cycle is directly applied to the bottom backplate, and the above steps 3, 4 and 5 are repeated.

Procedures for the electrical sinusoidal excitation

For the electrical sinusoidal excitation, some major steps to conduct one test using the top backplate for excitation are listed in the following,

1. Adjust the laser beam from the vibrometer in the focus and position the laser spot inside the center hole of the top backplate so that the center velocity response of the diaphragm can be measured
2. Electrically ground the diaphragm and bottom backplate
3. Initially, apply the designed sinusoidal signal with a voltage amplitude of $V_0 = 5 \text{ V}$ and a frequency around one half of the linear resonant frequency of the diaphragm directly to the top backplate of the microphone
4. Measure the dynamic steady state response of the center velocity of the diaphragm via the laser vibrometer system and save the time-history data for the further analysis
5. Keep the voltage amplitude fixed ($V_0 = 5 \text{ V}$) and change the excitation frequency close to first frequency point and take the measurement again

6. Change the applied sinusoidal wave voltage amplitude V_0 to 20 and 25 V and repeat steps 4 and 5 for the two applied voltages respectively.

Similarly, for the tests using the bottom backplate for excitation, the middle diaphragm and top backplate are electrically grounded. A sinusoidal signal with a voltage amplitude of $V_0 = 5$ V and a frequency of 92.7 kHz is directly applied to the bottom backplate, and the above steps 3, 4, 5 and 6 are repeated.

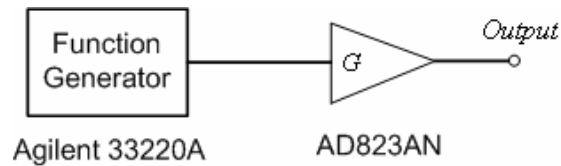


Figure 6-3. Simplified circuit to generate the high voltage signal.

To ensure the repeatability, for each type of experiment, one test using the top/bottom backplate for excitation is repeated 5 times in different time slots. As shown in Figure 6-3, the high-voltage ($\geq 20V$) signal required by the experiments is generated by using an Agilent function generator (33220A) and an operational amplifier (AD823AN, Analog Devices, Inc.).

Results of Electrical Square Wave Excitation

In this section, the experimental results for the electrical square wave excitation are presented. System parameters are extracted from the transient experimental data via a MTS approximate solution, which is discussed in Eqs. (4.33)-(4.37) of Section 4.3 (Approximate MTS Solution for the Electrical Square Wave Excitation). For the electrical square wave excitation, the dynamic response of the center velocity of the diaphragm is recorded for 100 ensembles. The trapezoidal rule is applied to numerically integrate the measured average center velocity to yield the center displacement [108].

Because the time step is small ($0.39 \mu\text{s}$), the numerical integration error is small and can be neglected (the details are provided in the uncertainty analysis in Appendix E).

Results of Bottom Backplate Excitation

Shown in Figure 6-4 is the measured ensemble-averaged center velocity (up-stroke) response of the diaphragm excited by a uni-polar 1 kHz square wave with an amplitude of 5V. As seen from the plot, the center velocity decays quickly to zero. The corresponding integrated center displacement response is shown in Figure 6-5. The drift in the steady state of the integrated center displacement response is due to the experiment setup because the laser vibrometer does not measure the static velocity. It should be pointed out that the system parameters are extracted only from the transient response data of the integrated center displacement. Therefore, the accuracy of the extracted system parameters is not affected by the undesired drift.

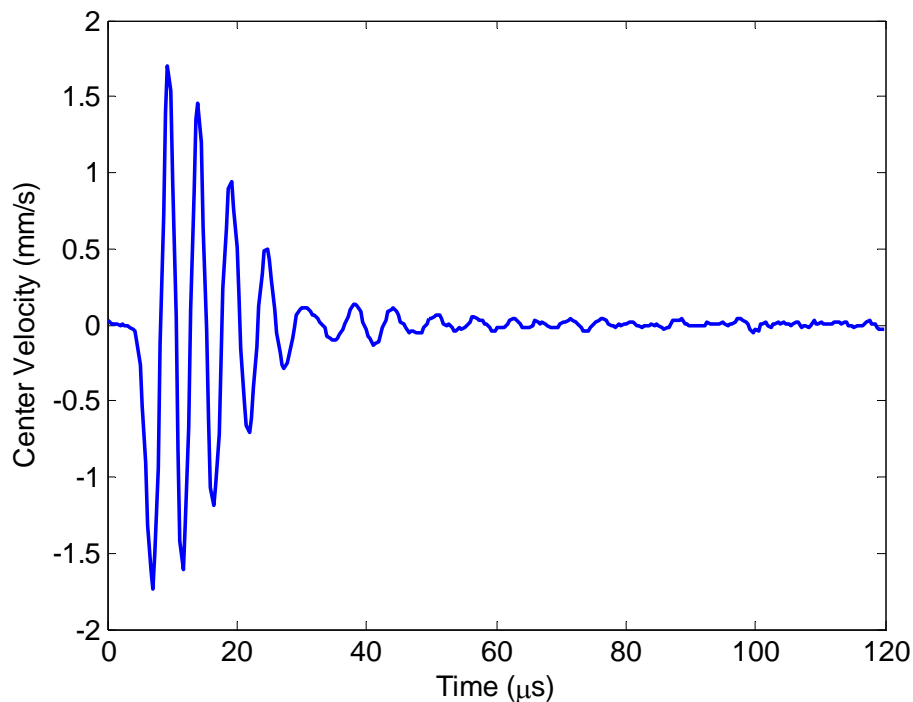


Figure 6-4. Measured averaged center velocity response for an applied square wave with an amplitude of 5V.

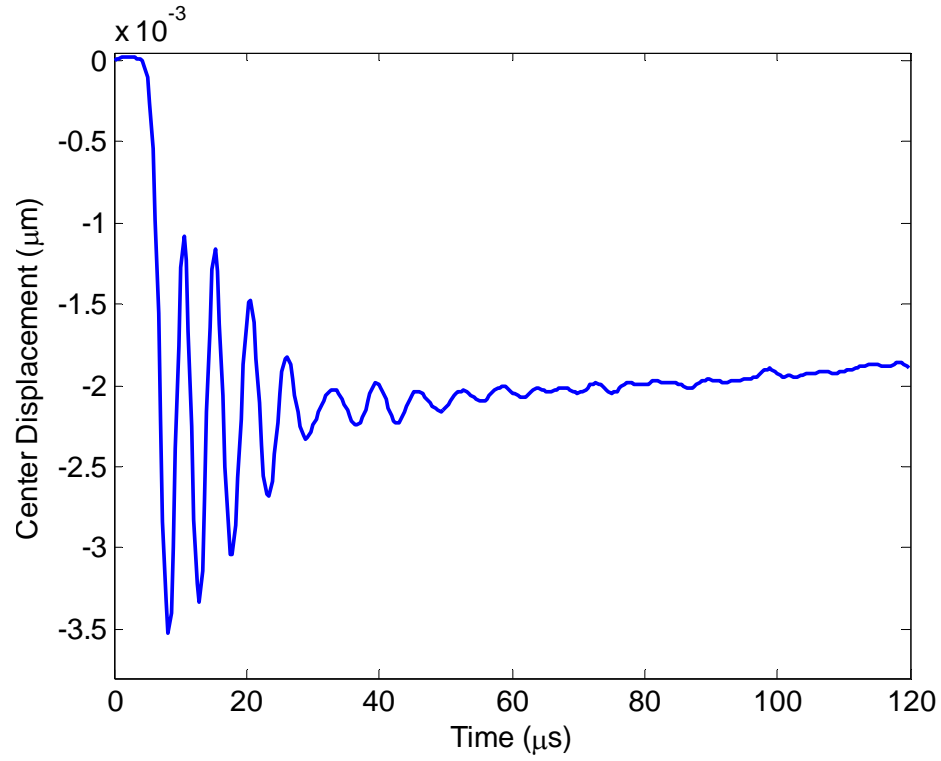


Figure 6-5. Integrated center displacement response for an applied square wave with an amplitude of 5V.

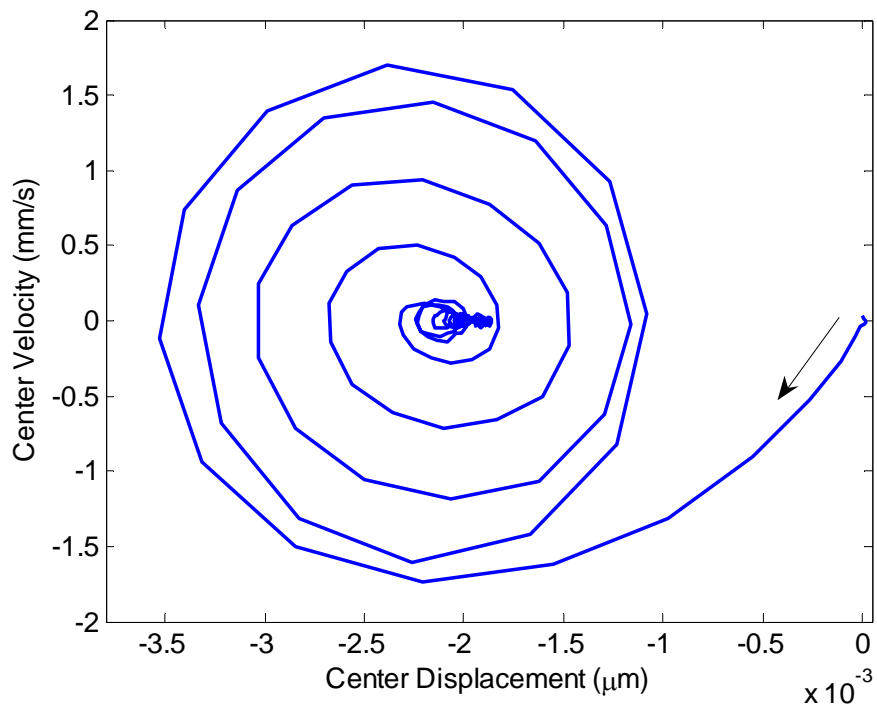


Figure 6-6. Constructed phase plot for an applied square wave with an amplitude of 5V.

A phase plot is constructed in Figure 6-6 based on the measured velocity and integrated displacement responses. The system spirals into a fixed point. By using Eq. (4.34) in Chapter 4, a nonlinear least-squares curve-fitting procedure is carried out in MATLAB to obtain system parameters ζ , ω_0 , β , Γ and d_0 from the transient response data of the integrated center displacement. Figure 6-7 shows a comparison plot of the integrated and curve-fit center displacement results. The system parameters identified from the curve fit to the analytical approximate solution are summarized in Table 6-1.

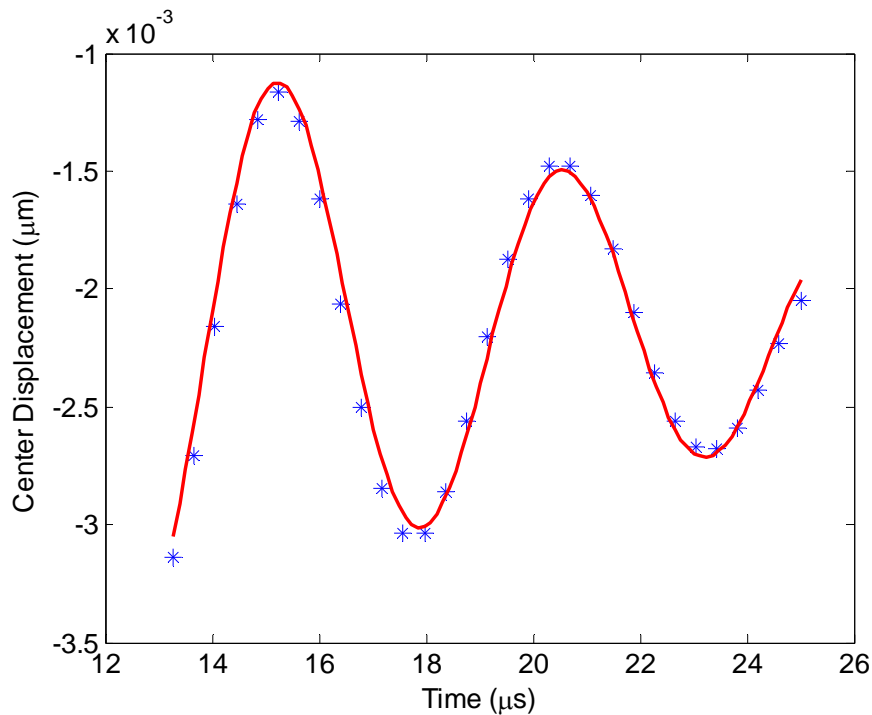


Figure 6-7. Comparison of integrated and curve-fit center displacements for an applied square wave with an amplitude of 5V.

Table 6-1. Results of system parameters of the bottom backplate excitation.

System parameter	Curve-fitting result
d_0 (m)	2.052e-6
$\omega_0/2\pi$ (Hz)	188.0e3
ζ	6.970e-2
β (N/m ³ /kg)	1.224e23
Γ (m ² /kg)	[†] 112.6

[†]value for 5V only.

Results of Top Backplate Excitation

Shown in Figure 6-8 is a measured ensemble-averaged center velocity response (up-stroke) of the diaphragm excited by a uni-polar 1 kHz square wave with an amplitude of 18 V. As seen from the plot, the center velocity decays quickly to zero. The corresponding integrated center displacement response is shown in Figure 6-9. Similarly, based on the measured velocity and integrated displacement responses, the constructed phase plot after 12 μs is generated in Figure 6-10, showing the system spirals into a fixed point.

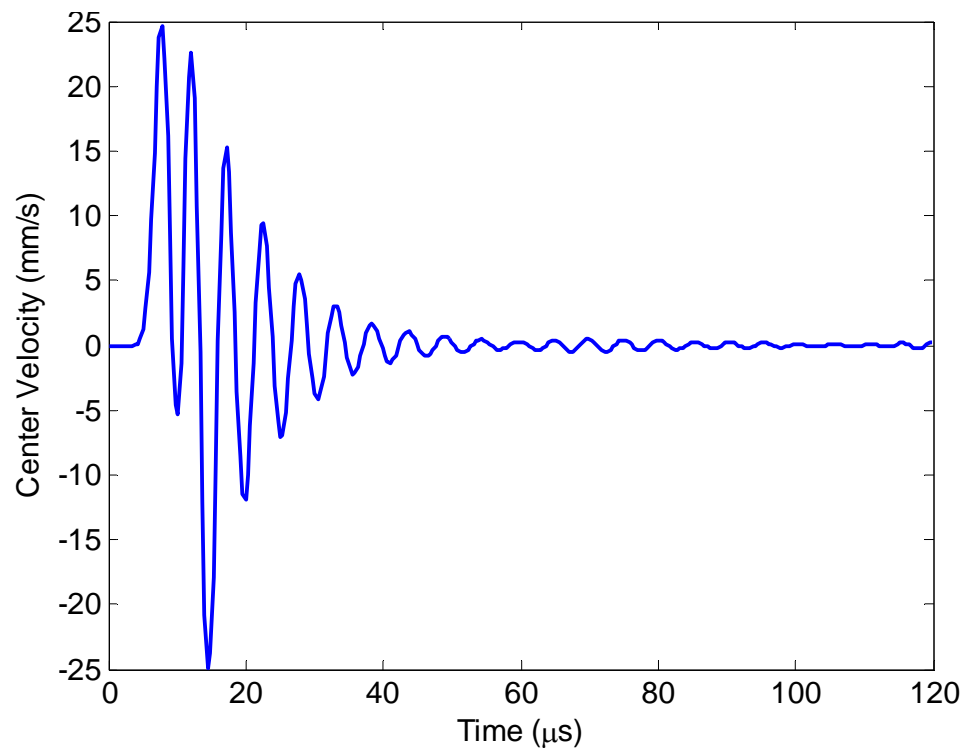


Figure 6-8. Measured averaged center velocity response for an applied square wave with an amplitude of 18V.

Similarly, by using Eq. (4.34) in Chapter 4, a set of system parameters can be extracted via a nonlinear least-squares curve-fitting technique from the transient response data of the integrated center displacement. Shown in Figure 6-11 is the comparison plot of the integrated and curve-fit center displacement results. The nonlinear least-squares

curve-fit results are in good agreement with the integrated results. The system parameters identified from the curve fit to the analytical approximate solution are summarized in Table 6-2.

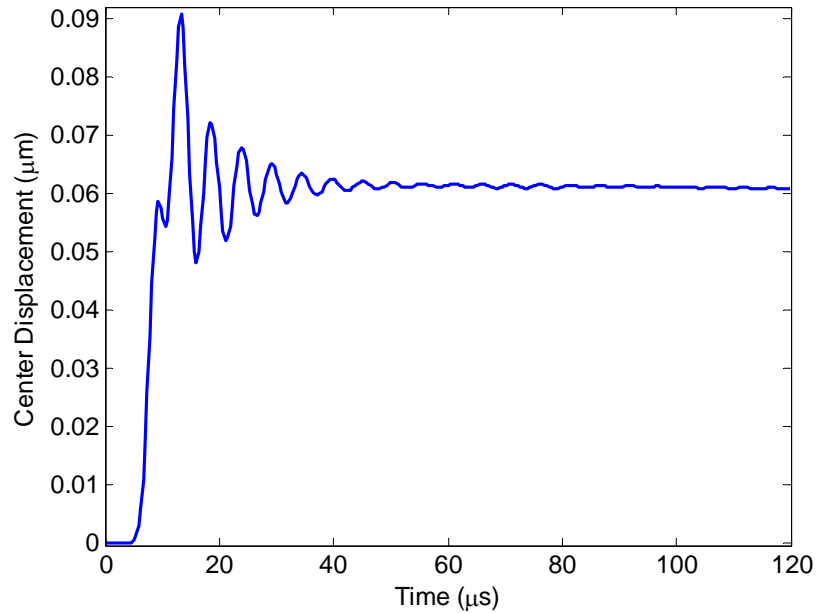


Figure 6-9. Integrated center displacement response for an applied square wave with an amplitude of 18V.

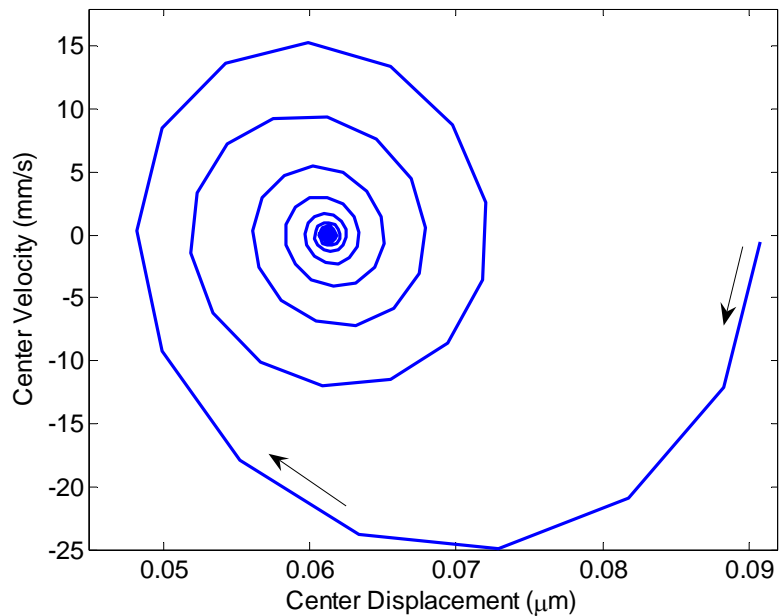


Figure 6-10. Constructed phase plot after 12 μs for an applied square wave with an amplitude of 18V.

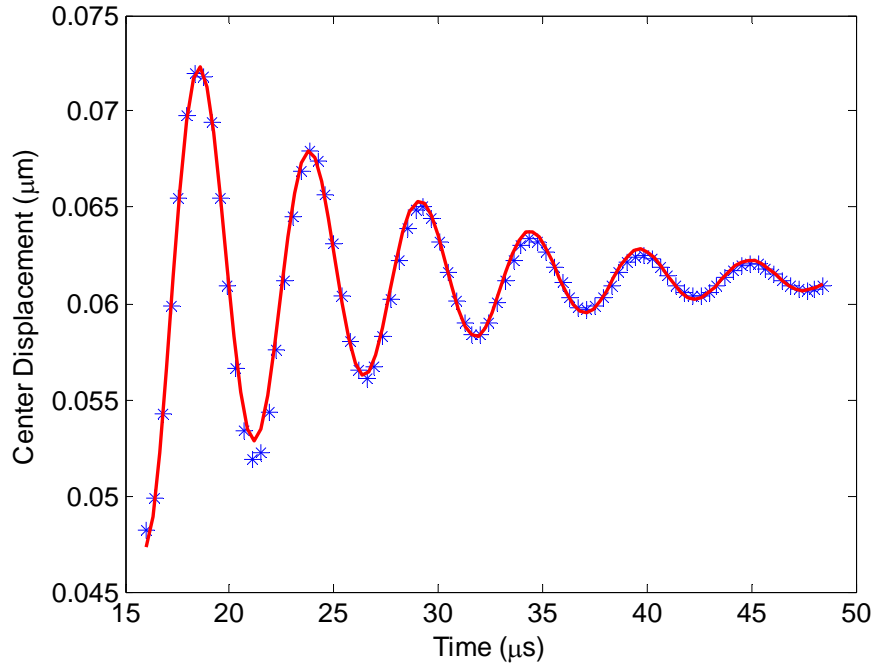


Figure 6-11. Comparison of integrated and curve-fit center displacements for an applied square wave with an amplitude of 18V.

Table 6-2. Results of system parameters of the top backplate excitation.

System parameter	Curve-fitting result
d_0 (m)	1.950e-6
$\omega_0/2\pi$ (Hz)	196.0e3
ζ	7.791e-2
β (N/m ³ /kg)	1.088e23
Γ (m ² /kg)	‡231.9

‡value for 18V only.

Results of Electrical Sinusoidal Excitation

In this section, the experimental results for the electrical sinusoidal excitation are presented. System parameters are extracted from the steady-state experimental data via a HB approximate solution, which is discussed in Eqs. (4.61)-(4.64) of Section 4.5 (Approximate HB Solution for the Electrical Sinusoidal Excitation). For the electrical sinusoidal excitation, a designed signal defined by Eqs. (4.43) and (4.44) in Chapter 4 is

applied directly to either bottom or top backplates of the microphone. The dynamic response of the center velocity of the diaphragm is recorded for 100 ensembles. As mentioned previously, two tests need to be conducted to extract system parameters based on a HB approximate method. For the first test, the sinusoidal excitation frequency is chosen to be around one half of the linear resonant frequency of the diaphragm, and the excitation frequency of the second test is chosen to be close to the frequency of the first test so that each system parameter is not changed. Also, the trapezoidal rule is applied to numerically integrate the measured average center velocity to yield the center displacement [108].

Results of Bottom Backplate Excitation

For the first test, the amplitude of sinusoidal excitation signal is 9V and its frequency is chosen to be 114.4 kHz. Shown in Figure 6-12 is the measured time-history of the ensemble-averaged center velocity in the steady state.

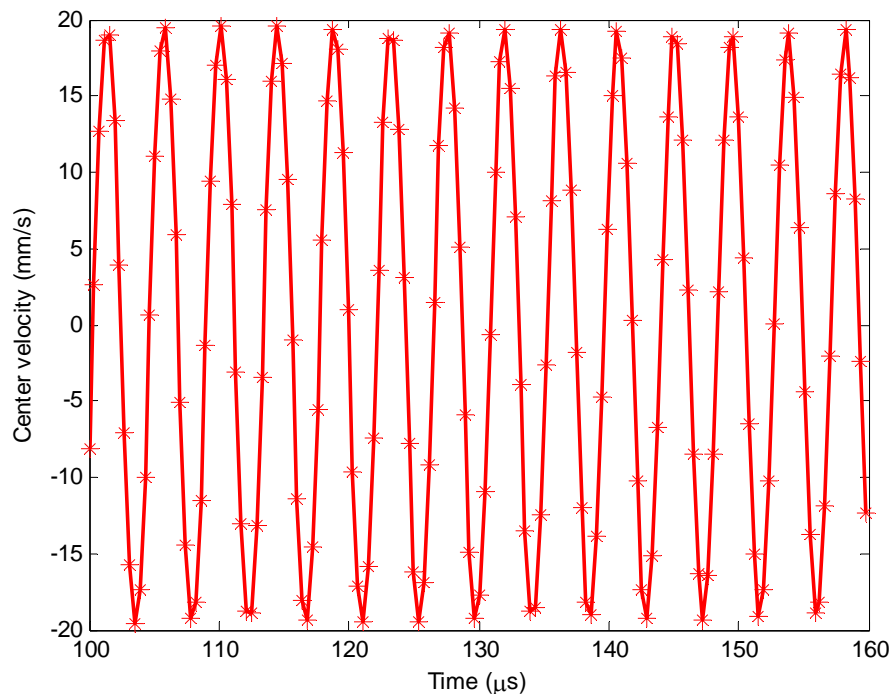


Figure 6-12. Measured averaged steady-state center velocity response (asterisk) for a sinusoidal excitation with an amplitude of 9V and a frequency of 114.4 kHz.

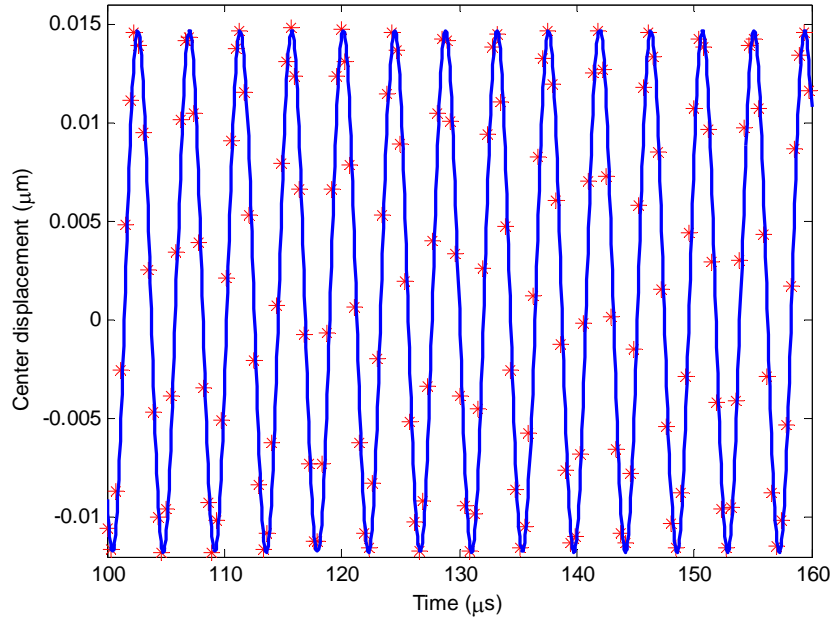


Figure 6-13. Comparison of the integrated (red asterisk) and curve-fitting (blue solid line) steady-state center displacement results for a sinusoidal excitation with an amplitude of 9V and a frequency of 114.4 kHz.

Table 6-3. Amplitudes and phase of the integrated averaged steady-state center displacement of the bottom backplate excitation.

Parameter	First test	Second test	Difference
$\Omega / 2\pi$ (kHz)	114.4	114.8	0.3%
A_0 (μm)	1.457e-3	1.440e-3	1.1%
A_2 (μm)	1.321e-2	1.323e-2	0.2%
φ (rad)	-1.453	-1.539	5.9%

By applying the trapezoidal rule, the corresponding time response of the integrated averaged center displacement in the steady state is shown in Figure 6-13. By using Eq. (4.57) in Chapter 4, a nonlinear least-squares curve-fitting technique is implemented in MATLAB to extract the amplitudes and phase (A_0 , A_2 and φ) from the steady-state center displacement response. The curve-fit center displacement response is also plotted in Figure 6-13, and the curve-fit parameters are summarized in Table 6-3. Similarly, for the second test, the frequency of the sinusoidal excitation is 114.8 kHz while its

amplitude is still 9 V. The final curve-fit results of the second test are listed in Table 6-3.

With the parameters in Table 6-3, system parameters ζ , ω_0 , β and Γ can be extracted by using Eq. (4.65) in Chapter 4 for the bottom backplate excitation. The final set of system parameters are listed in the following table.

Table 6-4. Results of system parameters of the bottom backplate excitation.

System parameter	Curve-fitting result
$\omega_0/2\pi$ (kHz)	230.3
ζ	5.482e-2
β (N/m ³ /kg)	1.470e23
Γ (m ² /kg)	[†] 67.48

[†]value for 9V only.

Results of Top Backplate Excitation

During the experiments using the top backplate for excitation, the amplitude of the sinusoidal excitation signal is 8.3V and the frequencies of the two tests are 114.0 kHz and 114.4 kHz respectively. After obtaining the measured ensemble-averaged steady-state center velocity responses, a nonlinear least-squares curve-fitting is carried out to extract the amplitudes and phase (A_0 , A_2 and φ) for each test respectively. Finally, the curve-fit results are summarized in Table 6-5. Similarly, with the parameters in Table 6-5, system parameters ζ , ω_0 , β and Γ can be extracted by using Eq. (4.65) in Chapter 4.

The final set of system parameters are listed in Table 6-6.

Table 6-5. Amplitudes and phase of the integrated averaged steady-state center displacement of the top backplate excitation.

Parameter	First test	Second test	Difference
$\Omega/2\pi$ (kHz)	114.0	114.4	0.4%
A_0 (μm)	6.08e-4	6.08e-4	0.2%
A_2 (μm)	4.198e-3	4.037e-3	0.4%
φ (rad)	-2.223	-2.263	1.8%

Table 6-6. Results of system parameters of the top backplate excitation.

System parameter	Curve-fitting result
$\omega_0/2\pi$ (kHz)	218.6
ζ	5.533e-2
β (N/m ³ /kg)	1.470e23
Γ (m ² /kg)	[‡] 30.08

[‡]value for 8.3V only.

Discussion of Analysis Results

In the previous section, no uncertainties are assumed with the measured velocity and the physical dimensions/material properties of the microphone. However, there always exist some uncertainty sources in the experiments and physical microphone devices, for example, the variations of physical dimensions and material properties, which can be caused by the fabrication process. Therefore, uncertainty analysis of the experimentally extracted identified system parameters needs to be conducted. The detailed uncertainty analysis is included in Appendix E and the final uncertainty analysis results are summarized in Table 6-7.

Table 6-7. Theoretical mean values and uncertainties of system parameters for a given 95% confidence level.

System parameter	Mean	Uncertainty	Percentage
$\omega_0/2\pi$ (Hz)	193.5e3	10.20e3	5.3%
ζ	7.272e-2	1.337e-2	18%
β (N/m ³ /kg)	1.219e23	0.1409e23	12%
Γ (m ² /kg)	329.2	2.901	0.9%

From Table 3-1 in Chapter 3, the nominal values of system parameters of the microphone are calculated and listed in Table 6-8. As we can see from Table 6-7 and Table 6-8, the nominal values of system parameters fall within their theoretical uncertainty ranges for a given 95% confidence level respectively. Also from Table 6-1, Table 6-2 and Table 6-7, the experimentally extracted linear natural frequency, damping

ratio and nonlinear stiffness parameter based on the MTS approximate solution fall within their conservative theoretical ranges for a 95% confidence level respectively.

Table 6-8. Nominal values of system parameters of the microphone.

System parameter	Nominal value
$\omega_0/2\pi$ (Hz)	185.5e3
ζ	8.091e-2
β (N/m ³ /kg)	1.127e23
Γ (m ² /kg)	332.2

From Table 6-4, Table 6-6 and Table 6-7, the experimentally extracted system parameters, obtained from the HB approximate solution, do not fall within their conservative theoretical ranges. Possible reasons are the relatively large bias error caused by the HB approximate solution/algorithm (see Chapter 4 for details, primarily due to the fact that higher order harmonics were not included in the HB solution) and the conservative nature of the uncertainty analysis (see Appendix E for details).

The differences between system parameters identified through square and sinusoidal wave excitation experiments respectively (Table 6-1, Table 6-2, Table 6-4, Table 6-6) are mainly due to the different dual-backplate capacitive microphones tested during each type of experiment. For either electrical square or sinusoidal wave excitation experiments, discrepancies between the experimentally identified system parameters of both bottom and top backplate excitations respectively are mainly due to the different bottom and top capacitors, such as unequal air gaps and electrode areas.

It is shown that Γ is a constant for a given set of parameters from the lumped element modeling based on a simple equal-area parallel-plate assumption. However, analysis results shown in Table 6-1, Table 6-2, Table 6-4, Table 6-6 indicate that it is a function of the applied voltage, which means that the equivalent area for calculating electrostatic forces depends on the applied voltage (assuming the lumped mass is fixed).

The changing experimental behavior of Γ could be due to several reasons: 1) in a physical device, the top backplate area is larger than the diaphragm area, and the diaphragm area is larger than the bottom backplate area; therefore the equal-area assumption is not accurate in practice [79, 93, 121, 122]; 2) the backplates are perforated with holes, which decreases the overlapping area and generates extra fringing field effect when calculating the electrostatic forces; and 3) the overlapping area and fringing field effect could change due to the different bending shapes of the plates when different voltages are applied between the backplate and diaphragm. Since Γ plays an important role in determining the electrostatic force and the sensitivity of the microphone for a given bias voltage, further investigation needs to be conducted in the future.

Summary

In this chapter, the nonlinear identification of system parameters of the microphone through a series of preliminary experiments is presented. The measured center velocity and integrated center displacement results for both electrical square and sinusoidal wave excitation experiments are provided. Based on the approximate MTS and HB solutions presented in Chapter 4, and a nonlinear least-squares curve-fitting technique, system parameters are extracted from two types of experimental data respectively. The uncertainty analysis in Appendix E shows that the experimentally extracted linear natural frequency, damping ratio and nonlinear stiffness parameter based on the MTS approximate solution fall within their conservative theoretical ranges for a 95% confidence level.

CHAPTER 7 CONCLUSIONS AND FUTURE WORK

This chapter summarizes the important results presented in this dissertation. Concluding remarks as well as recommendations for future work are discussed.

Conclusions

An investigation of the electromechanical nonlinear dynamics of a dual-backplate capacitive MEMS microphone has been presented through the theoretical analysis, numerical simulation and preliminary experimental characterization. A large displacement solution via an energy method has been utilized to provide linear and cubic lumped stiffnesses of the circular diaphragm of the microphone. A nonlinear dynamic model of the microphone has been developed based on lumped element modeling. Theoretical lumped stiffnesses of the diaphragm are verified by nonlinear finite element analyses (FEA) and the errors for the linear and cubic stiffnesses are approximately 1.3% and 5.0% respectively. The coupled nonlinear electromechanical simulations show that the difference between the simulated and modeled electrostatic forces is 17% at 25V for the top capacitor and 17% at 33.5V for the bottom capacitor.

Quasi-static pull-in due to an applied DC voltage has been investigated by both analytical and graphical approaches. The critical quasi-static pull-in voltage is found to be approximately 41V. The quasi-static operation range of the microphone is obtained for a given DC voltage by a 1-D basin of attraction. The phenomenon of quasi-static pull-in is illustrated by a subcritical pitchfork bifurcation. A potential advantage of the mechanical geometric nonlinearity is explored, and the quasi-static stable operation range

of the microphone can be increased by enlarging the gap and/or decreasing the thickness of the diaphragm. Further studies show that the stable operational range of the microphone could benefit from the addition of geometric nonlinearity into the system. However, the linearity and dynamic range of the microphone are affected unfavorably by the addition of geometric nonlinearity.

Investigation of dynamic pull-in due to a mechanical shock load has also been presented. A non-dimensional governing equation has been formulated for the dynamic pull-in study. By using a phase portrait and basin of attraction, a mechanical shock load is related to dynamic pull-in. A relation between the critical DC voltage and critical characteristic parameter of a mechanical shock load has been established when dynamic pull-in occurs. Further study shows that dynamic pull-in can potentially take place below the critical quasi-static pull-in voltage due to a large mechanical shock load. The investigation of dynamic pull-in due to an acoustical pulse, in the form of an N-wave, is provided. By using numerical simulations, a dynamic pull-in threshold curve has been obtained in terms of the duration time and amplitude of the N-wave for a given DC bias voltage. The effects of the damping and geometric nonlinearity on the dynamic pull-in limit are also studied.

Studies of dynamic pull-in show that several nonlinearities (geometric, electrostatic and mechanical/acoustical shock) compete with each other. An increased electrostatic nonlinearity and/or an increased mechanical/acoustical shock load destabilize the system while an increased geometric nonlinearity helps to stabilize the microphone and expands its stable operational range.

Nonlinear approximate analytical solutions to the governing equations for the microphone under both electrical square and sinusoidal excitations are obtained to extract system parameters from experimental data. Specifically, for the first time, an approximate analytical solution to a general damped second-order system with quadratic and cubic nonlinearities and non-zero step loading is obtained via a multiple time scales (MTS) method. An approximate analytical solution to a general inhomogeneous nonlinear damped second order system under the harmonic excitation is obtained via a harmonic balance (HB) method. Different forms of the derived MTS approximate solution are provided and can be applied to many other applications, such as the study of a large-angle motion of a simple pendulum [72]. Discussions and validity regions of the derived MTS and HB approximate solutions are provided. Also, two steady-state approximate solutions for the microphone under the sinusoidal acoustical pressure excitation are provided via HB and MTS methods.

A series of preliminary experiments are conducted and system parameters are extracted from two types of experimental data respectively. The preliminary uncertainty analysis, which includes only the uncertainties caused by fabrication, shows that the experimentally extracted linear natural frequency, damping ratio and nonlinear stiffness parameter fall within their conservative theoretical ranges for a 95% confidence level.

Recommendations for Future Work

In the first-generation dual-backplate capacitive MEMS microphone, the top backplate has the largest area while the bottom backplate has the smallest area. The thickness of the top backplate is same with the diaphragm and smaller than the thickness of the bottom backplate. Further analysis shows that the top backplate has the highest compliance, followed by the middle diaphragm and bottom backplate, respectively.

Since the stable operational range of the microphone will be reduced by the compliant backplates; therefore, in the future design, two backplates need to be further stiffened. Theoretically, there are many ways to achieve this goal, such as increasing the thickness of the backplate or using some material with a higher Young's modulus than that of polysilicon. Practically, however, due to the physical constraints imposed by the SUMMiT V process at Sandia National Laboratories, the thickness, residual stress and the material property of each layer are fixed [66, 98]. One possible way to stiffen the backplates of the microphone is through the deposition of extra layers with desired tensile stresses on each backplate during the post-processing.

Some additional future contributions could be:

- Experimental results presented are preliminary, and relatively large errors could possibly exist for the extracted system parameters. To obtain more accurate and reliable results, characterization experiments need to be repeated for the applied electrical excitations with a wide range of voltage amplitudes on more released microphone devices. Also, the presented uncertainty analysis in this dissertation is conservative since it only considers the uncertainties caused by the fabrication process. More accurate uncertainty analyses might be conducted.
- The stiffnesses of the backplates might be experimentally characterized via a laser vibrometer. The top backplate can be accessed directly by a laser beam. To be able to characterize the bottom backplate, the microphone chip might need to be flipped such that the laser beam can impinge the bottom backplate through the back cavity.
- Experiments for the microphone under the sinusoidal pressure wave excitation might be carried out in a plane wave tube (PWT) with an expanded bandwidth over the linear natural frequency of the microphone. The obtained experiment results can be compared with the theoretical analysis results presented in this dissertation.
- Pull-in experiments for the microphone under the acoustic pressure and electrical voltage excitations might be carried out. The obtained experimental results can be compared with the theoretical analysis results presented in this dissertation.
- Since dynamic pull-in can dangerously take place below the quasi-static pull-in voltage due to the complex interaction of nonlinearities, the study of dynamic effects on the pull-in limit becomes very important for many electrostatically actuated MEMS devices. The dynamic pull-in analyses for the AC voltage

excitation with a frequency close to the first resonant frequency of the microphone could be carried out. This study could include an approximate analytical solution for a parametrically excited system via a multiple time scales method, and bifurcation and instability analyses.

APPENDIX A
LARGE DISPLACEMENT ENERGY SOLUTION OF A CIRCULAR DIAPHRAGM

The detailed steps to derive the large displacement solution for a clamped circular diaphragm based on the energy method [97, 99] are presented in this appendix. As mentioned in Chapter 3, the polar coordinate is introduced to facilitate the analysis for a circular diaphragm. When large displacements occur, the radial displacement in the neutral plane of the diaphragm cannot be neglected. The displacement of a point in the neutral plane of a circular diaphragm is decomposed into two components: $u(r)$ in the radial direction and $w(r)$ perpendicular to the neutral plane as shown in Figure 3-4.

The shape of the transverse deflection surface of a circular diaphragm is assumed to be similar with the small displacement case, which is defined in Eq. (3.7) as follows

$$w(r) = w_0 \left(1 - \frac{r^2}{a^2} \right)^2, \quad (\text{A.1})$$

where w_0 is the unknown center displacement and needs to be determined. The assumed transverse deflection satisfies the clamped boundary conditions

$$w(a) = \left. \frac{dw(r)}{dr} \right|_{r=a} = 0. \quad (\text{A.2})$$

To satisfy the clamped boundary conditions, the radial displacement $u(r)$ must vanish at the edge and the origin of the circular diaphragm; therefore, the following polynomial is used to approximate the complex expression of the radial displacement [99]

$$u(r) = r(a - r)(C_1 + C_2 r), \quad (\text{A.3})$$

where C_1 and C_2 are the two unknown constants.

Based on the von Kármán plate theory, the strain-displacement relations [99, 101] in the radial and tangential directions are given by

$$\varepsilon_r = \frac{du}{dr} + \frac{1}{2} \left(\frac{dw}{dr} \right)^2, \quad (\text{A.4})$$

and

$$\varepsilon_\theta = \frac{u}{r}. \quad (\text{A.5})$$

By applying Hooke's law for the 2D case [123], the following relations can be obtained

$$\varepsilon_r = \frac{1}{E} (\sigma_r - \nu \sigma_\theta) = \frac{1}{Eh} (N_r - \nu N_\theta), \quad (\text{A.6})$$

and

$$\varepsilon_\theta = \frac{1}{E} (\sigma_\theta - \nu \sigma_r) = \frac{1}{Eh} (N_\theta - \nu N_r), \quad (\text{A.7})$$

where σ_r and σ_θ are the stresses in the radial and tangential directions respectively, and N_r and N_θ are the corresponding forces per unit length in the radial and tangential directions. Solving N_r and N_θ from Eqs. (A.6) and (A.7) simultaneously yields

$$N_r = \frac{Eh}{1 - \nu^2} (\varepsilon_r + \nu \varepsilon_\theta), \quad (\text{A.8})$$

and

$$N_\theta = \frac{Eh}{1 - \nu^2} (\varepsilon_\theta + \nu \varepsilon_r). \quad (\text{A.9})$$

Therefore the strain energy due to the transverse bending $w(r)$ is calculated as

$$V_b = \frac{D}{2} \int_0^{2\pi} \int_0^a \left[\left(\frac{\partial^2 w}{\partial r^2} \right)^2 + \frac{1}{r^2} \left(\frac{\partial w}{\partial r} \right)^2 + \frac{2\nu}{r} \frac{\partial w}{\partial r} \frac{\partial^2 w}{\partial r^2} \right] r dr d\theta = \frac{32\pi D}{3} \frac{w_0^2}{a^2}. \quad (\text{A.10})$$

The strain energy due to the in-plane stretching $u(r)$ is

$$V_s = h \int_0^{2\pi} \int_0^a \left(\frac{\sigma_r \varepsilon_r}{2} + \frac{\sigma_\theta \varepsilon_\theta}{2} \right) r dr d\theta = \int_0^{2\pi} \int_0^a \left(\frac{N_r \varepsilon_r}{2} + \frac{N_\theta \varepsilon_\theta}{2} \right) r dr d\theta. \quad (\text{A.11})$$

The total strain energy is the sum of two strain energy components due to the transverse bending and in-plane stretching respectively, and it is given by

$$V = V_b + V_s. \quad (\text{A.12})$$

Also the external work done by the uniform transverse pressure is calculated as

$$\Omega = \int_0^{2\pi} \int_0^a p w(r) r dr d\theta = \frac{\pi}{3} p a^2 w_0. \quad (\text{A.13})$$

The total potential energy is obtained as

$$\Pi = V - \Omega = V_b + V_s - \Omega. \quad (\text{A.14})$$

According to the principle of the minimum potential energy [97] when an equilibrium is reached, the three unknowns: w_0 (the center displacement), C_1 and C_2 , can be determined by solving the following equations simultaneously

$$\begin{cases} \frac{\partial \Pi}{\partial C_1} = 0 \\ \frac{\partial \Pi}{\partial C_2} = 0. \\ \frac{d\Pi}{dw_0} = 0 \end{cases} \quad (\text{A.15})$$

Specifically, for a polysilicon diaphragm, the Poisson's ratio is $\nu = 0.22$. Substituting Eqs. (A.1), (A.3), (A.4), (A.5), (A.8), and (A.9) into Eq. (A.11), and evaluating the result with $\nu = 0.22$ yield

$$V_s = 0.8533 E h a^4 C_1^2 + (0.9904 E h a^5 C_2 - 0.293 E h a w_0^2) C_1$$

$$+0.3852Eha^6C_2^2 + 0.1434Ehw_0^2a^2C_2 + 1.006Eh\frac{w_0^4}{a^2}. \quad (\text{A.16})$$

By substituting Eqs. (A.10), (A.16) and (A.13) into Eq. (A.14), finally, we can solve Eqs. (A.15) simultaneously as follows

$$C_1 = 1.2652\frac{w_0^2}{a^3}, \quad (\text{A.17})$$

$$C_2 = -1.8129\frac{w_0^2}{a^3}, \quad (\text{A.18})$$

and

$$w_0 = \frac{pa^4}{64D} \frac{1}{1 + 0.4708\frac{w_0^2}{h^2}}. \quad (\text{A.19})$$

Substituting Eqs (A.17) and (A.18) back into Eqs. (A.16) and (A.12), we can obtain the results for the strain energy in terms of w_0

$$V_s = 2.511\pi D \frac{w_0^4}{a^2h^2}. \quad (\text{A.20})$$

and

$$V = V_b + V_s = \frac{32}{3}\pi D \frac{w_0^2}{a^2} \left(1 + 0.2354\frac{w_0^2}{h^2} \right). \quad (\text{A.21})$$

The final approximate expression for the large transverse displacement solution can be obtained by substituting the solution of w_0 from Eq. (A.19) into Eq. (A.1).

Rewriting Eq. (A.19) becomes

$$w_0 \left(1 + 0.4708\frac{w_0^2}{h^2} \right) = \frac{pa^4}{64D}. \quad (\text{A.22})$$

As we can see from Eq. (A.22), a cubic equation for the center displacement w_0 is obtained. The small factor $0.4708 w_0^2/h^2$ represents a geometric nonlinearity (nonlinear spring hardening effect) due to the in-plane stretching when large displacements occur.

As seen from Eq. (A.1), the assumed mode shape based on this energy approach is not affected by the applied pressure. Shown in Figure 3-5 is a plot of different normalized mode shapes for several pressure values. In the plot, three normalized mode shapes are generated based on the exact solution given in the reference [100]. As we can see from Figure 3-5, for larger pressure values (for example, 100000 Pa), the assumed mode shape used in the energy approach is not accurate. However, for our 2000Pa microphone design, the assumed mode shape in the energy approach is in good agreement with the exact mode shape as shown in Figure 3-5.

APPENDIX B
APPROXIMATE SOLUTION FOR A GENERAL NONLINEAR SECOND ORDER
SYSTEM

This appendix provides the mathematical background and detailed derivation of the formula used in the electrical square wave excitation experiments to extract system parameters for a dual-backplate capacitive MEMS microphone.

Introduction

From Chapter 4, for the characterization experiments with the Polytec laser vibrometer, no acoustical pressure exists on the diaphragm and only a uni-polar square wave $V(t)$ is applied directly to bottom (or top) backplate with diaphragm and the other backplate electrically grounded. During the up-stroke of the square wave, and if the voltage is applied to the top backplate, the approximate governing equation for the forced vibration of the diaphragm is as follows,

$$\ddot{x} + \beta_1 \dot{x} + \beta_2 x + \beta_3 x^2 + \beta_4 x^3 = \beta_5, \quad (\text{B.1})$$

where

$$\beta_1 = \frac{b}{M_{me}}, \quad (\text{B.2})$$

$$\beta_2 = \frac{k_1 + k_c}{M_{me}} - \frac{\varepsilon_0 A_{me} V_0^2}{M_{me} d_0^3}, \quad (\text{B.3})$$

$$\beta_3 = -\frac{3\varepsilon_0 A_{me} V_0^2}{2M_{me} d_0^4}, \quad (\text{B.4})$$

$$\beta_4 = \frac{k_3}{M_{me}} - \frac{2\varepsilon_0 A_{me} V_0^2}{M_{me} d_0^5}, \quad (\text{B.5})$$

and

$$\beta_5 = \frac{\varepsilon_0 A_{me} V_0^2}{2M_{me} d_0^2}. \quad (\text{B.6})$$

Physically, Eq. (B.1) represents a more general damped second order system with both quadratic and cubic nonlinearities (β_3 and β_4) and a non-zero external step loading (β_5). During the down-stroke of the square wave, the governing equation for the free vibration of diaphragm is

$$M_{me} \ddot{x} + b\dot{x} + (k_1 + k_c)x + k_3 x^3 = 0. \quad (\text{B.7})$$

The above equation can be rewritten as

$$\ddot{x} + \beta_1 \dot{x} + \beta_2' x + \beta_4' x^3 = 0, \quad (\text{B.8})$$

where

$$\beta_1 = \frac{b}{M_{me}}, \quad (\text{B.9})$$

$$\beta_2' = \beta_2 \Big|_{V_0=0} = \frac{k_1 + k_c}{M_{me}}, \quad (\text{B.10})$$

and

$$\beta_4' = \beta_4 \Big|_{V_0=0} = \frac{k_3}{M_{me}}. \quad (\text{B.11})$$

Eq. (B.7) or (B.8) is a special case of the general equation Eq. (B.1). Since there is no closed-form solution to Eq. (B.1), in the next section, its approximate solution is obtained by a multiple time scales method. The approximate solution to Eq. (B.7) or (B.8) can be then obtained by altering the general approximate solution to Eq. (B.1).

Approximate Solution by the Multiple Time Scales Method

To proceed with the approximate solution, we need to non-dimensionalize the governing equation in Eq. (B.1), which finally leads to

$$y'' + \alpha_1 y' + \alpha_2 y + \alpha_3 y^2 + \alpha_4 y^3 = \alpha_5, \quad (\text{B.12})$$

where

$$y = \frac{x}{d_0}, \quad (\text{B.13})$$

$$y' = \frac{dy}{d\tau}, \quad (\text{B.14})$$

$$y'' = \frac{d^2 y}{d\tau^2}, \quad (\text{B.15})$$

$$\tau = \omega_0 t, \quad (\text{B.16})$$

$$\omega_0 = \sqrt{(k_1 + k_c)/M_{me}}, \quad (\text{B.17})$$

$$\alpha_1 = \frac{b}{M_{me} \omega_0}, \quad (\text{B.18})$$

$$\alpha_2 = 1 - \frac{\varepsilon_0 A_{me} V_0^2}{M_{me} \omega_0^2 d_0^3}, \quad (\text{B.19})$$

$$\alpha_3 = -\frac{3\varepsilon_0 A_{me} V_0^2}{2M_{me} d_0^3 \omega_0^2}, \quad (\text{B.20})$$

$$\alpha_4 = \frac{k_3 d_0^2}{M_{me} \omega_0^2} - \frac{2\varepsilon_0 A_{me} V_0^2}{M_{me} d_0^3 \omega_0^2}, \quad (\text{B.21})$$

and

$$\alpha_5 = \frac{\varepsilon_0 A_{me} V_0^2}{2M_{me} d_0^3 \omega_0^2}. \quad (\text{B.22})$$

The approximate solution of Eq. (B.12) is assumed as a second order expansion in terms of a small positive parameter ε (a book keeping parameter),

$$y(\tau) = y_0(\tau_0, \tau_1, \tau_2) + \varepsilon y_1(\tau_0, \tau_1, \tau_2) + \varepsilon^2 y_2(\tau_0, \tau_1, \tau_2), \quad (\text{B.23})$$

where the multiple independent time scales are defined as

$$\tau_0 = \tau, \tau_1 = \varepsilon\tau, \text{ and } \tau_2 = \varepsilon^2\tau. \quad (\text{B.24})$$

Therefore, the time derivatives with respect to t become the following expansion terms of the partial derivatives with respect to the corresponding time scales

$$\frac{d}{d\tau} = D_0 + \varepsilon D_1 + \varepsilon^2 D_2, \quad (\text{B.25})$$

and

$$\frac{d^2}{d\tau^2} = D_0^2 + 2\varepsilon D_0 D_1 + 2\varepsilon^2 D_0 D_2 + \varepsilon^2 D_1^2, \quad (\text{B.26})$$

where

$$D_0 = \frac{d}{d\tau_0}, D_1 = \frac{d}{d\tau_1} \text{ and } D_2 = \frac{d}{d\tau_2}. \quad (\text{B.27})$$

The coefficients in Eq. (B.12) are further ordered to show up in the $O(\varepsilon^2)$ by doing the following substitution

$$\alpha_1 = \varepsilon^2 \mu_1, \alpha_2 = \Omega^2, \alpha_3 = \varepsilon^2 \mu_3 \text{ and } \alpha_4 = \varepsilon^2 \mu_4. \quad (\text{B.28})$$

Then Eq. (B.12) is changed into

$$y'' + \varepsilon^2 \mu_1 y' + \Omega^2 y + \varepsilon^2 \mu_3 y^2 + \varepsilon^2 \mu_4 y^3 = \alpha_5. \quad (\text{B.29})$$

After the substitution of Eqs. (B.23), (B.24), (B.25), (B.26) and (B.27) into Eq. (B.29), the individual terms in the above equation are

$$\begin{aligned} y'' &= D_0^2 y_0 + \varepsilon (2D_0 D_1 y_0 + D_0^2 y_1) \\ &+ \varepsilon^2 (2D_0 D_2 y_0 + D_1^2 y_0 + 2D_0 D_1 y_1 + D_0^2 y_2) + O(\varepsilon^3), \end{aligned} \quad (\text{B.30})$$

$$\varepsilon^2 \mu_1 y' = \varepsilon^2 (\mu_1 D_0 y_0) + O(\varepsilon^3), \quad (\text{B.31})$$

$$\Omega^2 y = \Omega^2 y_0 + \varepsilon (\Omega^2 y_1) + \varepsilon^2 (\Omega^2 y_2) + O(\varepsilon^3), \quad (\text{B.32})$$

$$\varepsilon^2 \mu_3 y^2 = \varepsilon^2 (\mu_3 y_0^2) + O(\varepsilon^3), \quad (\text{B.33})$$

and

$$\varepsilon^2 \mu_4 y^3 = \varepsilon^2 (\mu_4 y_0^3) + O(\varepsilon^3). \quad (\text{B.34})$$

The following expressions are obtained after separating Eq. (B.29) into orders of ε

$$O(\varepsilon^0): D_0^2 y_0 + \Omega^2 y_0 = \alpha_5, \quad (\text{B.35})$$

$$O(\varepsilon^1): D_0^2 y_1 + \Omega^2 y_1 = -2D_0 D_1 y_0, \quad (\text{B.36})$$

and

$$O(\varepsilon^2): D_0^2 y_2 + \Omega^2 y_2 = -2D_0 D_1 y_1 - 2D_0 D_2 y_0 - D_1^2 y_0 - \mu_1 D_0 y_0 - \mu_3 y_0^2 - \mu_4 y_0^3. \quad (\text{B.37})$$

The general solution to Eq. (B.35) is

$$y_0 = \frac{\alpha_5}{\alpha_2} + A(\tau_1, \tau_2) e^{i\Omega\tau_0} + \bar{A}(\tau_1, \tau_2) e^{-i\Omega\tau_0}, \quad (\text{B.38})$$

where $\frac{\alpha_5}{\alpha_2}$ is a particular solution, and $A(\tau_1, \tau_2)$ and $\bar{A}(\tau_1, \tau_2)$ are complex conjugates.

The following expression is obtained by substituting Eq. (B.38) into (B.36)

$$D_0^2 y_1 + \Omega^2 y_1 = -2i\Omega \left[e^{i\Omega\tau_0} D_1 A(\tau_1, \tau_2) - e^{-i\Omega\tau_0} D_1 \bar{A}(\tau_1, \tau_2) \right]. \quad (\text{B.39})$$

Elimination of the secular terms (the term that makes the solution divergent and unbounded) in Eq. (B.39) requires that $D_1 A(\tau_1, \tau_2)$ and $D_1 \bar{A}(\tau_1, \tau_2)$ are zero, which means that A and \bar{A} are only functions of τ_2 . Therefore, the solution for Eq. (B.39) can be written as

$$y_1 = B(\tau_1, \tau_2) e^{i\Omega\tau_0} + \bar{B}(\tau_1, \tau_2) e^{-i\Omega\tau_0}, \quad (\text{B.40})$$

where $B(\tau_1, \tau_2)$ and $\bar{B}(\tau_1, \tau_2)$ are complex conjugates. Substituting Eqs. (B.38) and

(B.40) into the right hand side of Eq. (B.37) yields

$$-2D_0 D_1 y_1 = -2i\Omega (D_1 B) \cdot e^{i\Omega\tau_0} + 2i\Omega (D_1 \bar{B}) \cdot e^{-i\Omega\tau_0}, \quad (\text{B.41})$$

$$-2D_0D_2y_0 = -2i\Omega(D_2A) \cdot e^{i\Omega\tau_0} + 2i\Omega(D_2\bar{A}) \cdot e^{-i\Omega\tau_0}, \quad (\text{B.42})$$

$$-D_1^2y_0 = 0, \quad (\text{B.43})$$

$$-\mu_1D_0y_0 = -i\Omega\mu_1A \cdot e^{i\Omega\tau_0} + i\Omega\mu_1\bar{A} \cdot e^{-i\Omega\tau_0}, \quad (\text{B.44})$$

$$-\mu_3y_0^2 = -2\mu_3\frac{\alpha_5}{\alpha_2}A \cdot e^{i\Omega\tau_0} - 2\mu_3\frac{\alpha_5}{\alpha_2}\bar{A} \cdot e^{-i\Omega\tau_0} + O.H.T., \quad (\text{B.45})$$

and

$$-\mu_4y_0^3 = -3\mu_4A\left(\frac{\alpha_5^2}{\alpha_2^2} + A\bar{A}\right) \cdot e^{i\Omega\tau_0} - 3\mu_4\bar{A}\left(\frac{\alpha_5^2}{\alpha_2^2} + A\bar{A}\right) \cdot e^{-i\Omega\tau_0} + O.H.T., \quad (\text{B.46})$$

where *O.H.T.* are other harmonic terms that are neglected in the following analysis.

Elimination of the secular terms in Eq. (B.37) requires

$$e^{i\Omega\tau_0} : -2i\Omega D_1B - 2i\Omega D_2A - i\mu_1\Omega A - 2\mu_3\frac{\alpha_5}{\alpha_2}A - 3\mu_4\left(\frac{\alpha_5^2}{\alpha_2^2} + |A|^2\right)A = 0, \quad (\text{B.47})$$

and

$$e^{-i\Omega\tau_0} : 2i\Omega D_1\bar{B} + 2i\Omega D_2\bar{A} + i\mu_1\Omega\bar{A} - 2\mu_3\frac{\alpha_5}{\alpha_2}\bar{A} - 3\mu_4\left(\frac{\alpha_5^2}{\alpha_2^2} + |A|^2\right)\bar{A} = 0. \quad (\text{B.48})$$

Eqs. (B.47) and (B.48) are not independent because they are complex conjugates.

Hence, if one of them is satisfied, the other is automatically satisfied. Only Eq. (B.47) is considered in the following analysis. Since A is only a function of the time scale τ_2 , it follows from Eq. (B.47) that $B \propto \tau_1$. Therefore x_1 is unbounded as $\tau_1 \rightarrow \infty$ unless

$$D_1B = 0. \quad (\text{B.49})$$

Using Eq. (B.49), Eq. (B.47) can be rewritten as

$$-2i\Omega D_2A - i\mu_1\Omega A - \left(2\mu_3\frac{\alpha_5}{\alpha_2} + 3\mu_4\frac{\alpha_5^2}{\alpha_2^2}\right)A - 3\mu_4A|A|^2 = 0. \quad (\text{B.50})$$

The polar forms for the $A(\tau_2)$ and $\bar{A}(\tau_2)$ can be written as

$$A(\tau_2) = \frac{1}{2} R(\tau_2) e^{i\phi(\tau_2)} \quad (\text{B.51})$$

and

$$\bar{A}(\tau_2) = \frac{1}{2} R(\tau_2) e^{-i\phi(\tau_2)}, \quad (\text{B.52})$$

where R is the amplitude of x_0 and ϕ is the phase angle. Substituting Eq. (B.51) into

(B.50) and separating each term into the real and imaginary components results in

$$-2i\Omega D_2 A = \left[\frac{dR}{d\tau_2} \sin(\phi) + \frac{d\phi}{d\tau_2} R \cdot \cos(\phi) \right] \Omega - \left[\frac{dR}{d\tau_2} \cos(\phi) - \frac{d\phi}{d\tau_2} R \cdot \sin(\phi) \right] \Omega \cdot i, \quad (\text{B.53})$$

$$-i\mu_1 \Omega A = \frac{1}{2} R \mu_1 \Omega \cdot \sin(\phi) - \frac{1}{2} R \mu_1 \Omega \cdot \cos(\phi) \cdot i, \quad (\text{B.54})$$

$$\begin{aligned} -\left(2\mu_3 \frac{\alpha_5}{\alpha_2} + 3\mu_4 \frac{\alpha_5^2}{\alpha_2^2} \right) A &= -\frac{1}{2} R \left(2\mu_3 \frac{\alpha_5}{\alpha_2} + 3\mu_4 \frac{\alpha_5^2}{\alpha_2^2} \right) \cdot \cos(\phi) \\ &\quad - \frac{1}{2} R \left(2\mu_3 \frac{\alpha_5}{\alpha_2} + 3\mu_4 \frac{\alpha_5^2}{\alpha_2^2} \right) \cdot \sin(\phi) \cdot i, \end{aligned} \quad (\text{B.55})$$

and

$$-3\mu_4 A |A|^2 = -\frac{3}{8} \mu_4 R^3 \cos(\phi) - \frac{3}{8} \mu_4 R^3 \sin(\phi) \cdot i. \quad (\text{B.56})$$

Therefore, the real and imaginary components in the left hand side of Eq. (B.50)

are

$$\begin{aligned} \text{Real: } &\left[\frac{d\phi}{d\tau_2} R \Omega - \frac{1}{2} R \left(2\mu_3 \frac{\alpha_5}{\alpha_2} + 3\mu_4 \frac{\alpha_5^2}{\alpha_2^2} \right) - \frac{3}{8} \mu_4 R^3 \right] \cdot \cos(\phi) \\ &+ \left(\frac{dR}{d\tau_2} \Omega + \frac{1}{2} R \mu_1 \Omega \right) \cdot \sin(\phi) = 0, \end{aligned} \quad (\text{B.57})$$

and

$$\begin{aligned} \text{Imag: } & \left[\frac{d\phi}{d\tau_2} R\Omega - \frac{1}{2} R \left(2\mu_3 \frac{\alpha_5}{\alpha_2} + 3\mu_4 \frac{\alpha_5^2}{\alpha_2^2} \right) - \frac{3}{8} \mu_4 R^3 \right] \cdot \sin(\phi) \\ & + \left(\frac{dR}{d\tau_2} \Omega + \frac{1}{2} R\mu_1\Omega \right) \cdot \cos(\phi) = 0. \end{aligned} \quad (\text{B.58})$$

Solving Eqs. (B.57) and (B.58) simultaneously results in

$$\frac{dR}{d\tau_2} + \frac{1}{2} \mu_1 R = 0, \quad (\text{B.59})$$

and

$$\frac{d\phi}{d\tau_2} - \frac{2\mu_3\alpha_5\alpha_2 + 3\mu_4\alpha_5^2}{2\Omega\alpha_2^2} - \frac{3\mu_4}{8\Omega} R^2 = 0. \quad (\text{B.60})$$

The solutions for R and ϕ are

$$R(\tau_2) = R_0 e^{-\frac{1}{2}\mu_1\tau_2}, \quad (\text{B.61})$$

and

$$\phi(\tau_2) = \frac{2\mu_3\alpha_5\alpha_2 + 3\mu_4\alpha_5^2}{2\Omega\alpha_2^2} \tau_2 - \frac{3\mu_4 R_0^2}{8\Omega\mu_1} e^{-\mu_1\tau_2} + \phi_0, \quad (\text{B.62})$$

where R_0 and ϕ_0 are constants determined by the initial conditions. Combining Eqs.

(B.23), (B.38), (B.51), (B.61) and (B.62), the approximate solution for the transient

motion $y(\tau)$ is

$$\begin{aligned} y(\tau) & \approx y_0(\tau_0, \tau_1, \tau_2) = \frac{\alpha_5}{\alpha_2} + A(\tau_2) e^{i\Omega\tau_0} + \bar{A}(\tau_2) e^{-i\Omega\tau_0} = \frac{\alpha_5}{\alpha_2} + R \cdot \cos(\Omega\tau_0 + \phi) \\ & = \frac{\alpha_5}{\alpha_2} + R_0 e^{-\frac{1}{2}\mu_1\tau_2} \cos\left(\Omega\tau_0 + \frac{2\mu_3\alpha_5\alpha_2 + 3\mu_4\alpha_5^2}{2\Omega\alpha_2^2} \tau_2 - \frac{3\mu_4 R_0^2}{8\Omega\mu_1} e^{-\mu_1\tau_2} + \phi_0 \right). \end{aligned} \quad (\text{B.63})$$

From Eqs. (B.16), (B.24) and (B.28), we have the following expressions

$$\tau_0 = \omega_0 t, \quad (\text{B.64})$$

$$\mu_1 \tau_2 = \alpha_1 \omega_0 t, \quad (\text{B.65})$$

$$\frac{2\mu_3\alpha_5\alpha_2 + 3\mu_4\alpha_5^2}{2\Omega\alpha_2^2}\tau_2 = \frac{2\alpha_2\alpha_3\alpha_5 + 3\alpha_4\alpha_5^2}{2\Omega\alpha_2^2}\omega_0 t, \quad (\text{B.66})$$

and

$$\frac{\mu_4}{\mu_1} = \frac{\alpha_4}{\alpha_1}. \quad (\text{B.67})$$

Using Eqs. (B.13), (B.28), (B.63) to (B.67), finally the general multiple time scales solution for $x(t)$ is

$$x(t) = \frac{\alpha_5}{\alpha_2}d_0 + R_0d_0e^{-\frac{1}{2}\alpha_1\omega_0 t} \cos \left[\left(\sqrt{\alpha_2} + \frac{2\alpha_2\alpha_3\alpha_5 + 3\alpha_4\alpha_5^2}{2\alpha_2^{\frac{5}{2}}} \right) \omega_0 t - \frac{3\alpha_4R_0^2}{8\alpha_1\sqrt{\alpha_2}} e^{-\alpha_1\omega_0 t} + \phi_0 \right]. \quad (\text{B.68})$$

APPENDIX C
COEFFICIENTS OF THE APPROXIMATE HARMONIC BALANCE SOLUTION

The expressions for the coefficients in Eqs. (4.62) and (4.64) are provided in this appendix as follows

$$B_{11} = 0, \quad (\text{C.1})$$

$$B_{12} = A_0 - A_2^2 - 2A_0^2 + A_0^3 + \frac{3}{2}A_2^2A_0, \quad (\text{C.2})$$

$$B_{13} = -2A_0^4 + \frac{3}{2}A_2^2A_0 + \frac{15}{8}A_2^4A_0 + A_0^5 + A_0^3 + 5A_2^2A_0^3 - 6A_2^2A_0^2 - \frac{3}{4}A_2^4, \quad (\text{C.3})$$

$$B_{14} = -1, \quad (\text{C.4})$$

$$B_{21} = \Omega \left(2A_2A_0 - A_2A_0^2 - A_2 - \frac{1}{4}A_2^3 \right) \sin(\varphi), \quad (\text{C.5})$$

$$B_{22} = \left(\frac{1}{2}A_2 + \frac{3}{2}A_2A_0^2 + \frac{3}{8}A_2^3 - 2A_2A_0 \right) \cos(\varphi), \quad (\text{C.6})$$

$$B_{23} = \left(\frac{3}{8}A_2^3 + \frac{5}{16}A_2^5 + \frac{15}{4}A_2^3A_0^2 - 3A_2^3A_0 + \frac{5}{2}A_2A_0^4 + \frac{3}{2}A_2A_0^2 - 4A_2A_0^3 \right) \cos(\varphi), \quad (\text{C.7})$$

$$B_{24} = -\frac{1}{2}, \quad (\text{C.8})$$

$$B_{31} = \Omega \left(A_2A_0^2 + A_2 + \frac{1}{4}A_2^3 - 2A_2A_0 \right) \cos(\varphi), \quad (\text{C.9})$$

$$B_{32} = \left(\frac{1}{2}A_2 + \frac{3}{2}A_2A_0^2 + \frac{3}{8}A_2^3 - 2A_2A_0 \right) \sin(\varphi), \quad (\text{C.10})$$

$$B_{33} = \left(\frac{3}{8}A_2^3 + \frac{5}{16}A_2^5 + \frac{15}{4}A_2^3A_0^2 - 3A_2^3A_0 + \frac{5}{2}A_2A_0^4 + \frac{3}{2}A_2A_0^2 - 4A_2A_0^3 \right) \sin(\varphi), \quad (\text{C.11})$$

$$B_{34} = 0, \quad (\text{C.12})$$

$$C_1 = 4A_2^2 A_0 \Omega^2 - 4A_2^2 \Omega^2, \quad (\text{C.13})$$

$$C_2 = \Omega^2 \left(2A_2 A_0^2 + \frac{3}{2} A_2^3 + 2A_2 - 4A_2 A_0 \right) \cos(\varphi), \quad (\text{C.14})$$

and

$$C_3 = \Omega^2 \left(2A_2 A_0^2 + \frac{3}{2} A_2^3 + 2A_2 - 4A_2 A_0 \right) \sin(\varphi). \quad (\text{C.15})$$

APPENDIX D
APPROXIMATE SOLUTIONS FOR A SINUSOIDAL ACOUSTICAL PRESSURE
EXCITATION

This appendix provides the mathematical background and derivation of the approximate solutions for the microphone under the sinusoidal acoustical pressure excitation. From Chapter 4, during the sinusoidal acoustical pressure excitation, no AC excitations exist between the diaphragm and backplates. DC voltages ($\pm V_b$) are applied to bias the bottom and top backplates with respect to the diaphragm. The governing equation is as follows,

$$M_{me}\ddot{x} + b\dot{x} + (k_1 + k_c)x + k_3x^3 = -\frac{\varepsilon A_{me}}{2} \left[\frac{V_b^2}{(d_0 + x)^2} - \frac{V_b^2}{(d_0 - x)^2} \right] + A_{me}p_0 \cos(\omega_p t), \quad (\text{D.1})$$

where V_b is the applied DC bias voltage, p_0 and ω_p are the amplitude and driving frequency of the acoustical plane wave respectively.

A Taylor's series expansion for the nonlinear net electrostatic force up to the 3rd order results in

$$-\frac{\varepsilon_0 A_{me}}{2} \left[\frac{V_b^2}{(d_0 + x)^2} - \frac{V_b^2}{(d_0 - x)^2} \right] \approx \frac{2\varepsilon_0 A_{me} V_b^2}{d_0^3} x + \frac{4\varepsilon_0 A_{me} V_b^2}{d_0^5} x^3. \quad (\text{D.2})$$

For the accuracy of the above 3rd order Taylor's series expansion, please see Figure 4-14 in Chapter 4 for details. Substitution of Eq. (D.2) into (D.1) yields

$$M_{me}\ddot{x} + b\dot{x} + (k_1 + k_c - k_{1E})x + (k_3 - k_{3E})x^3 = A_{me}p_0 \cos(\omega_p t), \quad (\text{D.3})$$

where the two equivalent electrical spring constants are defined as follows,

$$k_{1E} \triangleq \frac{2\varepsilon_0 A_{me} V_b^2}{d_0^3}, \quad (\text{D.4})$$

and

$$k_{3E} \triangleq \frac{2\varepsilon_0 A_{me} V_b^2}{d_0^5}. \quad (\text{D.5})$$

Physically, Eq. (D.3) represents a damped second order system with only cubic mechanical and electrical nonlinearities and an external excitation. Mathematically, Eq. (D.3) represents a forced damped Duffing's equation, and there is no closed-form solution to it. In the following section, two approximate methods (harmonic balance method and multiple time scales method) are used to obtain its approximate solutions in the steady state.

Prior to finding the approximate solutions in the steady state, we need to non-dimensionalize the governing equation in Eq. (D.3), which finally leads to

$$y'' + 2\bar{\zeta} y' + y + \bar{\theta} y^3 = \bar{P} \cos(\Omega\tau), \quad (\text{D.6})$$

where

$$y = \frac{x}{d_0}, \quad (\text{D.7})$$

$$y' = \frac{dy}{d\tau}, \quad (\text{D.8})$$

$$y'' = \frac{d^2 y}{d\tau^2}, \quad (\text{D.9})$$

$$\tau = \bar{\omega}_0 t, \quad (\text{D.10})$$

$$\bar{\omega}_0 = \sqrt{(k_1 + k_c - k_{1E})/M_{me}}, \quad (\text{D.11})$$

$$\bar{\zeta} = \frac{b}{2M_{me}\bar{\omega}_0}, \quad (\text{D.12})$$

$$\bar{\theta} = \frac{k_3 - k_{3E}}{M_{me} \bar{\omega}_0^2} d_0^2, \quad (\text{D.13})$$

$$\bar{P} = \frac{p_0 A_{me}}{M_{me} \bar{\omega}_0^2 d_0}, \quad (\text{D.14})$$

and

$$\Omega = \frac{\omega_p}{\bar{\omega}_0}, \quad (\text{D.15})$$

where y and y' are the non-dimensional center displacement and velocity of the diaphragm respectively, $\bar{\omega}_0$ is the modified natural frequency of the system, τ is the dimensionless time, $\bar{\zeta}$ is the modified damping ratio, $\bar{\theta}$ is the modified nonlinear stiffness parameter, \bar{P} is the external forcing parameter and Ω is the ratio of the pressure driving frequency over the system's natural frequency.

HB Approximate Solution

The harmonic balance approximate solution to Eq. (D.6) in the steady state is expressed in a Fourier series as follows [72]

$$y(\tau) = \sum_{n=0}^{\infty} a_n \cos[n(\Omega\tau + \phi)], \quad (\text{D.16})$$

where a_n is the amplitude of the n^{th} harmonic and ϕ is the phase angle. Therefore, the time derivatives are

$$y' = -\sum_{n=0}^{\infty} n\Omega a_n \sin(\varphi_n) \quad (\text{D.17})$$

and

$$y'' = -\sum_{n=0}^{\infty} n^2 \Omega^2 a_n \cos(\varphi_n), \quad (\text{D.18})$$

where

$$\varphi_n = n(\Omega\tau + \phi). \quad (\text{D.19})$$

If only the first three terms ($n=0,1$ and 2) in Eq. (D.16) are considered, by substituting Eqs. (D.16), (D.17) and (D.18) into Eq. (D.6), we have

$$\begin{aligned} & \left[-a_1\Omega^2 \cos(\varphi_1) - 4a_2\Omega^2 \cos(\varphi_2) \right] + 2\bar{\zeta} \left[-a_1\Omega \sin(\varphi_1) - 2a_2\Omega \sin(\varphi_2) \right] + \left[a_0 + a_1 \cos(\varphi_1) + a_2 \cos(\varphi_2) \right] \\ & \bar{\theta} \left[a_0^3 + 3a_0^2 a_1 \cos(\varphi_1) + 3a_0^2 a_2 \cos(\varphi_2) + 3a_1^2 a_0 \frac{1 + \cos(2\varphi_1)}{2} + 3a_2^2 a_0 \frac{1 + \cos(2\varphi_2)}{2} \right. \\ & \left. \frac{3}{4} a_1^3 \cos(\varphi_1) + \frac{1}{4} a_1^3 \cos(3\varphi_1) + 3a_1^2 a_2 \cos(\varphi_2) \frac{1 + \cos(2\varphi_1)}{2} + 3a_2^2 a_1 \cos(\varphi_1) \frac{1 + \cos(2\varphi_2)}{2} \right. \\ & \left. \frac{3}{4} a_2^3 \cos(\varphi_2) + \frac{1}{4} a_2^3 \cos(3\varphi_2) + 3a_0 a_1 a_2 \cos(\varphi_1) + 3a_0 a_1 a_2 \cos(\varphi_1 + \varphi_2) \right] = \bar{P} \cos(\Omega\tau). \quad (\text{D.20}) \end{aligned}$$

Also we have the following identities

$$\cos(\varphi_1) = \cos(\Omega\tau) \cos(\phi) - \sin(\Omega\tau) \sin(\phi) \quad (\text{D.21})$$

and

$$\sin(\varphi_1) = \sin(\Omega\tau) \cos(\phi) + \cos(\Omega\tau) \sin(\phi). \quad (\text{D.22})$$

For the first order approximation, the low order terms (constant, $\cos(\Omega\tau)$ and $\sin(\Omega\tau)$) are kept and higher order terms ($\cos(2\Omega\tau)$, $\sin(2\Omega\tau)$, etc.) are neglected.

The low order terms can be collected as follows by using Eqs. (D.20), (D.21) and (D.22)

$$\text{Constant : } a_0 \left[1 + \bar{\theta} \left(a_0^2 + \frac{3}{2} a_1^2 + \frac{3}{2} a_2^2 \right) \right] = 0, \quad (\text{D.23})$$

$$\cos(\Omega\tau) : \left\{ \frac{3}{4} \bar{\theta} a_1^3 + a_1 \left[1 - \Omega^2 + \bar{\theta} \left(3a_0^2 + 3a_0 a_2 + \frac{3}{2} a_2^2 \right) \right] \right\} \cos(\phi) - 2\bar{\zeta} \Omega a_1 \sin(\phi) = \bar{P}, \quad (\text{D.24})$$

and

$$\sin(\Omega\tau) : -\left\{\frac{3}{4}\bar{\theta}a_1^3 + a_1\left[1 - \Omega^2 + \bar{\theta}\left(3a_0^2 + 3a_0a_2 + \frac{3}{2}a_2^2\right)\right]\right\}\sin(\phi) - 2\bar{\zeta}\bar{\Omega}a_1\cos(\phi) = 0. \quad (\text{D.25})$$

For Eq. (D.23), one solution of a_0 is

$$a_0 = 0. \quad (\text{D.26})$$

Since we are seeking a first order approximation, the second order term in Eq. (D.16) is set to zero, which means

$$a_2 = 0. \quad (\text{D.27})$$

Substituting Eqs.(D.26) and (D.27) into Eqs. (D.24) and (D.25) respectively, we have

$$\cos(\Omega\tau) : \left[\frac{3}{4}\bar{\theta}a_1^3 + a_1(1 - \Omega^2)\right]\cos(\phi) - 2\bar{\zeta}\bar{\Omega}a_1\sin(\phi) = \bar{P} \quad (\text{D.28})$$

and

$$\sin(\Omega\tau) : -\left[\frac{3}{4}\bar{\theta}a_1^3 + a_1(1 - \Omega^2)\right]\sin(\phi) - 2\bar{\zeta}\bar{\Omega}a_1\cos(\phi) = 0. \quad (\text{D.29})$$

By squaring Eqs. (D.28) and (D.29) respectively, and adding the two resulting equations together, we have

$$\left[\frac{3}{4}\bar{\theta}a_1^3 + a_1(1 - \Omega^2)\right]^2 + (2\bar{\zeta}\bar{\Omega}a_1)^2 = \bar{P}^2. \quad (\text{D.30})$$

Namely,

$$\frac{9}{16}\bar{\theta}^2a_1^6 + \frac{3}{2}\bar{\theta}(1 - \Omega^2)a_1^4 + \left[(1 - \Omega^2)^2 + (2\bar{\zeta}\bar{\Omega})^2\right]a_1^2 - \bar{P}^2 = 0, \quad (\text{D.31})$$

where a_1 can be solved for a given set of parameters. From Eq. (D.29), we can solve ϕ as follows

$$\phi = \tan^{-1} \frac{2\bar{\zeta}\bar{\Omega}}{(1-\bar{\Omega}^2) + 0.75\bar{\theta}a_1^2}. \quad (\text{D.32})$$

Therefore, the steady-state approximate solution for Eq. (D.6) is

$$y(\tau) \approx a_1 \cos(\bar{\Omega}\tau + \phi). \quad (\text{D.33})$$

Finally, the steady-state approximate solution for Eq. (D.6) is

$$x(t) = yd_0 \approx a_1 d_0 \cos \left[\omega_p t + \tan^{-1} \frac{2\bar{\zeta}\bar{\Omega}}{(1-\bar{\Omega}^2) + 0.75\bar{\theta}a_1^2} \right], \quad (\text{D.34})$$

where a_1 can be determined by solving Eq. (D.31) for given parameters.

MTS Approximate Solution

To find the multiple time scales solution, first we need to change the original governing equation defined in Eq. (D.6) by introducing the following transformations [72]

$$\varepsilon = \bar{\theta}, \quad (\text{D.35})$$

$$\bar{\zeta} = \varepsilon\mu, \quad (\text{D.36})$$

$$\bar{P} = 2\varepsilon f, \quad (\text{D.37})$$

and

$$\bar{\Omega} = 1 + \varepsilon\sigma. \quad (\text{D.38})$$

where ε is a small perturbation parameter. μ , f and σ are new introduced variables.

Substituting Eqs. (D.36), (D.37) and (D.38) into Eq. (D.6) yields

$$y'' + y + \varepsilon(2\mu y' + y^3) = 2\varepsilon f \cos(\tau + \varepsilon\sigma\tau). \quad (\text{D.39})$$

Since $\varepsilon < 1$ (for example, Table 4-9), we can have the following power expression for $y(\tau)$ with a first-order approximation,

$$y(\tau) \approx y_0(\tau_0, \tau_1) + \varepsilon y_1(\tau_0, \tau_1), \quad (\text{D.40})$$

where y_0 and y_1 are two unknown functions that need to be determined, τ_0 and τ_1 are the fast time scale (representing the fast dynamics) and slow time scale (representing the slow dynamics) respectively,

$$\tau_0 = \tau \quad (\text{D.41})$$

and

$$\tau_1 = \varepsilon \tau. \quad (\text{D.42})$$

Therefore, the time derivatives with respect to t become the following expansion terms of the partial derivatives with respect to the corresponding time scales

$$y' = \frac{\partial}{\partial \tau} y(\tau, \varepsilon) = \frac{\partial y}{\partial \tau_0} \frac{d\tau_0}{d\tau} + \frac{\partial y}{\partial \tau_1} \frac{d\tau_1}{d\tau} = D_0 y + \varepsilon D_1 y, \quad (\text{D.43})$$

and

$$y'' = \frac{\partial^2}{\partial \tau^2} y(\tau, \varepsilon) = D_0^2 y + 2\varepsilon D_0 D_1 y + \varepsilon^2 D_1^2 y, \quad (\text{D.44})$$

where

$$D_0 = \frac{\partial}{\partial \tau_0}, \quad (\text{D.45})$$

and

$$D_1 = \frac{\partial}{\partial \tau_1}. \quad (\text{D.46})$$

Substituting Eqs. (D.40), (D.43) and (D.44) into Eq. (D.39) yields

$$\begin{aligned} & (D_0^2 + 2\varepsilon D_0 D_1 + \varepsilon^2 D_1^2)(y_0 + \varepsilon y_1) + (y_0 + \varepsilon y_1) + 2\varepsilon \mu (D_0 + \varepsilon D_1)(y_0 + \varepsilon y_1) \\ & + \varepsilon (y_0^3 + 3\varepsilon y_0^2 y_1 + 3\varepsilon^2 y_1^2 y_0 + \varepsilon^3 y_1^3) = 2\varepsilon f \cos(\tau_0 + \sigma \tau_1). \end{aligned} \quad (\text{D.47})$$

By collecting low order terms and neglecting higher order terms ($O(\varepsilon^2)$) from Eq.

(D.47), we have

$$\text{Constant : } D_0^2 y_0 + y_0 = 0, \quad (\text{D.48})$$

and

$$\varepsilon : D_0^2 y_1 + y_1 = -2D_1 D_0 y_0 - 2\mu D_0 y_0 - y_0^3 + 2f \cos(\tau_0 + \sigma\tau_1). \quad (\text{D.49})$$

A general solution to Eq. (D.48) is

$$y_0(\tau_0, \tau_1) = a_1(\tau_1) \cos[\tau_0 + \phi(\tau_1)], \quad (\text{D.50})$$

where $a_1(\tau_1)$ is the amplitude and $\phi(\tau_1)$ is the phase angle. It is convenient to rewrite

Eq. (D.50) in a complex form as follows

$$y_0(\tau_0, \tau_1) = A_1(\tau_1) e^{i\tau_0} + \bar{A}_1(\tau_1) e^{-i\tau_0}, \quad (\text{D.51})$$

where

$$A_1(\tau_1) = \frac{1}{2} a_1(\tau_1) e^{i\phi(\tau_1)}, \quad (\text{D.52})$$

and

$$\bar{A}_1(\tau_1) = \frac{1}{2} a_1(\tau_1) e^{-i\phi(\tau_1)}. \quad (\text{D.53})$$

It follows that

$$D_0 y_0 = iA_1 e^{i\tau_0} - i\bar{A}_1 e^{-i\tau_0} \quad (\text{D.54})$$

and

$$D_1 D_0 y_0 = iA_1' e^{i\tau_0} - i\bar{A}_1' e^{-i\tau_0}. \quad (\text{D.55})$$

Substituting Eqs. (D.54) and (D.55) into Eq. (D.49) and neglecting higher order terms

($O(\varepsilon^2)$) finally leads to

$$D_0^2 y_1 + y_1 = -2i(A_1' e^{i\tau_0} - \bar{A}_1' e^{-i\tau_0}) - 2\mu i(A_1 e^{i\tau_0} - \bar{A}_1 e^{-i\tau_0}) - (3A_1^2 \bar{A}_1 e^{i\tau_0} + 3\bar{A}_1 A_1^2 e^{-i\tau_0}) + 2f \frac{e^{i\tau_0} + e^{-i\tau_0}}{2} e^{i\sigma\tau_1}. \quad (\text{D.56})$$

Elimination of the secular terms (which makes the solution divergent and unbounded) in the above equation requires

$$e^{i\tau_0} : -2i(A_1' + \mu A_1) - 3A_1^2 \bar{A}_1 + f e^{i\sigma\tau_1} = 0 \quad (\text{D.57})$$

and

$$e^{-i\tau_0} : 2i(\bar{A}_1' + \mu \bar{A}_1) - 3\bar{A}_1^2 A_1 + f e^{-i\sigma\tau_1} = 0. \quad (\text{D.58})$$

Eqs. (D.57) and (D.58) are not independent because they are complex conjugates. Hence, if one of them is satisfied, the other is automatically satisfied. Only Eq. (D.57) is considered in the following analysis. From Eq. (D.52), we have

$$A_1' = \frac{d}{d\tau_1} A_1(\tau_1) = \frac{1}{2} a_1' e^{i\phi(\tau_1)} + \frac{1}{2} a_1 i \phi' e^{i\phi(\tau_1)}. \quad (\text{D.59})$$

Substituting Eqs. (D.52), (D.53) and (D.59) into Eq. (D.57) results in

$$e^{i\tau_0} : -2i \left[\frac{1}{2} a_1' e^{i\phi(\tau_1)} + \frac{1}{2} a_1 i \phi' e^{i\phi(\tau_1)} + \mu \frac{1}{2} a_1 e^{i\phi(\tau_1)} \right] - \frac{3}{8} a_1^3 e^{i\phi(\tau_1)} + f e^{i\sigma\tau_1} = 0. \quad (\text{D.60})$$

Eliminating $e^{i\phi(\tau_1)}$ on both sides of Eq. (D.60) leads to

$$e^{i\tau_0} : -i(a_1' + a_1 i \phi' + \mu a_1) - \frac{3}{8} a_1^3 + f e^{i(\sigma\tau_1 - \phi)} = 0. \quad (\text{D.61})$$

Separating Eq. (D.61) into real and imaginary parts yields

$$\text{Imag: } -(a_1' + \mu a_1) + f \sin(\sigma\tau_1 - \phi) = 0. \quad (\text{D.62})$$

and

$$\text{Real: } a_1 \phi' - \frac{3}{8} a_1^3 + f \cos(\sigma\tau_1 - \phi) = 0. \quad (\text{D.63})$$

Finally, we obtain the following equations by rearranging Eqs. (D.62) and (D.63) respectively

$$a_1' = -\mu a_1 + f \sin(\sigma \tau_1 - \phi), \quad (\text{D.64})$$

and

$$a_1 \phi' = \frac{3}{8} a_1^3 - f \cos(\sigma \tau_1 - \phi). \quad (\text{D.65})$$

The above equations represent an nonlinear non-autonomous (time-dependent) system. In order to make them easy to solve, we introduce the following transformation

$$r(\tau_1) = \sigma \tau_1 - \phi(\tau_1). \quad (\text{D.66})$$

Eqs. (D.64) and (D.65) are then changed into the following equations

$$a_1' = -\mu a_1 + f \sin(r), \quad (\text{D.67})$$

and

$$a_1 r' = -\sigma a_1 + \frac{3}{8} a_1^3 - f \cos(r). \quad (\text{D.68})$$

The above equations represent an autonomous system and are easier to solve. Since we only consider the steady state solution around the fixed point (or equilibrium point), it follows

$$a_1' = 0 = -\mu a_1 + f \sin(r), \quad (\text{D.69})$$

and

$$r' = 0 = -\sigma + \frac{3}{8} a_1^2 - \frac{f}{a_1} \cos(r). \quad (\text{D.70})$$

Eliminating all r terms in Eqs. (D.69) and (D.70) leads to

$$(\mu a_1)^2 + a_1^2 \left(\frac{3}{8} a_1^2 - \sigma \right)^2 = f^2. \quad (\text{D.71})$$

After rearrangement, we finally obtain the following equation for the amplitude of the first order term in Eq. (D.40)

$$\frac{9}{64}a_1^6 + \frac{3}{4}\sigma a_1^4 + (\sigma^2 + \mu^2)a_1^2 - f^2 = 0, \quad (\text{D.72})$$

where

$$\sigma = \frac{\Omega - 1}{\varepsilon}, \quad (\text{D.73})$$

$$\mu = \frac{\bar{\zeta}}{\varepsilon}, \quad (\text{D.74})$$

and

$$f = \frac{\bar{P}}{2\varepsilon}. \quad (\text{D.75})$$

After we solve a_1 from Eq. (D.72) for given parameters, $\phi(\tau_1)$ is solved by using Eqs. (D.66), (D.69), (D.73), and (D.74) as follows

$$\phi(\tau_1) = \sigma\tau_1 - r(\tau_1) = \frac{\Omega - 1}{\varepsilon}\tau_1 - \sin^{-1}\left(\frac{2\varepsilon\mu a_1}{\bar{P}}\right) = (\Omega - 1)\tau - \sin^{-1}\left(\frac{2\bar{\zeta}a_1}{\bar{P}}\right). \quad (\text{D.76})$$

Therefore, for a given set of parameters, a_1 and $\phi(\tau_1)$ can be solved from Eqs. (D.72) and (D.76) respectively. Since we only consider a first-order approximation solution for $y(\tau)$, from Eqs. (D.40) and (D.50), the approximate solution in the steady state for Eq. (D.39) is

$$y(\tau) \approx y_0(\tau_0, \tau_1) = a_1(\tau_1) \cos[\tau_0 + \phi(\tau_1)] = a_1 \cos\left[\Omega\tau - \sin^{-1}\left(\frac{2\bar{\zeta}a_1}{\bar{P}}\right)\right]. \quad (\text{D.77})$$

Finally, the steady-state approximate solution for $x(t)$ is

$$x(t) = yd_0 \approx a_1 d_0 \cos \left[\Omega \tau - \sin^{-1} \left(\frac{2\bar{\zeta} a_1}{\bar{P}} \right) \right], \quad (\text{D.78})$$

where a_1 can be determined by solving Eq. (D.72) for given parameters.

APPENDIX E UNCERTAINTY ANALYSIS

This appendix presents an uncertainty analysis of the experimentally identified system parameters. In Chapter 6, no uncertainties are assumed with the measured velocity and the physical dimensions/material properties of the microphone. However, there always exist some uncertainty sources in the experiments and physical microphone devices, for example, the variations of physical dimensions and material properties, which can be caused by the fabrication process. To carry out uncertainty analysis for the identified system parameters in this appendix, first, different uncertainty analysis approaches are briefly discussed. Then, uncertainties are discussed from the following possible sources: 1) experimental velocity and displacement results; 2) approximate solutions and nonlinear least-squares algorithms; and 3) the fabrication process. Finally, a linear analytical method is chosen and applied to propagate the uncertainties caused only by fabrication into the corresponding uncertainty ranges of experimentally extracted system parameters.

Uncertainty Analysis Methods

In practice, three different approaches are employed to conduct uncertainty analysis: an analytical method, a perturbation method and the Monte Carlo method [124-130]. For relatively simple equations, an analytical method is commonly used to conduct the quantitative uncertainty analysis for the statistical error propagation [126, 129, 130]. If the input variables of the equation or system are statistically independent and only the total small uncertainty for each input variable is considered, a linear version of the

analytical method can be obtained by using a 1st order Taylor series expansion [126]. Since it is easy to implement and not computationally costly, a linear analytical method is widely used in many engineering fields. Since the data reduction equations for the system parameters of the microphone are obtained via LEM, a linear analytical method will be used for the uncertainty analysis.

For more complex equations, an analytical approach is much more difficult to apply. Therefore, in these cases, its use is not practical or possible and some numerical methods are introduced to perform the uncertainty analysis. Two major numerical methods are briefly discussed in the following.

In a perturbation approach, instead of finding sensitivity coefficients (derivatives) analytically, sensitivity coefficients are computed numerically [124]. A small perturbation (usually total uncertainty) for each input independent variable is assumed in a perturbation method and nonlinear effects could be included into the propagation. Some major steps for a perturbation method are described as follows. First, the change for the desired output function is calculated when each input variable is perturbed by its uncertainty estimate for a given confidence interval, with other input variables fixed at their respective mean values. The total uncertainty for the desired output function is computed as a root-sum-square of the respective changes due to all the perturbed input variables [131].

The Monte Carlo method is the most commonly applied numerical technique for uncertainty analysis [125, 127]. Due to the inherent approximation in the linear analytical approach, uncertainty analyses conducted directly by the Monte Carlo simulations yield more accurate results. However, the Monte Carlo simulations are

computationally costly, especially in the cases where hundreds or thousands of input variables are needed. To carry out the Monte Carlo simulations, some major steps are summarized as follows. First, for each input variable, one value of its uncertainty is generated randomly from the computer for a given confidence interval. Then a “measured” value of this variable is obtained by adding the generated uncertainty value to its mean value. After obtaining all “measured” values of all independent variables, the desired output result is calculated using the data reduction equation [127]. The above process simulates running the experiment once and needs to be repeated N times to achieve converged statistics, where N usually is a relatively large integer number (for example, 10000). After running the simulations, the mean, variance and other statistical moments of the distribution of the simulated output result are computed respectively. Finally, after obtaining converged statistics, the uncertainty for the simulated output result is estimated. In practice, the Monte Carlo simulations can be performed in many ways. For example, running simulation in MATLAB is a typical choice in the field of engineering.

Uncertainty Sources

There exist many uncertainty sources in the experiments and physical microphone devices, some contributes significantly to the uncertainties of system parameters and some contributions are small and can be neglected. Uncertainty contributors are discussed in the following section.

Uncertainty in the Experimental Data

The measurement velocity resolution of the laser vibrometer is $1.5 \mu\text{m/s}$ [119]. It can be calculated that the minimum detectable displacement is approximately 2.4pm at 100 kHz and 0.24pm at 1 MHz . The random uncertainty of the measured center velocity

currently cannot be obtained since the laser vibrometer only gave out the final mean value of each measured velocity although 100 ensemble averages were used. If all 100 ensemble data points for each velocity can be obtained, we can calculate the standard deviation and mean value of each velocity, and finally the random uncertainty can be calculated for a given confidence interval [127].

The trapezoidal rule was used to numerically integrate the measured center velocity to yield the center displacement. Since 8192 sample points were used within a 3.2 ms record time, the sampling time step (Δt) is approximately 0.39 μs . The integration truncation error [108] for the trapezoidal rule typically is $O(\Delta t^3)$, which is approximately on the order of 10^{-20} and can be neglected. Also, the random uncertainty of the integrated center displacement currently is not available due to the reason for the measured velocity. As we can see from the above analysis, the bias errors for both center velocity and displacement are small and can be neglected in the uncertainty propagation.

Errors of Approximate Solutions and Nonlinear Least-Squares Algorithms

To obtain the errors caused by approximate solutions and nonlinear least-squares algorithms, three different applied voltages and given theoretical system parameters (ω_0 , ζ , β and Γ) are used to run simulations with the full-blown nonlinear equation in MATLAB. The three different voltages are chosen such that the system responses fall into the linear, weakly nonlinear and highly nonlinear regions respectively. Then, based on the simulated system responses, the approximate solutions and nonlinear least-squares algorithms are applied to extract system parameters for each test case respectively. Finally, extracted system parameters are compared with their given values and errors are calculated for each test case respectively. The detailed results are summarized in Chapter

4 under the sections of validity regions of MTS and HB approximate solutions. In conclusion, the maximum error caused by the MTS approximate solution and nonlinear least-squares curve-fitting algorithm is less than 1% for the electrical square wave excitation case. The maximum error caused by the HB approximate solution and nonlinear least-squares curve-fitting algorithm is less than 4.4% for the electrical sinusoidal wave excitation case.

Uncertainties Caused by the Fabrication Process

From the reproducibility data of the fabrication process [98], for a 95% confidence interval, the uncertainties of some structural parameters are listed in Table E-1. Also from the reference [132], the uncertainty range of the Young's modulus of polysilicon is obtained and listed in Table E-1.

Table E-1. Uncertainties caused by the fabrication process for a 95% confidence level.

Parameter	Mean	Uncertainty
Thickness of the diaphragm (m)	2.27e-6	0.2e-7
Thickness of the top backplate (m)	2.27e-6	0.12e-7
Thickness of the bottom backplate (m)	2.51e-6	0.6e-8
Gap between the diaphragm and top backplate (m)	2.00e-6	0.5e-6
Gap between the diaphragm and bottom backplate (m)	2.20e-6	0.5e-6
Young's modulus of polysilicon (Pa)	173e9	20.0 e9

Preliminary Uncertainty Analysis Results

From the previous discussion of the uncertainty sources, the random uncertainties in the experimental data are currently not available. And only the bias errors caused by the approximate solutions and nonlinear least-squares curve-fitting algorithms are available. Therefore, in this section, only the uncertainties caused by the fabrication process are considered and propagated into the uncertainty ranges of system parameters. It should be pointed out that the estimated uncertainty ranges of system parameters in this

section are conservative since other two uncertainty sources are not included in the uncertainty analysis.

From the reproducibility data of the fabrication process [98], for a 95% confidence interval, we have

$$h = \bar{h} \pm \Delta h = 2.27 \pm 0.02 \mu m, \quad (\text{E.1})$$

$$h_{tp} = \bar{h}_{tp} \pm \Delta h_{tp} = 2.27 \pm 0.012 \mu m. \quad (\text{E.2})$$

$$h_{bp} = \bar{h}_{bp} \pm \Delta h_{bp} = 2.51 \pm 0.006 \mu m. \quad (\text{E.3})$$

$$d_{tp} = \bar{d}_{tp} \pm \Delta d_{tp} = 2.0 \pm 0.5 \mu m. \quad (\text{E.4})$$

and

$$d_{bp} = \bar{d}_{bp} \pm \Delta d_{bp} = 2.2 \pm 0.5 \mu m. \quad (\text{E.5})$$

where h , h_{tp} and h_{bp} are the thicknesses of the diaphragm, top and bottom backplates respectively. d_{tp} and d_{bp} are the gaps between the diaphragm and top and bottom backplates respectively. Also the bar sign above each variable denotes the mean value and the Δ sign denotes the corresponding variation. Same symbols apply for notations in the following analysis. For the Young's modulus of polysilicon, from the reference [132], we have

$$E = \bar{E} \pm \Delta E = 173 \pm 20 \text{ GPa}. \quad (\text{E.6})$$

Since the uncertainty range for the radius of the diaphragm is not provided in the reproducibility data of the fabrication process [98], in the following analysis, we assume that the radius of the diaphragm is $a = 230 \mu m$.

From Chapter 3, we have

$$k_1 = k_1(E, h) = \frac{64D\pi}{3a^2} = \frac{16Eh^3\pi}{9a^2(1-\nu^2)}, \quad (\text{E.7})$$

and

$$k_3 = k_3(E, h) = \frac{10.044D\pi}{a^2h^2} = \frac{0.837E\pi h}{a^2(1-\nu^2)}, \quad (\text{E.8})$$

where k_1 and k_3 are the lumped stiffnesses of the diaphragm respectively, and they are functions of E and h respectively if other parameters are specified. Also we can have

$$M_{me} = M_{me}(h) = \frac{\pi a^2 h \rho}{5}, \quad (\text{E.9})$$

and

$$b = b(d_{ip}, d_{bp}, h_{ip}, h_{bp}) = \frac{4\mu\pi a^4}{3n_{ip}d_{ip}^3} B(A_{ip}) + \frac{4\mu\pi a^4}{3n_{bp}d_{bp}^3} B(A_{bp}) + \frac{8\mu\pi h_{ip}n_{ip}}{A_{ip}^2} + \frac{8\mu\pi h_{bp}n_{bp}}{A_{bp}^2}, \quad (\text{E.10})$$

where M_{me} is the lumped mass of the diaphragm and b is the total lumped damping.

From Chapter 4, we have

$$\omega_0(E, h) = \sqrt{\frac{k_1 + k_c}{M_{me}}} = \sqrt{\frac{k_1(E, h) + k_c}{M_{me}(h)}}, \quad (\text{E.11})$$

$$\zeta(d_{ip}, d_{bp}, h_{ip}, h_{bp}, E, h) = \frac{b}{2M_{me}\omega_0} = \frac{b(d_{ip}, d_{bp}, h_{ip}, h_{bp})}{2M_{me}(h)\omega_0(E, h)}, \quad (\text{E.12})$$

$$\beta(E, h) = \frac{k_3}{M_{me}} = \frac{k_3(E, h)}{M_{me}(h)}, \quad (\text{E.13})$$

and

$$\Gamma(h) = \frac{A_{me}}{M_{me}} = \frac{A_{me}}{M_{me}(h)}, \quad (\text{E.14})$$

where ω_0 is the first linear natural frequency, ζ is the damping ratio, β is the nonlinear stiffness parameter and Γ is the ratio of the lumped area over lumped mass.

To propagate the uncertainties of the physical quantities defined from Eqs. (E.1) to (E.6) into the uncertainties of ω_0 , ζ , β and Γ respectively, a linear analytical method [126, 127, 133] is used here. First, we need to calculate the mean values for each system parameter. By using Eqs. (E.1) to (E.10), the mean values for each system parameter are calculated as follows

$$\bar{\omega}_0 = \sqrt{\frac{k_1(\bar{E}, \bar{h}) + k_c}{M_{me}(\bar{h})}} = 1216e3 \text{ rad/s}, \quad (\text{E.15})$$

$$\bar{\zeta} = \frac{b(\bar{d}_{tp}, \bar{d}_{bp}, \bar{h}_{tp}, \bar{h}_{bp})}{2M_{me}(\bar{h})\bar{\omega}_0(\bar{E}, \bar{h})} = 7.272e-2, \quad (\text{E.16})$$

$$\bar{\beta} = \frac{k_3(\bar{E}, \bar{h})}{M_{me}(\bar{h})} = 1.219e23 \text{ N/m}^3/\text{kg}, \quad (\text{E.17})$$

and

$$\bar{\Gamma} = \frac{A_{me}}{M_{me}(\bar{h})} = 329.2 \text{ m}^2/\text{kg}. \quad (\text{E.18})$$

The uncertainties defined in Eqs. (E.1) to (E.6) are assumed to be uncorrelated and small; therefore, a 1st order Taylor series approximation can be used to propagate these uncertainties into the uncertainties of system parameters as follows,

$$\Delta\omega_0 = \sqrt{\left(\frac{\partial\omega_0}{\partial E}\Delta E\right)^2 + \left(\frac{\partial\omega_0}{\partial h}\Delta h\right)^2} = 64.09e3 \text{ rad/s}, \quad (\text{E.19})$$

$$\begin{aligned} \Delta\zeta &= \sqrt{\left(\frac{\partial\zeta}{\partial d_{tp}}\Delta d_{tp}\right)^2 + \left(\frac{\partial\zeta}{\partial d_{bp}}\Delta d_{bp}\right)^2 + \left(\frac{\partial\zeta}{\partial h_{tp}}\Delta h_{tp}\right)^2 + \left(\frac{\partial\zeta}{\partial h_{bp}}\Delta h_{bp}\right)^2 + \left(\frac{\partial\zeta}{\partial E}\Delta E\right)^2 + \left(\frac{\partial\zeta}{\partial h}\Delta h\right)^2} \\ &= 1.337e-2, \end{aligned} \quad (\text{E.20})$$

$$\Delta\beta = \sqrt{\left(\frac{\partial\beta}{\partial E}\Delta E\right)^2 + \left(\frac{\partial\beta}{\partial h}\Delta h\right)^2} = 1.409e22 \text{ N/m}^3/\text{kg}, \quad (\text{E.21})$$

and

$$\Delta\Gamma = \sqrt{\left(\frac{\partial\Gamma}{\partial h}\Delta h\right)^2} = \left|\frac{\partial\Gamma}{\partial h}\Delta h\right| = 2.901 \text{ m}^2/\text{kg}, \quad (\text{E.22})$$

where the partial derivatives are sensitivity coefficients, which relate the changes of the input quantities into the changes of the output quantities in a root-sum-square fashion [129, 130]. Table E-2 lists all the sensitivity coefficients used in the uncertainty analysis and the final uncertainty analysis results are summarized in Table E-3.

Table E-2. Sensitivity coefficients used in the uncertainty analysis.

Sensitivity coefficient	Value
$\frac{\partial\omega_0}{\partial E}$	$3.172\text{e-}6 \text{ (s}^{-1} \cdot \text{Pa}^{-1}\text{)}$
$\frac{\partial\omega_0}{\partial h}$	$4.573\text{e}11 \text{ (s}^{-1} \cdot \text{m}^{-1}\text{)}$
$\frac{\partial\zeta}{\partial d_{tp}}$	$-1.772\text{e}4 \text{ (m}^{-1}\text{)}$
$\frac{\partial\zeta}{\partial d_{bp}}$	$-1.837\text{e}4 \text{ (m}^{-1}\text{)}$
$\frac{\partial\zeta}{\partial h_{tp}}$	$1.209\text{e}4 \text{ (m}^{-1}\text{)}$
$\frac{\partial\zeta}{\partial h_{bp}}$	$7.964\text{e}3 \text{ (m}^{-1}\text{)}$
$\frac{\partial\zeta}{\partial E}$	$-1.897\text{e-}13 \text{ (m}^{-1}\text{)}$
$\frac{\partial\zeta}{\partial h}$	$-5.938\text{e}4 \text{ (m}^{-1}\text{)}$
$\frac{\partial\beta}{\partial E}$	$7.047\text{e}11 \text{ (kg}^{-1} \cdot \text{m}^{-1}\text{)}$
$\frac{\partial\beta}{\partial h}$	$0 \text{ (N} \cdot \text{m}^{-4} \cdot \text{kg}^{-1}\text{)}$
$\frac{\partial\Gamma}{\partial h}$	$-1.450\text{e}8 \text{ (m} \cdot \text{kg}^{-1}\text{)}$

Table E-3. Theoretical mean values and uncertainties of system parameters caused by fabrication for a given 95% confidence level.

System parameter	Mean	Uncertainty	Percentage
$\omega_0/2\pi$ (Hz)	193.5e3	10.20e3	5.3%
ζ	7.272e-2	1.337e-2	18%
β (N/m ³ /kg)	1.219e23	0.1409e23	12%
Γ (m ² /kg)	329.2	2.901	0.9%

LIST OF REFERENCES

1. Mueller, T.J., *Aeroacoustic Measurements*. 2002, New York: Springer. p. 1-23, 158-179.
2. Scheeper, P.R., Van der Donk, A.G.H., Olthuis, W. and Bergved, P., *A Review of Silicon Microphones*. *Sensors and Actuators A*, 1994. 44: p. 1-11.
3. Hunt, F.V., *Electroacoustics: the Analysis of Transduction, and its Historical Background*. 1954, New York: Acoustical Society of America. p. 3-9, 103-105, 181-187, 194-199.
4. Nathanson, H.C., Newell, W.E., Wickstrom, R.A., and Davis, J.R., *The Resonant Gate Transistor*. *IEEE Transactions on Electron Devices*, 1967. ED-14(3): p. 117-133.
5. Senturia, S.D., *Microsystems Design*. 2001, Norwell, MA: Kluwer Academic Publishers. p. 130-138, 391-397.
6. Malatkar, P., *Nonlinear Vibrations of Cantilever Beams and Plates. Ph.D. Dissertation*. 2003. Blacksburg, VA: Virginia Polytechnic Institute and State University.
7. Homentcovschi, D. and Miles, R.N., *Viscous Damping of Perforated Planar Micromechanical Structures*. *Sensors and Actuators A*, 2005. 119(2): p. 544-552.
8. Homentcovschi, D. and Miles, R.N., *Modeling of Viscous Damping of Perforated Planar Microstructures Applications in Acoustics*. *Journal of the Acoustical Society of America*, 2004. 116: p. 2939-2947.
9. Lifshitz, R. and Roukes, M.L., *Thermoelastic Damping in Micro- and Nanomechanical Systems*. *Physical Review B*, 2000. 61(8): p. 5600-5609.
10. Srikar, V.T. and Senturia, S.D., *Thermoelastic Damping in Fine Grained Polysilicon Flexural Beam Resonators*. *Journal of Microelectromechanical Systems*, 2002. 11: p. 499-504.
11. Syed Asif, S.A., Walh, K.J., and Colten, R.J., *Nanoindentation and Contact Stiffness Measurements Using Force Modulation with a Capacitive Load-Displacement Transducer*. *Review of Scientific Instruments*, 1999. 70(5): p. 2408-2413.

12. Borovsky, B., Krim, J., Syed Asif, S.A., and Walh, K.J., *Measuring Nanomechanical Properties of a Dynamic Contact Using an Indenter Probe and Quartz Crystal Microbalance*. Journal of Applied Physics, 2001. 90(12): p. 6391-6396.
13. Zhang, W., Baskaran, R., and Turner, K.L., *Effect of Cubic Nonlinearity on Auto-Parametrically Amplified Resonant MEMS Mass Sensor*. Sensors and Actuators A, 2002. 102: p. 139-150.
14. Zhang, W. and Turner, K.L., *A Mass Sensor Based on Parametric Resonance*. in *Proceedings of 2004 Solid-State Sensor, Actuator and Microsystems Workshop*. 2004. Hilton Head Island, SC. p. 49-52.
15. Lerch, R., *Sensors for Measuring Sound*, in *Mechanical Sensors*, Bau, H., DeRooij, N.F. and Kloeck, B., Editor. 1996, John Wiley & Sons: New York. p. 611-621.
16. Eargle, J., *The Microphone Book*. 2001, Woburn, MA: Focal Press. p. 1-8, 125-137.
17. Scheeper, P.R., Nordstrand, B., Gullov, J.O., Liu, B., Clausen, T., Midjord, L., and Storgaard-Larsen, T., *A New Measurement Microphone Based on MEMS Technology*. Journal of Microelectromechanical Systems, 2003. 12(6): p. 880-891.
18. Bay, J., Hansen, O., and Bouwstra, S., *Micromachined Double Backplate Differential Capacitive Microphone*. Journal of Micromechanics and Microengineering, 1999. 9: p. 30-33.
19. Bay, J., Hansen, O., and Bouwstra, S., *Design of a Silicon Microphone with Differential Read-Out of a Sealed Double Parallel-Plate Capacitor*. Sensors and Actuators A, 1996. 53: p. 232-236.
20. Bay, J., *Silicon Microphone for Hearing Aid Applications*. Ph.D. Dissertation. 1997. Netherlands: University of Twente.
21. Arnold, D.P., Gururaj, S., Bhardwaj, S., Nishida, T., and Sheplak, M., *A Piezoresistive Microphone for Aeroacoustic Measurements*. in *Proceedings of 2001 ASME IMECE, paper no. MEMS-23841*. 2001. New York, NY.
22. Arnold, D.P., Cattafesta, L.N., Nishida, T., and Sheplak, M., *MEMS-Based Acoustic Array Technology*. Journal of the Acoustical Society of America, 2003. 113(1): p. 289-298.
23. Bernstein, J., *A Micromachined Condenser Hydrophone*. in *Proceedings of IEEE Solid-State Sensor and Actuator Workshop*. 1991. Hilton Head Island, SC. p. 161-165.

24. Suzuki, K., Higuchi, K., and Tanigawa, H., *A Silicon Electrostatic Ultrasonic Transducer*. IEEE Trans. Ultrason. Ferroelectr. Freq. Control, 1989. 36(6): p. 620-627.
25. Madou, M., *Fundamentals of Microfabrication*. 1997, Boca Raton: CRC Press. p. 183-187, 259-265.
26. Gray, P.R., Hurst, P.J., Lewis, S.H., and Meyer, R.G., *Analysis and Design of Analog Integrated Circuits*. 2001, New York: John Wiley & Sons, Inc. p. 748-755.
27. Wong, G.S.K. and Embleton, T.F.W., *AIP Handbook of Condenser Microphones: Theory, Calibration, and Measurements*. 1995: American Institute of Physics. p. 1-7, 37-68.
28. *International Standard on Measurement Microphones, Part 4: Specifications for Working Standard Microphones*. 1995: International Electrotechnical Commission (IEC). p. 11. IEC 1094-4: 1995.
29. Rossi, M., *Acoustics and Electroacoustics*. 1988, Norwood, MA: Artech House. p. 245-308, 309-373.
30. Humphreys, W.M., Gerhold, C.H., Zuckerwar, A.J., Herring, G.C., and Bartram, S.M., *Performance Analysis of a Cost-Effective Electret Condenser Microphone Directional Array*. in *Proceedings of 9th AIAA/CEAS Aeroacoustics Conference and Exhibit, paper no. AIAA2003-3195*. 2003. Hilton Head, SC.
31. *International Standard on Measurement Microphones, Part 1: Specifications for Laboratory Standard*. 2000: International Electrotechnical Commission (IEC). p. 17. IEC 61094-1: 2000.
32. Cady, W.G., *Piezoelectricity*. 1964, New York: Dover Publications. p. 1-8.
33. IEEE, *IEEE Standard on Piezoelectricity*. 1987: IEEE. ANSI/IEEE Std 176-1987.
34. Kim, E.S., Kim, J.R., and Muller, R.S., *Improved IC-Compatible Piezoelectric Microphone and CMOS Process*. Journal of Microelectromechanical Systems, 1991: p. 270-273.
35. Royer, M., Holmen, J.O., Wurm, M.A., Aadland, O.S., and Glenn, M., *ZnO on Si Integrated Acoustic Sensor*. Sensors and Actuators, 1983. 4: p. 357-362.
36. Sessler, G.M., *Acoustic Sensors*. Sensors and Actuators A, 1991. 25-27: p. 323-330.
37. Smith, C.S., *Piezoresistance Effect in Germanium and Silicon*. Physical Review, 1954. 94: p. 42-49.

38. Sheplak, M., Seiner, J. M., Breuer, K. S., and Schmidt, M. A., *A MEMS Microphone for Aeroacoustics Measurements*. in *Proceedings of 37th AIAA Aerospace Sciences Meetings and Exhibit*, paper no. AIAA99-0606. 1999. Reno, NV.
39. Saini, R., Bhardwaj, S., Nishida, N., and Sheplak, M., *Scaling Relations for Piezoresistive Microphones*. in *Proceedings of IMECE 2000, MEMS Vol. 2*. 2000. Orlando, FL. p. 241-248.
40. Bilaniuk, N., *Optical Microphone Transduction Techniques*. *Applied Acoustics*, 1997. 50: p. 35-63.
41. Hall, N.A., Bicen, B., Jeelani, M.K., Lee, W., Qureshi, S., and Degertekin, F.L., *Micromachined Microphone with Diffraction-Based Optical Displacement Detection*. *Journal of Acoustical Society of America*, 2005. 118(5): p. 3000-3009.
42. Kadirvel, K., Taylor, R., Horowitz, S., Hunt, L., Sheplak, M., and Nishida, T., *Design and Characterization of a MEMS Optical Microphone for Aeroacoustic Measurement*. in *Proceedings of 42nd AIAA Aerospace Sciences Meeting and Exhibit*, paper no. AIAA2004-1030. 2004. Reno, NV.
43. Paritsky, A. and Kots, A., *Fiber Optic Microphone for Harsh Environment*. in *Proceedings of SPIE Conference on Harsh Environment Sensors II*, 3852-17. 1999. Boston, MA.
44. Kadirvel, K., *Design and Characterization of a MEMS Optical Microphone for Aeroacoustic Measurement*. *Master Thesis*. 2002. Gainesville, FL: University of Florida.
45. Voorthuyzen, J.A., Sprengels, A.J., Van der Donk, A.G.H., Scheeper, P.R., and Bergveld, P., *Optimization of Capacitive Microphone and Pressure Sensor Performance by Capacitor-electrode Shaping*. *Sensors and Actuators A*, 1991. 25-27: p. 331-336.
46. Bouwstra, S., Storgaard-Larsen, T., Scheeper, P.R., Gullov, J.O., Bay, J., Mullenborg, M., and Rombach, P., *Silicon Microphones - a Danish Perspective*. *Journal of Micromechanics and Microengineering*, 1998. 8: p. 64-68.
47. Thielemann, C. and Hess, G., *A Micromachined Capacitive Electret Microphone*. in *Proceedings of SPIE - The International Society for Optical Engineering*. 1999. p. 748-756.
48. Hsieh, W.H., Hsu, T.Y., and Tai, Y.C., *A Micromachined Thin-Film Teflon Electret Microphone*. in *1997 International Conference on Solid-State Sensors and Actuators (Transducers'97)*. 1997. Chicago, IL. p. 425-428.

49. Hohm, D. and Gerhard-Multhaupt, R., *Silicon-Dioxide Electret Transducers*. Journal of the Acoustical Society of America, 1984. 75: p. 1297-1298.
50. Sprenkels, A.J., Groothengel, R.A., Verloop, A.J., and Bergveld, P., *Development of an Electret Microphone in Silicon*. Sensors and Actuators, 1989. 17: p. 509-512.
51. Puers, R. and Lapadatu, D., *Electrostatic Forces and Their Effects on Capacitive Mechanical Sensors*. Sensors and Actuators A, 1996. 56: p. 203-210.
52. Rombach, P., Müllenborn, M., Klein, U., and Rasmussen, K., *The First Low Voltage, Low Noise Differential Silicon Microphone, Technology Development and Measurement Results*. Sensors and Actuators A, 2002. 95: p. 196-201.
53. Skvor, Z., *On the Acoustical Resistance Due to Viscous Losses in the Air Gap of Electrostatic Transducers*. Acustica, 1967. 19: p. 295-299.
54. van Kampen, R.P., Vellekoop, M.J., Sarro, P.M., and Wolffenbuttel, *Application of Electrostatic Feedback to Critical Damping of an Integrated Silicon Capacitive Accelerometer*. Sensors and Actuators A, 1994. 43: p. 100-106.
55. Bergqvist, J. and Rudolf, F., *A New Condenser Microphone in Silicon*. Sensors and Actuators A, 1990. 21-23: p. 123-125.
56. Bergqvist, J., Rudolf, F., Maisano, J., Parodi, F., and Rossi, M., *A Silicon Condenser Microphone with a Highly Perforated Backplate*. in *Proceedings of 6th International Conference on Solid-State Sensors and Actuators (Transducers '91)*. 1991. San Francisco, CA. p. 266-269.
57. Kuhnel, W. and Hess, G., *A Silicon Condenser Microphone with Structured Back Plate and Silicon Nitride Membrane*. Sensors and Actuators A, 1992. 30: p. 251-258.
58. Bourouina, T., Spirkovitch, S., Baillieu, F., and Vauge, C., *A New Silicon Condenser Microphone with a p+ Silicon Membrane*. Sensors and Actuators A, 1992. 31: p. 149-152.
59. Scheeper, P.R., *A Silicon Condenser Microphone: Materials and Technology*. Ph.D. Dissertation. 1993. Netherlands: University of Twente.
60. Zou, Q., Liu, Z., and Liu, L., *Theoretical and Experimental Studies of Single-Chip-Processed Miniature Silicon Condenser Microphone with Corrugated Diaphragm*. Sensors and Actuators A, 1997. 63: p. 209-215.
61. Schafer, D., Shoaf, S., and Loeppert, P., *Micromachined condenser microphone for hearing aid use*. in *IEEE Solid-State Sensor and Actuator Workshop*. 1998. Hilton Head Island, SC. p. pp. 27-30.

62. Torkkeli, A., Rusanen, O., Saarilahti, J., Seppa, H., Sipola, H., and Hietanen, J., *Capacitive Microphone with Low-Stress Polysilicon Backplate*. Sensors and Actuators A, 2000. 85: p. 116-123.
63. Rombach, P., Müllenborn, M., Klein, U., and Rasmussen, K., *The First Low Voltage, Low Noise Differential Condenser Silicon Microphone*. in *Proceedings of 14th European Conference on Solid-State Transducers*. 2000. Copenhagen, Denmark. p. 213-216.
64. Hansen, S.T., Ergun, A.S., Liou, W., Auld, B.A., and Khuri-Yakub, B.T., *Wideband Micromachined Capacitive Microphones with Radio Frequency Detection*. Journal of the Acoustical Society of America, 2004. 116(2): p. 828-842.
65. Martin, D.T., Kadirvel, K., Liu, J., Fox, R.M., Sheplak, M., and Nishida, T., *Surface and Bulk Micromachined Dual Backplate Condenser Microphone*. in *Proceedings of 18th IEEE International Conference on MEMS*. 2005. Miami, FL. p. 319-322.
66. Martin, D.T., Liu, J., Kadirvel, K., Fox, R.M., Sheplak, M., and Nishida, T., *Development of a MEMS Dual Backplate Capacitive Microphone for Aeroacoustic Measurements*. in *Proceedings of the 44th AIAA Aerospace Sciences Meeting and Exhibit, paper no. AIAA2006-1246*. 2006. Reno, NV.
67. Pedersen, M., *Development of Microelectromechanical Systems Capacitive Microphone for High-Frequency Applications*. Journal of the Acoustical Society of America, 2006. 119(5): p. 3378.
68. Loepfert, P.V. and Lee, S.B., *SiSonic - The First Commercialized MEMS Microphone*. in *2006 Solid-State Sensors, Actuators, and Microsystems Workshop*. 2006. Hilton Head Island, SC. p. 27-30.
69. Nayfeh, A.H. and Balachandran, B., *Applied Nonlinear Dynamics: Analytical, Computational, and Experimental Methods*. 1995, New York: John Wiley & Sons, Inc. p. 20-50, 68-80, 208-212.
70. Marquez, H.J., *Nonlinear Control Systems: Analysis and Design*. 2003, Hoboken, NJ: John Wiley. p. 65-70, 107-115.
71. Virgin, L.N., *Introduction to Experimental Nonlinear Dynamics: a Case Study in Mechanical Vibration*. 2000, New York, NY: Cambridge University Press. p. 203-207.
72. Nayfeh, A.H. and Mook, D.T., *Nonlinear Oscillations*. 1979, New York: John Wiley & Sons. p. 56-60, 119-124, 340-345.

73. Moon, F.C., *Chaotic Vibrations: an Introduction for Applied Scientists and Engineers*. 1987, New York, NY: John Wiley & Sons. p. 302-318.
74. Lam, L., *Introduction to Nonlinear Physics*. 1997, New York, NY: Springer. p. 123-126.
75. Kaplan, D. and Glass, L., *Understanding Nonlinear Dynamics*. Textbooks in Mathematical Sciences. 1995, New York, NY: Springer. p. 15-20.
76. Glendinning, P., *Stability, Instability and Chaos: an Introduction to the Theory of Nonlinear Differential Equations*. 1994, New York, NY: Cambridge University Press. p. 30-40.
77. Bequette, B.W., *Process Dynamics: Modeling, Analysis, and Simulation*. 1998, Upper Saddle River, NJ: Prentice Hall PTR. p. 150-152.
78. Faris, W.F., Abdel-Rahman, E.M., and Nayfeh, A.H., *Mechanical Behavior of an Electrostatically Actuated Micropump*. in *Proceedings of the 43rd AIAA/ASME/ASCE/AHS/ASC Structures, Structural Dynamics and Materials Conference, paper no. AIAA2002-1303*. 2002. Denver, CO.
79. Zavracky, P.M., Majumder, S., and McGruer, N.E., *Micromechanical Switches Fabricated Using Nickel Surface Micromachining*. *Journal of Microelectromechanical Systems*, 1997. 6(1): p. 3-9.
80. Gupta, R.K. and Senturia, S.D., *Pull-In Time Dynamics as a Measure of Absolute Pressure*. in *Proceedings of Tenth Annual International Workshop on Micro Electro Mechanical Systems, MEMS '97*. 1997. Nagoya, Japan. p. 290-294.
81. Taylor, G.I., *The Coalescence of Closely Spaced Drops When They are at Different Electric Potentials*. *Proceedings of the Royal Society A*, 1968. 306: p. 423-434.
82. Pedersen, M., Olthuis, W., and Bergveld, P., *Harmonic Distortion in Silicon Condenser Microphone*. *Journal of the Acoustical Society of America*, 1997. 102(3): p. 1582-1587.
83. Wangsness, R.K., *Electromagnetic Fields*. 1986, New York: John Wiley & Sons. p. 51-58, 98-105.
84. Nemirovsky, Y. and Bochobza-Degani, O., *A Methodology and Model for the Pull-In Parameters of Electrostatic Actuators*. *Journal of Microelectromechanical Systems*, 2001. 10(4): p. 601-615.
85. Zhang, W., Baskaran, R. and Turner, K.L., *Nonlinear Behavior of a Parametric Resonance-Based Mass Sensor*. in *Proceedings of 2002 ASEM International*

Mechanical Engineering Congress & Exposition, paper no. IMECE2002-33261.
2002. New Orleans, LA.

86. Younis, M.I., Abdel-Rahman, E.M., and Nayfeh, A.H., *A Reduced-Order Model for Electrically Actuated Microbeam-Based MEMS*. Journal of Microelectromechanical Systems, 2003. 12(5): p. 672-680.
87. Abdel-Rahman, E.M., Younis, M.I., and Nayfeh, A.H., *Characterization of the Mechanical Behavior of an Electrically Actuated Microbeam*. Journal of Micromechanics and Microengineering, 2002. 12: p. 759-766.
88. Zhao, X., Abdel-Rahman, E.M., and Nayfeh, A.H., *A Reduced-Order Model for Electrically Actuated Microplates*. Journal of Micromechanics and Microengineering, 2004. 14: p. 900-906.
89. Vogl, G.W. and Nayfeh, A.H., *A Reduced-Order Model for Electrically Actuated Clamped Circular Plates*. Journal of Micromechanics and Microengineering, 2005. 15: p. 684-690.
90. Vogl, G.W. and Nayfeh, A.H., *A Reduced-Order Model for Electrically Actuated Clamped Circular Plates*. in *Proceedings of ASME Design Engineering Technical Conference (DETC'03), paper no. DETC/VIB2003-48530*. 2003. Chicago, IL.
91. Abdel-Rahman, E.M., Nayfeh, A.H., and Younis, M.I., *Dynamics of an Electrically Actuated Resonant Microsensor*. in *Proceedings of the International Conference of MEMS, NANO and Smart Systems*. 2003. Banff, Canada. p. 188-196.
92. Younis, M.I. and Nayfeh, A.H., *A Study of the Nonlinear Response of a Resonant Microbeam to an Electric Actuation*. Nonlinear Dynamics, 2003. 31: p. 91-117.
93. Chowdhury, S., Ahmadi, M., and Miller, W.C., *Nonlinear Effects in MEMS Capacitive Microphone Design*. in *Proceedings of the 2003 International Conference on MEMS, NANO and Smart Systems (ICMENS'03)*. 2003. Banff, Alberta, Canada. p. 297-302.
94. Nadal-Guardia, R., Brosa, A.M., and Dehe, A., *AC Transfer Function of Electrostatic Capacitive Sensors Based on the 1-D Equivalent Model: Application to Silicon Microphones*. Journal of Microelectromechanical Systems, 2003. 12(6): p. 972-978.
95. Fargas-Marques, A. and Shkel, A.M., *On Electrostatic Actuation Beyond Snapping Condition*. in *2005 IEEE Sensors*. 2005. Irvine, CA. p. 600-603.

96. Elata, D. and Bamberger, H., *On the Dynamic Pull-In of Electrostatic Actuators with Multiple Degrees of Freedom and Multiple Voltage Sources*. Journal of Microelectromechanical Systems, 2006. 15(1): p. 131-140.
97. Reddy, J.N., *Theory and Analysis of Elastic Plates*. 1999, Philadelphia, PA: Taylor & Francis. p. 47-92.
98. *MEMS Advanced Design Short Course Notes*. 2002. Albuquerque, NM: Sandia National Laboratories. p. 5-21.
99. Timoshenko, S. and Krieger, S.W., *Theory of Plates and Shells*. 1959, New York: McGraw-Hill. p. 396-404.
100. Sheplak, M. and Dugundji, J., *Large Deflections of Clamped Circular Plates Under Initial Tension and Transitions to Membrane Behavior*. Journal of Applied Mechanics, 1998. 65(1): p. 107-115.
101. Nayfeh, A.H. and Pai, P.F., *Linear and Nonlinear Structural Mechanics*. Nonlinear Science, ed. Nayfeh, A.H. 2004, New Jersey: John Wiley & Sons. p. 403-415.
102. Tilmans, H.A.C., *Equivalent Circuit Representation of Electromechanical Transducers: II. Distributed-Parameter Systems*. Journal of Micromechanics and Microengineering, 1997. 7: p. 285-309.
103. Tilmans, H.A.C., *Equivalent Circuit Representation of Electromechanical Transducers: I. Lumped-Parameter Systems*. Journal of Micromechanics and Microengineering, 1996. 6: p. 157-176.
104. Blackstock, D.T., *Fundamentals of Physical Acoustics*. 2000, New York: John Wiley & Sons. p. 144-156.
105. Leissa, A., *Vibration of Plates*. 1993: Acoustical Society of America. p. 1-10.
106. COVENTOR. 2003, Coventor, Inc.: 4001 Weston Parkway, Cary, NC 27513.
107. Mann, B.P. and Koplów, M.A., *Symmetry breaking bifurcations of a parametrically excited pendulum*. Nonlinear Dynamics, 2006. 46(4): p. 427-437.
108. Chapra, S.C. and Canale, R.P., *Numerical Methods for Engineers: with Software and Programming Applications*. 4th ed. 2002, New York: McGraw-Hill. p. 440-470.
109. Dormand, J.R. and Prince, P.J., *A Family of Embedded Runge-Kutta Formulae*. Journal of Computational and Applied Mathematics, 1980. 6: p. 19-26.

110. Li, G.X. and Shemansky, F.A., *Drop Test and Analysis on Micromachined Structures*. Sensors and Actuators, 2000. A85: p. 280-286.
111. McIntyre, D.G., Cunningham, S.J., Carper, J.S., Jaramillo, P.D., Tatic-Lucic, S., and Starr, L.E., *Characterization of the Influence of Fabrication Methods on Microstructure Failure*. Sensors and Actuators, 1997. A60: p. 181-185.
112. Tanner, D.M., Walraven, J.A., Helgesen, K., Irwin, L.W., Brown, F., Smith, N.F., and Masters, N., *MEMS Reliability in Shock Environments*. in *IEEE International Reliability Physics Symposium*. 2002. San Jose, CA. p. 129-138.
113. Meirovitch, L., *Elements of Vibration Analysis*. 2nd ed. 1994, New York: McGraw-Hill Company. p. 89-95.
114. Meirovitch, L., *Fundamentals of Vibrations*. 2nd ed. 2003, New York: McGraw-Hill Company. p. 98-105.
115. Younis, M.I. and Miles, R., *Response of MEMS Devices under Shock Loads*. in *Proceedings of ASME International Mechanical Engineering Congress and Exposition (IMECE'05)*, paper no. IMECE2005-81217. 2005. Orlando, FL.
116. Husic, J.M. and Gopal, M., *Non-Linear Dynamic Analysis of a Superplug Door Module Response to a Door Slam Event*. in *Proceedings of the 1999 SAE Noise and Vibration Conference*, paper no. 1999-01-0406. 1999. Traverse City, MI.
117. Scholl, D. and Amman, S., *A New Wavelet Technique for Transient Sound Visualization and Application to Automotive Door Closing Events*. in *Proceedings of the 1999 SAE Noise and Vibration Conference*, paper no. 1999-01-1682. 1999. Traverse City, MI. p. 257-260.
118. Hamilton, M.F. and Blackstock, D.T., *Nonlinear Acoustics*. 1998, San Diego, CA: Academic Press. p. 109-113.
119. *User Manual: Laser Doppler Vibrometer*. 1997. Auburn, MA: Polytec PI, Inc. p. 50-70.
120. *User Manual: Olympus BX60 Microscope*. 1999: Olympus America Inc., Microscopes & Imaging Systems, www.Olympusamerica.com.
121. Osterberg, P.M., Gupta, R.K., Gilbert, J.R., and Senturia, S.D., *Quantitative Models for the Measurement of Residual Stress, Poisson Ratio and Young's Modulus Using Electrostatic Pull-In of Beams and Diaphragms*. in *Proceedings of Solid-State Sensors and Actuators Workshop*. 1994. Hilton Head, SC. p. 184-188.

122. Artz, B.E. and Cathey, L.W., *A Finite Element Method for Determining Structural Displacements Resulting from Electrostatic Forces*. in *Proceedings of Solid-State Sensors and Actuators Workshop*. 1992. Hilton Head, SC. p. 190-193.
123. Borest, A.P. and Schmidt, R.J., *Advanced Mechanics of Materials*. 2003, New York: John Wiley & Sons. p. 147-160.
124. Moffat, R.J., *Using Uncertainty Analysis in the Planning of an Experiment*. *Journal of Fluids Engineering*, 1985. 107: p. 173-178.
125. Manno, I., *Introduction To the Monte-Carlo Method*. 1999, Portland, OR: International Specialized Book Service Inc. p. 1-20.
126. *Guide to the Expression of Uncertainty in Measurement*. 1993. Geneva: International Organization for Standardization (ISO). ISBN 92-67-10188-9.
127. Coleman, H.W. and Steele, W.G., *Experimentation and Uncertainty Analysis for Engineers*. 1999, New York: John Wiley & Sons. p. 202-229.
128. Taylor, B.N. and Kuyatt, C.E., *Guidelines for Evaluating and Expressing the Uncertainty of NIST Measurement Results*. 1994, Gaithersburg, MD: National Institute of Standards and Technology.
129. Kline, S.J., *The Purposes of Uncertainty Analysis*. *Journal of Fluids Engineering*, 1985. 107: p. 153-160.
130. Kline, S.J. and McClintock, F.A., *Describing Uncertainties in Single-Sample Experiments*. *Mechanical Engineering*, 1953. 75(1): p. 3-8.
131. Schultz, T., *Acoustic Impedance Testing for Aeroacoustic Applications*. *Ph.D. Dissertation*. 2006. Gainesville, FL: University of Florida.
132. Sharpe, W.N., Jackson, K.M., Hemker, K.J., and Xie, Z., *Effect of Specimen Size on Young's Modulus and Fracture Strength of Polysilicon*. *Journal of Microelectromechanical Systems*, 2001. 10: p. 317-326.
133. Bendat, J.S. and Piersol, A.G., *Random Data: Analysis and Measurement Procedures*. 2000, New York: John Wiley & Sons. p. 272-286.

BIOGRAPHICAL SKETCH

Jian Liu received a B.E. in aerospace engineering and a M.S. in mechanical engineering from Nanjing University of Aeronautics and Astronautics, Nanjing, China, in 1998 and 2001 respectively. He also received a M.S. in aerospace engineering from the University of Florida, Gainesville, FL, in 2003. He is currently a doctoral student in the Department of Mechanical and Aerospace Engineering at the University of Florida. His dissertation focuses on the nonlinear dynamics of a dual-backplate capacitive MEMS microphone.